RECENT PROGRESS IN SURFACE ELECTROMAGNETIC MODES

EDITED BY: Lin Chen, Fei Gao, Wei E. I. Sha and Zhi Ning Chen

PUBLISHED IN: Frontiers in Physics

frontiers Research Topics

About Frontiers

Frontiers is more than just an open-access publisher of scholarly articles: it is a pioneering approach to the world of academia, radically improving the way scholarly research is managed. The grand vision of Frontiers is a world where all people have an equal opportunity to seek, share and generate knowledge. Frontiers provides immediate and permanent online open access to all its publications, but this alone is not enough to realize our grand goals.

Frontiers Journal Series

The Frontiers Journal Series is a multi-tier and interdisciplinary set of open-access, online journals, promising a paradigm shift from the current review, selection and dissemination processes in academic publishing. All Frontiers journals are driven by researchers for researchers; therefore, they constitute a service to the scholarly community. At the same time, the Frontiers Journal Series operates on a revolutionary invention, the tiered publishing system, initially addressing specific communities of scholars, and gradually climbing up to broader public understanding, thus serving the interests of the lay society, too.

Dedication to Quality

Each Frontiers article is a landmark of the highest quality, thanks to genuinely collaborative interactions between authors and review editors, who include some of the world's best academicians. Research must be certified by peers before entering a stream of knowledge that may eventually reach the public - and shape society; therefore, Frontiers only applies the most rigorous and unbiased reviews.
Frontiers revolutionizes research publishing by freely delivering the most outstanding research, evaluated with no bias from both the academic and social point of view. By applying the most advanced information technologies, Frontiers is catapulting scholarly publishing into a new generation.

What are Frontiers Research Topics?

Frontiers Research Topics are very popular trademarks of the Frontiers Journals Series: they are collections of at least ten articles, all centered on a particular subject. With their unique mix of varied contributions from Original Research to Review Articles, Frontiers Research Topics unify the most influential researchers, the latest key findings and historical advances in a hot research area! Find out more on how to host your own Frontiers Research Topic or contribute to one as an author by contacting the Frontiers Editorial Office: frontiersin.org/about/contact

ISSN 1664-8714
ISBN 978-2-88966-984-4
DOI 10.3389/978-2-88966-984-4

RECENT PROGRESS IN SURFACE ELECTROMAGNETIC MODES

Topic Editors:
Lin Chen, University of Shanghai for Science and Technology, China
Fei Gao, Zhejiang University, China
Wei E. I. Sha, Zhejiang University, China
Zhi Ning Chen, National University of Singapore, Singapore

Citation: Chen, L., Gao, F., Sha, W. E. I., Chen, Z. N., eds. (2021). Recent Progress in Surface Electromagnetic Modes. Lausanne: Frontiers Media SA. doi: 10.3389/978-2-88966-984-4

Table of Contents

frontiers in Physics

EDITORIAL
published: 13 May 2021
doi: 10.3389/fphy.2021.684584

Check for updates

Editorial: Recent Progress in Surface Electromagnetic Modes

Lin Chen[1]*, *Fei Gao*[2], *Wei E. I. Sha*[3] and *Zhi Ning Chen*[4]

[1] *Shanghai Key Lab of Modern Optical System, University of Shanghai for Science and Technology, Shanghai, China,* [2] *Key Laboratory of Advanced Micro/Nano Electronic Devices & Smart Systems of Zhejiang, College of Information Science and Electronic Engineering, Zhejiang University, Hangzhou, China,* [3] *State Key Laboratory of Modern Optical Instrumentation, College of Information Science and Electronic Engineering, Zhejiang University, Hangzhou, China,* [4] *Department of Electrical and Computer Engineering, National University of Singapore, Singapore, Singapore*

Keywords: surface modes, spoof plasmonics, metasurface, local field enhancement, localized surface plasmons

Editorial on the Research Topic

Recent Progress in Surface Electromagnetic Modes

Surface electromagnetic (EM) waves, decaying away from an interface between two different materials/structures, have a long history. By combining Maxwell's equations with material properties and boundary conditions, the surface excitations are characterized in terms of their dispersion, spatial profile, and field confinement. The earliest description of Surface EM waves was established in the context of radio waves propagating along the surface of a conductor of finite conductivity [1, 2]. In parallel to these two well-known contributions, another observation of anomalous intensity drops in spectra when visible light reflects at metallic gratings was also found in the visible domain [3] and later explained by Fano [4]. The concept of surface plasmon polaritons (SPPs) in the visible domain was first proposed by connecting fast electron beams at thin metallic foils [5] with diffraction gratings in the optical domain [6]. Although Ritchie proposed that fast electrons can be used for the excitation of surface plasmons in metal, the requirements of a high electric voltage and a vacuum environment make it impossible for practical applications. In this special issue, Liu et al. give an overview of recent breakthroughs in the low-energy direct excitation of surface plasmons based on an inelastic electron tunneling effect in tunnel junctions. As we have known, one advantage of SPPs is local electric field enhancement with a subwavelength scale, which benefits SPP-based sensors exhibiting high sensitivity and miniaturized size for single molecular sensing applications. The mini-review of Liu and Ma summarizes highly sensitive one-dimensional waveguide SPPs sensors in optical range with unique properties of easy integration, the confinement of light to scales one-tenth wavelength, and low cost. Another advantage of SPPs is the breakthrough of the diffraction limit of imaging resolution. The paper by Wang et al. demonstrates that the resolution of ghost imaging can be improved markedly by combining the SPPs structures with the high-frequency information through the structure algorithm. Another paper in this Research Topic by Li et al. demonstrates that the localized buried InGaAs channel n-MOSFETs has a lower leakage current compared to the surface InGaAs channel n-MOSFETs.

On the other hand, research in this field was limited to the visible or near-infrared spectrum for a long time due to the decrease in field penetration into the conductor at lower frequencies. However, as the surface of perfect conductors is textured, electromagnetic surface waves closely resembling SPPs can also be supported at the microwave and terahertz bands [7], which have even been known in the earlier middle of the 20 century [8, 9]. These spoof SPPs show rich physics and could have a number of important applications. Tang et al. propose broadband and high-efficiency conversion between the rectangular waveguide and the planar spoof SPPs at microwave frequencies, which could easily be extended in plasmonic circuits at terahertz frequencies. Besides

OPEN ACCESS

Edited and reviewed by:
Lorenzo Pavesi,
University of Trento, Italy

****Correspondence:***
Lin Chen
linchen@usst.edu.cn

Specialty section:
This article was submitted to Optics and Photonics, a section of the journal Frontiers in Physics

Received: *23 March 2021*
Accepted: *29 March 2021*
Published: *13 May 2021*

Citation:
Chen L, Gao F, Sha WEI and Chen ZN (2021) Editorial: Recent Progress in Surface Electromagnetic Modes. Front. Phys. 9:684584. doi: 10.3389/fphy.2021.684584

SPPs in the visible range or spoof SPPs at lower frequencies, there are other basic types of plasmonic excitations-localized surface plasmons (LSPs), which are referred to as the localized oscillations of electrons in metal nanoparticles. It is natural to extend the scope of spoof plasmonics to LSPs, known as "spoof LSPs," which have been found in metallic periodically textured sunflower shaped particles or metallic spiral structures both in the microwave [10] and terahertz range [11]. Zhou et al. investigate an electrically two-way Fano resonance switch in the two concentric spoof LSPs by loading a Schottky barrier diode at microwave frequencies. Liao et al. explore novel antenna composed of metallic spiral structure for spoof magnetic LSPs with horizontally polarized omnidirectional radiation. A groundless Spoof SPPs waveguide was applied to feed the antenna to effectively excite the spoof LSPs mode. At millimeter or terahertz frequencies, the transmission coefficient of ultrathin Spoof SPPs waveguide is usually measured by a vector network analyzer using an expanded module with two probe pins placed at ports IN and OUT to introduce and detect millimeter/terahertz signals from the expanded module [12]. The contribution by Su et al. considers the uncertainty and the impact of imperfect load calibration standard for on wafer calibration method, which benefits the measurement of planar millimeter/terahertz Spoof SPPs circuit.

In parallel to the spoof SPPs concept, another major original concept is metasurface, which exhibits the capacity of EM wavefront manipulation due to the interaction between an EM wave and two-dimensional meta-atom structures [13]. Their advent dramatically expanded the strong wavefront modulation capabilities of photonic materials and devices within the sub-wavelength scale. We note that the corrugated metallic surfaces mentioned above are also examples of metasurfaces with engineered electric responses. Xiong and Li present a simple free-standing double-layer all metallic metasurface by crossing fractal patterned aluminum foil, with high transmittance and low loss. Li et al. propose a transmission-type fused silica metasurface to manipulate the terahertz wavefront with the function of one/multi-spot focusing and non-diffracting Bessel beam generation. Wang and Zhai perform a microwave reflective angle insensitive circular polarization regulator using a chiral metasurface based on the unit cell having a z-shaped structure. Furthermore, there are several extended contributions with reconfigurable metasurfaces and metadevices. Xiong et al. describe the active control of terahertz wave transmission using Inorganic perovskite quantum dots embedded metasurface. Ding et al. examine a novel periodic metasurface structure with a through-hole array to improve the gain and radiation of the microstrip antenna. Ni et al. presented a broadband high gain polarization reconfigurable antenna based on metasurfaces. Ji et al. realize a terahertz reflective isolator based on the unique non-reciprocal magneto-plasmonic properties of InSb/dielectric interface to form a resonance cavity between the InSb and metasurface. Chen et al. study a graphene-based terahertz photodetector with metasurface to manipulate the surface EM modes. The photoresponse is enhanced due to the localized EM resonance, resulting in a nearly perfect absorption of the incident terahertz radiation.

Since the seminal works of Ebbesen [14], Pendry [7], and Capasso [13], the study of surface EM modes has been rediscovered and reemerged as an exciting field of research. More recently, the phenomena associated with surface EM modes are rapidly extending and significant work carried out in this field, such as Tamm plasmon-polaritons [15], edge state modes [16], effective SPPs (LSPs) [17], etc.

This Research Topic contains 16 articles devoted to the multifaceted development of ongoing studies in the area of surface EM modes. We add here relevant review articles [18, 19] and hope that this collection will serve as a useful compendium, contributing to growing interest and significant advances in this field that will benefit physicists and engineers in this ongoing field.

The 2021 IEEE APS will be held from December 4 to 10, 2021 in Marina Sands, Singapore. The focus will be state-of-the-art research in antennas, propagation, electromagnetic engineering, and radio science. Information about the Symposium can be found at the website https://2021apsursi.org/.

AUTHOR CONTRIBUTIONS

All authors listed have made a substantial, direct and intellectual contribution to the work, and approved it for publication.

FUNDING

This work has received funding in part from the Shanghai Shuguang Program (No. 18SG44).

ACKNOWLEDGMENTS

The Research Topic editors appreciate the multifaceted contributions of the authors, reviewers, and Frontiers staff who assisted in preparing the manuscripts.

REFERENCES

1. Sommerfeld A. Über die Fortpflanzung electrodynamischer Wellen längs eines Drahtes. *Ann Phys und Chemie*. (1899) 67:233–90. doi: 10.1002/andp.18993030202
2. Zenneck J. Über die Fortpflanzung ebener elektromagnetischer Wellen längs einer ebenen Leiterfläche und ihre Beziehung zur drahtlosen Telegraphie. *Ann d Phys*. (1907) 23:846–86. doi: 10.1002/andp.19073281003
3. Wood RW. On a remarkable case of uneven distribution of light in a diffraction grating spectrum. *Proc Phys Soc London*. (1902) 18:269–75. doi: 10.1080/14786440209462857
4. Fano U. The theory of anomalous diffraction gratings and of quasi-stationary waves on metallic surfaces (Sommerfeld's waves). *J Opt Soc Am*. (1941) 31:213–22. doi: 10.1364/JOSA.31.000213
5. Ritchie RH. Plasma losses by fast electrons in thin films. *Phys Rev*. (1957) 106:874–1. doi: 10.1103/PhysRev.106.874

6. Ritchie RH, Arakawa ET, Cowan JJ, Hamm RN. Surface-plasmon resonance effect in grating diffraction. *Phys Rev Lett.* (1968) 21:1530–33. doi: 10.1103/PhysRevLett.21.1530
7. Pendry JB, Martín-Moreno L, Garcia-Vidal FJ. Mimicking surface plasmons with structured surfaces. *Science.* (2004) 305:847–8. doi: 10.1126/science.1098999
8. Oliner AA, Hessel A. Guided waves on sinusoidally-modulated reactance surface. *IRE Trans Antennas Propag.* (1959) 7:161–5. doi: 10.1109/TAP.1959.1144771
9. Harvey FA. Periodic and guiding structures at microwave frequencies. *IRE Trans. Microw Theory Techn.* (1960) 8:30–61. doi: 10.1109/tmtt.1960.1124658
10. Pors A, Moreno E, Martin-Moreno L, Pendry JB, Garcia-Vidal FJ. Localized spoof plasmons arise while texturing closed surfaces. *Phys Rev Lett.* (2012) 108:223905. doi: 10.1103/PhysRevLett.108.223905
11. Chen L, Xu NN. Defect-induced Fano resonances in corrugated plasmonic metamaterials. *Adv Opt Mater.* (2017) 5:1600960. doi: 10.1002/adom.201600960
12. Chen L, Liao DG, Guo XG, Zhao JY, Zhu YM, Zhuang SL. Terahertz time domain spectroscopy and micro-cavity components for probing samples: a review. *Front Inf Technol Electron Eng.* (2019) 20:591. doi: 10.1631/FITEE.1800633
13. Yu N, Genevet P, Kats MA, Aieta F, Tetienne JP, Capasso F, et al. Light propagation with phase discontinuities: generalized laws of reflection and refraction. *Science.* (2011) 334:333–7. doi: 10.1126/science.1210713
14. Ebbesen TW, Lezec HJ, Ghaemi HF, Thio T, Wolff PA. Extraordinary optical transmission through sub-wavelength hole arrays. *Nature.* (1998) 391:667–69. doi: 10.1038/35570
15. Afinogenov BI, Bessonov VO, Soboleva IV, Fedyanin AA. Ultrafast all-optical light control with tamm plasmons in photonic nanostructures. *ACS Photonics.* (2019) 6:844–50. doi: 10.1021/acsphotonics.8b01792
16. Zeng Y, Chattopadhyay U, Zhu B. Electrically pumped topological laser with valley edge modes. *Nature.* (2020) 578:246–50. doi: 10.1038/s41586-020-1981-x
17. Li Z, Liu LL, Fernandez-Dominguez AT, Shi JF, Gu CQ, Garcia-Vidal FJ, et al. Mimicking localized surface plasmons with structural dispersion. *Adv Opt Mater.* (2020) 7:10. doi: 10.1002/adom.201900118
18. Gao Z, Wu L, Gao F, Luo Y, Zhang B. Spoof plasmonics: from metamaterial concept to topological description. *Adv Mater.* (2018) 30:1706683.doi: 10.1002/adma.201706683
19. Zhang X, Xu Q, Xia L, Li Y, Gu J, Tian Z, et al. Terahertz surface plasmonic waves: a review. *Adv. Photonics.* (2020) 2:014001.doi: 10.1117/1.AP.2.1.014001

Conflict of Interest: The authors declare that the research was conducted in the absence of any commercial or financial relationships that could be construed as a potential conflict of interest.

frontiers in Physics

ORIGINAL RESEARCH
published: 27 February 2020
doi: 10.3389/fphy.2020.00023

Terahertz Transmission Characteristics of Free-Standing Fractal Jesus-Cross Structure

*Ri-Hui Xiong and Jiu-sheng Li**

Centre for THz Research, China Jiliang University, Hangzhou, China

We have fabricated a Jesus-cross structure on aluminum foil using the femtosecond laser technique. Using the terahertz time-domain spectroscopy (THz-TDS) system, the transmission properties of free-standing double-layer crossing fractal structure are tested. The parameters of the proposed structure were optimized using the finite element frequency domain technology of commercial software CST Microwave Studio package. The dimensions of the aluminum foil periodically patterned with crossing fractal structure are 1.5 × 1.5 cm^2. The resonant frequencies of the proposed structure are 0.216 and 0.735 THz with 3-dB bandwidths of 62 and 15 GHz, respectively. The transmission ratio can reach to 0.89 and 0.57. It indicates the structure having dual-band filtering performance. This work has the potential to open a new avenue as a filter working for free-space terahertz radiation.

Keywords: terahertz transmission, transmission ratio, fractal, CST, THz-TDS

OPEN ACCESS

Edited by:
Lin Chen,
University of Shanghai for Science and Technology, China

Reviewed by:
Dejun Liu,
Shanghai Normal University, China
Qiye Wen,
University of Electronic Science and Technology of China, China
Min Hu,
University of Electronic Science and Technology of China, China

****Correspondence:***
Jiu-sheng Li
lijsh2008@126.com

Specialty section:
This article was submitted to Optics and Photonics, a section of the journal Frontiers in Physics

Received: *04 November 2019*
Accepted: *27 January 2020*
Published: *27 February 2020*

Citation:
Xiong R-H and Li J (2020) Terahertz Transmission Characteristics of Free-Standing Fractal Jesus-Cross Structure. Front. Phys. 8:23. doi: 10.3389/fphy.2020.00023

INTRODUCTION

Nowadays, terahertz (THz) wave has attracted widespread concern due to its unique applications such as wireless communication, imaging, security, etc. As an essential part of a terahertz wave system, terahertz wave manipulation is highly required. Different functional THz devices have been reported, such as modulator [1], filters [2, 3], switches [4–6], phase shifters [7], polarizers [8], absorbers [9, 10], and splitters [11–13]. We all know that terahertz wave filter is a kind of important signal processing device [14–16]. However, most of the reported terahertz filters are fabricated using photolithography processes, which results in high cost and is time consuming. Recently, various concepts of terahertz wave filters utilizing liquid crystal, frequency selective surface (FSS), graphene, photonic crystal, or metamaterial have been described [17–24]. To the best of our knowledge, relatively few studies on simple and efficient method to fabricate terahertz filter are reported. Therefore, terahertz filters are required for further research, and it is very valuable to find a simple method for fabricating terahertz filter.

In this article, we present a free-standing double-layer crossing fractal structure, which consists of symmetrical periodic metallic crossing fractal patterned on aluminum foil. We demonstrate a technique using femtosecond laser for aluminum foil fabrication to make a compact and free-standing terahertz band-pass filter. Theoretical simulation was carried out using the full-wave finite element frequency domain method of the commercial software CST Microwave Studio package. The measured terahertz transmission response spectrum shows a reasonable correspondence with simulation. The designed structure has simplicity, small size, high transmittance, and low loss.

In addition, the free-standing double-layer crossing fractal-based terahertz filters are suitable for application in terahertz systems due to their small size and fabrication using femtosecond laser high-precision micromachining technology. This work has the potential to open a new avenue as a dual-band filter working for free-space terahertz wave radiation.

DEVICE STRUCTURE DESIGN AND PARAMETERS STUDY

The structure of the present free-standing crossing fractal is depicted in **Figure 1**. The array of crossing fractal structures is fabricated on aluminum foil with a conductivity of 3.56×10^7 S/m. The geometrical parameters of the crossing fractal unit cell are of *a*, *g*, *h*, and *t*. The structure is calculated using CST Microwave Studio. The unit cell is applied with periodic boundary conditions. Terahertz propagation vector is perpendicularly incident to the crossing fractal structure. The optimized dimensions of the crossing fractal structure are as follows: $a = 500\,\mu$m, aluminum foil thickness of $10\,\mu$m, $t = 45\,\mu$m, $h = 480\,\mu$m, $s = 135\,\mu$m, and $g = 30\,\mu$m. Here, we have simulated the frequency behavior of the power transmission based on the varied parameters such as lattice period *a* and distance between two layer aluminum foils *t*. **Figure 2** shows the frequency behavior of the crossing fractal-air-crossing fractal power transmission for different lattice periods of the crossing fractal geometrical parameter *a* as the other parameters using their optimized values. From **Figure 2**, one sees that the lattice period *a* mainly controls the first resonance frequency of the proposed structures. Particularly, it can be found that the first resonance frequency moves downward as the lattice period *a* increases. For the crossing fractal-air-crossing fractal structure, one can see that the first resonant central frequency is 0.24 THz with transmittance of 0.96. At this time, the 3-dB bandwidth is 0.189–0.287 THz, covering the terahertz communication region, when *a* equals $500\,\mu$m. In addition, the second resonant central frequency is 0.64 THz. The 3-dB bandwidth is from 0.584 to 0.704 THz.

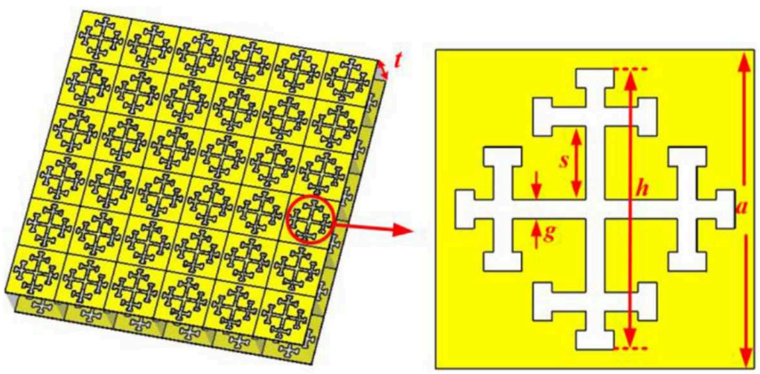

FIGURE 1 | Schematic of the free-standing double-layer crossing fractal structure and unit cell.

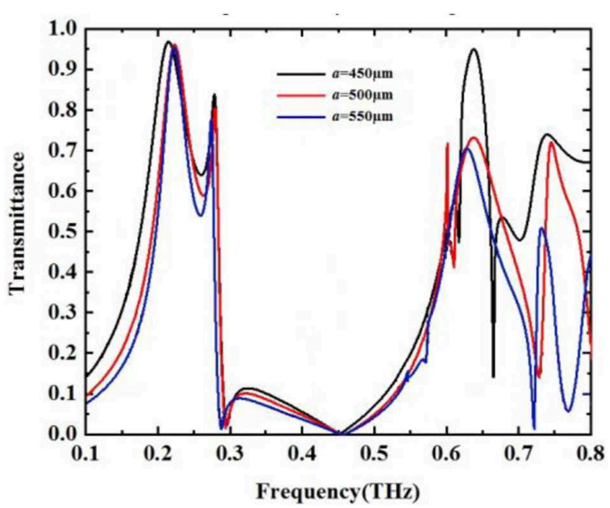

FIGURE 2 | Transmittance spectra of the proposed crossing fractal-air-crossing fractal structure for various values of *a*.

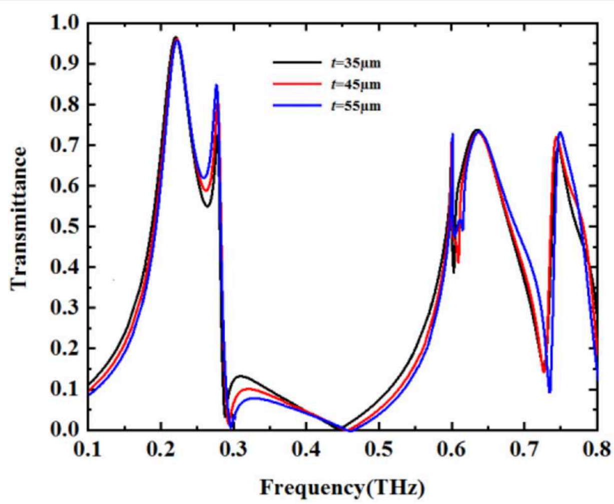

FIGURE 3 | Transmittance spectra of the proposed crossing fractal-air-crossing fractal structure for various values of *t*.

When the distance between two layer aluminum foils (t) changes from 35 to 55 μm, the other sizes of the proposed crossing fractal structure still adopt the optimized values. **Figure 3** depicts the terahertz power transmission with different frequencies. It can be noted that the first and the second resonance central frequencies move downward as the distance between two layer aluminum foils of the parameter t is increased on the crossing fractal-air-crossing fractal structure. When t is equal to 45 μm, the two resonant peaks are of 0.24 and 0.64 THz, respectively. The 3-dB bandwidth of the first and second resonance peaks range from 0.189 to 0.287 THz and from 0.584 to 0.704 THz, respectively. To

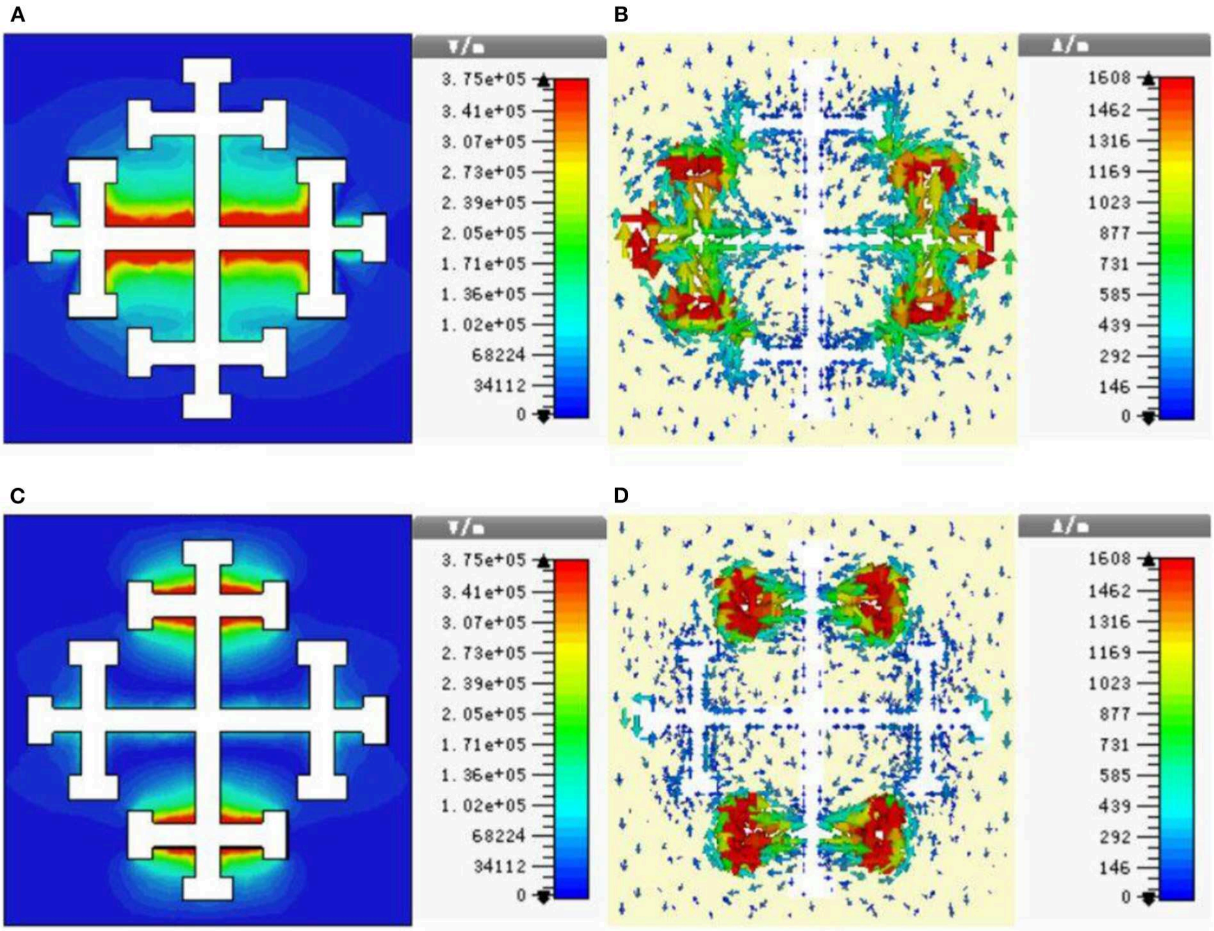

FIGURE 4 | Electric field distribution of the unit cell at the resonance frequency of **(A)** 0.24 THz and **(C)** 0.64 THz and the simulated surface current distribution on the crossing fractal layer at the resonance frequency of **(B)** 0.24 THz and **(D)** 0.64 THz.

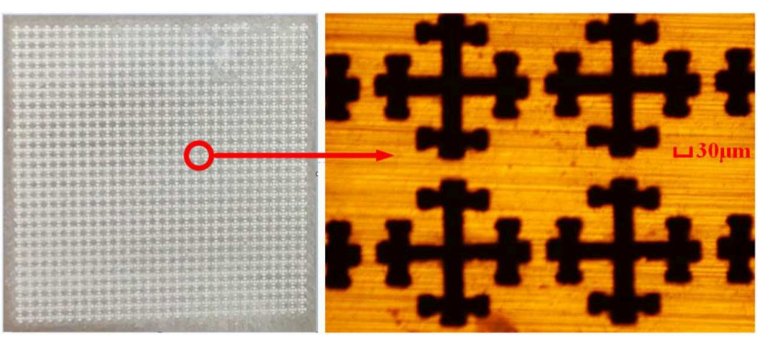

FIGURE 5 | Photography of the fabricated structure and a local enlarged microscopic image.

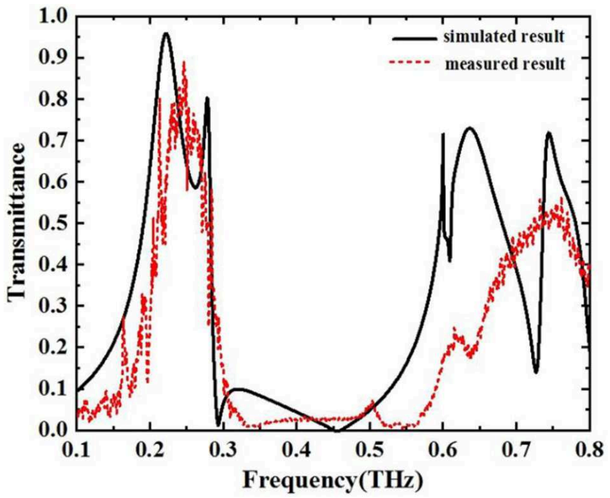

FIGURE 6 | Measured transmittance spectra of the proposed two-layer crossing fractal structure.

cover the terahertz communication frequency band, we set the gap between two layer aluminum foils (t) as 45 μm. To clarify the transmission mechanism of the proposed structure, we simulated the electric field and surface current of double-layer crossing fractal structure. From **Figures 4A,B**, we can find that the resonance of 0.24 THz is generated by the electric dipole response of two perpendicular crossing arms. The surface current mainly flows on the perpendicular metal arms of the crossing fractal pattern (see **Figure 4B**). For the resonance frequency of 0.64 THz, as shown in **Figures 4C,D**, the resonance is stimulated by the electric dipole response of the horizontal arm. The surface free charge accumulated at the left and right areas of the horizontal arm forms the external electric field (see **Figure 4D**). It is pretty obvious that the first and the second transmission peaks are associated with the resonances of the crossing fractal structure.

FABRICATION AND MEASUREMENT

According to the optimized physical dimensions, the proposed free-standing crossing fractal structure is fabricated on a 10-μm aluminum foil with a conductivity of 3.56×10^7 S/m using an ultrafast high-intensity laser technique. The femtosecond laser has 45 fs pulse width, 800 nm wavelength, and 1 kHz repetition rate. In addition, the laser with 50 μJ pulse energy, 10 μm spot size, and 1 mm/s moving speed is employed to fabricate crossing fractal structure. The aluminum foil is placed on a precise computer-controlled platform. An objective lens is used to focus the femtosecond laser on the aluminum foil surface. **Figure 5** shows the photography of the fabricated structure and a local enlarged microscopic image. A Z2 THz-TDS system from Zomega Co. Ltd. is employed to test the terahertz power transmission of the present crossing fractal-air-crossing fractal structure at room temperature of 25°C. To achieve a high signal/noise ratio in the frequency range from 0.2 to 0.8 THz, each spectrum was obtained by averaging three scans. Thus, the results provided here are repeatable and credible. **Figure 6** shows the measured and simulated transmittance spectra of the proposed crossing fractal structure. The transmittance of the single-layer structure can be given by $S = |S_{21}|^2$, where S_{21} is the transmission coefficient. Similarly, the power transmittance of the two-layer structure is expressed as $T = |S|^2$. The measured results show that the crossing fractal-air-crossing fractal structure has a 3-dB bandwidth of 62 GHz from 0.216 to 0.278 THz with center frequency located at 0.245 THz, and 15 GHz from 0.66 to 0.81 THz with center frequency located at 0.735 THz. The first and the second transmission peaks of the crossing fractal-air-crossing fractal structure are 0.89 and 0.57, respectively. The experimental result has some striking discrepancy with the simulation due to the limitation of its mechanical tolerance, which has been neglected in our simulation.

CONCLUSION

In summary, we proposed a dual-band terahertz band-pass filter based on the free-standing crossing fractal structure working for free-space terahertz radiation. We analyzed the filtering spectrum performance with various geometrical parameters of the double-layer crossing fractal structure. Using the femtosecond laser technique, we have fabricated double-layer Jesus-cross structure on aluminum foil. The frequency response of the filter is tested using THz-TDS. The resonant peaks of the filter are at 0.245 THz with the transmittance of 0.89 and 0.735 THz with the transmittance of 0.57, respectively. The experimental result has some discrepancies with those of our simulation. Owing to the symmetrical characteristic of the free-standing crossing fractal structure, the proposed filter is polarization insensitive. Our design will have great potential applications in terahertz communications, imaging, and terahertz sensor systems due to its simple structure and ease of manufacturing.

DATA AVAILABILITY STATEMENT

All datasets generated for this study are included in the article/supplementary material.

AUTHOR CONTRIBUTIONS

R-HX carried out the whole experiment. JL wrote the paper. All authors discussed the results and contributed to the paper.

FUNDING

This work was supported by the National Natural Science Foundation of China (Grant Nos. 61871355 and 61831012).

REFERENCES

1. Han Z, Kohno K, Fujita H, Hirakawa K, Toshiyoshi H. MEMS reconfigurable metamaterial for terahertz switchable filter and modulator. *Opt Express*. (2014) **22**:21326–39. doi: 10.1364/OE.22.021326
2. Rao L, Yang D, Zhang L, Li T, Xia S. Design and experimental verification of terahertz wideband filter based on double-layered metal hole arrays. *Appl Opt*. (2012) **51**:912–8. doi: 10.1364/AO.51.000912
3. Miyamaru F, Hangyo M. Anomalous terahertz transmission through double-layer metal hole arrays by coupling of surface plasmon polaritons. *Phys Rev B*. (2005) **71**:165408. doi: 10.1103/PhysRevB.71.165408
4. Javan A, Granpayeh N. Terahertz wave switch based on photonic crystal ring resonators. *Opt. Quant Electron*. (2008) **40**:695–705. doi: 10.1007/s11082-008-9257-y
5. Li J, He J, Hong Z. Terahertz wave switch based on silicon photonic crystals. *Appl Opt*. (2007) **46**:5034–7. doi: 10.1364/AO.46.005034
6. Wilk R, Vieweg N, Kopschinski O, Koch M. Liquid crystal based electrically switchable Bragg structure for THz waves. *Opt Express*. (2009) **17**:7377–82. doi: 10.1364/OE.17.007377
7. Wu Y, Ruan X, Chen C, Shin Y, Lee Y, Niu J, et al. Graphene/liquid crystal based terahertz phase shifters. *Opt Express*. (2013) **21**:21395–402. doi: 10.1364/OE.21.021395
8. Huang Z, Parrott E, Park H, Chan H, MacPherson E. High extinction ratio and low transmission loss thin-film terahertz polarizer with a tunable bilayer metal wire-gridstructure. *Opt Lett*. (2014) **39**:793–6. doi: 10.1364/OL.39.000793
9. Fu SM, Zhong YK, Ju NP, Tu MH, Chen BR, Lin A. Broadband polarization-insensitive metamaterial perfect absorbers using topology optimization. *IEEE Photon J*. (2016) **8**:1–11. doi: 10.1109/JPHOT.2016.2602335
10. Tang JY, Xiao ZY, Xu KK, Ma XL, Wang ZH. Polarization-controlled metamaterial absorber with extremely bandwidth and wide incidence angle. *Plasmonics*. (2016) **11**:1393–9. doi: 10.1007/s11468-016-0189-2
11. Benjamin S, Weng B, Shepherd R, Abbott D, Fumeaux C. Inkjet printed conductive polymer-based beam-splitters for terahertz applications. *Opt Mater Express*. (2013) **3**:1242–9. doi: 10.1364/OME.3.001242
12. Lai W, Born N, Schneider L, Rahimi-Iman A, Balzer J, Koch M. Broadband antireflection coating for optimized terahertz beam splitters. *Opt Mater Express*. (2015) **5**:2812–9. doi: 10.1364/OME.5.002812
13. Li JS, Xu DG, Yao JQ. Compact terahertz wave polarizing beam splitter. *Appl Opt*. (2010) **49**:4494–7. doi: 10.1364/AO.49.004494
14. Kaliteevski MA, Brand S, Cook JG, Abram RA, Chamberlain JM. Terahertz filter based on refractive properties of metallic photonic crystal. *Opt Express*. (2008) **16**:7330–5. doi: 10.1364/OE.16.007330
15. Lo SZA, Murphy TE. Nanoporous silicon multilayers for terahertz filtering. *Opt Lett*. (2009) **34**:2921–3. doi: 10.1364/OL.34.002921
16. Liang L, Jin B, Wu J, Huang Y, Ye Z, Huang X, et al. A flexible wideband bandpass terahertz filter using multi-layer metamaterials. *Appl Phys B*. (2013) **113**:285–90. doi: 10.1007/s00340-013-5470-x
17. Lin Y, Qian Y, Ma F, Liu Z, Kropelnicki P, Lee C. Development of stress-induced curved actuators for a tunable THz filter based on double split-ring resonators. *Appl Phys Lett*. (2013) **102**:111908. doi: 10.1063/1.4798244
18. Lu M, Li W, Brown ER. Second-order bandpass terahertz filter achieved by multilayer complementary metamaterial structures. *Opt Lett*. (2011) **36**:1071–3. doi: 10.1364/OL.36.001071
19. Li S, Liu H, Sun Q, Huang N. A tunable terahertz photonic crystal narrow-band filter. *IEEE Photon Technol Lett*. (2015) 27:752–4. doi: 10.1109/LPT.2015.2391127
20. Vieweg N, Born N, Al-Naib I, Koch M. Electrically tunable terahertz notch filters. *Infrared J Millimeter Terahertz Waves*. (2012) **33**:327–32. doi: 10.1007/s10762-012-9877-y
21. Yang K, Liu S, Arezoomandan S, Nahata A, Sensale-Rodriguez B. Graphene-based tunable metamaterial terahertz filters. *Appl Phys Lett*. (2014) **105**:093105. doi: 10.1063/1.4894807
22. Correas-Serrano D, Gomez-Diaz JS, Carrier JP, Melcón ’AA. Graphene-based plasmonic tunable low-pass filters in the terahertz band. *IEEE Trans Nanotechnol*. (2014) **13**:1145–53. doi: 10.1109/TNANO.2014.2344973
23. Lee ES, Lee SG, Kee CS, Jeon TI. Terahertz notch and low-pass filters based on band gaps properties by using metal slits in tapered parallel-plate waveguides. *Opt Express*. (2011) 19:14852–9. doi: 10.1364/OE.19.014852
24. Chen L, Liao D, Guo X, Zhao J, Zhu Y, Zhuang S. Terahertz time-domain spectroscopy and micro-cavity components for probing samples: a review. *Front Inform Technol Electron Eng*. (2019). **20**:591–607. doi: 10.1631/FITEE.1800633

Conflict of Interest: The authors declare that the research was conducted in the absence of any commercial or financial relationships that could be construed as a potential conflict of interest.

frontiers in Physics

ORIGINAL RESEARCH
published: 06 March 2020
doi: 10.3389/fphy.2020.00051

Reliability of Buried InGaAs Channel n-MOSFETs With an InP Barrier Layer and Al_2O_3 Dielectric Under Positive Bias Temperature Instability Stress

Haiou Li [1], Kangchun Qu [1], Xi Gao [1], Yue Li [1], Yonghe Chen [1], Zhiping Zhou [1], Lei Ma [1], Fabi Zhang [1], Xiaowen Zhang [1], Tao Fu [1], Xingpeng Liu [1], Yingbo Liu [1], Tangyou Sun [1]* and Honggang Liu [2]*

[1] Guangxi Key Laboratory of Precision Navigation Technology and Application, Guilin University of Electronic Technology, Guilin, China, [2] Microwave Device and IC Department, Institute of Microelectronics, Chinese Academy of Sciences, Beijing, China

The positive bias temperature instability (PBTI) reliability of buried InGaAs channel n-MOSFETs with an InP barrier layer and Al_2O_3 gate dielectric under medium field (2.7 MV/cm) and high field (5.0 MV/cm) are investigated in this paper. The Al_2O_3/InP interface of the insertion of an InP barrier layer has fewer interface and border traps compared to that of the Al_2O_3/InGaAs interface. The subthreshold slope, transconductance, and shift of V_g are studied by using the direct-current I_d-V_g measurements under the PBTI stress. The experimental results show that the degradation of positive ΔV_g under the medium field stress is mainly caused by the acceptor trap, while the donor trap under the high field stress become dominant in the subthreshold region, which leads to the negative shift in V_g. The medium field stress-induced acceptor traps are attributed by the InP barrier layer in the subthreshold region, resulting that the low leakage current can be achieved in the buried InGaAs channel n-MOSFETs with an InP barrier layer compared to the surface InGaAs channel n-MOSFETs.

Keywords: PBTI, Al_2O_3/InP interface, InGaAs MOSFET, border trap, buried channel

OPEN ACCESS

Edited by:
Lin Chen,
University of Shanghai for Science and Technology, China

Reviewed by:
Yilin Sun,
Tsinghua University, China
Jifeng Liu,
Dartmouth College, United States

***Correspondence:**
Tangyou Sun
suntangyou@guet.edu.cn
Honggang Liu
liuhonggang@ime.ac.cn

Specialty section:
This article was submitted to Optics and Photonics, a section of the journal Frontiers in Physics

Received: *21 December 2019*
Accepted: *20 February 2020*
Published: *06 March 2020*

Citation:
Li H, Qu K, Gao X, Li Y, Chen Y, Zhou Z, Ma L, Zhang F, Zhang X, Fu T, Liu X, Liu Y, Sun T and Liu H (2020) Reliability of Buried InGaAs Channel n-MOSFETs With an InP Barrier Layer and Al_2O_3 Dielectric Under Positive Bias Temperature Instability Stress. Front. Phys. 8:51. doi: 10.3389/fphy.2020.00051

INTRODUCTION

InGaAs was considered for use as the n-type high-mobility channel material because it has higher electron mobility and smaller electron effective mass than that of silicon [1–3]. The complementary metal oxide semiconductor (CMOS) structure can be realized by integrating III-V n-MOSFETs and Ge p-MOSFETs on a Si CMOS platform [4–6]. However, one of the most critical problems that must be solved to realize III-V MOSFETs is the formation of a stable MOS interface with low trap density [7]. Compared with the SiO_2/Si system, the III-V native oxides negatively affect fermi-level pinning and current drift [8–10]. The atomic layer deposited (ALD) Al_2O_3 dielectric in surface InGaAs channel MOSFETs can achieve a thermally stable interface and large band offsets, as confirmed by the previous research on the dielectric layer of InGaAs MOSFETs [11–13]. However, Al_2O_3/InGaAs interface traps and border traps in the dielectric layer remain high, which reduces the effective channel mobility and results in reliability instability in InGaAs MOSFETs [14–16]. Based on the poor interface quality of InGaAs and Al_2O_3, the introduction of a barrier layer between the Al_2O_3 dielectric and InGaAs channel considerably improves channel electron mobility, transconductance, and drive current [17–19]. Although the InGaAs channel and Al_2O_3 dielectric are separated by the barrier layer, high interface traps and border traps considerably affect device reliability under bias temperature instability (BTI) stress [20–22]. To reduce interface defect density, the interface passivation techniques of N passivation treatment [23–25] and sulfur passivation treatment [26–28] have been investigated to improve the interface properties and reliability.

Bias temperature instability stress directly leads to the degradation of threshold voltage, subthreshold slope, and on-state current. The interface trap and border trap induced by bias temperature instability stress are also considered to be the causes of the degradation of III-V MOSFET performance. Li et al. investigated the surface InGaAs channel n-MOSFETs under positive bias temperature instability (PBTI) stress and recovery [29]. They explained that high defect density exists at the InGaAs and Al_2O_3 interface, which includes both interface traps and border traps, and the PBTI stress induces mainly border traps. However, few studies have reported the buried channel InGaAs MOSFETs with a barrier layer under PBTI stress.

In this paper, we experimentally studied the mechanisms of the buried InGaAs channel n-MOSFETs with an InP barrier layer under PBTI stress and recovery. The interface and border traps are estimated in the Al_2O_3/InP and Al_2O_3/InGaAs interfaces. The degradation of I_d-V_g during the PBTI tests shows a shift in V_g under a medium field (2.7 MV/cm), which is the opposite of that observed under a high field (5.0 MV/cm) in buried InGaAs channel n-MOSFETs. The effects of PBTI stress in the buried InGaAs channel n-MOSFETs with an Al_2O_3/InP interface were investigated by performing the subthreshold slope, transconductance, and V_g shift. The specific border traps are quantified to analyze the reliability of the device under the PBTI stress.

EXPERIMENTAL

Fabrication Process

The main structure of Si-based buried $In_{0.25}Ga_{0.75}As$ channel n-MOSFETs used in this paper is illustrated in **Figure 1**. The layer structure was grown on InP substrate by metal–organic chemical vapor deposition (MOCVD) and consisted of a 20 nm $In_{0.52}Al_{0.48}As$ buffer layer, a 2 nm $In_{0.6}Al_{0.4}As$ doping layer with Be doping concentration of 3×10^{18} cm^{-3}, a 5 nm $In_{0.52}Al_{0.48}As$ barrier layer, a 5 nm $In_{0.25}Ga_{0.75}As$ channel layer, a 3 nm InP barrier layer, and a 40 nm $In_{0.53}Ga_{0.47}As$ cap layer with N-type doping concentration of 2×10^{19} cm^{-3}. During the device fabrication process, benzocyclobutene (BCB) is used to bond the InP wafer to the Si wafer, and the two-step surface cleaning process was carried out. First, a 10% w/t HCl solution was applied for 1 min to remove the native oxide layer, and 20% w/t NH_4OH solution was applied for 6 min. Second, 20% $(NH_4)_2S$ solution was applied to passivate the interface of the InP barrier layer for 15 min at room temperature [26, 27]. Then, 8 nm of Al_2O_3 (i.e., gate dielectric) was deposited by Beneq TFS-200 atomic layer deposition (ALD) system at the substrate temperature of 300°C. A postdeposition anneal (PDA) was carried out at 400°C for 30 s in N_2 atmosphere. Ti/Au gate metal was evaporated by an

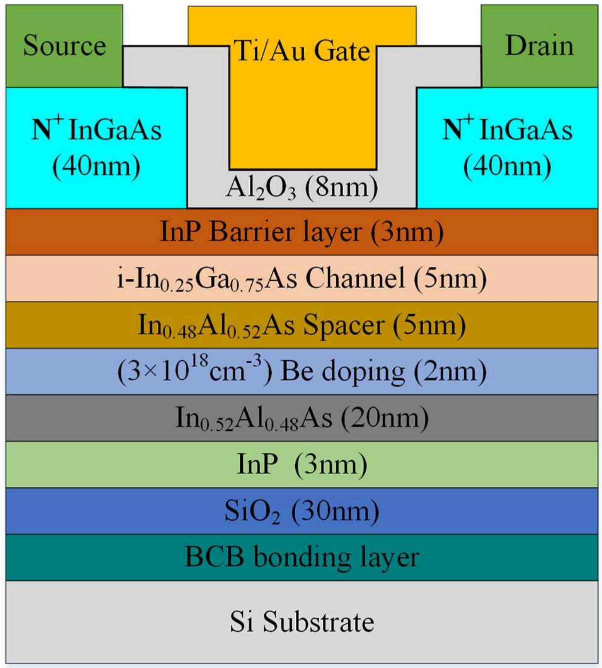

FIGURE 1 | Main structure of buried $In_{0.25}Ga_{0.75}As$ channel n-MOSFETs with 3 nm InP barrier layer and 8 nm Al_2O_3 gate dielectric.

electron beam system. The post metal anneals (PMA) at 300°C for 30 s in N_2 was carried out in the rapid thermal annealing system. Source and drain electrodes (Ni/Ge/Au/Ge/Ni/Au) were deposited by electron beam evaporation and annealing at 270°C for 3 min. The transistors have a 400-μm channel width and a 4-μm channel length (L).

Measurement Methods

DC current-voltage (I-V) characterization was achieved with an Agilent B1500A semiconductor device analyzer. In the I-V measurements [30], the drain voltage (V_d) was set to 50 mV, and the source and substrate were grounded. During the PBTI stress phase, two different gate voltages were selected during the PBTI stress phase, and the gate field strengths were calculated to be $E = 2.7$ and $E = 5.0$ MV/cm, respectively, based on the simulation, while $V_s = V_d = V_b = 0$ V. All DC I_d-V_g tests were carried out at room temperature (300 K). The PBTI test contains a 500 s stress phase and a 500 s recovery phase, as shown in **Figure 2**. During the stress phase, PBTI stress is set to 2.7 MV/cm and to 5 MV/cm for Al_2O_3 for a duration of 500 s. Before applying the stress, we first measured the initial I_d-V_g curve by using a fresh sample (I-line). After a 500-s PBTI stress, the S line was measured; the R lines were the I_d-V_g curves obtained from the sample during the 500 s recovery.

RESULTS AND DISCUSSION

Interface Characteristics

The distribution curves of interface trap density (D_{it}) are extracted from the multifrequency (1 MHz to 1 KHz) C-V

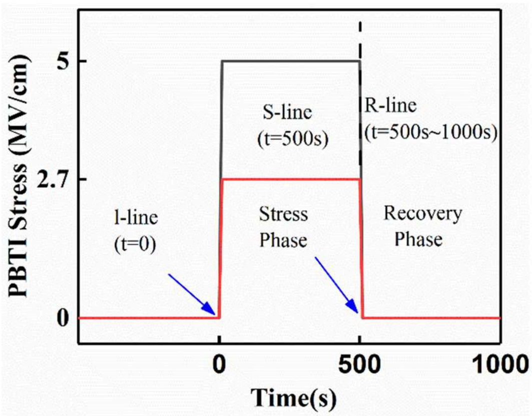

FIGURE 2 | Schematic diagram of the PBTI test setup. The PBTI test contains a 500 s stress phase and a 500 s recovery phase. During the stress phase, PBTI stress is set to be 2.7 and 5.0 MV/cm for Al_2O_3 for a duration of 500 s.

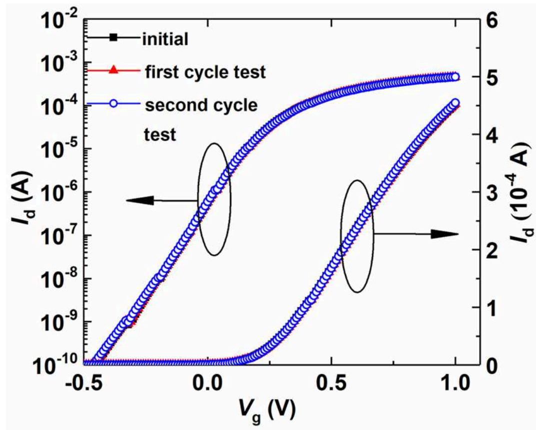

FIGURE 4 | Comparison of DC I_d-V_g measurement curves of the buried $In_{0.25}Ga_{0.75}As$ channel n-MOSFETs under different test cycles.

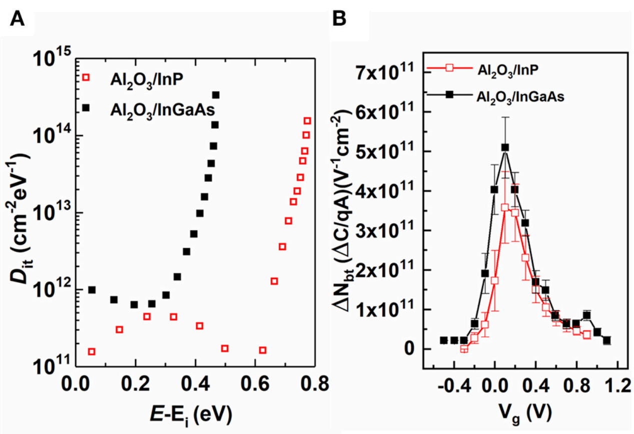

FIGURE 3 | Distribution curves of **(A)** the interface and **(B)** border trap densities of Al_2O_3/InGaAs and Al_2O_3/InP capacitances extracted from the multifrequency *C-V* measurement, respectively.

curves of the $Al_2O_3/In_{0.25}Ga_{0.75}As$ capacitance and Al_2O_3/InP capacitance, respectively, by using the Castagne-Vapaille method [31], as shown in **Figure 3A**. Because oxide traps (border trap) near the interface are mainly induced by the PBTI stress [32], InP/InGaAs interface trap can be negligible. The D_{it} distribution of Al_2O_3/InP is clearly below that of Al_2O_3/InGaAs, especially the downtrend of the D_{it} distribution of the Al_2O_3/InP interface near the mid-gap and is just opposite to the D_{it} distribution of the Al_2O_3/InGaAs interface near the mid-gap. Both Al_2O_3/InP and Al_2O_3/InGaAs interfaces are treated with sulfur passivation. The lower interface trap can be realized by employing an InP barrier layer. To further analyze the effect of the slow border trap between Al_2O_3/InP and Al_2O_3/InGaAs, the border trap density (ΔN_{bt}) [29] can be described by the *C-V* hysteresis curve shown in **Figure 3B**. The ΔN_{bt} distribution of the Al_2O_3/InP interface is less than that of Al_2O_3/InGaAs, which indicates that low border traps are achieved in the Al_2O_3/InP interface.

Direct-Current I_d-V_g Measurements

Unlike the Si MOSFET under positive bias temperature instability stress, the oxide traps of the InP/Al_2O_3 are generated during the stress phase. An uninterrupted cycle test on the same device can determine whether the test stress contributes to the I_d-V_g curve drift. The I_d-V_g curves of the buried InGaAs n-MOSFETs are shown in **Figure 4**. Compared with a fresh line, there is no distinct shift in I_d-V_g curves for either the subthreshold or the on-state region, and there is no clear change in current after the first cycle test. In the second cycle measurement curve, the I_d-V_g curves still do not show any shift. The subthreshold slope (*SS*) and on-state current remain the same compared with the fresh line, which indicates that neither negative nor positive charges were created under the measuring stresses.

According to the simulation results by Varghese et al. [33], the recoverable donor traps impact negative ΔV_g in the subthreshold region. Acceptor traps are essential for inducing a positive *I*-*V* curve shift in both the subthreshold and on-state regions. **Figures 5A,B** show the DC I_d-V_g curves measured for the fresh device before stress (*I* line) and under PBTI stress (*S* line) ($E = 2.7$ and $E = 5.0$ MV/cm) after 500 s as well as the recovery (*R* line) after 500 s. Compared with the *I*, *S*, and *R* lines in the medium and high fields (2.7 MV/cm and 5.0 MV/cm), there are two cases in the subthreshold region and in the on-state region. (1) In a medium field (E=2.7 MV/cm), the V_g shift ΔV_g at a constant drain current is positive both in the subthreshold and on-state regions, which indicates that negative charges were created after the PBTI stress. The I_d-V_g curve of the *R* line still demonstrates a negative shift in the on-state region compared with that of the *S* line. It is clear that acceptor traps, which are induced by the medium field strength stress, are recoverable. The stress-induced recoverable acceptor traps exist in the on-state region. However, the drain current of the *R* line coincides with that of *S* line in the subthreshold region, indicating the medium field strength stress-induced recoverable traps are not shown in the subthreshold region. (2) In a high field (E=5.0 MV/cm), the V_g

shift ΔV_g is negative in the subthreshold region, indicating donor traps are created after the PBTI stress of 5.0 MV/cm. The V_g shift ΔV_g is positive in the on-state region, demonstrating acceptor traps are created after the PBTI stress. The two crossing points, which mean a balance between acceptor trap and donor trap, are founded in 500 s of PBTI and 500 s of recovery with initial curve. The results show that donor traps induce negative V_{g} shift of I_{d}-V_{g} curves, larger shift with lower I_{d} current level. The acceptor traps induce positive shift of I_{d}-V_{g} curves, larger shift with higher I_{d} current level. The high field stress induced donor traps have a large density in distribution of energy gap, and their distribution extends to the conduction band, just opposite to the distribution trend of acceptor traps in the energy gap, which are consistent with that of the surface channel InGaAs n-MOSFETs [29, 33]. By comparing the *S* line with initial curve under the high field strength stress, the shift of crossing point is found to be negative in the *R* line with initial curve, indicating the donor traps are almost recoverable. Compared with the *S* line, the *R* line demonstrates a negative shift in the on-state region, indicating there are fewer recoverable donor traps than recoverable acceptor traps in the on-state region.

In surface channel InGaAs n-MOSFETs [29], stress-induced donor traps produce a negative shift in threshold voltage under the 2.7 MV/cm stress. However, stress-induced acceptor traps produce a positive shift in threshold voltage under the 2.7 MV/cm stress in buried channel InGaAs n-MOSFETs. Meanwhile, the I_{d}-V_{g} curves of the *S* and *R* lines do not have an offset in the subthreshold region. The results indicate that no donor traps are induced under medium field for the buried channel device. The Al_2O_3/InP interface has a lower interface trap density than that of the Al_2O_3/InGaAs interface in the distribution of energy gap, especially the downtrend of D_{it} distribution of the Al_2O_3/InP interface near the mid-gap, which is opposite of the D_{it} distribution of the Al_2O_3/InGaAs interface near the mid-gap shown in **Figure 3A**. The effect of low defect density is not serious in the recovery curve of the buried channel InGaAs n-MOSFETs in the subthreshold region under medium field strength, so buried channel InGaAs n-MOSFETs with Al_2O_3/InP interface show as a completely different trend than that of surface channel InGaAs n-MOSFETs in the recovery phase.

Time-dependence of ΔV_g in the on-state and subthreshold regions is shown in **Figures 6A,B** respectively. The value of ΔV_{g} shifts to positive direction in the on-state region under medium and high field strengths. From 500 to 1,000 s of recovery, ΔV_g of the two recovery curves continues the downward trend in the on-state region. The result shows recoverable acceptor traps have been proved to be recoverable in the on-state region under the field stress. The degradation of negative ΔV_g under high field stress is clearly smaller than the degradation of positive ΔV_g under medium field stress, indicating donor traps are induced under high field stress in the subthreshold region. Because stress-induced donor traps are fully recovered in the subthreshold region, V_g is totally recovered in the subthreshold region. The degradation of the subthreshold slope (*SS*) and transconductance (G_m) are reflected by the stress-induced border traps under medium and high fields, as shown in **Figures 7A,B**. The downtrends of ΔS and ΔG_m are clear during the recovery process from 500 to 1,000 s, revealing that stress-induced recoverable traps were released in the recovery process. When high field stress-induced recoverable donor traps become dominant in the subthreshold region, the degradation of ΔS and ΔG_m are more pronounced compared with that of medium field stress. This finding illustrates that the degradation of the subthreshold slope and the transconductance are mainly caused by the donor traps under the high field stress.

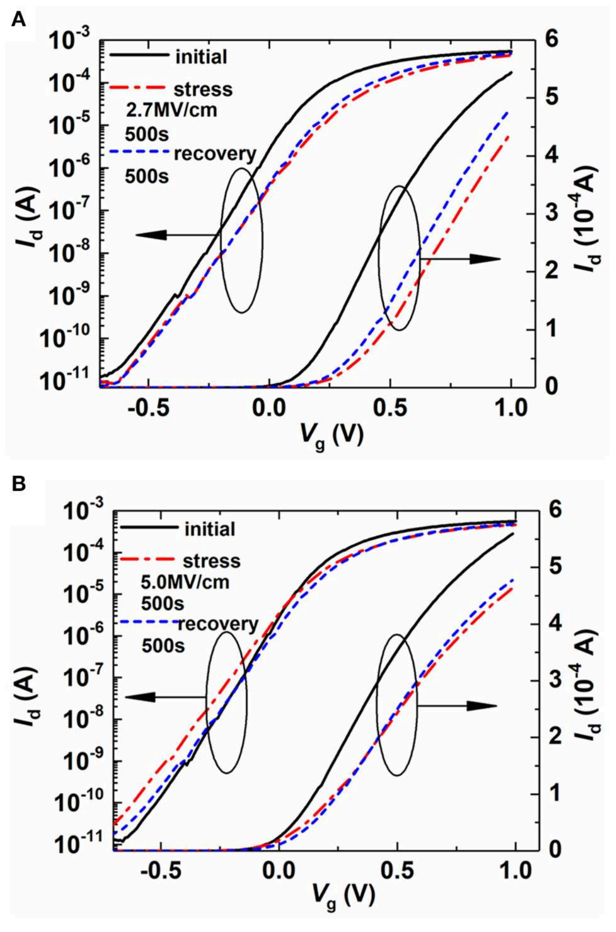

FIGURE 5 | DC I_d–V_g curves of buried $In_{0.25}Ga_{0.75}As$ channel n-MOSFETs after **(A)** 500 s of PBTI stress (E = 2.7 MV/cm) and **(B)** PBTI stress (E = 5.0 MV/cm) followed by 500 s of recovery.

Extractions of Trap Energy Densities

According to the similar explanation given by Li et al. [29], the distribution curves of border traps were investigated under the stress from ΔV_{g} among the *I*, *S*, and *R* lines. Specifically, (1) donor and acceptor traps are induced at the end of the 500 s stress. (2) Stress-induced donor traps fully recover, while acceptor traps are partially recoverable and partially permanent at the end of 500-s recovery. Although stress-induced acceptor traps are dominant, donor traps may also exist. To distinguish between donor traps and acceptor traps, $\Delta N_{\mathrm{ox}}^{\mathrm{AP}}(I_d)$ represents the density

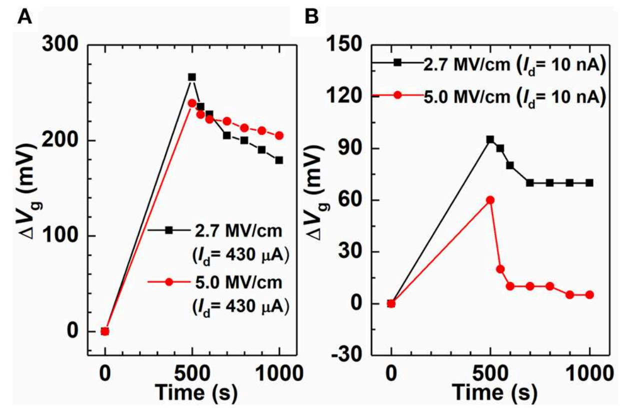

FIGURE 6 | Time-dependence of ΔV_g extracted in **(A)** I_d = 430 μA and **(B)** I_d = 10 nA at a constant field strength of E = 2.7 and E = 5.0 MV/cm in stress (0 and 500 s) and recovery (500–1,000 s) phases.

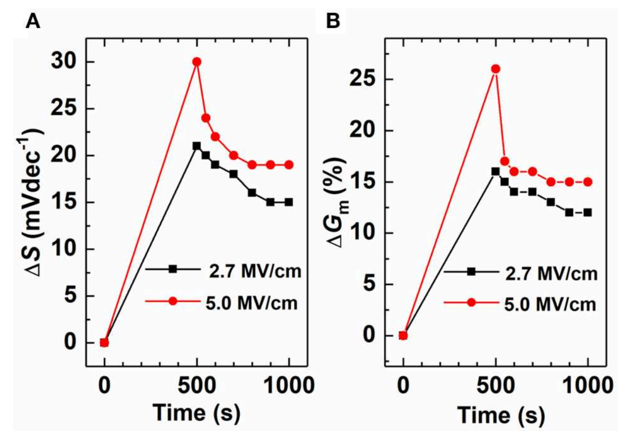

FIGURE 7 | Time-dependence of **(A)** ΔS and **(B)** ΔG_m in stress (0 and 500 s) and recovery (500–1,000 s) phases.

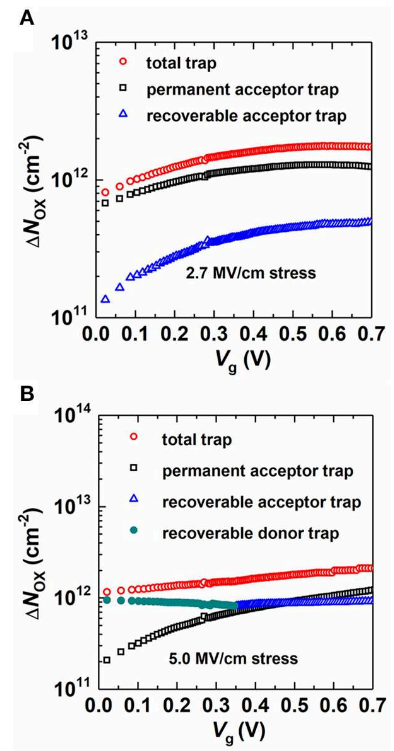

FIGURE 8 | Total trap, permanent acceptor trap, recoverable acceptor trap, and recoverable donor trap area density as a function of gate bias V_g at **(A)** E = 2.7 and **(B)** E = 5.0 MV/cm.

of negatively charged permanent acceptor traps, and $\Delta N_{ox}^{DR}(I_d)$ represents recoverable donor traps. $\Delta N_{ox}^{AP}(I_d)+\Delta N_{ox}^{AR}(I_d)$ or $\Delta N_{ox}^{AP}(I_d)+\Delta N_{ox}^{DR}(I_d)$ is the total trap, which represents the density difference of negatively charged acceptor traps or positively charged donor traps. $\Delta N_{ox}^{AR}(I_d)$-$\Delta N_{ox}^{DR}(I_d)$ is the density of negatively charged recoverable acceptor traps. These parameters can be obtained from:

$$\Delta N_{ox}^{AP}(I_d) = \left(\frac{C_{ox}}{q}\right)\Delta V_g^{IS}(I_d) \tag{1}$$

$$\Delta N_{ox}^{AP}(I_d) + \Delta N_{ox}^{AR}(I_d) = \left(\frac{C_{ox}}{q}\right)\Delta V_g^{IS}(I_d) \tag{2}$$

$$\Delta N_{ox}^{DR}(I_d) - \Delta N_{ox}^{AR}(I_d) = \left(\frac{C_{ox}}{q}\right)\Delta V_g^{IS}(I_d) - \left(\frac{C_{ox}}{q}\right)\Delta V_g^{IR}(I_d) \tag{3}$$

where C_{ox} is the gate oxide capacitor per unit area and q is the electron charge. We obtain $\Delta N_{ox}^{AP}(V_g)$, $\Delta N_{ox}^{DR}(I_d)$, $\Delta N_{ox}^{AR}(I_d)$, and $\Delta N_{ox}^{AR}(V_g)$+ $\Delta N_{ox}^{DR}(V_g)$ as functions of gate bias V_g, as shown in **Figures 8A,B**. For buried channel InGaAs MOSFETs, the magnitude of total traps is averagely 1.5 × 10^{12} cm^{-2} and 1.6 × 10^{12} cm^{-2} under medium and high field strengths, respectively, indicating more traps are induced by high field stress than the medium field stress. The medium field stress-induced permanent acceptor trap is calculated to be 1.1 × 10^{12} cm^{-2}, which is larger than recoverable acceptor trap with the average density of 3.8 × 10^{11} cm^{-2}. By comparison of the surface channel InGaAs MOSFETs, donor trap is not induced by the medium field stress in the buried InGaAs channel MOSFETs. However, the recoverable acceptor trap and recoverable donor trap are generated by the high field stress with a common density of 8.7 × 10^{11} cm^{-2}, and the permanent acceptor trap is averagely 7.7 × 10^{11} cm^{-2}. The results indicate that recoverable trap is easily induced by high field stress. Meanwhile, the medium field stress-induced permanent acceptor trap is larger than the high field stress-induced permanent acceptor trap in the subthreshold region, indicating the permanent acceptor trap and recoverable acceptor trap have been neutralized by recoverable donor trap in the high field stress.

Compared to the surface channel InGaAs n-MOSFETs by considering the experimental results of Li et al. [29], the impacts of PBTI stress on buried InGaAs channel n-MOSFETs are summarized as follows: (1) The D_{it} and ΔN_{bt} distribution of the Al_2O_3/InP interface is smaller than that of Al_2O_3/InGaAs interface through the sulfur passivation treatment, indicating the interface reliability of buried InGaAs channel n-MOSFETs are improved by the Al_2O_3/InP interface. (2) In the surface channel InGaAs n-MOSFETs with the Al_2O_3/InGaAs interface donor traps become the dominant under the medium field stress. In contrast, the medium field stress-induced the permanent acceptor trap and recoverable acceptor trap are contributed by the degradations of ΔV_g and ΔS in the buried InGaAs channel n-MOSFETs with the Al_2O_3/InP interface, which indicates that the generation of acceptor trap are attributed by the insertion of the InP barrier layer. (3) Compared to the surface InGaAs channel n-MOSFETs under the medium field stress, the acceptor trap become dominant in the subthreshold region for the buried channel one. The buried channel InGaAs MOSFETs is better to maintain the low off-state current developing III-V MOSFETs technology for low-power application.

CONCLUSIONS

In summary, the degradation of the buried InGaAs channel n-MOSFETs with an InP barrier layer under PBTI stress and recovery were investigated. The Al_2O_3/InP interface helps achieve low interface and border traps compared to the Al_2O_3/InGaAs interface through the sulfur passivation treatment. Contrary to the shift direction of V_g under the medium field stress in the surface InGaAs channel n-MOSFETs, the permanent acceptor trap of 1.1×10^{12} cm^{-2} and recoverable acceptor trap of 3.8×10^{11} cm^{-2} become the dominant to produce a positive shift in V_g in the buried InGaAs channel n-MOSFETs. The high field stress-induced recoverable donor trap of 8.7×10^{11} cm^{-2} cause degradation of ΔS and ΔG_m in the subthreshold region, whereas the degradation of I_d-V_g is contributed by the recoverable acceptor trap and permanent acceptor trap in the on-state region. Compared to the surface InGaAs channel n-MOSFETs under medium field stress, the low leakage current can be achieved in the buried InGaAs channel n-MOSFETs with an InP barrier layer.

DATA AVAILABILITY STATEMENT

All datasets generated for this study are included in the article/supplementary material.

AUTHOR CONTRIBUTIONS

HLi was the leader of the work and responsible for the main of experiment and paper writing. KQ, XG, YLi, YC, ZZ, and LM were responsible for single step of the fabrication process. FZ and XZ were responsible for device testing. TF, XL, YLiu, TS, and HLiu were mainly engaged in picture editing and related data processing. TS and HLiu contributed to the modification and suggestion in this paper.

FUNDING

This work was supported by National Natural Science Foundation of China (Nos. 11965009, 61874036, 61805053, and 61764001), Guangxi Innovation Research Team Project (No. 2018GXNSFGA281004), Guangxi Science and Technology Planning Project (Nos. AD18281030, AD18281084, AD18281034, and AD18281037), Guangxi Natural Science Foundation (Nos. 2016GXNSFDA380021, 2017GXNSFAA198164, 2018GXNSFBA050052, 2018GXNSFBA 281152, and 2018GXNSFAA281201), Guangxi Key Laboratory of Precision Navigation Technology and Application (Nos. DH201801, DH201808, DH201702, and DH201701), and Innovation Project of GUET Graduate Education (No. 2018YJCXB15).

REFERENCES

1. Alamo D, Jesus A. Nanometre-scale electronics with III-V compound semiconductors. *Nature*. (2011) **479**:317–23. doi: 10.1038/nature10677
2. Kulbachinskii VA, Yuzeeva NA, Galiev GB, Klimov EA, Vasil'evskii IS, Khabibullin RA, et al. Electron effective masses in an InGaAs quantum well with InAs and GaAs inserts. *Semicon Sci Technol*. (2012) **27**:035021. doi: 10.1088/0268-1242/27/3/035021
3. Selmi L, Caruso E, Carapezzi S, Visciarelli M, Gnani E, Zagni N, et al. Modelling nanoscale n-MOSFETs with III-V compound semiconductor channels: from advanced models for band structures, electrostatics and transport to TCAD. In: *IEEE International Electron Devices Meeting (IEDM)*, San Francisco, CA (2017).
4. Wu H, Ye PD. Fully depleted Ge CMOS devices and logic circuits on Si. *IEEE Electron Device Lett*. (2016) **63**:3028–35. doi: 10.1109/TED.2016.2581203
5. Tewari S, Biswas A, Mallik A. Investigation on high-performance CMOS with p-Ge and n-InGaAs MOSFETs for logic applications. *IEEE Trans Nano*. (2015) **14**:275–81. doi: 10.1109/TNANO.2015.2390295
6. Takagi S, Zhang R, Suh J, Kim SH, Yokoyama M, Nishi K, et al. III-V/Ge channel MOS device technologies in nano CMOS era. *J Appl Phys*. (2015) **54**:06FA01. doi: 10.7567/JJAP.54.06FA01
7. Guo Y, Li H, Robertson J. AlN and Al oxy-nitride gate dielectrics for reliable gate stacks on Ge and InGaAs channels. *J Appl Phys*. (2016) **119**:204101. doi: 10.1063/1.4951004
8. Franco J, Putcha V, Vais A, Sioncke S, Waldron N, Zhou D, et al. Characterization of oxide defects in ingaas mos gate stacks for high-mobility n-Channel MOSFETs. In: *IEEE International Electron Devices Meeting (IEDM)*, San Francisco, CA (2017).
9. Bouzid A, Pasquarello A. Electron trap states at InGaAs/oxide interfaces under inversion through constant Fermi-level abinitio molecular dynamics. *J Phys*. (2017) **29**:505702. doi: 10.1088/1361-648X/aa9a00
10. Mo J, Lind E, Roll G, Wernersson LE. Reduction of off-state drain leakage in InGaAs-based metal-oxide semiconductor field-effect transistors. *Appl Phys Lett*. (2017) **105**:033516. doi: 10.1063/1.4891569
11. He G, Zhu LQ, Sun ZQ, Wan Q, Zhang L. Integrations and challenges of novel high-k gate stacks in advanced CMOS technology. *Prog Mater Sci*. (2011) **56**:475–572. doi: 10.1016/j.pmatsci.2011.01.012
12. Tang K, Droopad R, Mclntyre PC. Bias temperature stress induced hydrogen depassivation from Al_2O_3/InGaAs interface defects. *J Appl Phys*. (2018) **123**:025708. doi: 10.1063/1.4994393
13. Tang K, Winter R, Zhang LL, Droopad R, Eizenberg M, McIntyre PC. Border trap reduction in Al_2O_3/InGaAs gate stacks. *Appl Phys Lett*. (2015) **107**:202102. doi: 10.1063/1.4936100
14. Minseok C, Anderson J, Walle CGVD. Native point defects and dangling bonds in α-Al_2O_3. *J Appl Phys*. (2013) **113**:044501. doi: 10.1063/1.47 84114
15. Kwon HM, Kim DH, Kim TW. Relationship between effective mobility and border traps associated with charge trapping in $In_{0.7}Ga_{0.3}As$

MOSFETs with various high-K stacks. *Appl Phys Express*. (2018) **11**:034101. doi: 10.7567/APEX.11.034101
16. Vais A, Franco J, Martens K, Lin D, Sioncke S, Putcha V, et al. A new quality metric for III-V/High-k MOS gate stacks based on the frequency dispersion of accumulation capacitance and the CET. *IEEE Electron Device Lett.* (2017) **38**:318–21. doi: 10.1109/LED.2017.2657794
17. Chang HD, Sun B, Xue BQ, Liu GM, Zhao W, Wang SK, et al. Effect of the Si-doped $In_{0.49}Ga_{0.51}P$ barrier layer on the device performance of $In_{0.4}Ga_{0.6}As$ MOSFETs grown on semi-insulating GaAs substrates. *Chin Phys B*. (2013) **22**:077306. doi: 10.1088/1674-1056/22/7/077306
18. Xue F, Zhao H, Chen YH, Wang Y, Wang Y, Zhou F, et al. High-k InGaAs metal-oxide-semiconductor field-effect-transistors with various barrier layer materials. *Appl Phys Lett*. (2011) **99**:033507. doi: 10.1063/1.3611502
19. Tewari S, Biswas A, Mallik A. Impact of different barrier layers and indium content of the channel on the analog performance of InGaAs MOSFETs. *IEEE Trans Electron Dev*. (2013) **60**:1584–89. doi: 10.1109/TED.2013.2249071
20. Krylov I, Ritter D, Eizenberg M. The role of the substrate on the dispersion in accumulation in III-V compound semiconductor-based metal-oxide-semiconductor gate stacks. *Appl Phys Lett*. (2015) **107**:103503. doi: 10.1063/1.4930202
21. Benbakhti B, Ayubi-Moak JS, Kalna K, Lin D, Hellings G, Brammertz G, et al. Impact of interface state trap density on the performance characteristics of different III–V MOSFET architectures. *Microelectron Reliab*. (2010) **50**:360–64. doi: 10.1016/j.microrel.2009.11.017
22. Deora S, Bersuker G, Loh WY, Veksler D, Matthews K, Kim TW, et al. Positive bias instability and recovery in InGaAs channel nMOSFETs. *IEEE Trans Device Mater Reliab.* (2013) **13**:507–14. doi: 10.1109/TDMR.2013.2284376
23. Wang SK, Sun B, Cao MM, Chang HD, Su YY, Li HO, et al. Modification of Al_2O_3/InP interfaces using sulfur and nitrogen passivations. *J Appl Phys.* (2017) **121**:184104. doi: 10.1063/1.4982904
24. Haimoto T, Hoshii T, Nakagawa S, Takenaka M, Takagi S. Fabrication and characterization of metal-insulator-semiconductor structures by direct nitridation of InP surfaces. *Appl Phys Lett*. (2010) **96**:012107. doi: 10.1063/1.3269906
25. Hoshii T, Yokoyama M, Yamada H, Hata M, Yasuda T, Takenaka M, et al. Impact of InGaAs surface nitridation on interface properties of InGaAs metal-oxidesemiconductor capacitors using electron cyclotron resonance plasma sputtering SiO_2. *Appl Phys Lett*. (2010) **97**:132102. doi: 10.1063/1.3464170
26. Wang SK, Cao MM, Sun B, Li HO, Liu HG. Reducing the interface trap density in Al_2O_3/InP stacks by low-temperature thermal process. *Appl Phys Express*. (2015) **8**:091201. doi: 10.7567/APEX.8.091201
27. Maeda F, Watanabe Y, Oshima M. Surface chemical bonding of $(NH_4)_2S_x$ treated InP(001). *Appl Phys Lett*. (1993) **62**:297–99. doi: 10.1063/1.108996
28. Jin HS, Cho YJ, Seok TJ, Kim DH, Kim DW, Lee SM, et al. Improved interface properties of atomic-layer-deposited HfO_2 film on InP using interface sulfur passivation with H2S pre-deposition annealing. *Appl Surf Sci*. (2015) **357**:2306–12. doi: 10.1016/j.apsusc.2015.09.232
29. Li ML, Jiao G, Hu Y, Xuan Y, Huang D, Ye PD. Reliability of high mobility InGaAs channel n-MOSFETs under BTI Stress. *IEEE Trans Dev Mater Reliab*. (2013) **13**:515–23. doi: 10.1109/TDMR.2013.2276075
30. Shen C, Li MF, Wang XP, Yeo YC, Kwong DLA. Fast measurement technique of MOSFET Id–Vg characteristics. *IEEE Electron Device Lett.* (2006) **27**:55–7. doi: 10.1109/LED.2005.861025
31. Castagne R, Vapaille A. Apparent interface state density introduced by the spatial fluctuations of surface potential in an MOS structure. *Electron Lett*. (1970) **6**:691. doi: 10.1049/el:19700481
32. Jiao GF, Yao CJ, Xuan Y, Huang DM, Ye PD, Li MF. Experimental investigation of border trap generation in InGaAs nMOSFETs with Al_2O_3 gate dielectric under PBTI stress. *IEEE Trans Electron Dev*. (2012) **6**:1661. doi: 10.1109/TED.2012.2190417
33. Varghese D, Xuan Y, Wu QY, Shen T, Ye PD, Alam MA. Multi-probe interface characterization of $In_{0.65}Ga_{0.35}As/Al_2O_3$ MOSFET. In: *IEEE International Electron Devices Meeting (IEDM)*. San Francisco, CA (2008).

Conflict of Interest: The authors declare that the research was conducted in the absence of any commercial or financial relationships that could be construed as a potential conflict of interest.

frontiers in Physics

ORIGINAL RESEARCH
published: 24 March 2020
doi: 10.3389/fphy.2020.00053

Check for updates

A Horizontally Polarized Omnidirectional Antenna Based on Spoof Surface Plasmons

Zhen Liao, Guo Qing Luo, Xin Yu Wu, Ben Geng Cai, Bai Cao Pan and Yu Jian Pan*

Key Laboratory of RF Circuits and System of Ministry of Education, Hangzhou Dianzi University, Hangzhou, China

As an analog of the role of surface plasmons in optical antenna, spoof surface plasmons enable far-field radiation of antenna at microwave frequencies. Here, a plasmonic metamaterial supporting spoof surface plasmons is experimentally demonstrated for horizontally polarized omnidirectional radiation in the microwave region. A simple and intuitive working principle in the spoof surface plasmonic metamaterial design is provided, along with full-wave simulations that agree well with the experimental results. The low profile and compact design with the omnidirectional radiation pattern promises a wide range of applications, such as ceiling antennas, surface-mounted indoor antennas, and automobile antennas in microwave and radio frequencies.

Keywords: metamaterials, spoof surface plasmons, spoof localized surface plasmons, omnidirectional antennas, magnetic resonance

OPEN ACCESS

Edited by:
Lin Chen,
University of Shanghai for Science and Technology, China

Reviewed by:
Shiyi Xiao,
Shanghai University, China
Junichi Fujikata,
Photonics Electronics Technology Research Association, Japan

****Correspondence:***
Guo Qing Luo
luoguoqing@hdu.edu.cn

Specialty section:
This article was submitted to Optics and Photonics, a section of the journal Frontiers in Physics

Received: *15 January 2020*
Accepted: *20 February 2020*
Published: *24 March 2020*

Citation:
Liao Z, Luo GQ, Wu XY, Cai BG, Cao Pan B and Pan YJ (2020) A Horizontally Polarized Omnidirectional Antenna Based on Spoof Surface Plasmons. Front. Phys. 8:53. doi: 10.3389/fphy.2020.00053

INTRODUCTION

Localized Surface Plasmon (LSP) characteristics of the metallic nano-rod have gained tremendous interest over the past few years, especially with respect to the promising candidate for optical antennas [1]. Optical antennas are strongly analogous to their radio frequency (RF) and microwave counterparts, their purpose is to convert the energy of free propagating radiation to localized energy, and vice versa [2–6]. However, there are crucial differences between their physical properties and scaling behavior. Firstly, the size of RF antennas and wavelength are similar, and are usually several centimeters. Whereas, optical antennas are always in subwavelength scale and generate subwavelength "hotspots" around them. Secondly, metals are supposed to be a perfect electrical conductor (PEC) at microwave and RF frequencies, nevertheless, they are plasmons described as free electron gas at optical frequencies [7]. Therefore, these differences pose another challenge and limit the ability to extend current understanding from RF antennas to the optical spectrum, and vice versa.

It has recently been shown that spiral corrugated metamaterials can support spoof surface plasmons modes whose resonant wavelengths are much larger than the size of the structures, usually termed spoof localized surface plasmon (spoof LSP) resonances [8–10]. The spoof LSP modes in this geometry is quantitatively investigated by a metamaterial approximation, in which a textured perfect electric conductor (PEC) is treated as a homogeneous effective medium [8]. Furthermore, the deep subwavelength metallic spiral structures (MSS) support spoof magnetic LSP resonance as well as electrical surface plasmon modes [10, 11]. Thanks to the existence of spoof LSP mode, all the capabilities found for LSP in the optical regime can be directly transferred to lower frequencies. This enables a wide range of applications, including energy transport [12, 13], sensing [14, 15], topological protection [16], and field enhancement [17] in microwave and RF frequencies.

Besides LSP, surface plasmon polaritons (SPPs) also have useful applications, such as SPP-enabled slow light devices [18] and SPP-induced transparency [19, 20]. At the same time, spoof surface plasmon polariton (SSPPs) at microwave frequencies exhibiting similar behaviors to real surface plasmon polariton (SPPs) have also been widely studied and applied to design transmission lines [21–24]. However, antennas based on spoof LSP resonances have not been achieved in a lower frequency range.

High performance antennas with omnidirectional radiation in the horizontal polarization are in great demand, fueled by the rapid growth of wireless communication systems. Horizontal polarization wireless signals equally cover all directions of the azimuthal plane, resulting in a 10-dB higher power gain than their vertically polarized counterparts [25, 26]. To date, various approaches have been developed to generate horizontally polarized omnidirectional beams, including the turnstile antennas consisting of cross dipoles in a horizontal plane [27, 28], a small loop antenna with uniform current distribution [7], the Alford loop antennas [29, 30], and dielectric resonator antenna (DRA) [31]. These methods, however, have several limitations. For instance, turnstile antennas have a narrow operating bandwidth. The small loop antenna has small radiation resistance and high reactance, which makes it difficult to be matched. The Alford loop antennas have an undesirable radiation performance in horizontal plane that occurs at high operating frequency. Meanwhile, the TE010 mode of a cylindrical dielectric resonator antenna (DRA) has azimuthal circulating electric fields, which are tangential to the circular plane. The DRA resonating at TE010 mode acts like a magnetic dipole in axial direction to radiate a horizontally polarized omnidirectional radiation pattern. Although the DRA has a subwavelength size, the antenna must have a certain thickness. The proposed DRA [31] achieves an omnidirectional radiation pattern for the horizontal component at 3 GHz, while its diameter is 25 mm and thickness is 4 mm.

In this paper, we introduce a new design of spoof surface plasmons antenna to mimic optical antennas with microwave frequencies. We present numerical and experimental demonstrations of the antenna composed of MSS structures for spoof magnetic LSP resonances with horizontally polarized omnidirectional radiation. The size of the particle is deep subwavelength. We have applied a groundless SSPPs waveguide to feed the antenna, in order to eliminate the ground effects in the field distribution and far-field pattern, as well as effectively excite spoof LSP resonance mode. We show explicitly that the surface wave modes have been converted to free-propagating radiation by using plasmonic metamaterials. The unique features and merits of this method include the reduced subwavelength size and the ultrathin thickness of the structure. The horizontally polarized omnidirectional radiation is thus verified, which paves the way toward practical applications of spoof surface plasmon metamaterials. Our proposed research also opens a new vista to account for the relationship between optical antennas and their RF counterparts.

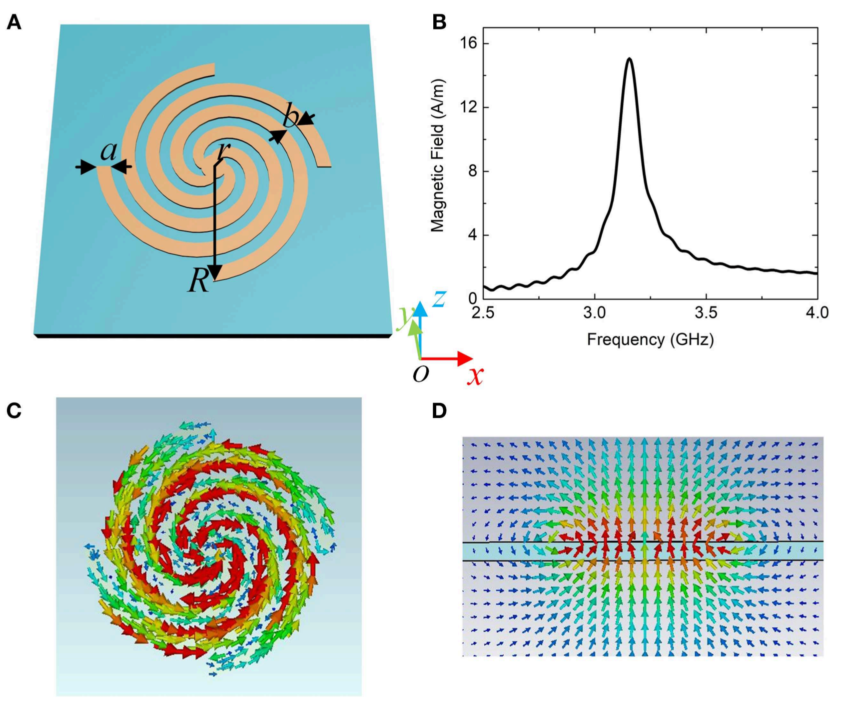

FIGURE 1 | (A) Schematic of the metallic spiral structure. **(B)** Magnetic field amplitude intensity detected at the center of the resonator. **(C)** Current distribution at $z = 0$. **(D)** Magnetic field vectors at $x = 0$.

PLASMONIC METAMATERIAL ANTENNA

Figure 1A shows the perspective view of the plasmonic metamaterial antenna, which consists of four spiral arms and an inner disk embedded in a substrate. The relative permittivity of the substrate is taken as 2.2 and the thickness is 1.5 mm. The geometry parameters are $r = 1$ mm, $a = 1.1$ mm, $R = 9.17$ mm, $a/b = 1.25$. We have performed numerical simulations based on commercial electromagnetic solver (CST Microwave Studio) to verify magnetic spoof LSP resonance mode in antenna. In the simulation, we have used an external magnetic field perpendicular to the substrate to excite the antenna element. The magnetic field at 1 mm above the center of the particle is plotted in **Figure 1B**. At about 3.16 GHz, the magnetic field reaches the peak, indicating that a large magnetic resonance is excited in the antenna [10, 11]. The current of the magnetic plasmonic resonance mode is plotted in **Figure 1C**. It shows a circulating current along the metal spiral arms, which can act as a magnetic dipole. Here, current distribution is in a small loop with a subwavelength circumference, which causes a small radiation resistance. In this way, this resonance mode has a high Q factor and narrow bandwidth. **Figure 1D** illustrates the magnetic field vector in $x = 0$ plane. The magnetic field lines circulate around the antenna like a magnetic dipole. Therefore, this spoof magnetic plasmonic resonance mode in the designed antenna can be considered to achieve a horizontally polarized omnidirectional radiation pattern, like a magnetic dipole.

As mentioned in Ref. [11], the spiral textured two-dimensional (2D) metal cylinder can be described by the effective medium theoretical model. Following this homogeneous metamaterial approximation, the geometric parameters of the MSS determine the effective permittivity and permeability, which are related to the spoof LSP resonances. Although the physical characteristics of the plasmonic metamaterial antenna is different from the textured 2D cylinder, the analytical model can direct the manipulation of spoof LSP resonances in the antenna in some sense. In order to study the relationship between the magnetic plasmonic resonance frequencies with the geometric parameters, numerical simulations were carried out using a CST Microwave Studio. When the radius $R = 9.17$ mm, the magnetic resonance frequencies for various filling factor a/b is presented in **Figure 2A**. As can be seen, the frequency is dependent on the filling factor variation, which decreases as the factor reduces. **Figure 2B** explores the dependence on radius R of the magnetic plasmonic resonance characteristics as $a/b = 1.25$. At small $R = 7$ mm, the frequency for the magnetic spoof LSP resonance is 5.5 GHz, which is the highest. The magnetic mode shifts toward 2.2 GHz as R increase to 11 mm. **Figure 2C** further gives the resonance frequency as a function of the inner radius r with $a/b = 1.25$, $R = 9.17$ mm, in which we see that the resonance frequency increases from about 3.14 to 4.32 GHz as r increases from 0.5 to 5 mm. More interesting, we found that the bigger the radius r the more effect is had on the resonance frequency. This can be attributed to the fact that the resonance frequency is related on the length of spiral grooves. Moreover, a larger radius r will result in greater variation in the length of spiral grooves.

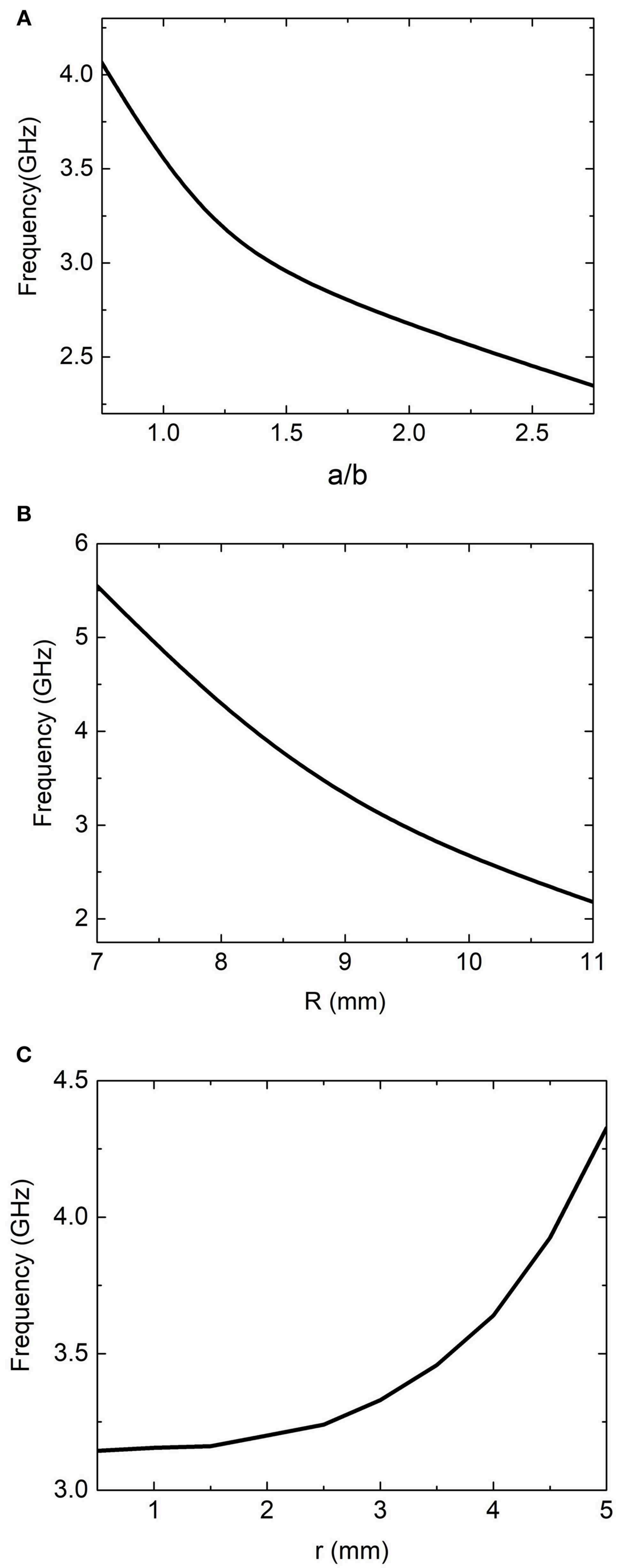

FIGURE 2 | The resonance frequencies of spoof magnetic plasmon modes as a function of the filling factor a/b **(A)**, outer radius R **(B)** and inner radius r **(C)**.

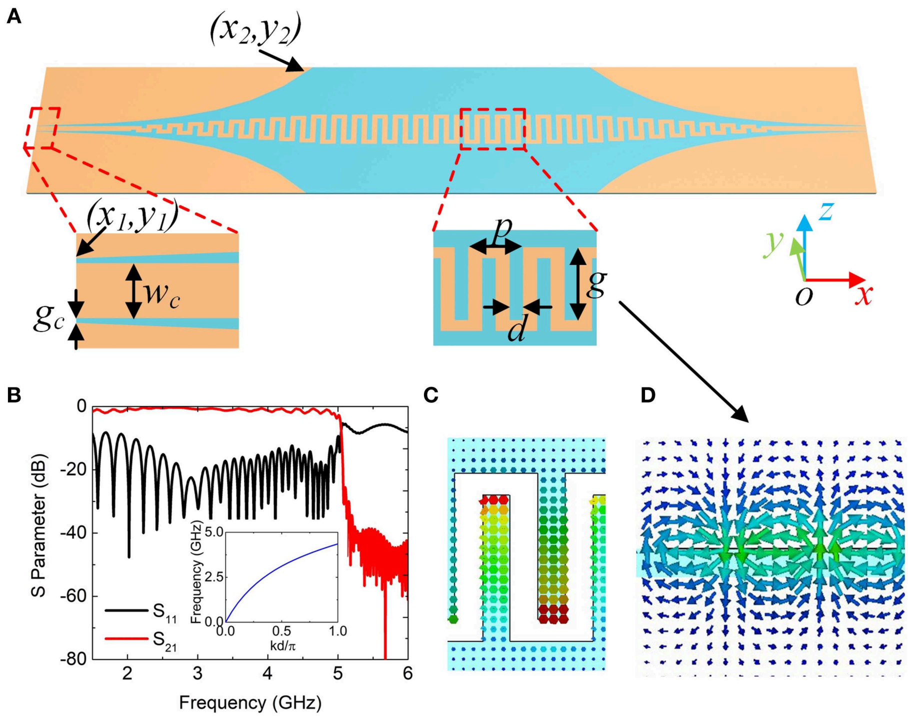

FIGURE 3 | (A) Proposed SSPPs waveguide composed of S-shaped unit cells connected to two CPW lines through the mode converter. The mode converter is composed of unit cells with gradually increasing groove depth and the flared ground plane. **(B)** Simulated transmission and reflection from the designed SSPPs waveguide solved by CST Microwave Studio. Inset: dispersion curves of the SSPPs cell calculated by eigen-mode; Magnetic field distributions at two cutting planes $z = 0$ **(C)** and $y = 0$ **(D)**.

In this case, we can manipulate the operating frequency of the magnetic resonance by adjusting the antenna structure parameters. An appropriate choice of the structure parameters allows the working frequency of plasmonic metamaterial antenna to meet different practical requests. More interestingly, the antenna with $R = 9$ mm corresponds to the resonance wavelength of about 100 mm. It is evident that the resonance wavelength of spoof magnetic LSP is much larger than the antenna size, indicating our design is a subwavelength antenna.

SSPPs GROUNDLESS FEEDING LINE

In order to excite the spoof magnetic LSP mode in antenna effectively and eliminate the ground impacts on the field, we consider a SSPPs waveguide. The proposed groundless SSPPs waveguide is configured by a meander line, as shown in **Figure 3A**. The waveguide is printed onto a piece of FR4 substrate [relative permittivity of $2.2(1 + i0.003)$] with thickness of 1.5 mm. Here, the SSPPs is fed by a coplanar waveguide (CPW). Therefore, the whole structure consists of two parts: a mode conversion and momentum matching section, and a SSPP transmission line. The dimensions g_c and w_c labeled in the left inset of **Figure 3A** are designed to achieve 50 Ω input impedance, in which $g_c = 0.2$ mm is the width of the symmetrical slots, and $w_c = 3$ mm is the width of the inner conductor line. As shown in **Figure 3A**, the convertor section comprises two symmetrically flared ground and an array of 10 distinctive "S" shape unit cells with their depth gradually increasing. The flared ground is set an exponential equation $y = C_1 e^{\alpha x} + C_2$, where $C_1 = \frac{y_1 - y_0}{e^{\alpha x_1} - e^{\alpha x_0}}$, $C_2 = \frac{y_0 e^{\alpha x_1} - y_1 e^{\alpha x_0}}{e^{\alpha x_1} - e^{\alpha x_0}}$, and the exponent parameter is $\alpha = 0.04$. The right inset of **Figure 3A** gives the sketch of SSPPs transmission line. The cycle of meander is set as $p = 9$ mm, while the groove depth and width are $g = 12$ and $d = 2.2$ mm, respectively. The dispersion curve of SSPPs unit cell is calculated and plotted in the inset of **Figure 3B**, which is analogous to the conventional SPPs in optical range. In this regard, the surface wave modes in the meander line is SSPPs slow wave mode. By the convertor section, a gradual mode conversion and momentum matching can be obtained between the guided wave in CPW and SSPPs modes. To confirm the transmission performance of the converter and SSPPs waveguide, we simulated the S parameters by CST Microwave Studio.

The simulated transmittance and reflectance spectra are presented in **Figure 3B**, in which the high transmission and low reflection are clearly observed in 1.5–5 GHz range. The suddenly dropped S_{21} at 5 GHz denotes the cut-off frequency of this SSPPs waveguide. According to the numerical calculation results in **Figure 2**, the designed SSPPs waveguide's operating frequency range can cover the resonance frequencies of the LSP resonance in MSS antenna. **Figure 3C** illustrates magnetic field vectors of SSPPs waveguide in the cutting plane $z = 0$ mm, while **Figure 3D** shows the magnetic field distribution in the cross-section $y = 0$ mm. From the distributions, we find that the magnetic field is located in the grooves and is perpendicular to the structure.

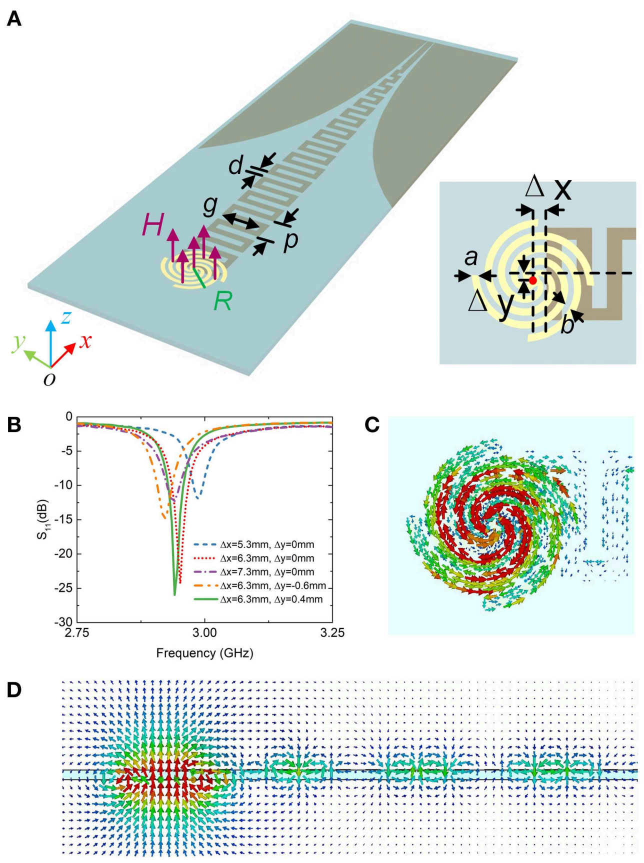

FIGURE 4 | (A) Plasmonic metamaterial antenna fed with the proposed SSPPs waveguide configuration. **(B)** S-parameter results for various MSS disk locations. **(C)** The simulated current distributions of the spoof plasmonic resonance mode and the feeding end. **(D)** Magnetic field vector distributions at cutting plane $y = 0$.

DISCUSSION OF ANTENNA PERFORMANCE

As mentioned in the above discussions, the equivalent magnetic dipole in antenna is vertical. For the sake of effective exciting, the magnetic fields of both spoof magnetic plasmonic mode in antenna and the SSSPs mode in plasmonic waveguide should be parallel to each other. In addition, the antenna and SSPP waveguide should be overlapped with each other. To this end, we consider the structure depicted schematically in **Figure 4A**. The proposed SSPPs waveguide is cut. The SSPPs waveguide and the antenna disk are printed on the bottom and top side of the FR4 substrate with 1.5 mm thickness, respectively. The geometry parameters of the antenna are set as inner radius $r = 1$ mm, $R = 9.17$ mm, $a = 1.1$ mm, $b = 0.88$ mm. And the period of meander is $p = 9$ mm, the groove depth $g = 12$ mm, and width $d = 2.2$ mm. In this case, the antenna without the feeding SSPPs waveguide resonates at 3.16 GHz at the spoof magnetic LSP resonance mode.

Δx and Δy can be used to adjust the location of antennas, which impacts on the excitation efficiency. By optimizing the dimensions of Δx and Δy to obtain the best performance of the lowest reflection, their optimized values are 6.3 and 0.4 mm, respectively, as plotted in **Figure 4B**. **Figure 4C** shows the surface current distribution in the MSS disk at 2.9 GHz. The resulting surface current exhibits a loop, which resembles the currents in the isolate antenna without the SSPPs feeding line **(Figure 1B)**. We also checked the magnetic field vectors in the cross-section $y = 0$ in **Figure 4D**, in which the magnetic fields transport in SSPPs waveguide and excite magnetic resonances in the antenna. The magnetic fields in antenna act like a magnetic dipole mode. The results demonstrate that the spoof magnetic surface plasmon resonance in antenna can be excited by the SSPPs waveguide effectively. Here, the spoof plasmonic antenna with the feeding configuration works at 2.9 GHz, while the resonance frequency of an isolated antenna is 3.15 GHz. The resonance frequency in the presence of the feeding line is shifted by 6.7%. The frequency deviation comes from the metal meander line, which is close to the antenna, and affects the field distribution of the resonance mode slightly.

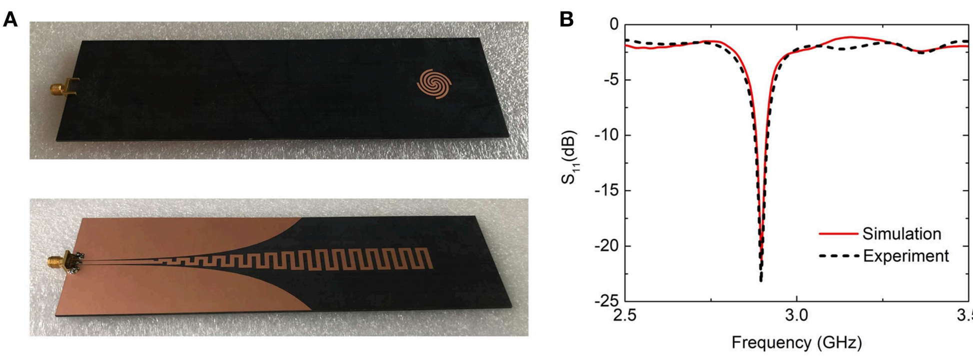

FIGURE 5 | (A) Photographs of the fabricated SSPPs waveguide feeding configuration and the plasmonic metamaterial antenna. **(B)** Comparison of scattering parameter results between simulation and experiment results for the antenna fed with the proposed SSPPs waveguide.

Please note that our design has some positive features, such as deep subwavelength size and low profile. However, the high Q factor of the spoof LSP resonance limits the bandwidth of the antenna. When we apply the antenna, we need to consider the balance between the size and the bandwidth.

FABRICATION AND EXPERIMENT

According to the parameters given before, a prototype of the proposed spoof plasmonic antenna was fabricated and measured. Two photographs of top view and bottom view of the fabricated prototype are presented in **Figure 5A**. **Figure 5B** depicts the simulated and measured reflection spectrums, which are in good agreement. In order to confirm the far-field behaviors of the antenna, the simulated and measured far-field patterns at resonance frequency are compared in **Figure 6**.

Figure 6 illustrates the E_θ and E_ϕ radiation patterns in three principal planes, *x-y*, *y-z*, and *x-z* plane. According to **Figure 1B**, the surface currents of magnetic mode circulate along the azimuthal direction, which result in the polarization of the far field along the azimuthal direction (ϕ). As expected, the magnitudes of the copolarized component (E_ϕ) is much higher than the cross-polarization (E_θ) of the radiated field in **Figure 6**. As can be seen from the E_ϕ radiation patterns in the azimuth plane (*x-y* plane), the antenna has an omnidirectional radiation pattern in **Figure 6A**. The radiation patterns at the elevation plane (*y-z* and *x-z* plane) show a quasi-eight shape in **Figures 6C,E**, respectively. The radiation patterns of the proposed spoof plasmonic antenna are very close to that of an ideal magnetic dipole. As expected, the radiation patterns cover both the upper and lower space equally. The slight asymmetric pattern might be due to the feed line. The SSPPs waveguide may slightly affect the current distribution in the antenna and shield the radiation of the antenna.

The simulation results for the total efficiency with lossless substrate and perfect PEC is 94%. The simulation results for the total efficiency for the lossy substrate and cooper loss is 94%. It exhibits a maximum radiation realized gain of 3.15 dBi in the x-y plane.

Measurements also present similar radiation patterns as those plotted here. The patterns show accurate agreement, except for the E_θ in the x-y plane. In **Figure 6B**, the cross-polarization levels of the simulated and measured results are −20 and −40 dB, respectively. Both of them are <-20 dB, whose difference in liner value is extremely tiny. The difference between the two results can be caused by the dielectric constant tolerance of the substrate and the change in the substrate thickness during the fabrication process.

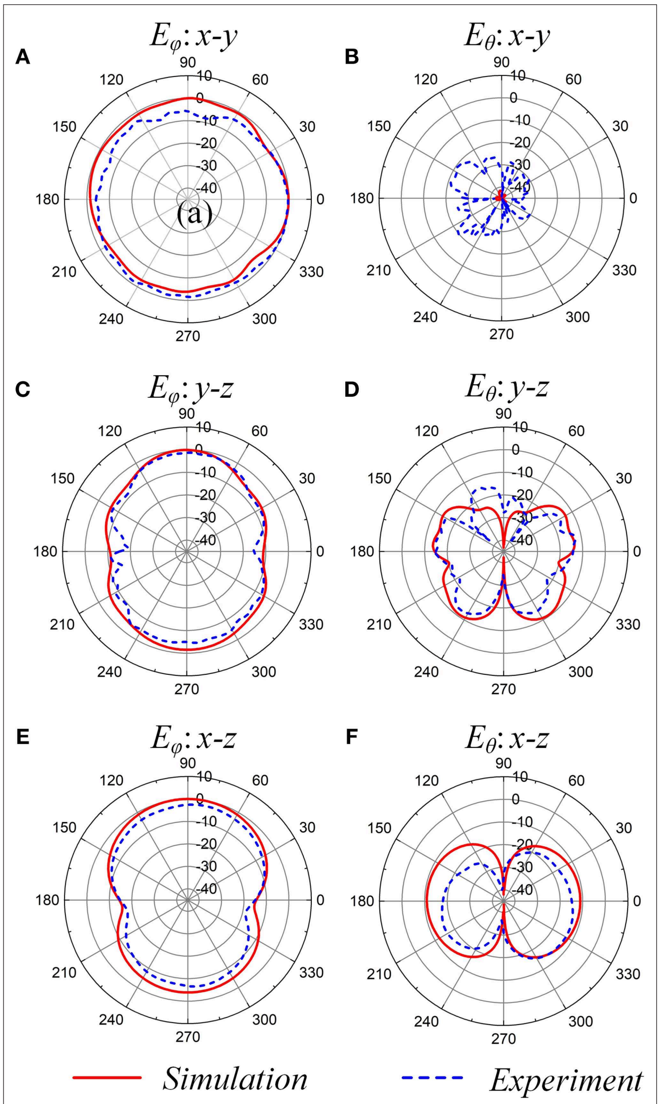

FIGURE 6 | Comparison of the far-field radiation patterns from the antenna between simulations and measurements. **(A)** E_ϕ in x–y plane. **(B)** E_θ in x–y plane. **(C)** E_ϕ in x–z plane. **(D)** E_θ in y–z plane. **(E)** E_ϕ in y–z plane. **(F)** E_θ in x–z plane.

CONCLUSION

In conclusion, we numerically and experimentally demonstrate horizontally polarized omnidirectional radiation using spoof surface plasmons metamaterial. The spoof plasmonic antenna shown here can be treated as a homogeneous effective medium. The magnetic spoof LSP of the metamaterial act as a magnetic dipole, which is used to achieve a horizontally polarized omnidirectional radiation pattern. A SSPPs transmission line is used to feed the antenna. We also verify through numerical simulations and experiments that the compact and subwavelength design works as predicted, showing its high suitability and usability with further practical applications. Moreover, since the design is analogous to its optical antenna counterpart, it will provide additional understanding from microwave antennas to optical antennas. Our results will enable many potential applications including, but not limited to, microwave and RF antennas, as well as terahertz beam generators.

DATA AVAILABILITY STATEMENT

All datasets generated for this study are included in the article/supplementary material.

AUTHOR CONTRIBUTIONS

ZL was the leader of the work and responsible for the main of experiment and paper writing. XW, BGC, BC, and YP were responsible for single step of the fabrication process. GL contributed to the modification and suggestion in this paper.

FUNDING

This work was supported in part by the National Natural Science Foundation of China (Grants Nos. 61701151, 61722107, and 61701145), the China Scholarship Council (CSC) (Grant CSC No. 201808330064), and Foundation of State Key Laboratory of Millimeter Waves, Southeast University, China, under Grant (No. K202009).

REFERENCES

1. Maier SA. *Plasmonics: Fundamentals and Applications*. New York, NY: Springer (2007). doi: 10.1007/0-387-37825-1
2. Park QH. Optical antennas and plasmonics. *Contemp Phy*. (2009) **50**:407–23. doi: 10.1080/00107510902745611
3. Choosak K, Silapunt R, Mohammed WS. Study of localized surface plasmon properties on metallic nano-rods towards optical antennas. In: *2014 International Electrical Engineering Congress (iEECON)* (Chonburi: IEEE) (2014). p. 1–4. doi: 10.1109/iEECON.2014.6925936
4. Kausar A, Reza A, Latef T, Ullah M, Karim M. Optical nano antennas: state of the art, scope and challenges as a biosensor along with human exposure to nano-toxicology. *Sensors*. (2015) **15:**8787–831. doi: 10.3390/s150408787
5. Bharadwaj P, Deutsch B, Novotny L. Optical antennas. *Adv Opt Photon*. (2009) **1:**438. doi: 10.1364/AOP.1.000438
6. Kumar A. Optical Nano-Antennas: Fabrication, Characterization and Applications. Illinois : University of Illinois at Urbana-Champaign (2011) 93.
7. Balanis CA. *Antenna Theory: Analysis and Design*. 3rd ed. Hoboken, NJ: John Wiley (2005).
8. Pors A, Moreno E, Martin-Moreno L, Pendry JB, Garcia-Vidal FJ. Localized spoof plasmons arise while texturing closed surfaces. *Phys Rev Lett*. (2012) **108**:223905. doi: 10.1103/PhysRevLett.108.223905
9. Shen X, Cui TJ. Ultrathin plasmonic metamaterial for spoof localized surface plasmons. *Laser Photonics Rev*. (2014) **8**:137–45. doi: 10.1002/lpor.201300144
10. Huidobro PA, Shen X, Cuerda J, Moreno E, Martin-Moreno L, Garcia-Vidal FJ, et al. Magnetic localized surface plasmons. *Phys Rev X*. (2014) **4**:021003. doi: 10.1109/MetaMaterials.2014.6948552
11. Liao Z, Fernández-Domínguez AI, Zhang J, Maier SA, Cui TJ, Luo Y. Homogenous metamaterial description of localized spoof plasmons in spiral geometries. *ACS Photonics*. (2016) **3**:1768–75. doi: 10.1021/acsphotonics.6b00488
12. Liao Z, Luo GQ, Cai BG, Pan BC, Cao WH. Subwavelength negative-index waveguiding enabled by coupled spoof magnetic localized surface plasmons. *Photonics Res*. (2019) **7**:274. doi: 10.1364/PRJ.7.000274
13. Liao Z, Luo GQ, Ma HF, Pan BC, Cai BG, Yu YF, et al. Localized surface magnetic modes propagating along a chain of connected subwavelength metamaterial resonators. *Phys Rev Appl*. (2018) **10**:034054. doi: 10.1103/PhysRevApplied.10.034054
14. Zhang Y, Zhou YJ, Cai J, Jiang JH. Amplification of spoof localized surface plasmons on active plasmonic metamaterials. *J Phys D Appl Phys*. (2018) **51**:295304. doi: 10.1088/1361-6463/aaca25
15. Zhou YJ, Li QY, Zhao HZ, Cui TJ. Gain-Assisted active spoof plasmonic fano resonance for high-resolution sensing of glucose aqueous solutions. *Adv Mater Technol*. (2019) **5**:1900767. doi: 10.1002/admt.201900767
16. Gao F, Gao Z, Shi X, Yang Z, Lin X, Xu H, et al. Probing topological protection using a designer surface plasmon structure. *Nat Commun*. (2016) **7**:1–9. doi: 10.1038/ncomms11619
17. Zhang J, Liao Z, Luo Y, Shen X, Maier SA, Cui TJ. Spoof plasmon hybridization: Spoof plasmon hybridization. *Laser Photonics Rev*. (2017) **11**:1600191. doi: 10.1002/lpor.201600191
18. Xiao S, He Q, Huang X, Tang S, Zhou L. Enhancement of light-matter interactions in slow-wave metasurfaces. *Phys Rev B*. (2012) **85**:085125. doi: 10.1103/PhysRevB.85.085125
19. Guo H, Lin J, Qiu M, Tian J, Wang Q, Li Y, et al. Flat optical transparent window: mechanism and realization based on metasurfaces. *J Phys D Appl Phys*. (2018) **51**:074001. doi: 10.1088/1361-6463/aaa451
20. Yang B, Liu T, Guo H, Xiao S, Zhou L. High-performance meta-devices based on multilayer meta-atoms: interplay between the number of layers and phase coverage. *Sci Bull*. (2019) **64**:823–35. doi: 10.1016/j.scib.2019.05.028
21. Shen X, Cui TJ, Martin-Cano D, Garcia-Vidal FJ. Conformal surface plasmons propagating on ultrathin and flexible films. *Proc Natl Acad Sci USA*. (2013) **110**:40–5. doi: 10.1073/pnas.1210417110
22. Kianinejad A, Chen ZN, Qiu C. Design and modeling of spoof surface plasmon modes-based microwave slow-wave transmission line. *IEEE Trans Micro Theory Tech*. (2015) **63**:1817–25. doi: 10.1109/TMTT.2015.2422694
23. Kianinejad A, Chen ZN, Qiu C. Full modeling, loss reduction, and mutual coupling control of spoof surface plasmon-based meander slow wave transmission lines. *IEEE Trans Micro Theory Tech*. (2018) **66**:3764–72. doi: 10.1109/TMTT.2018.2841857
24. Kianinejad A, Chen ZN, Qiu C. Low-Loss spoof surface plasmon slow-wave transmission lines with compact transition and high isolation. *IEEE Trans Micro Theory Tech*. (2016) **64**:3078–86. doi: 10.1109/TMTT.2016.2604807
25. Chizhik D, Ling J, Valenzuela RA. The effect of electric field polarization on indoor propagation. In: *IEEE 1998 International Conference on Universal Personal Communications ICUPC '98*. Florence (1998) **1**:459–462.
26. Soras C, Karaboikis M, Tsachtsiris G, Makios V. Analysis and design of an inverted-F antenna printed on a PCMCIA card for the 2.4 GHz ISM band. *IEEE Antenn Propag M*. (2002) **44:**37–44. doi: 10.1109/74.997891
27. Wei K, Zhang Z, Feng Z, Iskander MF. Periodic leaky-wave antenna array with horizontally polarized omnidirectional pattern. *IEEE Trans Antenn Propag*. (2012) **60:**3165–73. doi: 10.1109/TAP.2012.2196930
28. Zhang Y, Zhang Z, Li Y, Feng Z. A dual-loop antenna in a cage structure for horizontally polarized omnidirectional pattern. *IEEE Antenn Wirel Propag Lett*. (2013) **12:**1252–5. doi: 10.1109/LAWP.2013.2283543
29. Yu Y, Jolani F, Chen Z. A wideband omnidirectional horizontally polarized antenna for 4G LTE applications. *IEEE Antenn Wirel Propag Lett*. (2013) **12:**686–9. doi: 10.1109/LAWP.2013.2264545
30. Quan XL, Li R, Wang JY, Cui YH. Development of a broadband horizontally polarized omnidirectional planar antenna and its array for base stations. *Prog Electromagn Res*. (2012) **128:**441–56. doi: 10.2528/PIER12042405
31. Kianinejad A, Chen ZN, Zhang L, Liu W, Qiu CW. Spoof plasmon-based slow-wave excitation of dielectric resonator antennas. *IEEE Trans Antenn Propag*. (2016) **64:**2094–9. doi: 10.1109/TAP.2016.2545738

Conflict of Interest: The authors declare that the research was conducted in the absence of any commercial or financial relationships that could be construed as a potential conflict of interest.

ORIGINAL RESEARCH
published: 20 May 2020
doi: 10.3389/fphy.2020.00141

Terahertz Switch Utilizing Inorganic Perovskite-Embedded Metasurface

Ri-Hui Xiong [1], *Xiao-Qing Peng* [2] *and Jiu-Sheng Li* [1]*

[1] Centre for THz Research, China Jiliang University, Hangzhou, China, [2] State Grid Sichuan Electric Power Company, Chengdu, China

Various applications of terahertz technology require a large number of various terahertz wave control devices. Yet, high efficient and rapid-response terahertz switch is still a great challenge. Here, we introduce a new scheme, based on inorganic perovskite quantum dot ($CsPbBr_3$-QD)-embedded metasurface under different pump laser powers that realize terahertz wave high-speed switching performance. The off–on speed of the presented device achieves 8 MHz. This kind of components provides a new idea and a cost-effective functional solution for manipulating the terahertz waves in emerging terahertz devices and systems.

Keywords: terahertz wave switch, metasurface, switching speed, terahertz, inorganic pervoskite

OPEN ACCESS

Edited by:
Lin Chen,
University of Shanghai for Science and Technology, China

Reviewed by:
Fei Fan,
Nankai University, China
Rajour Tanyi Ako,
RMIT University, Australia

***Correspondence:**
Jiu-Sheng Li
lijsh2008@126.com

Specialty section:
This article was submitted to Optics and Photonics, a section of the journal Frontiers in Physics

Received: *22 January 2020*
Accepted: *09 April 2020*
Published: *20 May 2020*

Citation:
Xiong R-H, Peng X-Q and Li J-S (2020) Terahertz Switch Utilizing Inorganic Perovskite-Embedded Metasurface. Front. Phys. 8:141. doi: 10.3389/fphy.2020.00141

INTRODUCTION

Terahertz technology shows great promise for many applications including sensing, spectroscopy, non-destructive imaging, security monitoring, and wireless communications [1–4]. In particular, wireless communication using terahertz wave has attracted much interest due to large frequency bandwidth and high data transmission speed [5, 6]. These applications require the ability to flexibly manipulate terahertz wave in free space. Over the past several years, many kinds of terahertz wave devices have been reported such as filter [7], polarizer [8], power divider [9], modulator [10], absorber [11], switch [12], etc. As the core device of terahertz wave system, terahertz wave switch has received significant attention. Several techniques have been introduced to implement terahertz wave switch by applying external magnetism, electricity, temperature, and light illumination stimuli [13–17]. However, manipulating terahertz wave to achieve high efficient and rapid switching performance in a device is a great challenge.

Inorganic perovskite quantum dots ($CsPbBr_3$-QDs) have recently gained significant attention in photovoltaic applications demonstrating power conversion efficiencies in solar cells, high charge-carrier mobility [18, 19], and longer diffusion lengths [20]. Under the excitation of optical pump fluences, the perovskite exhibits high light absorption and short carrier recombination lifetime on nanosecond [21, 22]. Using these properties of perovskite, they are combined with subwavelength metasurface structures, and their properties can be enhanced or exploited as an efficient terahertz manipulation device. In this work, we described a method for the active control of terahertz wave transmission using $CsPbBr_3$-QD-embedded metasurface. By using commercially available finite difference frequency domain solver CST Microwave Studio, we obtained the optimized dimensions of the $CsPbBr_3$-QD-embedded metasurface. Finally, we experimentally demonstrate the switching phenomenon in the $CsPbBr_3$-QD embedded metasurface using optical stimuli. The proposed switch approach will be of great significance for practical terahertz applications.

DESIGN AND ANALYSIS

Figure 1A illustrates the configuration of the $CsPbBr_3$-QD-embedded metasurface-based terahertz wave switch. The top layer employs the inorganic perovskite QD-embedded metasurface as the geometric cell, and it is printed on a silicon oxide (100 nm)/high resistance silicon dielectric substrate with relative permittivity of $\varepsilon_{si} = 11.9$ and a thickness of 200 μm. The metasurface is made of copper with a conductivity of 5.96 $\times 10^7$ m/s and a thickness of 300 nm. The dielectric constant of copper from 0.2 THz to 1.0 THz is $\varepsilon_{cu} = -7.479 \times 10^4 + i2.723 \times 10^6 \sim -7.345 \times 10^4 + i5.338 \times 10^5$. The dielectric constant of inorganic perovskite QD perovskite in the frequency band 0.2∼1.0 THz is $\varepsilon_p = 9.2$ without laser irradiation [17]. The period of the unit cell is 100 μm. Optical microscope image of the fabricated $CsPbBr_3$-QD-embedded metasurface is shown in **Figure 1B**. We use the Drude model to describe the perovskite complex conductivity, which can be expressed by Yettapu et al. [22].

$$\delta(\omega) = \frac{\varepsilon_0 \omega_p^2}{t_\Gamma - i\omega}\left(1 + \frac{Ct_\Gamma}{t_\Gamma - i\omega}\right) \tag{1}$$

where $\omega_p = \sqrt{n}e^2/\varepsilon_0 m$ is the plasma frequency, t_Γ is the carrier scattering rate as $t_\Gamma = e/m^* v$, m^* is the carrier effective mass, $m = 0.5(m_e + m_h)$, $m_e = 0.22$, and $m_h = 0.24$. The C parameter, which represents the degree of carrier localization, may have values between 0 and −1. Without laser irradiate, we can choose $C = 0$. While with laser irradiate, we set $C = -1$. The relationship between the conductivity of perovskite and pump laser radiation can be obtained in Chanana et al. [23].

A commercially available finite difference frequency domain solver software CST Microwave Studio was used to simulate the metasurface structure. We use an adaptive mesh with a size of λ/10, where λ is the wavelength of incident radiation. The surrounding boundary condition was set as the periodic boundary, and an open boundary condition is set along the direction of the terahertz wave propagation. **Figure 2** shows the terahertz transmission spectra of the different parts of our proposed metasurface unit cell. One can see that only the $CsPbBr_3$-QD-embedded metasurface unit cell achieved narrow band resonance effects for enhancing the interaction between the terahertz wave and the metasurface. We also numerically analyze the terahertz transmission properties of the structure with different size parameters g, s, d, and a. In **Figure 3**, we can find that these parameters only have a weak influence on the position and width of transmission peak at 0.6 THz. After completing the optimization process, the geometrical dimensions of the geometric pattern metasurface have been set as follows: $a = 75$ μm, $g = 12$ μm, $s = 12$ μm, and $d = 70$ μm.

DEVICE FABRICATION

The metasurface was fabricated using the conventional photolithography technique. First, positive photoresist was coated on a silicon substrate and prebaked at 105°C for 1 min. Then, the mask was aligned and exposed under UV-light. The sample was immersed in the developer solution to remove the exposed part of the photoresist. A 300-nm-thick copper was deposited by thermal evaporation, and the sample was removed in acetone solution to obtain the designed metal pattern. Second, a thin layer of parylene c was deposited by vapor deposition to make the parylene film completely cover the sample, followed by a certain complementary pattern in the photoresist. The parylene film was etched with oxygen plasma, leaving a through hole, in which $CsPbBr_3$ perovskite QDs can be deposited. After solution casting and annealing of the desired $CsPbBr_3$ perovskite QD film, once the $CsPbBr_3$ perovskite QD film starts to crystallize, usually after 60 s, the parylene film will be layered. Finally, the samples were thoroughly annealed to obtain a high-quality polycrystalline pattern structure.

RESULTS AND DISCUSSION

A terahertz time domain spectroscopy (THz-TDS) system was used to measure the transmission spectra of the sample

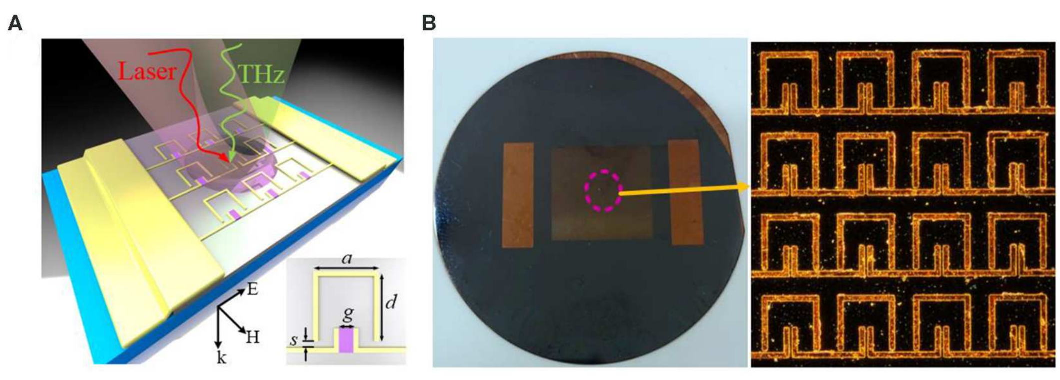

FIGURE 1 | (A) Three-dimensional schematic diagram of the proposed metasurface embedded with perovskite quantum dots ($CsPbBr_3$-QDs). **(B)** Optical microscope image of the fabricated $CsPbBr_3$-QD-embedded metasurface (geometric parameters of the metasurface unit cell, $a = 75$ μm, $g = 12$ μm, $s = 12$ μm, and $d = 70$ μm).

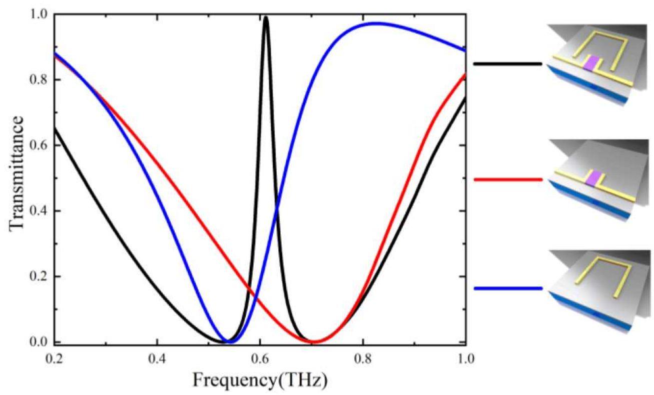

FIGURE 2 | Terahertz transmission spectra of the different parts of the proposed metasurface unit cell.

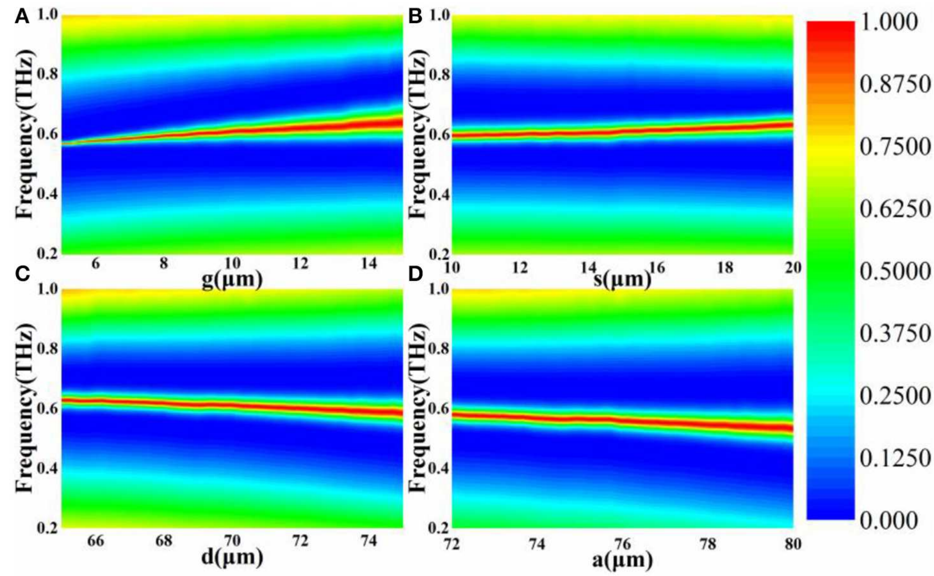

FIGURE 3 | Terahertz transmittance contour plot for various geometrical parameters values of our proposed $CsPbBr_3$-QD-embedded metasurface **(A)** *g*, **(B)** *s*, **(C)** *d*, **(D)** *a*.

with a different power density. The excitation source was a Ti:sapphire laser with 100-fs duration at 80-MHz repetition rate, and working wavelength at 780 nm. Terahertz pulse was generated using LT-GaAs photoconductive antenna, and a ZnTe nonlinear crystal was used to detect the terahertz signal. The $CsPbBr_3$-QD-embedded metasurfaces were placed at the confocal position of the system. The entire experiment was carried out in nitrogen environment. The recorded terahertz transmission time domain spectra are shown in **Figure 4A**, for varying the CW pumping laser fluence. **Figure 4B** shows the terahertz frequency domain spectra by Fourier transformation from the time domain data under various laser pump powers. In **Figure 4**, one can see that the transmission spectra of the $CsPbBr_3$-QD-embedded metasurface declines gradually as the pumping laser power increases. When the pumping power increases to 240 μJ/cm^2, the transmittances of the terahertz wave drops to 10.9% at 0.5 THz. It indicates that the sample can control the terahertz wave transmission under a different pump laser power.

The terahertz transmission switching performance of our proposed structure was investigated in terahertz continuous wave system (see **Figure 5**). **Figure 6** plots the measured dynamic characteristics of the proposed $CsPbBr_3$-QD-embedded metasurface structure with various laser pump fluences. **Figures 6A,B** illustrate the detected voltage signal waveform shape for switching speeds of 10 KHz and 8 MHz. One can see that the transmission amplitude of terahertz wave decreases with the switching speed increase from 10 KHz to 8 MHz.

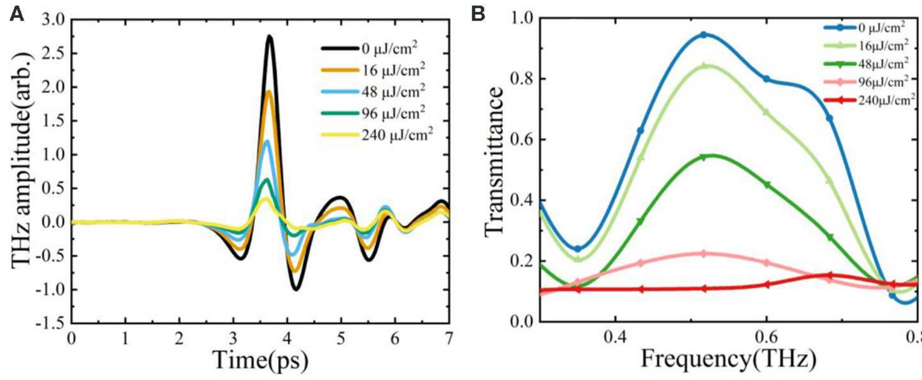

FIGURE 4 | (A) Measured terahertz transmission time domain spectra using the terahertz time domain spectroscopy (THz-TDS) under a different laser power. **(B)** Corresponding terahertz frequency domain spectra.

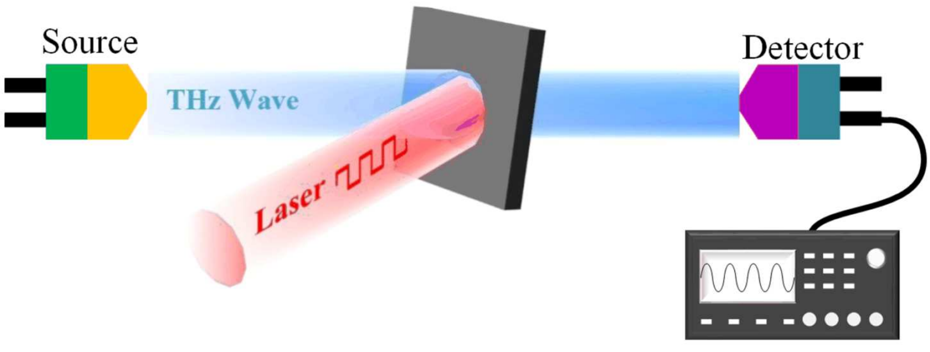

FIGURE 5 | Dynamic switching measurement using a backward-wave oscillator (BWO) CW terahertz source and Schottky diode detector.

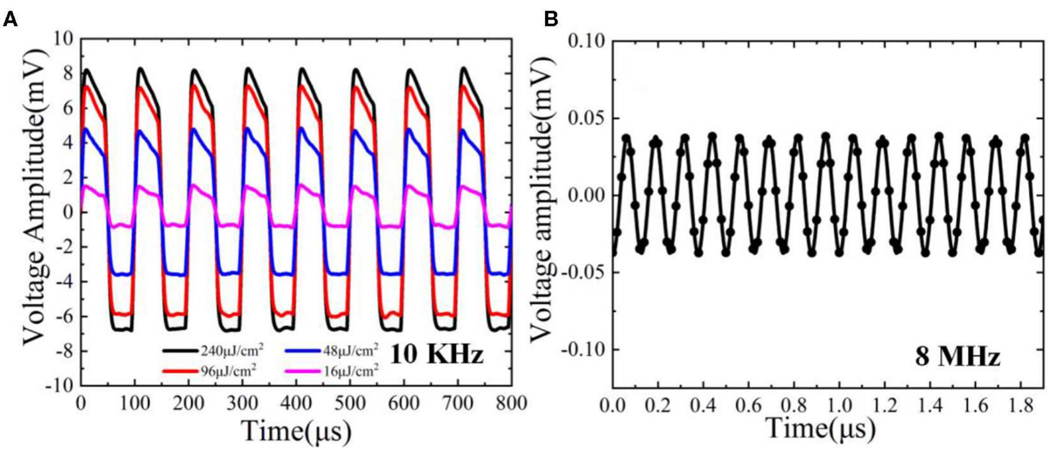

FIGURE 6 | (A) A 10-KHz switching speed under different pump laser fluencies. **(B)** An 8-MHz switching speed of the sample.

At switching speed of 8 MHz, the detected voltage amplitude falls to 0.05 mV. **Figure 7A** shows the terahertz transmission intensity distribution through the $CsPbBr_3$-QD-embedded metasurface structure without pump laser fluence. The terahertz wave transmission intensity drops to 10.9% of its original value under 240 μJ/cm^2 pump laser intensity. As depicted in **Figure 7B**, the corresponding extinction ratio is 83%. **Figure 7C** shows the extinction ratio dependence of the pump laser fluence

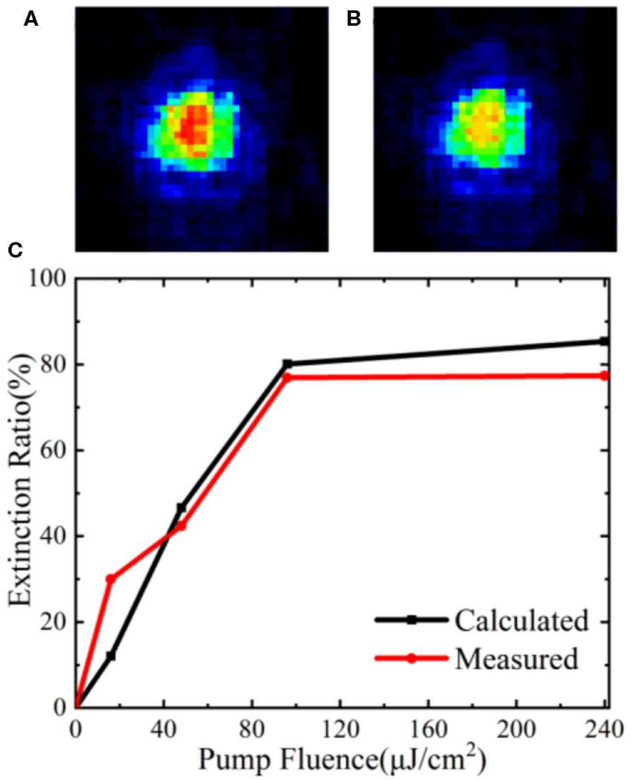

FIGURE 7 | Terahertz intensity distributions through the $CsPbBr_3$-QD-embedded metasurface. **(A)** 0 μJ/cm^2 and **(B)** 240 μJ/cm^2 pump laser intensity. **(C)** Extinction ratio dependence of pump laser intensity.

obtained by experiment and calculation. One sees that the $CsPbBr_3$-QD-embedded metasurface has low saturation pump laser intensity and high extinction ratio factor as a potential method to actively control the terahertz wave transmission. This work demonstrates a new approach for realizing active terahertz devices with improved functionalities.

CONCLUSION

We describe a method for the active control of terahertz wave transmission using $CsPbBr_3$-QD-embedded metasurface. The experimental results confirm the numerically simulated expectations. With the external applied pump laser irradiation, our presented terahertz device achieves high-efficiency terahertz wave switch with an off–on speed of 8 MHz. Owing to effective switching and easy fabrication, this device has promising applications as a controllable switch in future terahertz wave communication and imaging systems.

DATA AVAILABILITY STATEMENT

All datasets generated for this study are included in the article/supplementary material.

AUTHOR CONTRIBUTIONS

R-HX performed the THz measurements and did the calculations. X-QP fabricated and characterized the devices. J-SL concerned the devices structure and developed the theoretical model and guided the experimental work. All authors discussed the results and co-wrote the manuscript.

ACKNOWLEDGMENTS

The authors acknowledge valuable discussion on experiment with Dr. J. Liu. This work was sponsored by the National Natural Science Foundation of China (61871355, 61831012) and Zhejiang Lab (NO.2019LC0AB03).

REFERENCES

1. Chan W, Deibel J, Mittleman D. Imaging with terahertz radiation. *Report Progr Phys.* (2007) **70**:1325. doi: 10.1088/0034-4885/70/8/R02
2. Koenig S. Wireless sub-THz communication system with high data rate. *Nat Photon.* (2013) **7**:977. doi: 10.1038/nphoton.2013.275
3. Han P, Cho G, Zhang X. Time-domain transillumination of biological tissues with terahertz pulses. *Opt Lett.* (2000) **25**:242. doi: 10.1364/OL.25.000242
4. Savo S, Shrekenhamer D, Padilla W. Liquid crystal metamaterial absorber spatial light modulator for THz applications. *Adv Opt Mater.* (2014) **2**:275–9. doi: 10.1002/adom.201300384
5. Wang J, Tian H, Wang Y, Li X, Cao Y, Li L, et al. Liquid crystal terahertz modulator with plasmon-induced transparency metamaterial. *Opt Exp.* (2018) **26**:5769–76. doi: 10.1364/OE.26.005769
6. Sensale-Rodriguez B, Yan R, Kelly M. Broadband graphene terahertz modulators enabled by intraband transitions. *Nat Commun.* (2012) **3**:780. doi: 10.1038/ncomms1787
7. Tabatabaei F, Biabanifard M, Abrishamian M. Terahertz polarization-insensitive and all-optical tunable filter using Kerr effect in graphene disks arrays. *Optik.* (2019) **180**:526 doi: 10.1016/j.ijleo.2018.11.103
8. Yu T, Chi N, Tsai H, Wang S, Luo C, Chen K. Robust terahertz polarizers with high transmittance at selected frequencies through Si wafer bonding technologies. *Opt Lett.* (2017) **42**:4917 doi: 10.1364/OL.42.004917
9. Reichel K, Mendis R, Mittleman D. A broadband terahertz waveguide T-junction variable power splitter. *Sci Rep.* (2016) **6**:28925 doi: 10.1038/srep28925
10. Hochberg M, Baehrjones T, Wang G, Shearn M, Harvard K, Luo J. Terahertz all-optical modulation in a silicon-polymer hybrid system. *Nat Mater.* (2006) **5**:703–9 doi: 10.1038/nmat1719
11. Grant J, Ma Y, Saha S, Lok L, Khalid A, Cumming D. Polarization insensitive, broadband terahertz metamaterial absorber. *Opt Lett.* (2011) **36**:3476–8 doi: 10.1364/OL.36.003476
12. Kupchak C, Erskine J, England D, Sussman B. Terahertz-bandwidth switching of heralded single photons. *Opt Lett.* (2019) **44**:1427 doi: 10.1364/OL.44.001427
13. Li J, He J, Hong Z. Terahertz wave switch based on silicon photonic crystals. *Appl Opt.* (2007) **46**:5034–7. doi: 10.1364/AO.46.005034
14. Chen S, Fan F, Miao Y, He X, Zhang K, Chang S. Ultrasensitive terahertz modulation by silicon-grown MoS_2 nanosheets. *Nanoscale.* (2016) **8**:4713–9. doi: 10.1039/C5NR08101G

15. Zheng W, Fan F, Chen M, Chen S, Chang S. Optically pumped terahertz wave modulation in MoS_2-Si heterostructure metasurface. *AIP Adv.* (2016) **6**:075105. doi: 10.1063/1.4958878
16. Liu W, Fan F, Xu S, Chen M, Wang X, Chang S. Terahertz wave modulation enhanced by laser processed PVA film on Si substrate. *Sci Rep.* (2018) **8**:8304. doi: 10.1038/s41598-018-26778-7
17. Luo L, Wang K, Ge C, Guo K, Shen F, Yin Z, et al. Actively controllable terahertz switches with graphene-based nongroove gratings. *Photonics Res.* (2017) **5**:604. doi: 10.1364/PRJ.5.000604
18. Snaith H. Perovskites: the emergence of a new era for low-cost, high-efficiency solar cells. *J Phys Chem Lett.* (2013) **4**:3623–30. doi: 10.1021/jz4020162
19. Green M, Ho-Baillie A, Snaith H. The emergence of perovskite solar cells. *Nat Photon.* (2014) **8**:506–14. doi: 10.1038/nphoton.2014.134
20. Stranks S, Eperon G, Grancini G, Menelaou C, Alcocer M, Leijtens T, et al. Electron-hole diffusion lengths exceeding 1 micrometer in an organometal trihalide perovskite absorber. *Science.* (2013) **342**:341–4. doi: 10.1126/science.1243982
21. Herz L. Charge-carrier dynamics in organic-inorganic metal halide perovskites. *Annu Rev Phys Chem.* (2016) **67**:65–89. doi: 10.1146/annurev-physchem-040215-112222
22. Yettapu G, Talukdar D, Sarkar S, Swarnkar A, Nag A, Ghosh P. THz conductivity within colloidal $CsPbBr_3$ perovskite nanocrystals: remarkably high carrier mobilities and large diffusion lengths. *Nano Lett.* (2016) **16**:4838. doi: 10.1021/acs.nanolett.6b01168
23. Chanana A, Liu X, Zhang C, Vardeny Z, Nahata A. Ultrafast frequency-agile terahertz devices using methylammonium lead halide perovskites. *Sci Adv.* (2018) **4**:7353. doi: 10.1146/annurev-physchem-040215-112222

Conflict of Interest: The authors declare that the research was conducted in the absence of any commercial or financial relationships that could be construed as a potential conflict of interest.

frontiers in Physics

ORIGINAL RESEARCH
published: 30 June 2020
doi: 10.3389/fphy.2020.00216

Localized Electromagnetic Resonance Enabled THz Photothermoelectric Detection in Graphene

*Meng Chen, Yingxin Wang and Ziran Zhao**

National Engineering Laboratory for Dangerous Articles and Explosives Detection Technologies, Department of Engineering Physics, Tsinghua University, Beijing, China

OPEN ACCESS

Edited by:
Lin Chen,
University of Shanghai for Science and Technology, China

Reviewed by:
Li Tao,
The Chinese University of Hong Kong, China
Yaping Dan,
Shanghai Jiao Tong University, China

***Correspondence:**
Ziran Zhao
zhaozr@tsinghua.edu.cn

Specialty section:
This article was submitted to Optics and Photonics, a section of the journal Frontiers in Physics

Received: *22 March 2020*
Accepted: *20 May 2020*
Published: *30 June 2020*

Citation:
Chen M, Wang Y and Zhao Z (2020) Localized Electromagnetic Resonance Enabled THz Photothermoelectric Detection in Graphene. Front. Phys. 8:216. doi: 10.3389/fphy.2020.00216

We propose a graphene-based terahertz (THz) photodetector with a microstructure array designed to manipulate the surface electromagnetic modes. Benefiting from the generated localized electromagnetic resonance, a nearly perfect absorption to the incident THz radiation is observed, an asymmetrical temperature distribution is realized along the graphene channel under uniform THz illumination, and thereby an obvious photothermoelectric response is achieved. Polarization and geometry dependence of the photovoltage provides evidence that the photoresponse originated from the localized electromagnetic resonance. Our method is also suitable for other two-dimensional materials and shows promising applications for THz detection.

Keywords: photothermoelectric effect, THz, localized electromagnetic resonance, graphene, detector

INTRODUCTION

Surface electromagnetic mode, excited by specific structure and material, enables extreme light confinement at subwavelength scale to localize energy in micro-nano volumes and thus can greatly enhance the interaction between electromagnetic waves and matter [1, 2]. This unique property is generally named as localized electromagnetic resonance (LER) and the resulting new-emerging phenomena have inspired a worldwide effort to investigate their intrinsic physical mechanisms [3] and explore potential applications [4, 5]. Trapped in the LER, the photons are driven to interact with the electrons and phonons accompanying a fast and massive transform of energy. A portion of energy is re-emitted back to the free space via electron oscillation. Nevertheless, a major amount of energy is dissipated in the form of heat through the processes of photon-electron scattering, electron-phonon scattering, and the ultimate lattice vibration [6]. In addition to energy waste, the accumulation of heat is also detrimental for the devices with a complex and hyperfine structure to match the surface electromagnetic mode and may cause device deformation, leading to a performance degradation and life span shortening, but few attention has been paid to this problem.

On the other hand, the heat generated in LER also provides an energy source for voltage generation, playing an important role in the photothermoelectric (PTE) effect which exhibits significant potential applications for detection of low-energy photons [7], especially for the recent high-profile terahertz (THz) range [8]. Originating from the temperature gradient across the device channel, the PTE response ΔV is highly dependent on the temperature difference ΔT across the channel as depicted by $\Delta V= -S\Delta T$, where S is the Seebeck coefficient of the photoactive material [9]. Therefore, taking advantage of the unique properties of LER, i.e., the excellent light absorption and the large intensity of the localized field, the temperature gradient as well as the PTE response can be effectively enhanced [10]. Moreover, compared to the traditional PTE photodetectors in which the temperature gradient was realized by non-uniform illumination [11], spatially localized absorption in LER structures results in local heating of the channel material, allowing a uniform or even unfocused optical excitation. This strategy has been demonstrated in previous works by using conventional thermoelectric materials to construct the resonant structure. Mauser et al. reported a subwavelength grating-like thermoelectric nanostructures for resonant spectrally selective absorption, which created a large localized temperature gradient and realized a photoresponsivity of 38 VW^{-1} in visible range [12]. Based on guided-mode resonance effect, Monshat et al. proposed a photonic crystal resonator, achieving a narrowband visible absorptivity of 85.4% and a responsivity of 0.26 VW^{-1} [13]. Some other different resonant mechanisms were also employed for enhancement of the PTE response, such as the plasmonic nanostructure [14], metamaterial [15], metasurface [16], and so on [17, 18]. However, most of these former works were carried out in the infrared and visible regime, while the related research in THz band is still underexplored.

The recently emerging two dimensional materials such as graphene provides a new optoelectronic platform for developing novel functionalities, including low-energy photon detection [19] and integrated photon modulation [20]. The gapless nature brings graphene the ability in broadband absorption, making it a promising candidate for THz detection, and the bandwidth of graphene-based photodetectors can reach up to hundreds of GHz [21], as a consequence of its high carrier mobility. In addition, the electronic heat capacity of graphene is extremely low, which leads to a higher temperature rise for the same absorbed energy compared to other bulk material, highlighting its potential in acting as the channel material for PTE detectors [22]. However, limited by its petty small thickness, the absorption of graphene to the incident light is relatively weak, which is a major bottleneck in the application of graphene [23]. LER has been proved to be an important approach to enhance the interaction between matters and light [24–26]. In the LER region, several order of electromagnetic field intensity enhancement can be achieved, greatly increasing the absorption of materials. This scheme has been used to improve the absorptivity of graphene. On the other hand, LER shows great flexibility in manipulating the electromagnetic field distribution and thereby provides an effective way for constructing local absorption under uniform illumination. This feature facilitates significant application potential of LER in PTE detection, but there are still seldom works reported.

Here we develop a THz PTE detector integrated with graphene and LER microstructure. We adopt graphene as the channel material, and design a LER microstructure to enhance the absorption of graphene and produce a gradient temperature field. A sensitive and fast PTE response was observed in the proposed device under a uniform THz illumination, and characterizations of the response dependence on the microstructure geometry and THz polarization demonstrate that the PTE response is attributed to the asymmetrical field distribution induced by the LER microstructure.

DEVICE DESIGN AND FABRICATION

The device we proposed is shown in **Figure 1A**. The whole device was fabricated on a quartz substrate. A 200-nm thick Au with a 10-nm thick Ti adhesion layer, serving as a metal reflector, was deposited on the substrate by inductively coupled plasma chemical vapor deposition (ICPCVD), followed by growing an absorption layer of SiO_2 via plasma enhanced chemical vapor deposition (PECVD). Our graphene sample was grown on a copper foil by chemical vapor deposition (CVD) and then transferred onto the SiO_2 surface [27]. Oxygen plasma etching was employed to pattern the graphene into ribbons with a width of 50 μm and a period of 65 μm [28]. Finally, another 200-nm thick Au was deposited on the top, forming two electrodes located at both ends of the graphene ribbons, where one electrode comprises a resonant microstructure array with disc patterns and wires. The microstructure covers only half side of the graphene channel so as to generate an asymmetric structure.

The PTE effect or the thermoelectric effect originates from the temperature gradient across the channel. Without a temperature gradient, there is no electrical potential generated between the two channel ends, whether the channel is constructed by a single material or a complex heterojunction [29]. A common strategy involves limiting the heat energy in a local area of the channel and thereby forming a gradient temperature distribution [30]. This requires that the size of the heat source (a focused light beam or a microheater) is much smaller than the channel length. However, in the THz range, the light spot diameter is generally in the order of millimeter, thus requiring a channel with the similar scale. This makes it difficult to design miniaturized and arrayed THz PTE detector. While the device proposed here can solve this problem, as shown in **Figure 1A**. When THz wave is incident onto the device, it will be scattered by the metal microstructure. A portion of light is scattered into free space, while the other portion is coupled into the dielectric layer, reflected by the bottom metal layer, and returns back to the interface between the top Au layer and free space. When the two portions of light recombine destructively, i.e., meet the phase matching condition, the LER occurs and the incident energy will be concentrated within the interior of the device. **Figures 1B,C** show the simulated electric field distribution for a single unit of the microstructure array under LER condition. It is clear that the electric field intensity near the

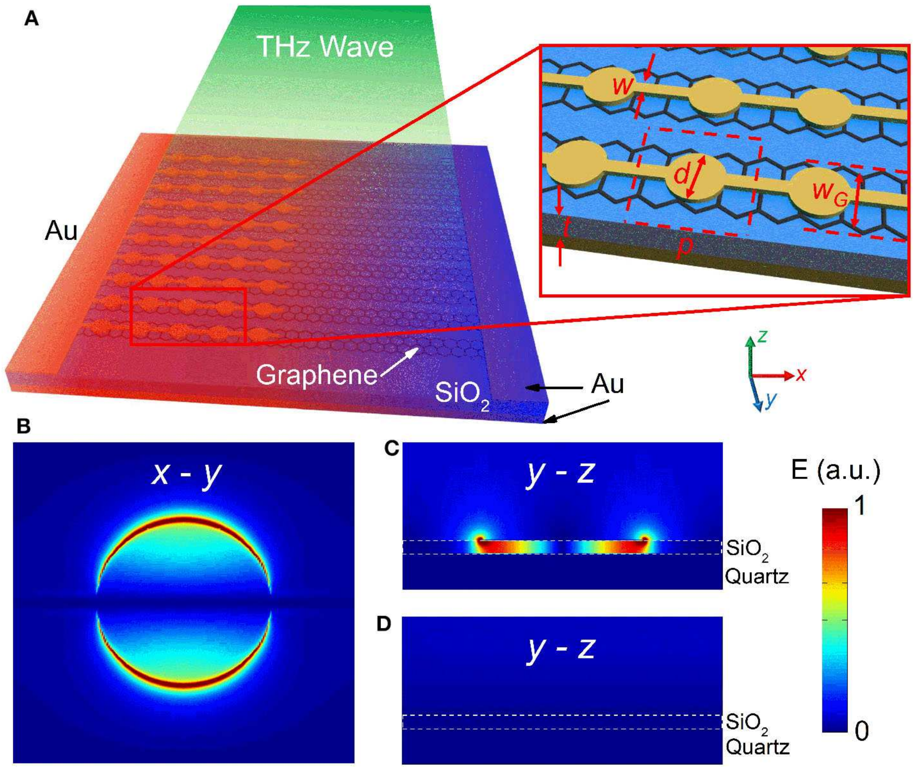

FIGURE 1 | (A) Schematic of the graphene device with a microstructured electrode. The inset shows the geometrical parameters of the microstructure. **(B)** The electric field distribution in the *x*-*y* plane (at the interface between the top Au layer and free space) and **(C)** in the *y*-*z* plane along the central axis as the LER occurs. **(D)** The *y*-*z* plane electric field distribution of the side without the LER structure.

edge of the metal disc is remarkably enhanced, and a majority of energy is retained within the SiO_2 dielectric layer. Such configuration is also known as a perfect metamaterial absorber, which possesses a theoretical absorptivity close to 100% [31]. Through the LER effect, the incident photons will be effectively absorbed by the dielectric layer. The specific absorption process involves photon-electron scattering, electron-phonon scattering and phonon-phonon scattering. Finally, the incident photon energy is converted into heat in the dielectric absorber layer so as to raise the temperature of the graphene channel via thermal diffusion. Due to that the metal microstructure only partially covers the graphene channel, there is no LER generated in the uncovered side. The electric field distribution of the uncovered side is drawn in **Figure 1D**, and the simulation indicates that the absorptivity of this side is lower than 1%. Without LER, a majority of the incident THz wave will be reflected back into free space directly by the bottom metal layer. The interaction distance between the THz wave and the device is about twice the dielectric layer thickness and thus is too thin to absorb the light energy effectively. Therefore, the temperature of the microstructure region locally increases, while that of the other side remains low. Obviously, benefiting from the LER mechanism, a gradient temperature distribution across the channel can be established even under uniform THz illumination.

Before device fabrication, specific geometrical parameters of the microstructure need to be precisely designed. The design goal is to optimize the resonant absorption of the microstructure at a frequency of 2.52 THz, the main output frequency of our available THz source, i.e., a far-infrared gas laser (FIRL 100, Edinburgh Instruments Ltd.). Here the finite difference time domain (FDTD solutions, Lumerical) method was employed to obtain the absorption spectrum of the resonant microstructure. The conductivity of Au was set as 4.56×10^7 Sm^{-1} [32], and the permittivity and loss tangent of SiO_2 were taken as 3.84 and 0.01, respectively, which were measured by a THz time-domain spectrometer. To estimate the parameters of graphene used in the simulation, several graphene devices were fabricated in advance by the same procedure as described above. The two-dimensional conductivity was measured to be $\sim$ 0.5 mS on average. Therefore, we set graphene as a conductive sheet with a two-dimensional conductivity of 0.5 mS in the simulation. A periodic boundary condition was used, and a *y*-polarization broadband THz source was incident along the –*z* direction. The reflectivity *R* of the device could be obtained directly from the simulation results, as shown in **Figure 2**, and then the absorptivity can be evaluated by $A = 1–R$.

The variable parameters of the microstructure include the disc diameter *d*, the periodic length *p*, the wire width *w*, and the thickness of the SiO_2 dielectric layer *t*, as denoted in the inset

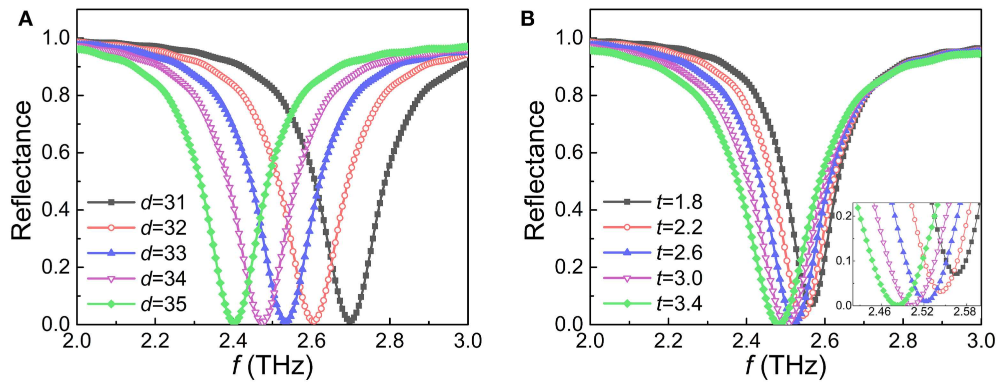

FIGURE 2 | **(A)** Reflectance spectra with different t ($d = 33\,\mu$m), and **(B)** different d ($t = 2.6\,\mu$m). The other parameters are $w = 3\,\mu$m and $p = 65\,\mu$m. The inset in **(B)** is a partial enlarged view around the resonance dips.

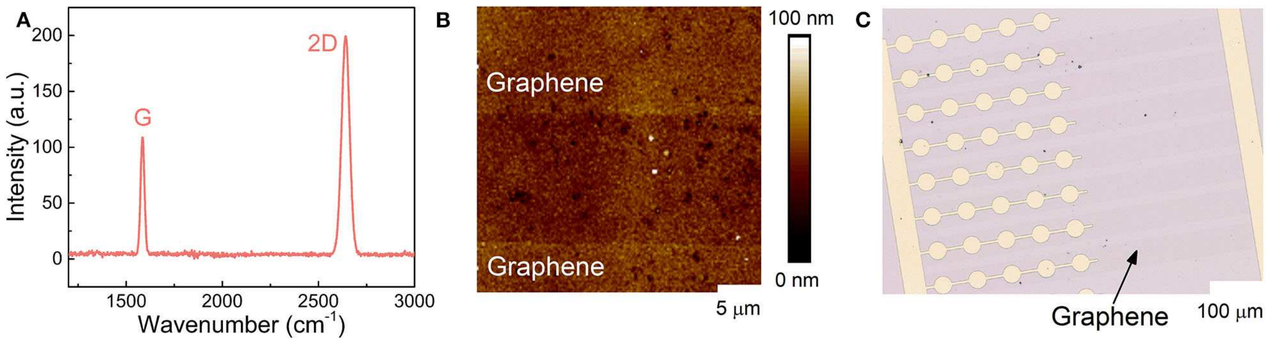

FIGURE 3 | **(A)** Raman spectrum and **(B)** AFM image of the fabricated graphene sample, **(C)** Optical micrograph of the device.

of **Figure 1A**. Note that d and p have similar influences on the resonance since both of them determine the geometry in the horizontal plane, and the effect of w can be neglected when it is far smaller than the wavelength. Here we mainly take into account the variation of t and d, as shown in **Figure 2**. Determined by the practical fabrication ability, the dielectric layer thickness t was taken in the range of 2∼3 μm. It can be found that the reflectance spectrum shows an obvious dip at the resonant frequency, and t has an impact on the resonant effect. The absorptivity peaks at $t = 2.6\,\mu$m for 2.52 THz. While as d increases for a fixed t, the corresponding resonant frequency redshifts. When $d = 33\,\mu$m, $t = 2.6\,\mu$m, $p = 65\,\mu$m and $w = 3\,\mu$m, the LER leads to a highest absorptivity of nearly one. Considering the discrepancy introduced in practical processing and the calculation error in the simulation, a series of devices with d varying between 31 and 35 μm were fabricated. This strategy ensures that an optimal device with a LER frequency located at 2.52 THz would be achieved.

EXPERIMENTAL RESULTS AND DISCUSSION

Firstly, we characterized the quality of graphene in our fabricated device. **Figure 3A** shows the Raman spectrum of the graphene channel excited at 633 nm, which displays two significant peaks at 1,584 and 2,641 cm^{-1}, corresponding to the G and 2D bands, respectively. The 2D band contains only a single and sharp peak, suggesting that the graphene is monolayer [33]. **Figure 3B** provides the atomic force microscope (AFM) image over a selected area within the graphene channel, and **Figure 3C** gives an optical microscope image of the device. We can see that the graphene channel is clearly visible, and the metal structures including the LER patterns and the electrodes were also well-fabricated.

Figure 4A illustrates a typical current-voltage (I-V) characteristic of our device ($d = 33\,\mu$m), where its nearly linear behavior implies that the graphene channel has an ohmic contact with the electrodes. The total resistance of our device calculated from this measurement is about 1,375 Ω. Then a 2.52 THz continuous-wave radiation chopped at 330 Hz was focused onto the device, and the produced photovoltage was measured by a current amplifier (SR570, Stanford Research Systems) and a lock-in amplifier (SR830, Stanford Research Systems). All the experiments were carried out at room temperature. **Figure 4B** shows the generated photovoltage as a function of the power actually received by the graphene channel, calculated by $P_{\text{channel}} = P_0 \times (A_{\text{channel}}/A_{\text{spot}})$, where P_0, A_{channel} and A_{spot} are the incident power, the channel area and the spot area, respectively. From the slope of the linearly

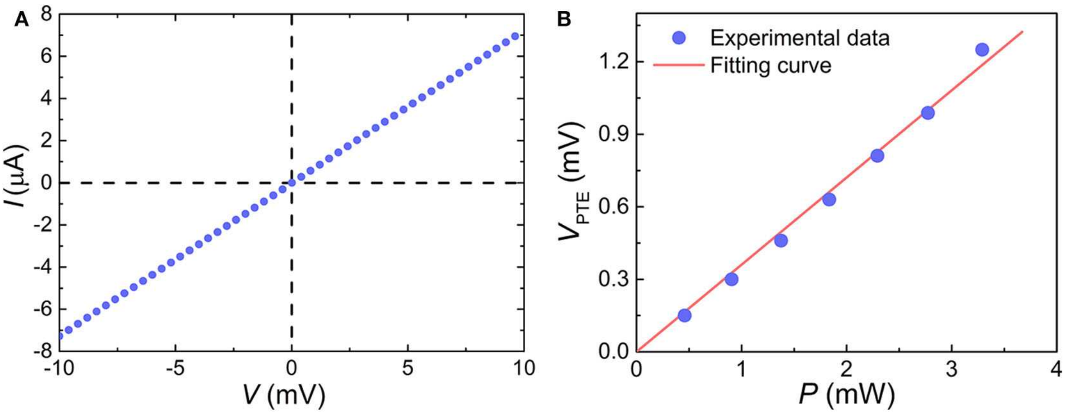

FIGURE 4 | (A) *I-V* characteristic of the graphene channel, **(B)** Power dependence of the photovoltage under 2.52 THz illumination.

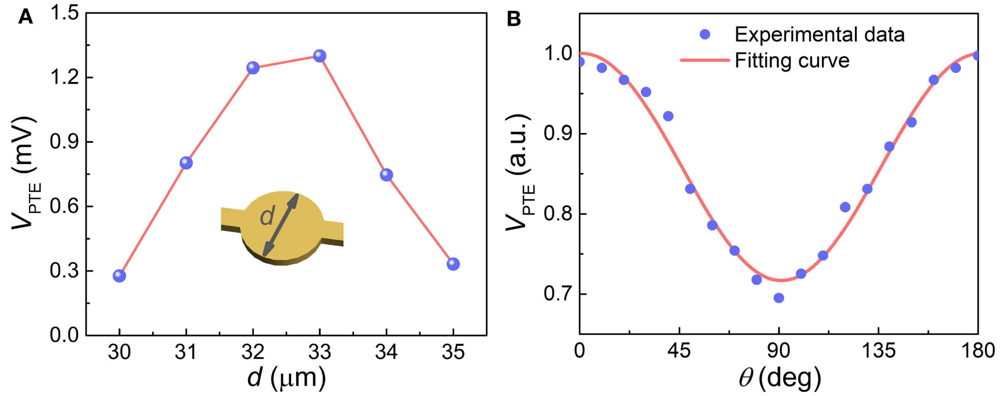

FIGURE 5 | (A) PTE response with different metal disc diameters. **(B)** Polarization dependence of the photovoltage (0° degree corresponds to the polarization parallel to the *y*-direction), and the red curve is a sine fit of the experimental data.

fitted line, we can obtain the photovoltage responsivity, whose value is $R_{\mathrm{PTE}} = 364.4\,\mathrm{mVW}^{-1}$. The temperature difference along the channel can be estimated by dividing the PTE photovoltage by S. Here we take S as 100 $\mu\mathrm{VK}^{-1}$ [34, 35], which results in a temperature difference of $\sim$10 K under a channel receiving power of 3 mW. The channel length is 600 μm, and thus the temperature gradient is $\sim$0.016 K $\mu\mathrm{m}^{-1}$ along the graphene channel. This value is sensible [34, 35] and can be further improved by optimizing the LER mode. For example, the LER mode with a stronger resonance and a smaller mode volumes is preferred because such mode can limit the energy in a smaller area and lead to a higher temperature gradient. Optimizing the LER field distribution to make the localized field closer to the graphene layer is another effective way since this can reduce the energy loss in the heat conduction.

Another approach to improve the responsivity of the device is optimizing the Seebeck coefficient of the graphene channel by electrostatic doping [34–36]. For example, fabricating a top-gate electrode on the right side of the channel can allow us to tune the carrier density of graphene, as well as its Fermi level and Seebeck coefficient. In this condition, the magnitude of PTE response can be deduced by $\Delta V = \Delta T_1 S_1 - \Delta T_2 S_2$, where ΔT_1 and ΔT_2 are the temperature rises of the left side and the right side, and S_1 and S_2 are their Seebeck coefficients, respectively. When the graphene in the right side is tuned to a reverse doping type, its S value will be opposite in sign to that of the left side. The generated photovoltage in the two parts of the channel is added in series, and thus an enhanced total photovoltage would be produced.

Because the PTE effect does not need a bias, its noise voltage is mainly determined by the Johnson–Nyquist (JN) noise, and the noise equivalent power (NEP) of the device can be calculated as follows [37]:

$$\mathrm{NEP} = \frac{\sqrt{4K_{\mathrm{B}}TR}}{R_{\mathrm{PTE}}} \tag{1}$$

where $K_{\mathrm{B}} = 1.38\times10^{-23}$ JK^{-1} is the Boltzmann constant, $T = 300\,\mathrm{K}$ is the environmental temperature, and R is the channel resistance of the device. The NEP of our device is 1.31×10^{-8} W $\mathrm{Hz}^{-1/2}$.

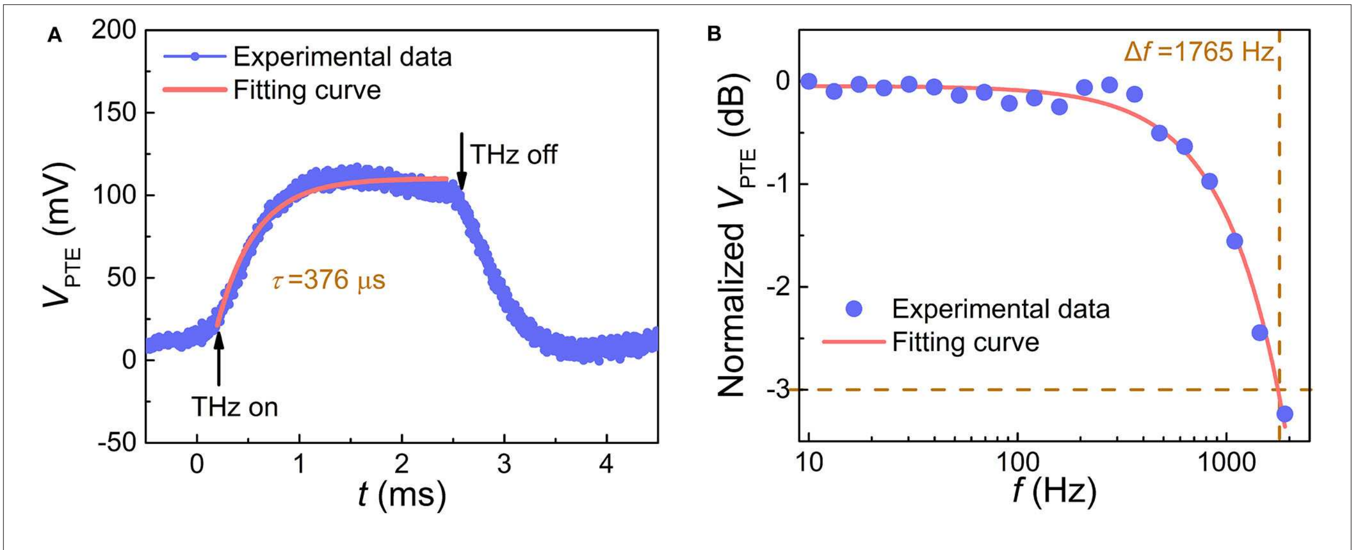

FIGURE 6 | (A) THz on/off switching curve and **(B)** modulation frequency dependent response of the graphene device under 2.52 THz illumination.

To demonstrate that PTE effect originated from the LER generated by the microstructure, the photovoltages of the devices with different metal disc diameters were measured, as given in **Figure 5A**. When $d = 31\,\mu\text{m}$, the photovoltage is about 0.3 mV. With increasing d, the photovoltage increases to 1.3 mV at $d = 33\,\mu\text{m}$ and then decreases again, revealing a consistent variation tendency with the absorption shown in **Figure 2A**. This is because that when $d = 33\,\mu\text{m}$, the resonance intensity reaches a maximum, and the absorption as well as the temperature rise are larger than that for other d values. In addition, the polarization-dependent responses were measured with a polarizer and a half-wave plate placed successively in the beam path after the THz source. **Figure 5B** shows the photovoltage vs. the polarization rotation angle θ of the incident THz radiation. The photovoltage is normalized to its maximum value, corresponding to the polarization perpendicular to the y-direction or the metal wires in the microstructure, defined as $\theta = 0°$. The polarization dependent ratio is about 0.18, calculated by $(V_{\max}-V_{\min})/(V_{\max}+V_{\min})$. This polarization dependence results from the polarization asymmetry of the microstructure, i.e., the existence of metal wires hampers the generation of the LER when the polarization is parallel to the wires. We also measured several devices without the LER structure and did not observe any effective response signals above the noise level, further confirming that the PTE responses is attributed to the LER mechanism.

The light on/off switching curve was measured with a current amplifier (SR570, Stanford Research Systems) and an oscilloscope (MSO64, Tektronix) to evaluate the response speed, as depicted in **Figure 6A**. By fitting the rising edge of this curve with an exponential function, the response time of our device is extracted to be 376 μs. **Figure 6B** shows the modulation frequency dependence of the PTE response. A similar fitting process indicates a 3 dB bandwidth of 1,765 Hz, confirming a response time in the order of submicrosecond scale. Note that the real response speed of the device may be faster than this value since the measurements here were partly limited by the bandwidth of the current amplifier. In general, the response speed of the graphene PTE detector mainly depends on two factors: the channel length and the thermal conductivity of the substrate [38]. With a shorter channel and a high thermal conductivity, the heat accumulation and diffusion over the channel can reach up to a steady state within a shorter time, indicating a faster response speed. By further optimizing the LER structure, such as reducing the period length, a shorter channel accompanying with a faster response speed can be achieved. Choosing the substrate material with a higher thermal conductivity is another strategy for improving the response speed.

CONCLUSION

In summary, we have proposed a novel graphene THz detector based on PTE effect enabled by the LER mechanism. The introduction of a LER microstructure enhances the absorption of graphene to THz wave and establishes a global temperature gradient across the graphene device channel even under a uniform illumination. The NEP of the detector is evaluated to be in the order of 10^{-8} WHz$^{-1/2}$, and the response time is in the microsecond level. Further improvement of the device performance can be implemented by optimizing the resonant mode of the microstructure to reduce the mode volume, enhance the resonant strength, and concentrate more thermal energy near the graphene layer. Our scheme of LER enhanced PTE effect can be also applicable for other two-dimensional materials, possesses high compatibility with traditional microelectronic processing technology, and paves a new way for developing high-performance room-temperature THz detectors.

DATA AVAILABILITY STATEMENT

The raw data supporting the conclusions of this article will be made available by the authors, without undue reservation.

AUTHOR CONTRIBUTIONS

ZZ conceived the idea. MC and YW led the design, fabrication, and measurements of the devices and co-wrote the manuscript. All authors contributed to the article and approved the submitted version.

FUNDING

The authors gratefully acknowledge financial support from the National Natural Science Foundation of China (Nos. U1930109 and U1633202) and the China Postdoctoral Science Foundation (No. 2018M640121).

REFERENCES

1. Safaei A, Chandra S, Leuenberger MN, Chanda D. Wide angle dynamically tunable enhanced infrared absorption on large-area nanopatterned graphene. *ACS Nano*. (2019) **13**:421–8. doi: 10.1021/acsnano.8b06601
2. Chen L, Xu N, Singh L, Cui T, Singh R, Zhu Y, et al. Defect-induced fano resonances in corrugated plasmonic metamaterials. *Adv Opt Mater*. (2017) **5**:1600960. doi: 10.1002/adom.201600960
3. Xu ST, Fan F, Ji YY, Cheng JR, Chang SJ. Terahertz resonance switch induced by the polarization conversion of liquid crystal in compound metasurface. *Opt Lett*. (2019) **44**:2450–53. doi: 10.1364/OL.44.002450
4. Chen L, Wei Y, Zang X, Zhu Y, Zhuang S. Excitation of dark multipolar plasmonic resonances at terahertz frequencies. *Sci Rep*. (2016) **6**:22027. doi: 10.1038/srep22027
5. Cheng J, Fan F, Chang S. Recent progress on graphene-functionalized metasurfaces for tunable phase and polarization control. *Nanomaterials Basel*. (2019) **9**:398. doi: 10.3390/nano9030398
6. Skoplaki E, Palyvos JA. On the temperature dependence of photovoltaic module electrical performance: a review of efficiency/power correlations. *Sol Energy*. (2009) **83**:614–24. doi: 10.1016/j.solener.2008.10.008
7. Koppens FH, Mueller T, Avouris P, Ferrari AC, Vitiello MS, Polini M. Photodetectors based on graphene, other two-dimensional materials and hybrid systems. *Nat Nanotechnol*. (2014) **9**:780–93. doi: 10.1038/nnano.2014.215
8. Wang Y, Niu Y, Chen M, Wen J, Wu W, Jin Y, et al. Ultrabroadband, sensitive, and fast photodetection with needle-like EuBiSe3 single crystal. *ACS Photon*. (2019) **6**:895–903. doi: 10.1021/acsphotonics.8b01527
9. Suzuki D, Oda S, Kawano Y. A flexible and wearable terahertz scanner. *Nat Photon*. (2016) **10**:809–13. doi: 10.1038/nphoton.2016.209
10. Dai W, Liang Y, Yang M, Schrecongost D, Gajurel P, Lee H, et al. Large and reconfigurable infrared photothermoelectric effect at oxide interfaces. *Nano Lett*. (2019) **19**:7149–54. doi: 10.1021/acs.nanolett.9b02712
11. Chen M, Wang Y, Wen J, Chen H, Ma W, Fan F, et al. Annealing temperature-dependent terahertz thermal-electrical conversion characteristics of three-dimensional microporous graphene. *ACS Appl Mater Inter*. (2019) **11**:6411–20. doi: 10.1021/acsami.8b20095
12. Mauser KW, Kim S, Mitrovic S, Fleischman D, Pala R, Schwab KC, et al. Resonant thermoelectric nanophotonics. *Nat Nanotechnol*. (2017) **12**:770–5. doi: 10.1038/nnano.2017.87
13. Monshat H, Liu L, Lu M. A narrowband photo-thermoelectric detector using photonic crystal. *Adv Opt Mater*. (2018) **7**:1801248. doi: 10.1002/adom.201801248
14. Shautsova V, Sidiropoulos T, Xiao X, Gusken NA, Black NCG, Gilbertson AM, et al. Plasmon induced thermoelectric effect in graphene. *Nat Commun*. (2018) **9**:5190. doi: 10.1038/s41467-018-07508-z
15. Luxmoore IJ, Liu PQ, Li P, Faist J, Nash GR. Graphene–metamaterial photodetectors for integrated infrared sensing. *ACS Photon*. (2016) **3**:936–41. doi: 10.1021/acsphotonics.6b00226
16. Fang J, Wang D, DeVault CT, Chung TF, Chen YP, Boltasseva A, et al. Enhanced graphene photodetector with fractal metasurface. *Nano Lett*. (2017) **17**:57–62. doi: 10.1021/acs.nanolett.6b03202
17. Muench JE, Ruocco A, Giambra MA, Miseikis V, Zhang D, Wang J, et al. Waveguide-integrated, plasmonic enhanced graphene photodetectors. *Nano Lett*. (2019) **19**:7632–44. doi: 10.1021/acs.nanolett.9b02238
18. Xu X, Kwon H, Gawlik B, Mohammadi Estakhri N, Alu A, Sreenivasan SV, et al. Enhanced photoresponse in metasurface-integrated organic photodetectors. *Nano Lett*. (2018) **18**:3362–7. doi: 10.1021/acs.nanolett.7b05261
19. Lundeberg MB, Gao Y, Woessner A, Tan C, Alonso-Gonzalez P, Watanabe K, et al. Thermoelectric detection and imaging of propagating graphene plasmons. *Nat Mater*. (2017) **16**:204–7. doi: 10.1038/nmat4755
20. Cai X, Sushkov AB, Jadidi MM, Nyakiti LO, Myers-Ward RL, Gaskill DK, et al. Plasmon-enhanced terahertz photodetection in graphene. *Nano Lett*. (2015) **15**:4295–302. doi: 10.1021/acs.nanolett.5b00137
21. Romagnoli M, Sorianello V, Midrio M, Koppens FHL, Huyghebaert C, Neumaier D, et al. Graphene-based integrated photonics for next-generation datacom and telecom. *Nat Rev Mater*. (2018) **3**:392–414. doi: 10.1038/s41578-018-0040-9
22. Tielrooij KJ, Massicotte M, Piatkowski L, Woessner A, Ma Q, Jarillo-Herrero P, et al. Hot-carrier photocurrent effects at graphene-metal interfaces. *J Phys Condens Mat*. (2015) **27**:164207. doi: 10.1088/0953-8984/27/16/164207
23. Rogalski A, Kopytko M, Martyniuk P. Two-dimensional infrared and terahertz detectors: outlook and status. *Appl Phys Rev*. (2019) **6**:021316. doi: 10.1063/1.5088578
24. Yang Y, Xu D, Zhang W. High-sensitivity and label-free identification of a transgenic genome using a terahertz meta-biosensor. *Opt Express*. (2018) **26**:31589–98. doi: 10.1364/OE.26.031589
25. Liu W, Fan F, Chang S, Hou J, Chen M, Wang X, et al. Nanoparticles doped film sensing based on terahertz metamaterials. *Opt Commun*. (2017) **405**:17–21. doi: 10.1016/j.optcom.2017.07.086
26. Venuthurumilli PK, Ye PD, Xu X. Plasmonic resonance enhanced polarization-sensitive photodetection by black phosphorus in near infrared. *ACS Nano*. (2018) **12**:4861–7. doi: 10.1021/acsnano.8b01660
27. Yoo TJ, Kim YJ, Lee SK, Kang CG, Chang KE, Hwang HJ, et al. Zero-bias operation of CVD graphene photodetector with asymmetric metal contacts. *ACS Photon*. (2017) **5**:365–70. doi: 10.1021/acsphotonics.7b01405
28. Deng T, Zhang Z, Liu Y, Wang Y, Su F, Li S, et al. Three-dimensional graphene field-effect transistors as high-performance photodetectors. *Nano Lett*. (2019) **19**:1494–503. doi: 10.1021/acs.nanolett.8b04099
29. Wang G, Zhang M, Chen D, Guo Q, Feng X, Niu T, et al. Seamless lateral graphene p-n junctions formed by selective in situ doping for high-performance photodetectors. *Nat Commun*. (2018) **9**:5168. doi: 10.1038/s41467-018-07555-6
30. Erikson KJ, He X, Talin AA, Mills B, Hauge RH, Iguchi T. Figure of merit for carbon nanotube photothermoelectric detectors. *ACS Nano*. (2015) **9**:11618–27. doi: 10.1021/acsnano.5b06160
31. Landy N, Sajuyigbe S, Mock J, Smith D, Padilla W. Perfect metamaterial absorber. *Phys Rev Lett*. (2008) **100**:207402. doi: 10.1103/PhysRevLett.100.207402
32. Shen X, Cui TJ. Photoexcited broadband redshift switch and strength modulation of terahertz metamaterial absorber. *J Opt*. (2012) **14**:114012. doi: 10.1088/2040-8978/14/11/114012
33. Ferrari AC, Meyer JC, Scardaci V, Casiraghi C, Lazzeri M, Mauri F, et al. Raman spectrum of graphene and graphene layers. *Phys Rev Lett*. (2006) **97**:187401. doi: 10.1103/PhysRevLett.97.187401
34. Castilla S, Terrés B, Autore M, Viti L, Li J, Nikitin AY, et al. Fast and sensitive terahertz detection using an antenna-integrated graphene

pn junction. *Nano Lett*. (2019) **19**:2765–73. doi: 10.1021/acs.nanolett.8b04171
35. Viti L, Purdie DG, Lombardo A, Ferrari AC, Vitiello MS. HBN-encapsulated, graphene-based, room-temperature terahertz receivers, with high speed and low noise. *Nano Lett*. (2020) **20**:3169–77. doi: 10.1021/acs.nanolett.9b05207
36. Hu J, Wu T, Tian J, Klimov NN, Newell DB, Chen YP. Coulomb drag and counterflow seebeck coefficient in bilayer-graphene double layers. *Nano Energy*. (2017) **40**:42–8. doi: 10.1016/j.nanoen.2017.07.035
37. Zak A, Andersson MA, Bauer M, Matukas J, Lisauskas A, Roskos HG, et al. Antenna-integrated 0.6 THz FET direct detectors based on CVD graphene. *Nano Lett*. (2014) **14**:5834–8. doi: 10.1021/nl5027309
38. Deng X, Wang Y, Zhao Z, Chen Z, Sun J-L. Terahertz-induced photothermoelectric response in graphene-metal contact structures. *J Phys D Appl Phys*. (2016) **49**:425101. doi: 10.1088/0022-3727/49/42/425101

Conflict of Interest: The authors declare that the research was conducted in the absence of any commercial or financial relationships that could be construed as a potential conflict of interest.

MINI REVIEW
published: 06 August 2020
doi: 10.3389/fphy.2020.00251

Excitation of Surface Plasmons by Inelastic Electron Tunneling

Lufang Liu[1], Yue Xu[1], Jiajie Zhu[1], Pan Wang[1,2], Limin Tong[1,3] and Alexey V. Krasavin[2]**

[1] State Key Laboratory of Modern Optical Instrumentation, College of Optical Science and Engineering, Zhejiang University, Hangzhou, China, [2] Department of Physics and London Centre for Nanotechnology, King's College London, London, United Kingdom, [3] Collaborative Innovation Center of Extreme Optics, Shanxi University, Taiyuan, China

Surface plasmons are usually excited by diffraction-limited optical methods with the use of bulky optical components, which greatly limits the miniaturization and chip-scale high-density integration of plasmonic devices. By integrating a plasmonic nanostructure with a tunnel junction, plasmonic modes in the nanostructure can be directly excited by low-energy tunneling electrons with the advantages including an ultra-small footprint and an ultra-fast speed. In this mini-review, recent progress in the electric excitation of localized and propagating surface plasmons by inelastic electron tunneling is overviewed.

Keywords: surface plasmons, tunnel junctions, inelastic tunneling, optical antennas, light emission, waveguiding

Edited by:
Lin Chen,
University of Shanghai for Science and Technology, China

Reviewed by:
Shuiyan Cao,
Nanjing University of Aeronautics and Astronautics, China
Tao Wang,
Soochow University, China

Correspondence:
Pan Wang
nanopan@zju.edu.cn
Alexey V. Krasavin
alexey.krasavin@kcl.ac.uk

Specialty section:
This article was submitted to Optics and Photonics, a section of the journal Frontiers in Physics

Received: *01 May 2020*
Accepted: *08 June 2020*
Published: *06 August 2020*

Citation:
Liu L, Xu Y, Zhu J, Wang P, Tong L and Krasavin AV (2020) Excitation of Surface Plasmons by Inelastic Electron Tunneling. Front. Phys. 8:251. doi: 10.3389/fphy.2020.00251

INTRODUCTION

Surface plasmons are highly confined electromagnetic modes coherently coupled to collective oscillations of free carriers at metallic (or doped semiconductor) interfaces. They exist in the form of surface plasmon polaritons (SPPs) propagating at an interface between a conductor and a dielectric or as localized surface plasmons (LSPs) supported by confined conductive nanostructures [1, 2]. Their ability to localize electromagnetic fields at a subwavelength scale and produce greatly enhanced local fields for strong light–matter interaction offers the opportunity to combine the advantages of nanoelectronics (small size) and dielectric nanophotonics (high speed), opening an avenue for merging electronics and photonics at the nanoscale [3]. In the past 20 years, a great progress has been made in the area of plasmonics, which have stimulated a variety of applications, such as nano waveguides [4–6], plasmonic lasers [7–9], ultrafast electro-optical [10–12] and all-optical [13, 14] modulation, photodetection [15, 16], bio-chemical sensing [17, 18], and enhancement of non linear optics [19, 20].

Usually, surface plasmons are excited by diffraction-limited optical methods with the use of bulky optical components (e.g., prisms, grating, objectives, etc.) [1], which greatly limits the miniaturization and chip-scale high-density integration of plasmonic devices. At the same time, there are some alternatives. In his seminal work, Ritchie proposed that fast electrons can be used for the excitation of surface plasmons in metal [21]. Later, both the excitation of SPPs [22, 23] and LSPs [24] have been experimentally demonstrated with high-energy (∼30 keV) electron beams with an advantage of highly precise and localized excitation (with a spatial resolution down to several nanometers). However, the requirements of a high electric voltage and a vacuum environment make it impossible for practical applications. Low-energy electrical excitation of SPPs has been demonstrated, e.g., by coupling plasmonic waveguides with electrically driven nano light sources [25, 26], but a highly compact and faster approach not related to the carrier lifetime would be highly desirable. In this mini-review, we focus on the recent breakthroughs in the low-energy direct excitation of surface plasmons based on an inelastic electron tunneling (IET) effect in tunnel junctions.

ORIGIN AND INITIAL STUDIES OF OPTICAL EMISSION BY IET

In 1976, Lambe and McCarthy [27] observed a broadband light emission from macroscopic planar metal-insulator-metal (MIM) tunnel junctions with an external quantum efficiency (EQE, i.e., electron-to-photon conversion efficiency) around 10^{-5}. This phenomenon can be explained in terms of IET-based excitation of surface plasmon modes subsequently coupled to photons on rough planar MIM tunnel junctions. When an electric bias is applied across an MIM structure with a nanometer-scale insulator thickness, electrons can quantum-mechanically tunnel through the insulating barrier. During the tunneling process (**Figure 1A**), most electrons tunnel elastically without energy loss, appearing as high-energy (in respect to the Fermi level) electrons on the other side of the junctions, so called "hot electrons." Some small fraction of electrons, however, tunnel inelastically, giving part of their energy to the excitation of plasmonic modes in the junction, which can then couple to extended propagating SPP modes or to free-space photons. The resulting emission spectral profile $I(\omega) \propto I_{tc}(V,\omega)\,\rho_{LDOS}\eta_{rad}$ is defined by the electromagnetic intensity spectrum of the tunneling current $I_{tc}(V,\omega) \propto \left(1 - \frac{\hbar\omega}{eV}\right)$ (which can be found from the calculation of the quantum transition matrix elements [30, 31] or from a Fourier transform of the tunneling current shot noise [32]), local density of optical states (LDOS) ρ_{LDOS} in the junction region and the radiative efficiency of the tunneling system in terms of generation of output photonic and/or plasmonic modes η_{rad}. In other words, the intrinsic electromagnetic spectrum from the tunneling current, $I_{tc}(V,\omega)$, is highly dependent on the applied bias V with a high-frequency cutoff ω_{co} (defined by the quantum relation for the maximal energy conversion $\hbar\omega_{co} = eV$) and a monotonic increase toward lower frequencies, and it is shaped into the final emission spectrum by the optical (frequently resonant) properties of the tunneling structure, defined by ρ_{LDOS} and η_{rad}. Later in the 1980's, IET-induced light emission was also reported from plasmonic tunnel junctions formed between a scanning tunneling microscope (STM) tip and a metallic substrate [33–35]. By analyzing the leakage radiation of a tunnel junction formed between an STM tip and a thin gold film in both image and Fourier planes, Wang et al. found that up to 99.5% of the detected photons come from leakage radiation of SPPs propagating on the gold film with the remaining photon emission attributed to the radiative decay of a localized plasmonic mode excited between the STM tip and the gold film [36], explicitly demonstrating the possibility of highly efficient coupling of inelastic tunneling to propagating plasmonic modes. Furthermore, despite its low EQE, this technique provides a high-spatial-resolution method for the study of LSPRs in metallic nanostructures [37–39]. At the same time, in combination with the atomic-scale spatial resolution of an STM, this approach has been developed into a useful optical spectroscopic method for single-molecule characterizations [40].

IET-GENERATED LIGHT EMISSION FROM OPTICAL ANTENNAS

Together with the success of IET-induced plasmon excitation and light emission in the STM research community comes its main challenge for the application in practical devices related to its low efficiencies, including internal quantum efficiency (IQE, inelastic tunneling efficiency, which is defined by the ratio of the generated plasmonic quanta and the number of overall tunneling events) and EQE (for photon-related applications). Overcoming this has attracted continuous research interest in the past four decades because of the ultra-small footprint of tunnel junctions, which allows for high-density integration, and the ultra-fast speed of the IET process (at a scale of few femtoseconds [41]), which offers the potential for ultra-fast direct modulation of the excitation. These efforts are further motivated by a theoretical prediction that the IQE can be of the order of 10%, known from the early days of the research [42]. From the theoretical point of view, the IQE of a plasmonic tunnel junction is defined by the electronic densities of states in both electrodes (as well as any other electronic states inside the junction area) and the LDOS in the tunnel junction, while the EQE is defined by a product of the IQE and the radiation efficiency of the tunnel junction [43–45]. By engineering the LDOS and radiation efficiency, a significant increase in both IQE and EQE has been recently demonstrated [28, 46–48]. For example, in 2015, Kern et al. demonstrated the first electrically driven optical antenna by integrating a tunnel junction into it [28]. In this experiment, the tunnel junction was fabricated by placing a gold nanoparticle into a gap formed between two arms of a linear dipole antenna as shown in the left panel of **Figure 1B**. The emission spectrum from the electrically driven optical antenna is then defined by the applied bias and the nanoantenna plasmonic resonance, which can be tuned by changing the geometry of the nanoantenna (right panel of **Figure 1B**). Taking advantage of the high LDOS and radiation efficiency of the resonant antenna design, the EQE was increased to $\sim 10^{-4}$, which is about two orders of magnitude higher than that for a non-resonant design. Later in the same year, Parzefall et al. achieved resonantly enhanced light emission by structuring an array of slot antennas on the bottom electrode of a vertical MIM tunnel junction formed by two gold electrodes and an insulating h-BN crystal [46]. Compared with an unstructured MIM tunnel junction, the EQE of the nanostructured junctions is increased by two orders of magnitude from $\sim 4 \times 10^{-7}$ to $\sim 2.5 \times 10^{-5}$ at a bias of 2.5 V due to the enhanced radiation efficiency $\sim 4 \times 10^{-3}$ provided by the slot antennas. The authors further demonstrated direct temporal modulation of light emission from the MIM tunnel junctions at frequencies up to 1 GHz. In 2018, implementing a tunnel junction produced by two chemically synthesized silver nanocubes assembled into an edge-to-edge configuration with the stabilizing polymer simultaneously working as the insulating barrier, Qian et al. obtained a record-high EQE of up to 2% at near-infrared frequencies [47]. Such excellent efficiency values are underlined by a very high LDOS in the tunneling junction (a factor of 3.1 × 10^5 higher than in vacuum) provided by an atomic-level quality of the gap between the silver single crystals and prominent 24.6% radiative efficiency of the implemented edge-to-edge nanoantenna design. In 2019, by cross-placing an Ag nanowire and an Au nanostripe, He et al. demonstrated the excitation of cavity plasmons with highly tuneable multiple emission peaks and narrow (tens of nanometers) line widths [49]. By using a dielectrophoresis trapping method, they further demonstrated efficient fabrication of nanoparticle-based electrically driven optical antennas with a measured EQE of ∼2.5 × 10^{-4} [50]. Looking into the tunneling system from a conceptual point of view, Uskov et al. theoretically showed that the close-to-unity IQE can be achieved by introducing a quantum well structure in the tunneling gap with the energy level in the well aligned in a way that the inelastic tunneling happens in a resonant manner while the elastic counterpart does not [44]. However, as the authors noticed, this is done on the expense of the overall value of the tunneling probability, which dramatically decreases.

Although the IQE and EQE in plasmonic tunnel junctions have been significantly improved by engineering the LDOS and radiation efficiency, the overall generated plasmonic or photonic power is still quite low (pW level or smaller), which causes a difficulty in the signal detection and greatly limits their applications. This, however, is mainly due to the intrinsically low tunneling current in single nanoscale tunnel junctions. A promising way to solve this problem is increasing the number and density of the optical antenna-coupled tunnel junctions. For example, by constructing a macroscopic and high-density plasmonic tunnel junction array at the top of a plasmonic metamaterial produced by vertically oriented gold nanorods (**Figure 1C**, nanorod areal density is around 1 × 10^{10} cm^{-2}), Wang et al. realized IET-driven light emission visible by the naked eye (**Figure 1D**) [29, 51]. The spectrum of the emission in this case is shaped by the metamaterial plasmonic modes, which can be tuned throughout the visible and near-infrared

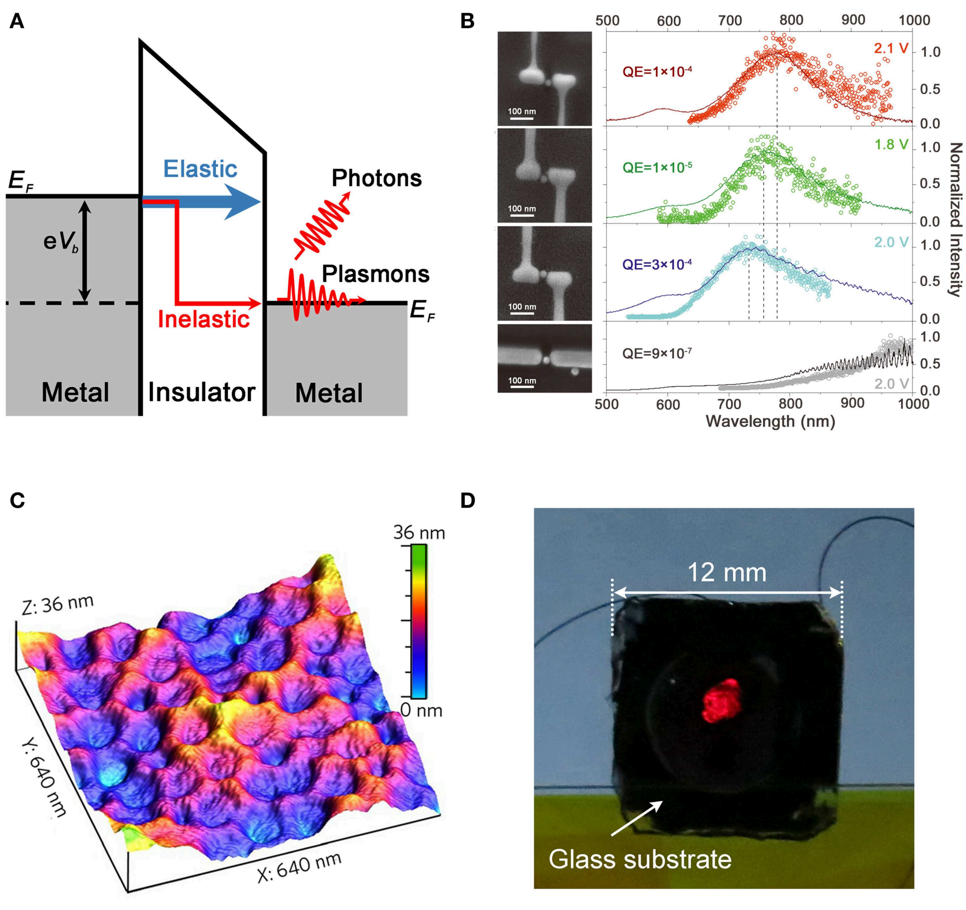

FIGURE 1 | (A) Schematic diagram of generation of surface plasmons and photons through IET. **(B)** Electroluminescence (data points) and scattering spectra (solid lines) for antennas with various geometries and a micrometer-long non-resonant wire, together with the corresponding SEM images. **(C)** Atomic force microscopy image of a gold nanorod array with the dips marking the positions of Au few nanometers below the surface of an Al_2O_3 matrix. **(D)** Photograph of an Au nanorod array electrically driven at a bias of 2.5 V. **(B)** is reprinted with permission from Ref. [28]. Copyright © 2015, Springer Nature. **(C,D)** are reprinted with permission from Ref. [29]. Copyright © 2018, Springer Nature.

ranges by tuning the metamaterial modes via the nanostructure geometric parameters [51]. The measured emission power was around 100 nW, which makes the signal detection trivial for applications such as optical sensing. Based on this, Wang et al. further demonstrated an ultra-compact electrically driven optical sensor by exploiting hot electrons generated via elastic tunneling (usually ignored, as it decays by the generation of heat) for the activation of chemical reactions in the junctions and IET-generated photons for the monitoring of this process [29].

IET-BASED EXCITATION OF WAVEGUIDED MODES

Apart from coupling to free-space light emission and 2D plasmonic modes, IET can also be coupled to waveguided plasmonic or photonic modes, which is highly desired for on-chip applications, as they have a crucial advantage as information carriers in comparison with traditional electronic signals in terms of a higher bandwidth and lower loss. In 2011, Bharadwaj et al. reported an electrical excitation of propagating SPPs in a Au nanowire (**Figure 2A**) [52]. A plasmonic mode excited with an STM tip at the left end of the nanowire by IET, was subsequently coupled to SPPs propagating along the nanowire and then converted to free-space photons at the right end. However, the excitation of propagating SPPs with the use of STM is difficult for practical applications where on-chip integration is highly desired. In this respect, a promising design was realized by integrating an electromigrated tunnel junction on the top of a dielectric-loaded surface plasmon waveguide (DLSPPW) (**Figure 2B**) [53] or by crossing a gold plasmonic waveguide and an thin aluminum strip covered with a nanoscale oxide layer [56, 57]. For the latter case, an SPP excitation efficiency exceeding 1% was reported [56], which was further explained by surface roughness–induced momentum matching between the MIM modes in the junction and the output SPP modes present in the system [57]. In 2019, Zhang et al. further demonstrated enhanced excitation of SPPs along an aluminum–air interface by fabricating an array of linear gold antennas on the top of an oxidized aluminum surface [58]. The emitted SPP power was increased to ∼10 pW, and the emission spectrum/polarization was controlled by the design of the antenna arrays. According to a recent calculation by Parzefall et al. [59], the IET-induced excitation efficiency of SPPs in extended conventional plasmonic waveguides is limited by a low coupling efficiency between the extremely confined MIM modes excited in the tunnel junction and the propagating waveguided SPPs due to the dramatic mismatch between their propagation constants. An additional problem might be caused by the low modal overlap. This shows that more attention is required in the future to improve the coupling efficiency, e.g., via structural design of the coupling area.

It is worth mentioning that in addition to plasmon excitation based on metallic tunnel junctions plasmon and light emission can also be generated with metal-insulator-semiconductor (MIS) tunnel junctions [60]. The advantage of the MIS tunnel junctions is that they can be directly integrated into, e.g., a silicon photonic waveguides for on-chip applications [61, 62]. Particularly, with the coupling efficiency of the hybrid junction optical mode to the silicon waveguide of ∼ 75%, Doderer et al. experimentally generated a waveguided optical power of 6.8 pW [61].

DIRECTIVITY CONTROL OF THE PLASMONIC EXCITATION AND LIGHT EMISSION

The ability to control the flow of optical energy is of great importance in nanophotonic applications. The directional control of SPPs and light emission excited by IET has been demonstrated in a variety of systems [54, 55, 63–65]. For

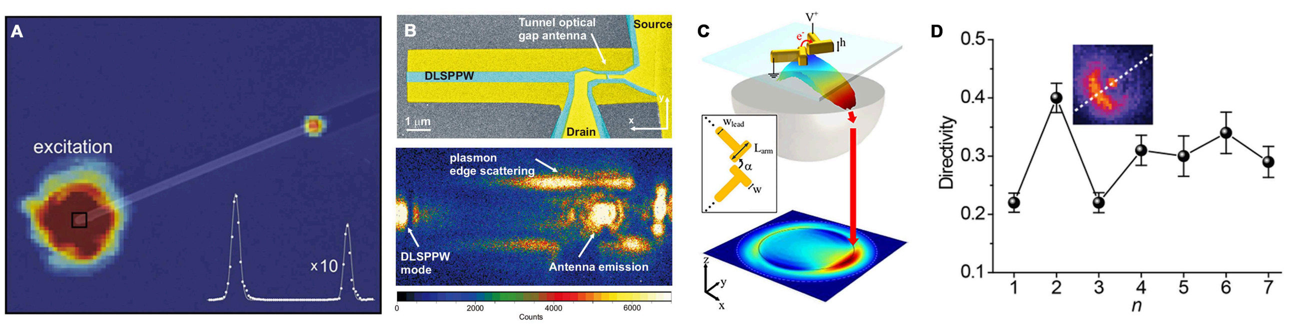

FIGURE 2 | (A) A map of optical emission intensity from an Au nanowire excited by an STM tip. **(B)** False color SEM image of a tunnel junction on the top of a DLSPPW waveguide, together with an optical intensity map, showing generation of the propagating plasmonic mode at the junction region and its outcoupling to the free-space radiation at the other end of the waveguide. **(C)** Tunneling-driven highly directional emission from a V-shaped nanoantenna. **(D)** The dependence of the directivity of the SPP excitation on the structural characteristics of self-assembled S(CH2)nBPh polymer molecules filling the tunneling gap defined by the chain parameter n. The inset shows an experimental measure defocused patterns corresponding to a tunnel junction with $n = 2$. **(A)** is reprinted with permission from Ref. [52]. © 2011 American Physical Society. **(B)** is reprinted with permission from Ref. [53]. Copyright © 2016 Optical Society of America. **(C)** is reprinted with permission from Ref. [54]. Copyright © 2017 American Chemical Society. **(D)** is reprinted with permission from Ref. [55]. Copyright © 2019 American Chemical Society.

example, Dong et al. demonstrated a directional control of SPP-assisted light emission from a gold stripe cavity with a directivity of extinction ratio around 2.6 : 1, which was realized by varying the distance between an STM probe and the edge of the cavity to attain a constructive or destructive interference with the generated and reflected SPP waves [63]. Taking advantage from an excellent directivity provided by optical antennas, Gurunarayanan et al. achieved a directivity of light emission of $\sim$ 5 dB by aligning two nanorod antennas edge-to-edge at an angle of 90° (**Figure 2C**) [54]. Such a strong directivity is provided by an interplay between the dipolar radiation pattern of the tunnel junction emission and the quadrupole-like resonance of the rod antennas. Recently, Kullock et al. obtained a directivity of light emission as high as 9.1 dB in an optical Yagi-Uda antenna with a tunneling feed [64]. The directivity control can also be achieved by placing molecules in the junction region, particularly utilizing their chemical composition and/or orientation [55, 65]. For example, implementing tunneling through a self-assembled monolayer of polymer molecules (**Figure 2D**, inset), Du et al. experimentally achieved directional launching of SPPs by adjusting the tilt angle of a self-assembled monolayer of $S(CH_2)_nBPh$ (BPh = biphenyl) molecules in respect to the electrode surface, which was realized by controlling the length of the alkyl chain n [55]. The highest directivity (defined as $\frac{I_L - I_R}{I_L + I_R}$, where I_L and I_R are the maximum intensities of left and right lobes of the emission pattern, respectively) of 0.4 was obtained for n = 2 (**Figure 2D**, main graph), corresponding to a left/right intensity ratio of $\sim$2.3.

CONCLUSION AND OUTLOOK

In this review, we have overviewed the recent developments in the IET-assisted excitation of surface plasmons, including both LSPRs and SPPs, which open an opportunity for the miniaturization and chip-scale integration of plasmonic devices. However, for practical applications, there are still many things to be done and questions to be answered. For example, how to improve the overall output power from single tunnel junctions? How to optimize the coupling efficiency between an MIM mode excited by IET and SPPs in an extended waveguide for on-chip integration? How to achieve narrow-band excitation of surface plasmons? Finally, the question of long-term stability of tunnel junctions is a key concern for applications. Despite these challenges, as an ultra-fast and compact approach that can bridge electronics and plasmonics directly at the nanoscale, IET-based plasmonic excitation will continue to attract research interest and find applications in areas, such as optical interconnections and sensing.

AUTHOR CONTRIBUTIONS

PW and LL organized and wrote the article. All the authors participated in discussion and revision.

FUNDING

This work was supported by the Fundamental Research Funds for the Central Universities.

REFERENCES

1. Zayats AV, Smolyaninov II, Maradudin AA. Nano-optics of surface plasmon polaritons. *Phys Rep.* (2005) **408**:131–314. doi: 10.1016/j.physrep.2004.11.001
2. Schuller JA, Barnard ES, Cai W, Jun YC, White JS, Brongersma ML. Plasmonics for extreme light concentration and manipulation. *Nat Mater.* (2010) **9**:193–204. doi: 10.1038/nmat2630
3. Brongersma ML, Shalaev VM. The case for plasmonics. *Science.* (2010) **328**:440–1. doi: 10.1126/science.1186905
4. Lal S, Link S, Halas NJ. Nano-optics from sensing to waveguiding. *Nat Photonics.* (2007) **1**:641–8. doi: 10.1038/nphoton.2007.223
5. Guo X, Ying Y, Tong L. Photonic nanowires: from subwavelength waveguides to optical sensors. *Acc Chem Res.* (2014) **47**:656–66. doi: 10.1021/ar400232h
6. Krasavin AV, Zayats AV. Guiding light at the nanoscale: numerical optimization of ultrasubwavelength metallic wire plasmonic waveguides. *Opt Lett.* (2011) **36**:3127–9. doi: 10.1364/OL.36.003127
7. Hill MT, Gather MC. Advances in small lasers. *Nat Photonics.* (2014) **8**:908–18. doi: 10.1038/nphoton.2014.239
8. Ma R, Oulton RF. Applications of nanolasers. *Nat Nanotechnol.* (2019) **14**:12–22. doi: 10.1038/s41565-018-0320-y
9. Wu H, Gao Y, Xu P, Guo X, Wang P, Dai D, et al. Plasmonic nanolasers: pursuing extreme lasing conditions on nanoscale. *Adv Opt Mater.* (2019) **7**:1900334. doi: 10.1002/adom.201900334
10. Krasavin AV, Zayats AV. Photonic signal processing on electronic scales: electro-optical field-effect nanoplasmonic modulator. *Phys Rev Lett.* (2012) **109**:053901. doi: 10.1103/PhysRevLett.109.053901
11. Melikyan A, Alloatti L, Muslija A, Hillerkuss D, Schindler PC, Li J, et al. High-speed plasmonic phase modulators. *Nat Photonics.* (2014) **8**:229–33. doi: 10.1038/nphoton.2014.9
12. Ayata M, Fedoryshyn Y, Heni W, Baeuerle B, Josten A, Zahner M, et al. High-speed plasmonic modulator in a single metal layer. *Science.* (2017) **358**:630–2. doi: 10.1126/science.aan5953
13. MacDonald KF, Samson ZL, Stockman MI, Zheludev NI. Ultrafast active plasmonics. *Nat Photonics.* (2009) **3**:55–8. doi: 10.1038/nphoton.2008.249
14. Wurtz GA, Pollard R, Hendren W, Wiederrecht GP, Gosztola DJ, Podolskiy VA, et al. Designed ultrafast optical nonlinearity in a plasmonic nanorod metamaterial enhanced by nonlocality. *Nat Nanotechnol.* (2011) **6**:107–11. doi: 10.1038/nnano.2010.278
15. Falk AL, Koppens FHL, Yu CL, Kang K, Snapp NdL, Akimov AV, et al. Near-field electrical detection of optical plasmons and single-plasmon sources. *Nat Phys.* (2009) **5**:475–9. doi: 10.1038/nphys1284
16. Knight MW, Sobhani H, Nordlander P, Halas NJ. Photodetection with active optical antennas. *Science.* (2011) **332**:702–4. doi: 10.1126/science.1203056
17. Nie S, Emory SR. Probing single molecules and single nanoparticles by surface-enhanced Raman scattering. *Science.* (1997) **275**:1102–6. doi: 10.1126/science.275.5303.1102
18. Liu N, Tang ML, Hentschel M, Giessen H, Alivisatos AP. Nanoantenna-enhanced gas sensing in a single tailored nanofocus. *Nat Mater.* (2011) **10**:631–6. doi: 10.1038/nmat3029
19. Kauranen M, Zayats AV. Nonlinear plasmonics. *Nat Photonics.* (2012) 6:737–48. doi: 10.1038/nphoton.2012.244
20. Krasavin AV, Ginzburg P, Zayats AV. Free-electron optical nonlinearities in plasmonic nanostructures: a review of the hydrodynamic description.

Laser Photon Rev. (2018) **12**:1700082. doi: 10.1002/lpor.201700082
21. Ritchie RH. Plasma losses by fast electrons in thin films. *Phys Rev.* (1957) **106**:874–81. doi: 10.1103/PhysRev.106.874
22. Bashevoy MV, Jonsson F, Krasavin AV, Zheludev NI, Chen Y, Stockman MI. Generation of traveling surface plasmon waves by free-electron impact. *Nano Lett.* (2006) **6**:1113–5. doi: 10.1021/nl060941v
23. Vesseur EJR, de Waele R, Kuttge M, Polman A. Direct observation of plasmonic modes in Au nanowires using high-resolution cathodoluminescence spectroscopy. *Nano Lett.* (2007) **7**:2843–6. doi: 10.1021/nl071480w
24. Nelayah J, Kociak M, Stéphan O, García de Abajo FJ, Tencé M, Henrard L, et al. Mapping surface plasmons on a single metallic nanoparticle. *Nat Phys.* (2007) **3**:348–53. doi: 10.1038/nphys575
25. Huang KCY, Seo M-K, Sarmiento T, Huo Y, Harris JS, Brongersma ML. Electrically driven subwavelength optical nanocircuits. *Nat Photonics.* (2014) **8**:244–9. doi: 10.1038/nphoton.2014.2
26. Koller D, Hohenau A, Ditlbacher H, Galler N, Reil F, Aussenegg F, et al. Organic plasmon-emitting diode. *Nat Photonics.* (2008) **2**:684–7. doi: 10.1038/nphoton.2008.200
27. Lambe J, McCarthy SL. Light emission from inelastic electron tunneling. *Phys Rev Lett.* (1976) **37**:923–5. doi: 10.1103/PhysRevLett.37.923
28. Kern J, Kullock R, Prangsma J, Emmerling M, Kamp M, Hecht B. Electrically driven optical antennas. *Nat Photonics.* (2015) **9**:582–6. doi: 10.1038/nphoton.2015.141
29. Wang P, Krasavin AV, Nasir ME, Dickson W, Zayats AV. Reactive tunnel junctions in electrically driven plasmonic nanorod metamaterials. *Nat Nanotechnol.* (2018) **13**:159–64. doi: 10.1038/s41565-017-0017-7
30. Persson BNJ, Baratoff A. Theory of photon emission in electron tunneling to metallic particles. *Phys Rev Lett.* (1992) **68**:3224–7. doi: 10.1103/PhysRevLett.68.3224
31. Johansson P. Light emission from a scanning tunneling microscope: fully retarded calculation. *Phys Rev B.* (1998) **58**:10823–34. doi: 10.1103/PhysRevB.58.10823
32. Rendell RW, Scalapino DJ. Surface plasmons confined by microstructures on tunnel junctions. *Phys Rev B.* (1981) **24**:3276–94. doi: 10.1103/PhysRevB.24.3276
33. Coombs J, Gimzewski J, Reihl B, Sass J, Schlittler R. Photon emission experiments with the scanning tunnelling microscope. *J Microsc.* (1988) **152**:325–36. doi: 10.1111/j.1365-2818.1988.tb01393.x
34. Gimzewski JK, Reihl B, Coombs JH, Schlittler RR. Photon-emission with the scanning tunnelling microscope. *Eur Phys J B.* (1988) **72**:497–501. doi: 10.1007/bf01314531
35. Johansson P, Monreal R, Apell P. Theory for light emission from a scanning tunneling microscope. *Phys Rev B Condens Matter.* (1990) **42**:9210–3. doi: 10.1103/physrevb.42.9210
36. Wang T, Boer-Duchemin E, Zhang Y, Comtet G, Dujardin G. Excitation of propagating surface plasmons with a scanning tunnelling microscope. *Nanotechnology.* (2011) **22**:175201. doi: 10.1088/0957-4484/22/17/175201
37. Silly F, Gusev AO, Taleb A, Charra F, Pileni MP. Coupled plasmon modes in an ordered hexagonal monolayer of metal nanoparticles: a direct observation. *Phys Rev Lett.* (2000) **84**:5840–3. doi: 10.1103/PhysRevLett.84.5840
38. Le Moal E, Marguet S, Rogez B, Mukherjee S, Dos Santos P, Boer-Duchemin E, et al. An electrically excited nanoscale light source with active angular control of the emitted light. *Nano Lett.* (2013) **13**:4198–205. doi: 10.1021/nl401874m
39. Le Moal E, Marguet S, Canneson D, Rogez B, Boer-Duchemin E, Dujardin G, et al. Engineering the emission of light from a scanning tunneling microscope using the plasmonic modes of a nanoparticle. *Phys Rev B.* (2016) **93**:035418. doi: 10.1103/PhysRevB.93.035418
40. Kuhnke K, Grosse C, Merino P, Kern K. Atomic-scale imaging and spectroscopy of electroluminescence at molecular interfaces. *Chem Rev.* (2017) **117**:5174–222. doi: 10.1021/acs.chemrev.6b00645
41. Fevrier P, Gabelli J. Tunneling time probed by quantum shot noise. *Nat Commun.* (2018) **9**:4940. doi: 10.1038/s41467-018-07369-6
42. Davis LC. Theory of surface-plasmon excitation in metal-insulator-metal tunnel junctions. *Phys Rev B.* (1977) **16**:2482–90. doi: 10.1103/PhysRevB.16.2482
43. Chen C, Bobisch CA, Ho W. Visualization of fermi's golden rule through imaging of light emission from atomic silver chains. *Science.* (2009) **325**:981–5. doi: 10.1126/science.1174592
44. Uskov AV, Khurgin JB, Protsenko IE, Smetanin IV, Bouhelier A. Excitation of plasmonic nanoantennas by nonresonant and resonant electron tunnelling. *Nanoscale.* (2016) **8**:14573–9. doi: 10.1039/c6nr01931e
45. Bigourdan F, Hugonin JP, Marquier F, Sauvan C, Greffet JJ. Nanoantenna for electrical generation of surface plasmon polaritons. *Phys Rev Lett.* (2016) **116**:106803. doi: 10.1103/PhysRevLett.116.106803
46. Parzefall M, Bharadwaj P, Jain A, Taniguchi T, Watanabe K, Novotny L. Antenna-coupled photon emission from hexagonal boron nitride tunnel junctions. *Nat Nanotechnol.* (2015) **10**:1058–63. doi: 10.1038/nnano.2015.203
47. Qian H, Hsu S, Gurunatha K, Riley CT, Zhao J, Lu D, et al. Efficient light generation from enhanced inelastic electron tunnelling. *Nat Photonics.* (2018) **12**:485–8. doi: 10.1038/s41566-018-0216-2
48. Parzefall M, Szabo A, Taniguchi T, Watanabe K, Luisier M, Novotny L. Light from van der waals quantum tunneling devices. *Nat Commun.* (2019) **10**:292. doi: 10.1038/s41467-018-08266-8
49. He X, Tang J, Hu H, Shi J, Guan Z, Zhang S, et al. Electrically driven highly tunable cavity plasmons. *ACS Photonics.* (2019) **6**:823–9. doi: 10.1021/acsphotonics.8b01620
50. He X, Tang J, Hu H, Shi J, Guan Z, Zhang S, et al. Electrically driven optical antennas based on template dielectrophoretic trapping. *ACS Nano.* (2019) **13**:14041–7. doi: 10.1021/acsnano.9b06376
51. Krasavin AV, Wang P, Nasir ME, Jiang Y, Zayats AV. Tunneling-induced broadband and tunable optical emission from plasmonic nanorod metamaterials. *Nanophotonics.* (2020) **9**:427–34. doi: 10.1515/nanoph-2019-0411
52. Bharadwaj P, Bouhelier A, Novotny L. Electrical excitation of surface plasmons. *Phys Rev Lett.* (2011) **106**:226802. doi: 10.1103/PhysRevLett.106.226802
53. Cazier N, Buret M, Uskov AV, Markey L, Arocas J, Des Francs GC, et al. Electrical excitation of waveguided surface plasmons by a light-emitting tunneling optical gap antenna. *Opt Express.* (2016) **24**:3873–84. doi: 10.1364/oe.24.003873
54. Gurunarayanan SP, Verellen N, Zharinov VS, Shirley FJ, Moshchalkov VV, Heyns M, et al. Electrically driven unidirectional optical nanoantennas. *Nano Lett.* (2017) **17**:7433–9. doi: 10.1021/acs.nanolett.7b03312
55. Du W, Han Y, Hu H, Chu H, Annadata HV, Wang T, et al. Directional excitation of surface plasmon polaritons via molecular through-bond tunneling across double-barrier tunnel junctions. *Nano Lett.* (2019) **19**:4634–40. doi: 10.1021/acs.nanolett.9b01665
56. Du W, Wang T, Chu H, Nijhuis CA. Highly efficient on-chip direct electronic-plasmonic transducers. *Nat Photonics.* (2017) **11**:623–7. doi: 10.1038/s41566-017-0003-5
57. Makarenko K, Hoang T, Duffin T, Radulescu A, Kalathingal V, Lezec H, et al. Efficient surface plasmon polariton excitation and control over outcoupling mechanisms in metal-insulator-metal tunneling junctions. *Adv Sci.* (2020) **7**:1900291. doi: 10.1002/advs.201900291
58. Zhang C, Hugonin JP, Coutrot AL, Sauvan C, Marquier F, Greffet JJ. Antenna surface plasmon emission by inelastic tunneling. *Nat Commun.* (2019) **10**:4949. doi: 10.1038/s41467-019-12866-3
59. Parzefall M, Novotny L. Light at the end of the tunnel. *ACS Photonics.* (2018) **5**:4195–202. doi: 10.1021/acsphotonics.8b00726
60. Goktas H, Gokhan FS, Sorger VJ. Electrical-driven plasmon source of silicon based on quantum tunneling. *ACS Photonics.* (2018) **5**:4928–36. doi: 10.1021/acsphotonics.8b01106
61. Doderer M, Parzefall M, Joerg A, Chelladurai D, Dordevic N, Fedoryshyn Y, et al. Light emission from a waveguide integrated MOS tunnel junction. In *2019 Conference on Lasers and Electro-Optics*. Conference on Lasers and Electro-Optics (2019).
62. Huang B, Gao S, Liu Y, Wang J, Liu Z, Guo Y, et al. Nano-antenna enhanced waveguide integrated light source based on an

MIS tunnel junction. *Opt Lett.* (2019) **44**:2330–3. doi: 10.1364/ol.44.002330
63. Dong Z, Chu H, Zhu D, Du W, Akimov YA, Goh WP, et al. Electrically-excited surface plasmon polaritons with directionality control. *ACS Photonics.* (2015) **2**:385–91. doi: 10.1021/ph5004303
64. Kullock R, Ochs M, Grimm P, Emmerling M, Hecht B. Electrically-driven Yagi-Uda antennas for light. *Nat Commun.* (2020) **11**:115. doi: 10.1038/s41467-019-14011-6
65. Du W, Wang T, Chu H, Wu L, Liu R, Sun S, et al. On-chip molecular electronic plasmon sources based on self-assembled monolayer tunnel junctions. *Nat Photonics.* (2016) **10**:274–80. doi: 10.1038/nphoton.2016.43

Conflict of Interest: The authors declare that the research was conducted in the absence of any commercial or financial relationships that could be construed as a potential conflict of interest.

frontiers in Physics

REVIEW
published: 14 August 2020
doi: 10.3389/fphy.2020.00312

One-Dimensional Plasmonic Sensors

Yitian Liu [1,2] *and Yaoguang Ma* [1,2]*

[1] *State Key Laboratory of Modern Optical Instrumentation, Zhejiang University, Hangzhou, China,* [2] *College of Optical Science and Engineering, Zhejiang University, Hangzhou, China*

Recent advances in surface plasmon sensors have significantly reduced the limitations of conventional optical sensors. With the recent development of micro- and nano-fabrication technology, miniaturized one-dimensional structures become a promising platform for surface plasmon sensors for its compactness and simple structure. In this review, we describe the generation of surface plasmon polaritons and the resonance conditions. Then we categorize surface plasmon sensors by the physical quantities they detect, elaborating their working principle, performance, and current development. Finally, we summarize both limitations and advances of various design methods to provide an outlook on future directions of this field.

Keywords: surface plasmon resonance, localized surface plasmon resonance, biochemical sensing, refractive index, waveguide, nanowires

Edited by:
Lin Chen,
University of Shanghai for Science and Technology, China

Reviewed by:
Ilia L. Rasskazov,
University of Rochester, United States
Junichi Fujikata,
Photonics Electronics Technology Research Association, Japan

****Correspondence:***
Yaoguang Ma
mayaoguang@zju.edu.cn

Specialty section:
This article was submitted to Optics and Photonics, a section of the journal Frontiers in Physics

Received: *04 April 2020*
Accepted: *07 July 2020*
Published: *14 August 2020*

Citation:
Liu Y and Ma Y (2020) One-Dimensional Plasmonic Sensors. Front. Phys. 8:312. doi: 10.3389/fphy.2020.00312

INTRODUCTION

Optical sensors are used for a broad range of applications, ranging from simple distance detection to providing artificial vision for object recognition. One of the critical challenges that modern sensor industry faces are to explore novel nanostructures with designer functions. Among the other nanotechnologies, the idea of utilizing surface plasmon polaritons (SPPs) proves itself useful over other competitors. Metallic nanostructures are promising for the generation and distribution of electromagnetic radiation in unprecedented ways. SPPs, also known in the literature as surface plasma waves (SPWs) [1], are coherent oscillations of free electrons at the interface between metal and dielectric [2]. They possess a series of novel optical properties, such as local electric field enhancement, deep subwavelength confinement of optical fields, etc. The highly confined electromagnetic field could break the optical diffraction limit, making SPP-based sensors exhibit high sensitivity and miniaturized size [3]. Also, the high energy density in the near field of SPPs contributes significantly to the sensor sensitivity for special applications, such as single molecular sensing. Compared to conventional techniques, such as fluorescence analysis, SPP-based sensors are more compatible with analyte and does not involve additional processes like labeling. And the application of SPPs has gained tremendous attention in optical sensing areas since its first gas sensing demonstration [4].

In the visible and infrared region, SPPs can be supported by one-dimensional structures. However, the electromagnetic characteristics of metals in the terahertz band are similar to perfect electrical conductors (PEC), and cannot support SPPs for practical applications [5]. Therefore, pleated subwavelength structures with different geometric features can support spoof SPPs in the terahertz band for sensing applications [6, 7]. Compared with these structures, one-dimensional waveguide structure has properties, such as mass production and low cost. Furthermore, one-dimensional structures are important for the integrated plasmonic circuit, which have attracted increasing attentions for flexible and compact applications in optical sensors [8–10]. Additionally, one-dimensional waveguide structure can guide SPPs along metal-dielectric interfaces beyond the diffraction limit and confine light to scales $< \lambda/10$ along relatively long distance [11], thus high sensitivity can be achieved in one-dimensional sensors.

In recent years, boosted by the dramatic progress made in micro- and nano-fabrication technology [12–14] these years, plasmonic sensors have demonstrated their advantages in various areas, such as chemical sensing [15–17], biological species [18, 19], environmental monitoring [20, 21], food safety [22–24], and medical diagnosis [8, 25–27]. Notably, these sensors offer distinguishing characteristics in biochemical analyses [28, 29]. Recently, an SPP-based test paper for rapid detection of COVID-19 has been released in Japan [30]. Antibiotic coated gold nanoparticles that undergo resonance peak shift show a distinct color change when COVID-19 viruses are captured. Similar methods are widely applied in pregnancy test.

In this review, we start with a brief introduction of the concept of SPPs at the interface of metal and dielectric interface, followed by a description of excitation and coupling schemes used for one-dimensional waveguiding structures. Then we give a short discussion on the distinction between localized surface plasmon polariton (LSPP) for small nanoparticles (NPs) and SPP in elongated nanostructures, such as metallic nanowires (NWs). In the third part, some critical applications for 1-D waveguide are presented, and these include a refractive index, pressure, and biochemical sensing. These demonstrations underline the advantages 1-D nanostructures bring to the nanoscience and nanotechnology field. Finally, we summarize the possible future developments of 1-D waveguide sensors, such as metallic nanowires, etc., in various research areas.

PHYSICS OF SURFACE PLASMONS

Optical Excitation of Surface Plasmon Polaritons

To describe these peculiar behaviors of SPPs, we start from the description of the motion of a free electron in metal:

$$m\frac{d^2x}{dt^2} + m\gamma\frac{dx}{dt} = -eE_0\exp(-i\omega t) \tag{1}$$

where x is the displacement of the electron, m is the electron mass, γ is the damping factor, e is the charge of an electron, E_0 is the amplitude of the external electric field, and ω is the angular frequency of the external electric field. By solving Equation (1), we get the Drude model of free electrons in metal as:

$$\varepsilon(\omega) = \varepsilon_r + i\varepsilon_i = 1 - \frac{{\omega_p}^2}{\omega(\omega+i\gamma)} \tag{2}$$

where ω_p stands for the plasma frequency. We assume $\gamma \ll \omega_p$ and then obtain the relation between the dielectric constant of metal and the frequency of the incident light.

SPPs are longitudinal waves propagating along an interface as shown in **Figure 1A**. The confinement is achieved due to the fact that the wave vector of SPPs is much larger than that of light wave in the dielectric. The wave vector of SPPs propagating along the metal surface is given by

$$k_{SPP} = \frac{\omega}{c}\sqrt{\frac{\varepsilon(\omega)\varepsilon_m}{\varepsilon(\omega)+\varepsilon_m}} \tag{3}$$

where ω is the angular frequency, c is the speed of light in vacuum, $\varepsilon(\omega)$, and ε_m are the dielectric constants of the dielectric and metal, respectively.

For a given wavelength, the light line always lies to the left of the SPP dispersion curve as shown in **Figure 1B**. The phase-matching condition therefore forbids a direct coupling between 3-dimensional light and 2-dimensional SPP. Various techniques utilizing prisms, gratings, highly focused beam, and optical nanofibers, etc., have been proposed to address this issue.

SPPs undergoes severe attenuation in the metal film layer, which decreases the intensity of the electromagnetic field. The propagation length of SPPs is defined as:

$$L = \frac{1}{2Im\{k_{spp}\}} \tag{4}$$

L typically ranges from 10 to 100 μm in the visible regime [31]. It limits the maximum size of SPP-based devices to ensure that the attenuation of energy is reasonable. The propagation length and penetration depth are both dependent on frequency. For frequencies close to the surface plasma frequency, SPPs exhibit strong field confinement to the interface and a short propagation distance at the same time, which is a trade-off between energy confinement and loss for SPP-based devices.

The penetration depth is defined to represent the distance from the interface when the amplitude of SPPs decays by a factor of $1/e$. According to the z component of wave vector in the metal layer and that in the dielectric layer solved by Maxwell's equation, the penetration depth is:

$$L_p = \frac{1}{Re\{k_z\}} \tag{5}$$

where $k_z = \sqrt{{k_{spp}}^2 - \varepsilon_i\left(\frac{\omega}{c}\right)^2}$, ε_i refers to ε_m in the metal layer and ε_d in the dielectric layer. In most cases, SPPs penetrate deeper into the dielectric layer than that in the metal layer, as indicated in **Figure 1A**. In SPP-based sensors, the penetration depth in the dielectric layer determines the actual sensing area.

Optical Excitation of Localized Surface Plasmon Polaritons

As is shown in **Figure 1C**, in contrast to SPPs that propagate along continuous metal surfaces, LSPPs are non-propagating excitations tightly confined to the nanostructure. Conduction electrons in the NPs oscillate collectively and locally with a resonant frequency, which depends upon the composition, size, geometry, dielectric environment, and particle-to-particle separation of NPs [32]. The excitation of LSPR gives rise to field enhancement of local electromagnetic fields on the surface of an NP or "hot spots" between NPs, and results in strong scattering and the absorption of the incident light. LSPP shows more significant potential for sensing analytes with small concentrations and provides an approach in surface plasmon-enhanced sensing.

Here we can use the quasi-static approximation (**Figure 1D**) since the radius of an NP is much smaller than the wavelength of

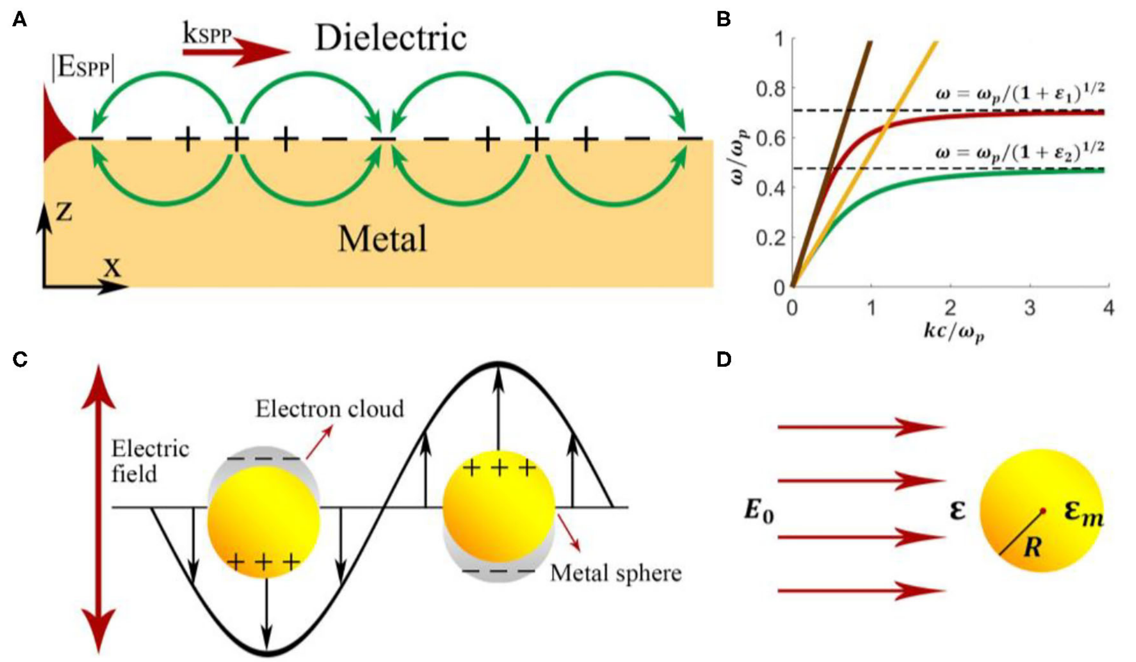

FIGURE 1 | Schematic illustration of **(A)** surface plasmon polaritons and **(B)** excitation of SPPs on the metal-vacuum interface. The two curves are the dispersion relation of SPPs on the metal-vacuum interface (red line) and that on the metal-GaAs interface (green line). The dispersion relations of light incident from vacuum and GaAs are plotted as the yellow line and the brown line, respectively. **(C)** Localized surface plasmon polaritons at the interface between metal nanoparticles and dielectric environment. **(D)** A metal nanoparticle with a radius *R* in the electric field E_0.

the incident light. According to the boundary conditions and the dipole model, the polarizability of the particle can be written as

$$\alpha = 4\pi R^3 \frac{\varepsilon-\varepsilon_m}{\varepsilon+2\varepsilon_m} \tag{6}$$

where ε and ε_m are the dielectric constant of the spherical particle and that of the environment, respectively. Further deduction gives the absorption cross-section and the scattering cross-section of the particle as

$$C_{abs} = kIm\{\alpha\} = 4k\pi R^3 Im\left\{\frac{\varepsilon-\varepsilon_m}{\varepsilon+2\varepsilon_m}\right\} \tag{7}$$

$$C_{scat} = \frac{k^4}{6\pi}|\alpha|^2 = \frac{8}{3}k^4\pi R^6\left|\frac{\varepsilon-\varepsilon_m}{\varepsilon+2\varepsilon_m}\right|^2 \tag{8}$$

As is shown in Equations (7) and (8), the scattering cross-section and the absorption cross-section is proportional to the 6th power and 3rd power of the radius, respectively. That is, light scattering accounts for the main contribution for relatively large particles, and for small particles, the proportion of light absorption is more substantial. The quasi-static model used here treats plasmonic particles as dipoles and neglects the delay effect as well as the damping effect. However, larger particles, especially particles with the diameter comparable to the wavelength, cannot be considered as dipoles. Higher-order modes must be taken into account when dealing with these problems. The sensible polarizability of metallic particles is calculated by the modified long-wavelength approximation model (MLWA) [3], which explains perfectly why the redshift of the LSPR peak position as the size of NPs increase, is a more sensible solution for polarizability of large metallic particles.

PERFORMANCE EVALUATION OF SURFACE PLASMON SENSORS

The principle of SPP sensing is based on the change of the SPP's spectra or intensity upon the change of environment. The first parameter we would take into account when designing a sensor is the sensitivity (*S*). It is determined by the ratio of the change in sensor output to the difference in the measured parameter. In the SPP-based sensors, the quantity measured is generally the refractive index (*n*), and the output quantity (*Y*), which could be the resonant angle, resonant wavelength, intensity of guided waves, and phase shift.

$$S = \frac{dY}{dn} \tag{9}$$

According to Equation (9), the sensitivity of intensity interrogation can be expressed in the unit of RIU^{-1} (*RIU* for Refractive Index Unit). In SPP sensors with wavelength modulation, the sensor output is the coupling wavelength and the sensitivity unit is usually μm/RIU or nm/RIU, which indicates the spectra position shifts vs. the change of analyte's RI. Moreover, the sensitivity of angular or phase modulation sensors is described in terms of rad/RIU or deg/RIU. By detecting the propagation constant differences, researchers can also achieve sensitivity in the form of rad/(μm·RIU).

Usually, sensitivity takes the global RI into account in physical sensing approaches. But the sensitivity of an SPP-based sensor only considers the RI changes in a local region, as electromagnetic field is confined tightly near the interface of metallic nanostructures, for example, the local RI difference caused by biomacromolecules. It's worth noting that, in LSPP-based biochemical sensors, the distribution of the electromagnetic field is not uniform on the surface of NPs. Generally, the electric field is distributed at locations with small curvature radius, tips, and gaps. Thus, it is essential to attach molecules to these local areas when designing the sensor to enhance sensitivity.

Resolution, or detection limit (*DL*), is another important parameter which is adjusted by the smallest variation in the environmental refractive index that can be detected by the sensor [33]. The noise of the output signal (σ) and the sensitivity of the sensor (*S*) determines it together. Therefore, sensors can exhibit high resolution by improving their signal-to-noise ratio or sensitivity.

$$DL = \frac{\sigma}{S} \tag{10}$$

Aside from the above-mentioned parameters, linearity and dynamic ranges are crucial evaluation parameters that describe the stability of SPP-based sensors. The linearity indicates the ratio of the sensor output to the parameter measurement and represents the sensor's stability during the detection process. A high linearity response of the regression line indicates an excellent sensor [34]. The dynamic range describes the span of the values of the measurand that can be measured by the sensor [35]. As for the refractive index sensors, dynamic range refers to the variety refractive index that sensors can measure under specific accuracy.

SURFACE PLASMON SENSORS BASED ON ONE-DIMENSIONAL WAVEGUIDE

Recent waveguide-based surface plasmon sensors can be categorized based on the physical quantities they measure. Moreover, to achieve high sensitivity and compactness simultaneously, one-dimensional waveguide structures, such as an integrated waveguide, optical fibers, and nanowires are mainly discussed.

Refractive Index Sensors

Since the invention of the first SPP-based sensor for gas detection [4], these sensors based on Otto structure and Kretschmann structure have been widely used in the fields of physical, chemical, and biological measurements. The refractive index alters when changes in these measured quantities take place. However, the conventional prism SPP-based sensor has bulky optical and mechanical components and has no advantages in integrated applications.

Optical Fiber-Based RI Sensors

Optical fiber based SPP sensors provide a favorable choice for miniaturized sensing and are incredibly suitable for *in vivo* applications. In 1993, Jorgenson et al. [15] proposed the first optical fiber-based SPP configuration without the bulk light coupling prism. By partially removing the fiber cladding and depositing a high reflective layer at the exposed position, a fiber-based SPP refractive index sensor was proposed utilizing the interaction of evanescent waves with SPPs.

Scientists proposed several approaches [36–38] to enhance the sensitivity of fiber-based SPP sensors. Monzón-Hernández et al. [37] deposited a thin metal layer on a single-mode tapered optical fiber, so the fundamental fiber mode can excite different surface plasmon modes to acquire multiple resonance peaks. The fiber-based sensor achieves a RI resolution of 7×10^{-7} RIU when monitoring the three most profound peaks. Gupta et al. [38] proposed a fiber-based SPP probe consists of a fiber core, silver layer, silicon layer, and sensing medium. This SPP sensor has shown a sensitivity increasing from 2.8452 to 5.1994 μm/RIU when employing a 10-nm-thick silicon layer. Additionally, this silicon layer can prevent the plasmonic layer from oxidation and help tune the resonance. Although optical fiber-based SPP sensors possess the advantages of miniaturization and high sensitivity, their sensing range is usually limited. And the necessary for a spectrometer with an expensive and bulk size makes it challenging to realize the low cost and compact of the overall system.

Integrated Waveguide-Based RI Sensors

Integrated waveguide SPP sensors are particularly promising in the development of miniaturized multi-channel on-chip sensing devices. Suzuki et al. [39] proposed a sensing system with dual LEDs and monitored the differential signal by photodiodes. This system is low-priced and compact since dual LEDs and photodiodes can replace laser and spectrometer, respectively.

The silicon-on-insulator (SOI) rib waveguide with a large cross-section has the characteristics of low transmission loss and integratable with optical fiber communication systems [40]. Yuan et al. proposed an SOI rib waveguide-based sensor by coupling light from single-mode fibers to various units of the SOI rib waveguide array [40]. The analyte refractive index are calculated from the shift of the reflection spectrum. Although the refractive index detection limit is higher (5.3×10^{-5} RIU) comparing with a single SPP sensor (5.04×10^{-7} RIU), it is more cost-effective and compact. Imprinting techniques that help fabricate these sensors with high throughput speed further lows the cost [41]. Using this fabrication method, Matsushita et al. fabricated polymer sensor chips with a refractive index resolution of 3.8×10^{-4} RIU and a noise fluctuation of ~1.2%.

Compared with sensors based on the intensity-detection method, SPP interferometry shows a resolution orders of magnitude higher [42, 43]. Mach-Zenhnder interferometer (MZI) based sensors are useful for restricted refractive index measurements, such as in fluid-based biological detection. Sheridan et al. build a model describing the dependency of MZI transmittance as a function of substrate index. Their model indicates that an increase in the refractive index sensitivity can

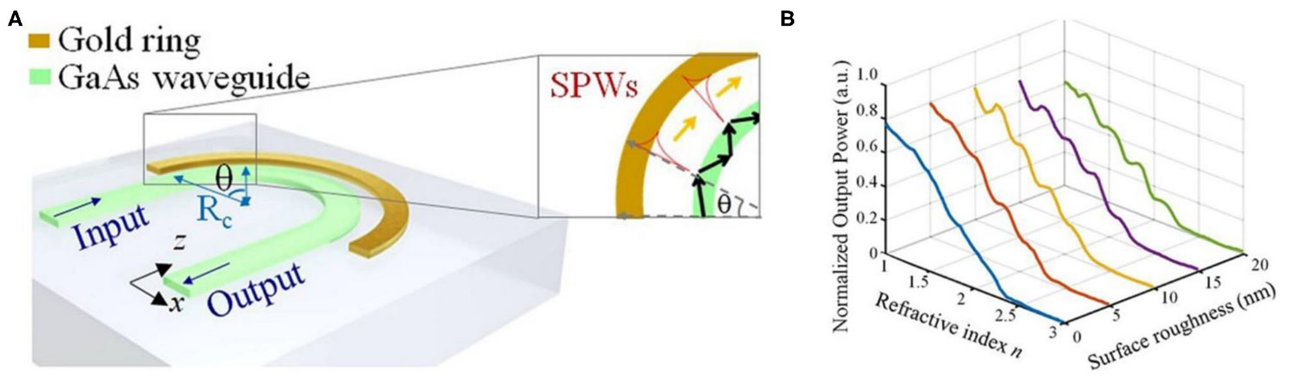

FIGURE 2 | Schematic and performance of a curved-waveguide-based SPP sensor [46]. **(A)** Schematic of a curved-waveguide-based SPP sensor. The configuration contains a curved GaAs waveguide surrounding by an outer gold ring. The inset picture shows multiple SPW excitations along the surface of the gold ring. **(B)** The performance of normalized output power vs. refractive index for different surface roughness σ ranging from 0 to 20 nm. Reprinted with permission from Cheng et al. [46] © Springer Nature.

be achieved compared to conventional waveguide SPP sensors when a phase bias is applied in one branch [44]. Based on MZI structure, Nemova et al. [45] explored a sensor tool with the phase Bragg grating imprinted in one branch, which serves for excitation of SPPs. The reported refractive index resolution is 3×10^{-7} RIU. However, the dynamic range is reduced by approximately two orders of magnitude compared to the intensity measuring sensor. Additionally, interferometry configuration can partially suppress unwanted refractive index changes act on both branches, like temperature or pressure variations. Cheng et al. [46] proposed a novel SPP sensor with an extensive dynamic range, high sensitivity, and compact structure numerically. This sensor includes a GaAs curved waveguide surrounding by an outer gold ring waveguide, as shown in **Figure 2A** [46]. Since the evanescent field changes with the background refractive index, the background refractive index can be obtained by measuring the output power of the waveguide. In **Figure 2B** [46], high linearity is achieved in the dynamic range of $n = 1$–2.36, considering the surface roughness of $\sigma = 5$ nm. The numerical resolution is as high as 4.53×10^{-10} RIU and is the same for both gas and liquid situations.

Biochemical Sensors

SPP biosensors are the primary technology used to study macromolecules and their functions in life science and medical research. Also, SPP biosensors can be implemented in pollutant detection, social health indicators detection, and food toxin detection. SPP biosensors are composed of an SPP sensor and a suitable bio-recognition element. The sensor tracks the refractive index change around the surface when bio-interactions take place, thus providing us the bio-information as designed.

Noble Metal Nanowire Based SPP Biochemical Sensors

Noble metal NW naturally acts as one-dimensional optical waveguide [47]. Despite its miniaturized footprint, NWs can confine light field tightly around the metal interface and to produce confinement beyond the diffraction limit. NWs have become a novel candidate for biochemical sensing in recent years since they are highly sensitive and are observable under an optical microscope [48].

Focusing light with parallel polarization onto the end of a NW could excite SPPs propagating in the NW. Here, **Figure 3A** [49] shows a structure of an NW sensor demonstrated by Wei et al. The structure consists of Ag NWs deposited on a glass substrate, coated with Al_2O_3 layers of different thickness T. The quantum dots (QDs) act as a local field reporter to give the image of near-field distributions near NWs. QD fluorescence captured by camera reveals the plasmon beating period (Λ) increases with the dielectric (Al_2O_3) thickness T dramatically. Λ increases from ∼1.7 µm (top) to 5.8 µm (bottom) with T changes from 30 to 80 nm. The NW plasmonic sensor detects the last mode position change of ∼360 nm per nanometer of Al_2O_3 coating, and the sensitivity can be further improved by enlarging for longer wires and more period.

Another approach uses the transmission spectra collected from the NW sensor. Gu et al. from Zhejiang University demonstrate a single-nanowire plasmonic sensor for hydrogen and humidity sensing [20]. During the sensing process, light is coupled from a silica fiber taper to the NWs and is collected by another fiber taper. For hydrogen sensing, using Pd-coated Au NW with an 80 nm diameter and a 25 µm length, an intensity change of ∼13 dB is achieved as the hydrogen concentration varied from 0 to 1.2%. For humidity sensing, polyacrylamide film-supported Ag NW is employed to achieve response time of 5 ms when relative humidity jumps from 82 to 70%, for its small interaction area and short length.

An NW-assembled MZI has been proposed by Wang et al. [50]. Two Au NWs and two fiber tapers forms the MZI by delicate micro manipulation. One NW is immersed in the measured liquid while the other is used as a reference. Based on the MZI structure, the molar concentration of benzene can be measured by detecting the propagation constant differences, achieving a sensitivity of 5.5π/(µm·RIU) with 660-nm-wavelength probing

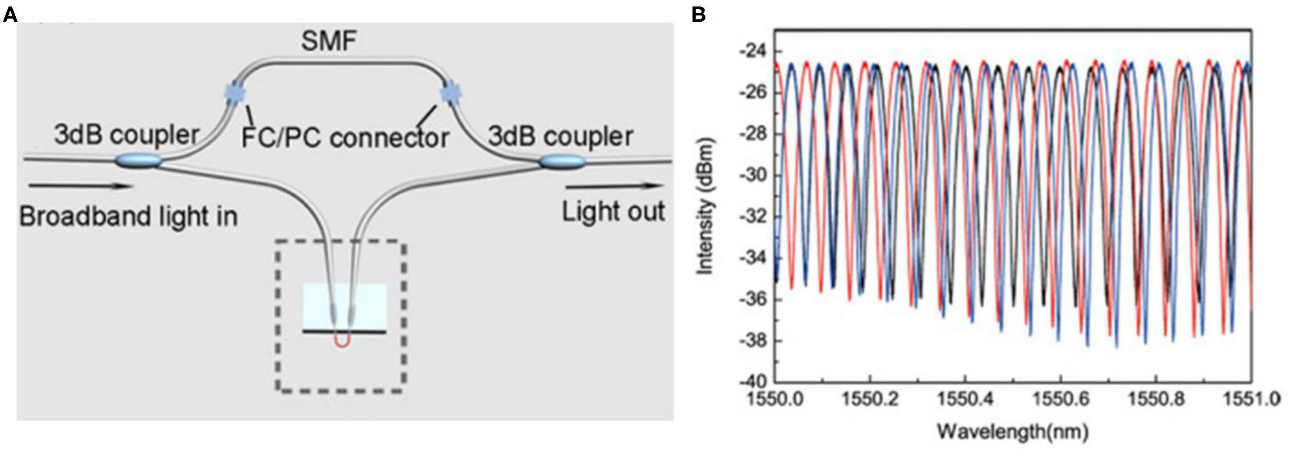

FIGURE 3 | Schematic and performance of an NW-assembled MZI sensor [17]. **(A)** All-fiber hybrid photonic-plasmonic MZI. **(B)** Spectral shifts of the interference peak when the probe is exposed to NH3 of 80 ppm (blue) and 160 ppm (red), respectively. Reprinted with permission from Li et al. [17] © The Optical Society.

light propagating in a 100-nm-diameter Au NW. The MZI sensor proposed by Li et al. is schematically illustrated in **Figure 3A** [17]. Two commercial Y-couplers are connected and an NW-assembled fiber-based plasmonic probe is inserted in one arm. **Figure 3B** [17] shows the spectral shift of the interference fringes when the probe is exposed to ammonia gas (NH_3) of 80 and 160 ppm. This sensor shows a detection limit lower than 80 ppm for NH_3 and a response time of 400 ms (rising time) and 300 ms (falling time).

Nanoparticle-Nanowire Hybrid Nanostructures Based Biochemical Sensors

SiO_x NW-Au NP composites have shown interesting plasmonic properties. Wang et al. [51] utilized a single gold-peapodded silica NWs structure and proposed a photo-enhanced oxygen sensing method. Compared to the bare SiO_2 NWs, Au-NP@SiO_2 NWs exhibit a significantly stronger LSPP-enhanced E field around the Au NPs surface for both TE and TM mode. The induced absorption originated from LSPR in NPs provides improved response and 750 s faster recovery time compared to bare SiO_2 NWs. A systematic and quantitative analysis of Au-NP@SiO_x NWs structure is presented by Gentile et al. [52].

Metal oxide semiconductors (MOSs), such as SnO_2 [53, 54] and iron oxides [55], are regarded as promising building blocks in biochemical sensing because of their sensitivity in gas sensing. Their success comes from the high surface to volume ratio and sensitive band structure dynamics in both oxidizing and reducing gasses. Embedded with NPs, the gas response performance of MOS-based gas sensors is improved. The hybrid NWs with a wrinkled γ-Fe_2O_3 outer shell and embedded Au NPs [56] exhibit excellent performance in ethanol sensing with high sensitivity and selectivity. Another NPs-decorated MOSs-based sensor [25] is presented for bio-sensing by Kim et al. from Dankook University. The sensor is fabricated by growing the ZnO NWs using hydrothermal synthesis and via the immobilization of Au NPs on the NWs. This hybrid structure sensor is especially useful for sensing prostate-specific antigen (PSA), which is a biomarker for prostate cancer detection and has a low reference level. With a sensitivity of 2.06 pg/ml in PSA detection, the hybrid sensor composed of ZnO NWs and Au NPs is expected to have broad applications in real-time label-free biosensors with high sensitivity.

Integrated Waveguide-Based Biochemical Sensors

In 2001, Dostálek et al. proposed an SPP sensor based on integrated optical waveguide structure, which consists of a channel waveguide covered with layer supporting SPPs [8]. By acquiring the normalized transmitted spectrum of two different sensing medium, variation of resonant wavelength is determined to quantify the RI of the sensing medium. This sensor shows a sensitivity of 2,100 nm/RIU. The integrated waveguide was fabricated by an ion-exchange method on a BK7 glass substrate, and the biosensor was applied in the detection of human choriogonadotropin (hCG). Another SPP sensor based on a miniaturized germanium-doped silicon dioxide waveguide has been demonstrated to show a slightly higher sensitivity (2,500 nm/RIU) [57]. This biosensor was fabricated by using a plasma-enhanced chemical vapor deposition (PECVD) method, which allows to control the RI difference between core and clad precisely. The waveguide-based biosensor works to monitor the interactions of protein A, monoclonal antibody, and avian leucosis virus. **Figure 4** [58] shows a novel planar waveguide SPP sensor based on the Otto configuration. The analyte is placed between the core and gold layer, and this configuration does not require any buffer layer, which makes the design of sensor simple. The inset figure [58] illustrates the shift in resonant wavelength for a small change in RI of analyte. The sensitivity of this sensor can then be computed and the value is 4,300 nm/RIU. Researchers have proposed several biosensors for similar structures [8, 59, 60], which requires light wave to be TM polarized since TE polarized mode cannot excite surface plasma wave. A polarization wavelength interrogation biosensor proposed by Chen et al. [27] can make both TE polarized mode, and TM polarized mode produces surface plasmonic resonance.

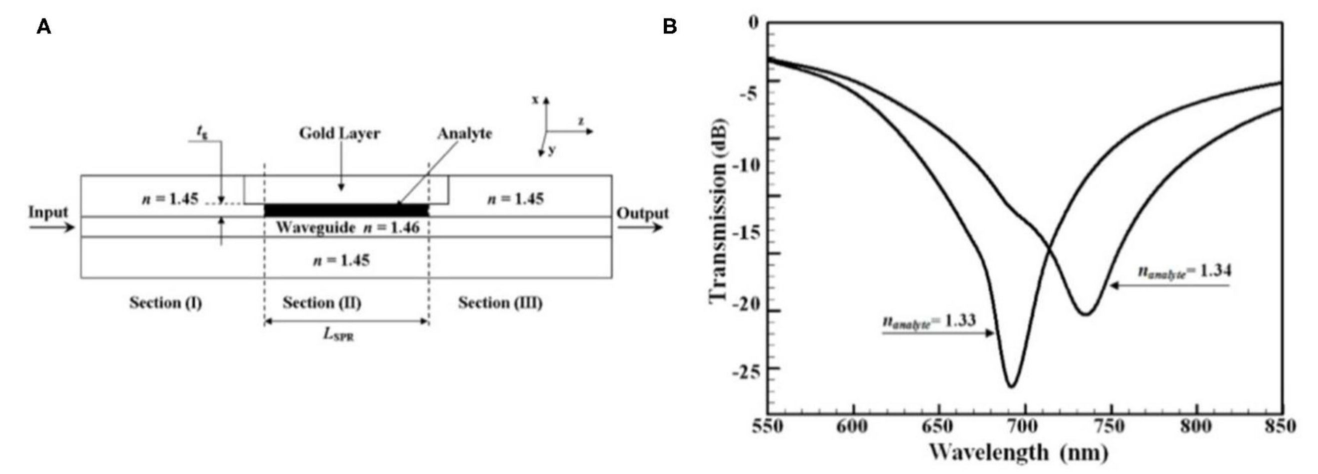

FIGURE 4 | Schematic and performance of the proposed waveguide SPP sensor [58]. **(A)** The cross section of the waveguide SPP sensor with input section (I), SPR section (II), and output section (III). **(B)** Shift in resonant wavelength with respect to $n_{analyte}$ in the proposed waveguide SPP biosensor with a 175 μm length of SPR section and a 175 nm thick analyte layer. Reprinted with permission from Akowuah et al. [58] © The Optical Society.

This biosensor was experimentally demonstrated to sense the medicine for heart disease (beta-blocker), with the sensitivity of 0.027 and 0.08 nm/ppm for TE polarized mode and TM polarized mode, respectively. The double slot hybrid plasmonic waveguide (DSHP) is an integrated waveguide made on a SiO_2 substrate by depositing Ag layer and etching part of it to create nanoscale slots. The plasmonic resonance shifts with the refractive index change of the liquid detected for estimating the presence of substances like diethyl ether ($(C_2H_5)_2O$) [16]. Also, this sensor can be used to detect the percentage of biomedical substances, such as hemoglobin in the blood of homosapiens [18]. A maximum sensitivity of 910 nm/RIU is reported.

Force and Pressure Sensors

Molecular force and pressure waves are used in various areas, including medical diagnosis, tumor ablation and geophysical exploration. To detect these physical quantities, nanostructure-based sensors are proposed. Ma et al. [61] demonstrated a nanofiber-based sensor to detect sound, which is an oscillating pressure wave. The sensor is composed of the SnO_2 nanofiber with compressible polymer cladding deposited on the surface and gold NPs decorating the fiber. Acoustic signatures, i.e., the pressure waves, can be detected by the output intensity of the transmitted light or by the scattering intensity of the individual NPs. This sensor exhibits a sensitivity $<10^{-8}$ W/m^2 under an audible frequency of 31 Hz and provides a novel method for acoustic signature analysis in miniaturized systems, such as cells or molecular machines. Based on the similar working principle, a SnO_2 nanofiber based force transducer [62] is developed with a distance sensitivity of angstrom-level and a force sensitivity of 160 fN. Researchers further used the transducer to detect sub-piconewton forces from the swimming action of bacteria with a sensitivity of −30 dB. Since the sensor has the ability to detect forces from multiple nanoparticles on a single fiber and the geometry can be inserted into small analytes, the nanofiber-based pressure sensor has great potential in biomechanical and intracellular studies.

Taking advantages of the orientational dependence of LSPR of Au nanorods (NRs), Fu et al. [63] developed a novel pressure sensor, which is a pressure-responsive polymer matrix with Au NRs embedded. Under an applied pressure, the deformation of the surrounding polymer takes place and Au NRs change their orientation, subsequently the intensity ratio of TE mode and TM mode of LSPR changes. The unique NR-based pressure sensor can be utilized for recording local distribution and magnitude of pressure and is particularly suitable for sensing in small areas with complex surface geometries.

CONCLUSION

In summary, we reviewed low-dimensional SPP sensors in this paper. **Table 1** presents the characteristics of some well-known low-dimensional plasmonic sensors. Being a label-free technique with small footprint and high sensitivity, micro- and nano-waveguide-based plasmonic sensing have been demonstrated in numerous areas, such as refractive index sensing, pressure sensing and biochemical sensing, especially. For biochemical sensing, plasmonic NW-based sensors and NPs-NWs hybrid structure based sensors are promising since their ultra-compact structure and high sensitivity for environmental changes. When it comes to the detection limit, medical diagnosis is one of the most demanding fields that require this feature, as SPP sensors with low detection limit can be applied in early detection of biomarkers. These nanosensors may probably find their applications in molecular machines and even cells systems. Another performance parameter, the dynamic range, is crucial for industrial applications, such as environmental monitoring.

Despite the high sensitivity compared to other sensing methods it acquires, the signal-to-noise ratio still needs some

TABLE 1 | Performance of low-dimensional plasmonic sensors.

Sensor configuration	Functional materials	Measured quantity	Performance	References
Fiber optic sensor	MMF coated with Ag	RI	Sensitivity of 4.5×10^{-4}~7.5×10^{-5} RIU^{-1}	[15]
Fiber optic sensor	Ag + Si coated on fiber	RI	Sensitivity of 5.1994 μm/RIU	[38]
Waveguide based sensor	SOI rib waveguide	RI	Sensitivity of 3.968×10^4 nm/RIU	[40]
Mach-Zehnder based sensor	Waveguide coated with Au	RI	Sensitivity of 8×10^{-7} RIU/deg	[45]
Curved waveguide based sensor	GaAs waveguide surrounding by a gold ring	RI	RI resolution of 4.53×10^{-10} and dynamic range from $n = 1$ to $n = 2.36$	[46]
NW based sensor	Ag NW	NH_3	Detection limit lower than 80 ppm for NH_3	[17]
NW based sensor	Au NW	Benzene	Sensitivity of 5.5π/(μm·RIU) for 50-nm-diameter NW	[50]
NW based sensor	Pd-coated Au NW	Hydrogen	Sensitivity of ~13 dB to 1.2% hydrogen	[20]
NP-NW hybrid sensor	Au-NPs@SiO_x NWs	O_2	The pressure of O_2 changes in the range 0~500 Torr	[51]
NP-NW hybrid sensor	Au-NPs@γ-Fe_2O_3 NWs	Ethanol	Sensitivity of 35.1 for 50 ppm ethanol	[56]
Waveguide based sensor	Au + Cr + Ta_2O_5 coated waveguide	hCG	Detection limit of 2 ng/ml for hCG	[8]
Waveguide based sensor	Au coated waveguide	Aqueous analyte	Sensitivity of 4,300 nm/RIU	[58]
DSHP waveguide based sensor	Etched Ag coated waveguide	Hemoglobin	Sensitivity of 910 nm/RIU	[18]
DSHP waveguide based sensor	Etched Ag + Si coated waveguide	$(C_2H_5)_2O$	27.67π (nm/RIU) at the wavelength of 1,550 nm	[16]
NF based sensor	SnO_2 nanofiber	Force	Force sensitivity of 160 fN	[62]
NR based sensor	Au NRs	Pressure	Record the distribution and magnitude of pressure between two contacting surfaces	[63]

improvement due to the disturbance from the environment. Notably, the simplicity, specificity, and reliability of NW-based biochemical sensors should all be taken into account when considering the practical sensing devices. The main challenge that SPP sensors face is the high-cost platforms, which is not affordable for small research groups or communities to invest. So, the challenges of designing a portable SPP-based sensor with high sensitivity, low detection limit, broad dynamic range, low cost, and high throughput fabrication still stands out for researchers to address.

Taking an outlook of the future trend in SPP sensing, portable sensors that are user-friendly, smart, and convenient for data transmittance could be developed. Even artificial intelligence can be involved to make the signal acquisition and analysis process simpler. For biochemical sensing, the disposability of the sample container should be considered properly in fluid chip technology. Moreover, slower flow-rate and smaller sample volume in real-time detection will contribute to the promising future of biochemical sensing.

AUTHOR CONTRIBUTIONS

YL and YM organized and wrote the article. YM supervised the team. All authors discussed and participated in revising the manuscript.

FUNDING

This work was partly supported by the National Natural Science Foundation of China (61905213).

REFERENCES

1. Wijaya E, Lenaerts C, Maricot S, Hastanin J, Habraken S, Vilcot J-P, et al. Surface plasmon resonance-based biosensors: From the development of different SPR structures to novel surface functionalization strategies. *Curr Opin Solid State Mater Sci.* (2011) **15**:208–24. doi: 10.1016/j.cossms.2011.05.001
2. Chen Y, Ming H. Review of surface plasmon resonance and localized surface plasmon resonance sensor. *Photonic Sens.* (2012) **2**:37–49. doi: 10.1007/s13320-011-0051-2
3. Tong L, Xu H. Surface plasmons—mechanisms, applications and perspectives. *Physics.* (2012) **41**:582–8.
4. Nylander C, Liedberg B, Lind T. Gas detection by means of surface plasmon resonance. *Sens Actuators.* (1982) **3**:79–88. doi: 10.1016/0250-6874(82)80008-5
5. Geng Y, Wang Z, Ma Y, Gao F. Topological surface plasmon polaritons. *Acta Phys Sin.* (2019) **68**:224101. doi: 10.7498/aps.68.20191085
6. Chen L, Zhu Y, Zang X, Cai B, Li Z, Xie L, et al. Mode splitting transmission effect of surface wave excitation through a metal hole array. *Light Sci Appl.* (2013) **2**:e60. doi: 10.1038/lsa.2013.16
7. Chen L, Liao DG, Guo XG, Zhao JY, Zhu YM, Zhuang Sl. Terahertz time-domain spectroscopy and micro-cavity components for probing samples: a review. *Front Inf Technol Electron Eng.* (2019) **20**:591–607. doi: 10.1631/FITEE.1800633

8. Dostálek J, Ctyroký J, Homola J, Brynda E, Skalský M, Nekvindová P, et al. Surface plasmon resonance biosensor based on integrated optical waveguide. *Sens Actuat B Chem.* (2001) **76**:8–12. doi: 10.1016/S0925-4005(01)00559-7
9. Slavik R, Homola J, Ctyroky J, Brynda E. Novel spectral fiber optic sensor based on surface plasmon resonance. *Sens Actuat B Chem.* (2001) **74**:106–11. doi: 10.1016/S0925-4005(00)00718-8
10. Sharma A, Jha R, Gupta B. Fiber-optic sensors based on surface plasmon resonance: a comprehensive review. *IEEE Sens J.* (2007) **7**:1118–29. doi: 10.1109/JSEN.2007.897946
11. Gramotnev DK, Bozhevolnyi SI. Plasmonics beyond the diffraction limit. *Nat Photonics.* (2010) **4**:83–91. doi: 10.1038/nphoton.2009.282
12. Lee B, Roh S, Park J. Current status of micro- and nano-structured optical fiber sensors. *Opt Fiber Technol.* (2009) **15**:209–21. doi: 10.1016/j.yofte.2009.02.006
13. Jain PK, El-Sayed MA. Plasmonic coupling in noble metal nanostructures. *Chem Phys Lett.* (2010) **487**:153–64. doi: 10.1016/j.cplett.2010.01.062
14. Anker J, Hall WP, Lyandres O, Shah N, Zhao J, Duyne R. Biosensing with plasmonic nanosensors. *Nat. Mater.* (2008) **7**:442–53. doi: 10.1038/nmat2162
15. Jorgenson RC, Yee SS. A fiber-optic chemical sensor based on surface plasmon resonance. *Sens Actuat B Chem.* (1993) **12**:213–20. doi: 10.1016/0925-4005(93)80021-3
16. Singh L, Bedi A, Kumar S. Diethyl ether sensor using double nanoslot hybrid plasmonic waveguide. *Front Opt.* (2017) JTu2A.65. doi: 10.1364/FIO.2017.JTu2A.65
17. Li X, Li W, Guo X, Lou J, Tong L. All-fiber hybrid photon-plasmon circuits: integrating nanowire plasmonics with fiber optics. *Opt Express.* (2013) **21**:15698–705. doi: 10.1364/OE.21.015698
18. Lakowicz JR, Vo-Dinh T, Bedi A, Singh L, Kumar S. SPR based hybrid plasmonic waveguide sensor for detection of causes of anemia in homosapiens. *Proc SPIE.* (2018) **10509**:15. doi: 10.1117/12.2285927
19. Ricciardi A, Crescitelli A, Vaiano P, Quero G, Consales M, Pisco M, et al. Lab-on-fiber technology: a new vision for chemical and biological sensing. *Analyst.* (2015) **140**:8068–79. doi: 10.1039/C5AN01241D
20. Gu F, Zeng H, Tong L, Zhuang S. Metal single-nanowire plasmonic sensors. *Opt Lett.* (2013) **38**:1826–8. doi: 10.1364/OL.38.001826
21. Sharma P, Asad S, Ali A. Bioluminescent bioreporter for assessment of arsenic contamination in water samples of India. *J Biosci.* (2013) **38**:251–8. doi: 10.1007/s12038-013-9305-z
22. Luo B, Yan Z, Sun Z, Li J, Zhang L. Novel glucose sensor based on enzyme-immobilized 81° tilted fiber grating. *Opt Express.* (2014) **22**:30571–8. doi: 10.1364/OE.22.030571
23. Wan M, Luo P, Jin J, Xing J, Wang Z, Wong STC. Fabrication of localized surface plasmon resonance fiber probes using ionic self-assembled gold nanoparticles. *Sensors (Basel).* (2010) **10**:6477–87. doi: 10.3390/s100706477
24. Nanduri V, Bhunia AK, Tu S-I, Paoli GC, Brewster JD. SPR biosensor for the detection of L. monocytogenes using phage-displayed antibody. *Biosens Bioelectron.* (2007) **23**:248–52. doi: 10.1016/j.bios.2007.04.007
25. Kim H-M, Park J-H, Lee S-K. Fiber optic sensor based on ZnO nanowires decorated by Au nanoparticles for improved plasmonic biosensor. *Sci Rep.* (2019) **9**:15605. doi: 10.1038/s41598-019-52056-1
26. Harshita C, Rajinder SK, Balveer P. Photonic crystal waveguide-based biosensor for detection of diseases. *J. Nanophotonics.* (2016) **10**:1–10. doi: 10.1117/1.JNP.10.036011
27. Tzyy-Jiann W, Cheng-Wei T, Fu-Kun L, Hsuen-Li C. Surface plasmon resonance waveguide biosensor by bipolarization wavelength interrogation. *IEEE Photonics Technol Lett.* (2004) **16**:1715–7. doi: 10.1109/LPT.2004.828376
28. Boozer C, Kim G, Cong S, Guan H, Londergan T. Looking towards label-free biomolecular interaction analysis in a high-throughput format: a review of new surface plasmon resonance technologies. *Curr Opin Biotechnol.* (2006) **17**:400–5. doi: 10.1016/j.copbio.2006.06.012
29. Homola J. Present and future of surface plasmon resonance biosensors. *Anal Bioanal Chem.* (2003) **377**:528–39. doi: 10.1007/s00216-003-2101-0
30. *Kurabo.* (2020). Available online at: https://www.kurabo.co.jp/news/products/ (accessed July 7, 2020).
31. Ma Y, Li X, Yu H, Tong L, Gu Y, Gong Q. Direct measurement of propagation losses in silver nanowires. *Opt Lett.* (2010) **35**:1160–2. doi: 10.1364/OL.35.001160
32. Caucheteur C, Guo T, Albert J. Review of plasmonic fiber optic biochemical sensors: improving the limit of detection. *Anal Bioanal Chem.* (2015) **407**:3883–97. doi: 10.1007/s00216-014-8411-6
33. Roh S, Chung T, Lee B. Overview of the characteristics of micro- and nano-structured surface plasmon resonance sensors. *Sensors (Basel).* (2011) **11**:1565–88. doi: 10.3390/s110201565
34. Chakma S, Khalek MA, Paul BK, Ahmed K, Hasan MR, Bahar AN. Gold-coated photonic crystal fiber biosensor based on surface plasmon resonance: design and analysis. *Sens Bio-Sensing Res.* (2018) **18**:7–12. doi: 10.1016/j.sbsr.2018.02.003
35. Homola J, Piliarik M. Surface Plasmon Resonance (SPR) sensors. In: Homola J, editor. *Surface Plasmon Resonance Based Sensors*. Berlin; Heidelberg: Springer Berlin Heidelberg (2006). p. 45–67.
36. Jha R, Verma R, Gupta B. Surface plasmon resonance-based tapered fiber optic sensor: sensitivity enhancement by introducing a teflon layer between core and metal layer. *Plasmonics.* (2008) **3**:151–6. doi: 10.1007/s11468-008-9068-9
37. Monzón-Hernández D, Villatoro J. High-resolution refractive index sensing by means of a multiple-peak surface plasmon resonance optical fiber sensor. *Sens Actuat B Chem.* (2006) **115**:227–31. doi: 10.1016/j.snb.2005.09.006
38. Bhatia P, Gupta B. Surface-plasmon-resonance-based fiber-optic refractive index sensor: sensitivity enhancement. *Appl Opt.* (2011) **50**:2032–6. doi: 10.1364/AO.50.002032
39. Suzuki A, Kondoh J, Matsui Y, Shiokawa S, Suzuki K. Development of novel optical waveguide surface plasmon resonance (SPR) sensor with dual light emitting diodes. *Sens Actuat B Chem.* (2005) **106**:383–7. doi: 10.1016/j.snb.2004.08.021
40. Yuan D, Dong Y, Liu Y, Li T. Design of a high-performance micro integrated surface plasmon resonance sensor based on silicon-on-insulator rib waveguide array. *Sensors (Basel).* (2015) **15**:17313–28. doi: 10.3390/s150717313
41. Matsushita T, Nishikawa T, Yamashita H, Kishimoto J, Okuno Y. Development of new single-mode waveguide surface plasmon resonance sensor using a polymer imprint process for high-throughput fabrication and improved design flexibility. *Sens Actuat B Chem.* (2008) **129**:881–7. doi: 10.1016/j.snb.2007.09.084
42. Kabashin AV, Nikitin PI. Surface plasmon resonance interferometer for bio- and chemical-sensors. *Opt Commun.* (1998) **150**:5–8. doi: 10.1016/S0030-4018(97)00726-8
43. Nikitin PI, Beloglazov AA, Kochergin VE, Valeiko MV, Ksenevich TI. Surface plasmon resonance interferometry for biological and chemical sensing. *Sens Actuat B Chem.* (1999) **54**:43–50. doi: 10.1016/S0925-4005(98)00325-6
44. Sheridan AK, Harris RD, Bartlett PN, Wilkinson JS. Phase interrogation of an integrated optical SPR sensor. *Sens Actuat B Chem.* (2004) **97**:114–21. doi: 10.1016/j.snb.2003.08.005
45. Nemova G, Kabashin A, Kashyap R. Surface plasmon-polariton Mach-Zehnder refractive index sensor. *J Opt Soc Am B.* (2008) **25**:1673–77. doi: 10.1364/JOSAB.25.001673
46. Cheng Y-C, Chang Y-J, Chuang Y-C, Huang B-Z, Chen CC. A plasmonic refractive index sensor with an ultrabroad dynamic sensing range. *Sci Rep.* (2019) **9**:5134. doi: 10.1038/s41598-019-41353-4
47. Kim S, Yan R. Recent developments in photonic, plasmonic and hybrid nanowire waveguides. *J Mater Chem C.* (2018) **6**:11795–816. doi: 10.1039/C8TC02981D
48. Niedziółka-Jönsson J, Mackowski S. Plasmonics with metallic nanowires. *Materials (Basel).* (2019) **12**:1418. doi: 10.3390/ma12091418
49. Wei H, Zhang S, Tian X, Xu H. Highly tunable propagating surface plasmons on supported silver nanowires. *Proc Natl Acad Sci USA.* (2013) **110**:4494–9. doi: 10.1073/pnas.1217931110
50. Wang Y, Guo X, Tong L, Lou J. Modeling of Au-nanowire waveguide for plasmonic sensing in liquids. *J Lightwave Technol.* (2014) **32**:4233–8. doi: 10.1109/JLT.2014.2354696
51. Wang S-B, Huang Y-F, Chattopadhyay S, Jinn Chang S, Chen R-S, Chong C-W, et al. Surface plasmon-enhanced gas sensing in single gold-peapodded silica nanowires. *NPG Asia Mater.* (2013) **5**:e49. doi: 10.1038/am.2013.17
52. Gentile A, Ruffino F, Boninelli S, Grimaldi MG. Silica nanowire–Au nanoparticle pea-podded composites: synthesis and structural analyses. *Thin Solid Films.* (2015) **589**:755–63. doi: 10.1016/j.tsf.2015.07.011

53. Kolmakov A, Klenov DO, Lilach Y, Stemmer S, Moskovits M. Enhanced gas sensing by individual SnO2 nanowires and nanobelts functionalized with PD catalyst particles. *Nano Lett.* (2005) **5**:667–73. doi: 10.1021/nl050082v
54. Cattabiani N, Baratto C, Zappa D, Comini E, Donarelli M, Ferroni M, et al. Tin oxide nanowires decorated with Ag nanoparticles for visible light-enhanced hydrogen sensing at room temperature: bridging conductometric gas sensing and plasmon-driven catalysis. *J Phys Chem C.* (2018) **122**:5026–31. doi: 10.1021/acs.jpcc.7b09807
55. Peeters D, Barreca D, Carraro G, Comini E, Gasparotto A, Maccato C, et al. Au/ε-Fe2O3 nanocomposites as selective NO2 gas sensors. *J Phys Chem C.* (2014) **118**:11813–9. doi: 10.1021/jp5032288
56. Li N-M, Li K-M, Wang S, Yang K-Q, Zhang L-J, Chen Q, et al. Gold embedded maghemite hybrid nanowires and their gas sensing properties. *ACS Appl Mater Interfaces.* (2015) **7**:10534–40. doi: 10.1021/acsami.5b02087
57. Huang J-G, Lee C-L, Lin H-M, Chuang T-L, Wang W-S, Juang R-H, et al. A miniaturized germanium-doped silicon dioxide-based surface plasmon resonance waveguide sensor for immunoassay detection. *Biosens Bioelectron.* (2006) **22**:519–25. doi: 10.1016/j.bios.2006.07.030
58. Akowuah EK, Gorman T, Haxha S. Design and optimization of a novel surface plasmon resonance biosensor based on Otto configuration. *Opt Express.* (2009) **17**:23511–21. doi: 10.1364/OE.17.023511
59. Weiss MN, Srivastava R, Groger H. Experimental investigation of a surface plasmon-based integrated-optic humidity sensor. *Electron Lett.* (1996) **32**:842–3. doi: 10.1049/el:19960520
60. Mouvet C, Harris RD, Maciag C, Luff BJ, Wilkinson JS, Piehler J, et al. Determination of simazine in water samples by waveguide surface plasmon resonance. *Anal Chim Acta.* (1997) **338**:109–17. doi: 10.1016/S0003-2670(96)00443-6
61. Ma Y, Huang Q, Li T, Villanueva J, Nguyen NH, Friend J, et al. A local nanofiber-optic ear. *ACS Photonics.* (2016) **3**:1762–7. doi: 10.1021/acsphotonics.6b00424
62. Huang Q, Lee J, Arce FT, Yoon I, Angsantikul P, Liu J, et al. Nanofibre optic force transducers with sub-piconewton resolution via near-field plasmon–dielectric interactions. *Nat Photonics.* (2017) **11**:352–5. doi: 10.1038/nphoton.2017.74
63. Fu L, Liu Y, Wang W, Wang M, Bai Y, Chronister EL, et al. A pressure sensor based on the orientational dependence of plasmonic properties of gold nanorods. *Nanoscale.* (2015) **7**:14483–8. doi: 10.1039/C5NR03450G

Conflict of Interest: The authors declare that the research was conducted in the absence of any commercial or financial relationships that could be construed as a potential conflict of interest.

frontiers in Physics

ORIGINAL RESEARCH
published: 21 August 2020
doi: 10.3389/fphy.2020.00316

Design of Broadband High Gain Polarization Reconfigurable Fabry-Perot Cavity Antenna Using Metasurface

Chun Ni[1]*, *Changqing Liu*[2], *Zhongxiang Zhang*[1], *Mingsheng Chen*[1], *Liang Zhang*[1] and *Xianliang Wu*[2]

[1] *Anhui Province Key Laboratory of Simulation and Design for Electronic Information System, The School of Electronic Information and Electrical Engineering, Hefei Normal University, Hefei, China,* [2] *Key Lab of Intelligent Computing & Signal Processing, Ministry of Education, Anhui University, Hefei, China*

A broadband high gain polarization reconfigurable antenna based on metasurface has been presented. The antenna is composed of a planar metasurface, a slot antenna and an air cavity. The metasurface is made up of 64 identical patches, and all the patches are on the top surface of the substrate. The spatial equivalent circuit of the metasurface is discussed and two approximate calculation formulas of the equivalent circuit are obtained. The antenna can be reconfigured to linear polarization, left-hand and right-hand circular polarizations by adjusting the relative positions between the metasurface and the planar slot antenna. The gain of the antenna is improved. In order to verify these methods, the antenna is studied and designed to operate at around 11GHz. The simulated and measured results show that the 3dB axis ratio bandwidth is 10–12 GHz (fractional bandwidth 18.18%) and maximum gain of 14.6 dBi.

Keywords: metasurface, polarization reconfiguration, Fabry-Perot cavity, high gain, slot antenna

OPEN ACCESS

Edited by:
Wei E. I. Sha,
Zhejiang University, China

Reviewed by:
Nobuhiko Yokoshi,
Osaka Prefecture University, Japan
Junichi Fujikata,
Photonics Electronics Technology Research Association, Japan

Correspondence:
Chun Ni
chunni_hfnu@sina.com

Specialty section:
This article was submitted to Optics and Photonics, a section of the journal Frontiers in Physics

Received: *03 February 2020*
Accepted: *10 July 2020*
Published: *21 August 2020*

Citation:
Ni C, Liu C, Zhang Z, Chen M, Zhang L and Wu X (2020) Design of Broadband High Gain Polarization Reconfigurable Fabry-Perot Cavity Antenna Using Metasurface. Front. Phys. 8:316. doi: 10.3389/fphy.2020.00316

INTRODUCTION

Metamaterials, such as metasurface (MS), electromagnetic band gap (EBG), photonic band gap (PBG), frequency selective surface (FSS) and left handed metamaterials (LFM), are commonly designed by arranging a number of electrically small scatterers in regular or irregular periods within a space region to obtain some special electromagnetic behaviors [1–5]. In recent years, reconfigurable antennas based on metasurface have been attracting a wide attention of researchers [6–10]. Reconfigurable antennas generally include operating frequency, radiation pattern, and polarization modes tunability, which can well meet the complex communication systems and multitasking demands [11–13]. Polarization reconfigurable antennas are usually able to achieve polarization mode transitions. For example, the antenna can be reconfigured to left-hand circular polarization (LHCP), right-hand circular polarization (RHCP) and linear polarization [14–17]. The direction of the electric field vector is changed at the time of reconstruction. Frequency reconfigurable antennas are very useful owing to their tunable operating frequency, which can be classified into two types, band switching and continuous tuning, respectively [18–21]. The radiation pattern of an antenna can be classified into omnidirectional radiation, bidirectional radiation, unidirectional radiation and multidirectional radiation. Radiation pattern reconfigurable antennas can usually be switched from one radiation pattern to another.

Just as a two-dimensional equivalent of metamaterial, metasurface, which cannot be really found in the nature, is essentially periodic arrangements of scatterers or apertures in order to achieve the characteristics of specialized engineering [22, 23]. Research shows that MS can be used to enhance the performance of antennas. Thus, much research work

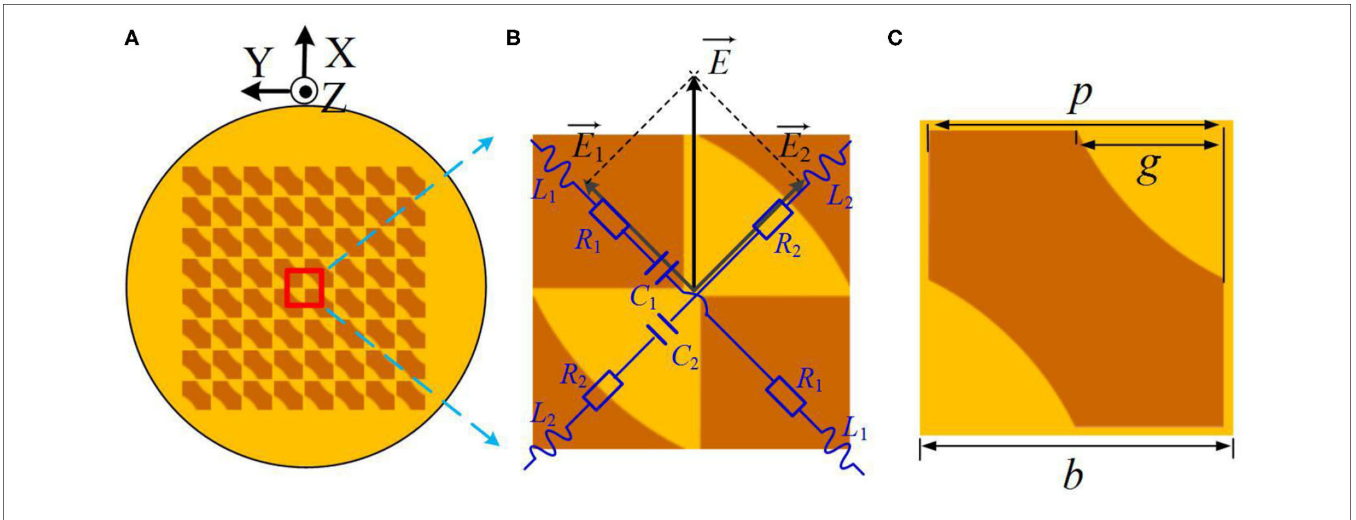

FIGURE 1 | Geometry of proposed MS. **(A)** top view of the MS, **(B)** Unit cell with corners truncated, and **(C)** Schematic with the size parameters of the patch.

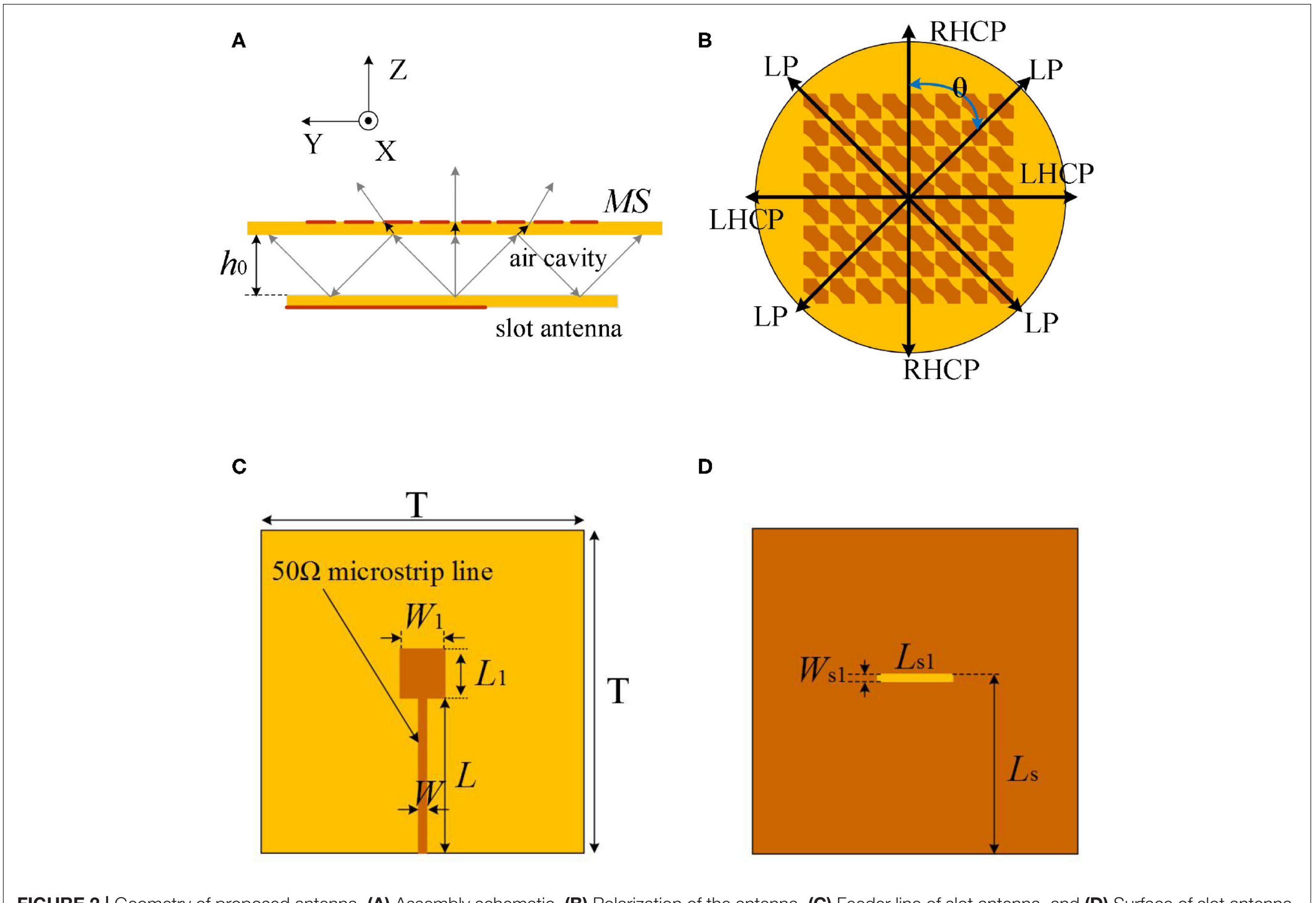

FIGURE 2 | Geometry of proposed antenna. **(A)** Assembly schematic, **(B)** Polarization of the antenna, **(C)** Feeder line of slot antenna, and **(D)** Surface of slot antenna.

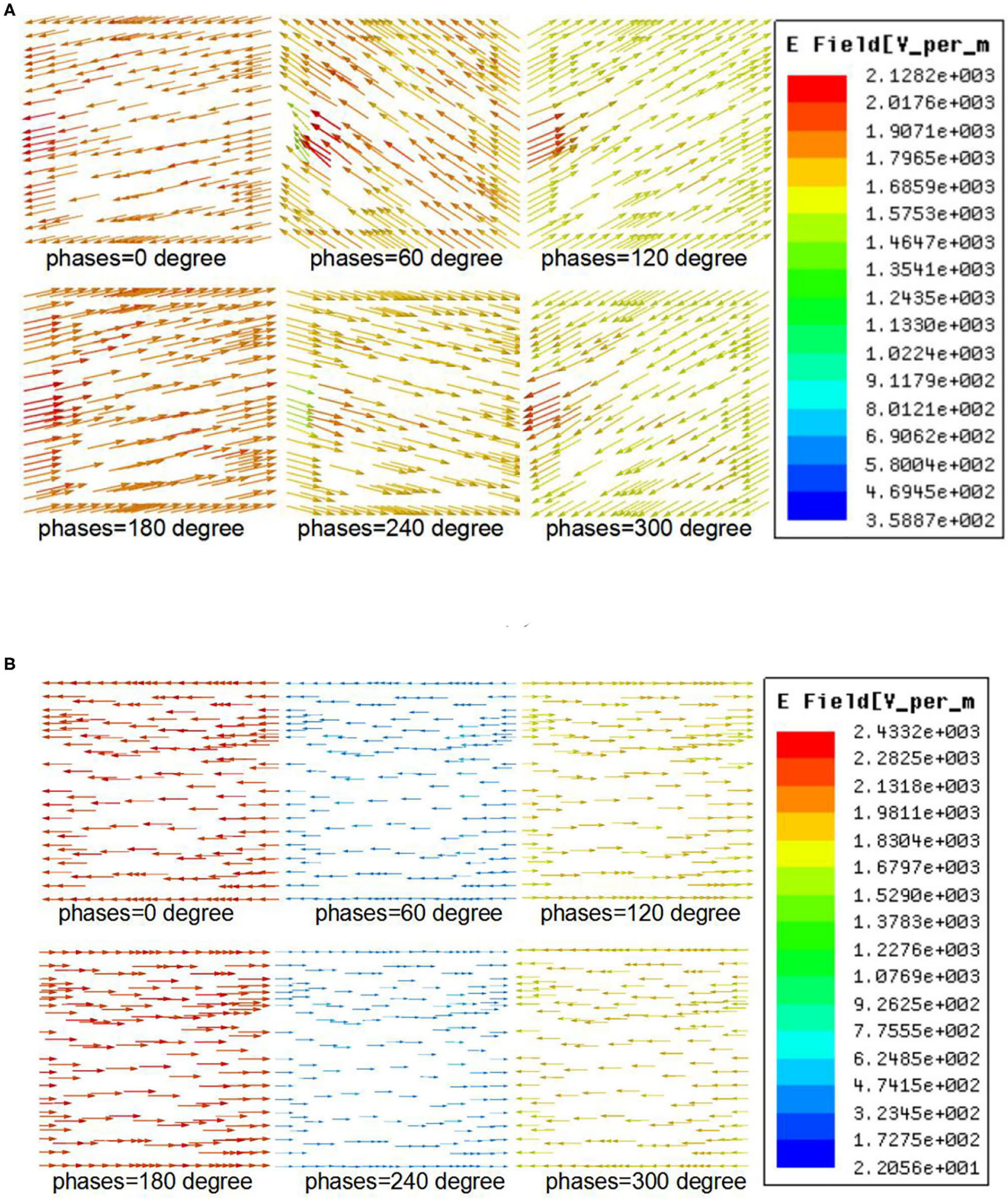

FIGURE 3 | Electric field distribution at f = 11 GHz for the unit cell of the proposed MS. **(A)** $\theta = 0°$ and **(B)** $\theta = 45°$.

has been carried out in the field of improving antenna gain, achieving polarization reconfigurable and frequency reconfigurable antennas by using MS.

In literature [24], a frequency and polarization reconfigurable antenna consisting of a frequency reconfigurable MS, a polarization reconfigurable MS and a microstrip patch antenna with the same diameter is proposed. The polarization reconfigurable MS consists of periodic corner-truncated square elements placed on the upper surface of the frequency reconfigurable MS, and the microstrip patch antenna placed in the bottom layer as a source antenna. By rotating the frequency reconfiguration MS, the designed antenna has a tuning range of 4.0–4.35 GHz. By rotating the polarizable reconfigurable surface, the designed antenna can realize the transformation of linear and circular polarization at 5.0–5.2GHz (relative bandwidth 4%). In [25], the studies of polarization reconfigurable antenna with a slot antenna and an asymmetric corss shaped MS are conducted. The linear polarization of the slot antenna is reconfigured into LHCP and RHCP by rotating the MS around the center of the slot antenna. The designed polarization reconfigurable antenna has a 3dB axis ratio (AR) bandwidth of 4.29–4.41 GHz (relative bandwidth 2.7%). In [22], A radiation pattern reconfigurable antenna based on MS is proposed. The operating frequency range of the designed radiation pattern reconfigurable antenna is 5.4–5.6 GHz. A low profile broadband circularly polarized MS antenna was proposed in [26]. The MS consisting of 4 × 4 square metal patches to realize the miniaturization of the antenna.The 3 dB axial ratio bandwidth is 1.4–1.62 GHz (relative bandwidth 14.5%).

The operating bandwidth of the previously published literature with polarization reconfigurable and radiation pattern reconfigurable antenna is often subject to the restriction of the structure of MS, As is in [26], the 3 dB AR is only 14.5%. In this paper, a polarization reconfigurable antenna using an improved MS is proposed. When the antenna operates in circular polarization, there will be three inflection points in the AR curve. Thus, the 3 dB AR bandwidth is expanded greatly.

In this paper, a reconfigurable antenna using an improved MS is proposed. The 3 dB AR bandwidth is expanded greatly. To clearly show that this antenna can provide circular polarization radiation, the vector electric field at different phases from 0 to 360 degrees, at the antenna aperture in the far field is analyzed. Our work extracts and analyses the equivalent circuit parameters of the improved MS. In the new design, Fabry-Perot cavity antenna and MS are combined to expand the bandwidth of antenna, improve the gain of antenna, and realize polarization reconfiguration.

TOPOLOGY STRUCTURE AND PRINCIPLE OF OPERATION OF THE RECONFIGURABLE POLARIZATION CONVERTER

As is shown in **Figure 1**, the proposed MS is made up of 64 identical periodic patches, and all the patches are on the top surface of the dielectric substrate. In **Figure 1A**, the structure within the area enclosed by the red curve can be considered as a unit cell. In order to analyze the polarization properties of the MS, the unit cell is enlarged and redrawn, as is presented in **Figure 1B**.

The perpendicular E-field components broken down by the MS will cause two different impedances. The expression for two impedances is shown in Equations (1) and (2).

$$Z_1 = 2R_1 + j\omega(2L_1) + \frac{1}{j\omega C_1} = R_{Z1} + jX_{Z1} \tag{1}$$

$$Z_2 = 2R_2 + j\omega(2L_2) + \frac{1}{j\omega C_2} = R_{Z2} + jX_{Z2} \tag{2}$$

The spatial equivalent circuit of the metal microstrip structure is discussed in literature [27]. The equivalent circuit of the

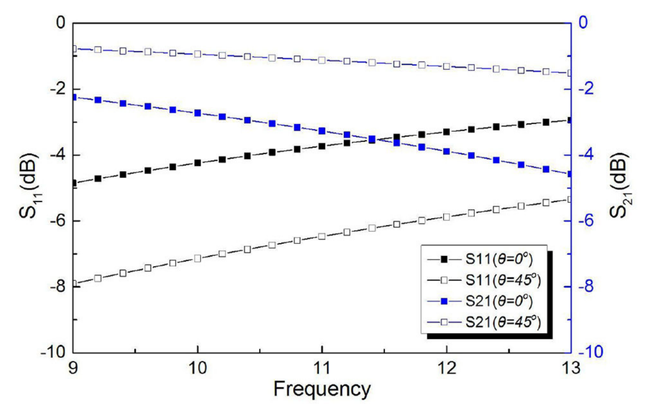

FIGURE 4 | The simulated amplitude of the reflection and transmission coefficients of the metasurface's unit cell.

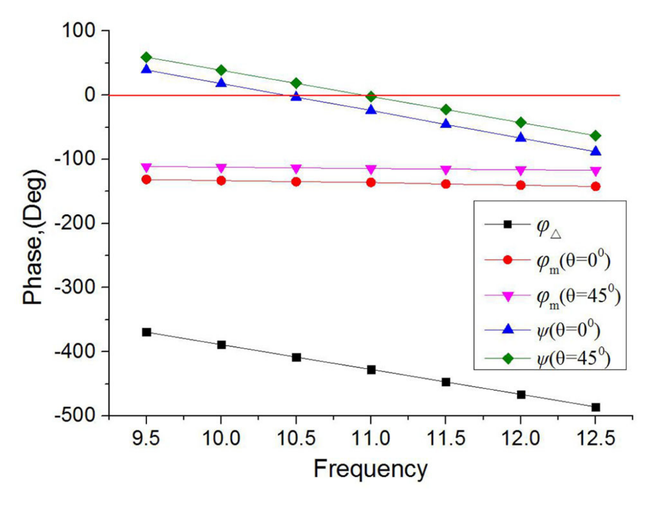

FIGURE 5 | The path difference φ_Δ, the reflection phase φ_m of the metasurface and the total phase difference Ψ at different frequencies.

metasurface is analyzed and two approximate calculation formulas of the equivalent circuit are obtained. As is shown in Equations (3) and (4), ε_0 is the permittivity and μ_0 is the permeability of the free space; ε_r is dielectric constant of substrate; γg is the relative distance of two patches, which is related to the dimension of the patch and the cutting part; η is length of the truncated patch; p is the length of the patch; b is the length of the unit cell.

$$C = \varepsilon_0 \varepsilon_r \frac{2\sqrt{2}b}{\pi} \ln\left(\frac{1}{\sin\left(\frac{\gamma g \pi}{2\sqrt{2}b}\right)}\right) \tag{3}$$

$$L = \mu_0 \frac{b}{\sqrt{2}\pi} \ln\left(\frac{1}{\sin\left(\frac{\eta\pi}{2\sqrt{2}b}\right)}\right), \quad \eta = \sqrt{2}b - \gamma g \tag{4}$$

According to Equations (3) and (4), when γg increases, the L_2 increases and the C_2 decreases. Thus, the value of X_{Z2} becomes large, making Z_2 less capacitive than Z_1. The phase difference between Z_1 and Z_2 can be achieved by varying the dimension of the truncated corners. When the unit cell is truncated such that $|Z_1| = |Z_2|$, and $\angle Z_2 - \angle Z_1 = 90°$, then $|E_1| = |E_2|$ and $\angle\vec{E}_2 - \angle\vec{E}_1 = 90°$. The antenna will be RHCP. As is shown in **Figure 2B**, when the MS is rotated 45° or 135° in the counterclockwise direction, the antenna is changed to LP. When the rotation angle is 90°, the antenna is reconfigured to LHCP. The schematic assembly of antenna is drawn in **Figure 2A**. It can be seen that the reconfigurable antenna presented in this paper consists of a slot antenna, a supersurface and an air cavity. These three components together form the Fabry-Perot cavity antenna in structure.

The property of the metasurface layer is highly relevant with the characteristics of the fabry-perot resonator antenna. In addition, the frequency resonance of an fabry-perot resonator antenna can be described as

$$2n\pi = \frac{4\pi h_0}{c} f + \varphi_m + \varphi_r, \quad n = 0, 1, 2..... \tag{5}$$

where φ_m and φ_r, respectively, represent the reflection phases of the metasurface layer and the ground plane, and h_0 is the height of the fabry-perot cavity. Supposing that the ground plane is perfectly electric conducting ($\varphi_r = -\pi$) and the reflection

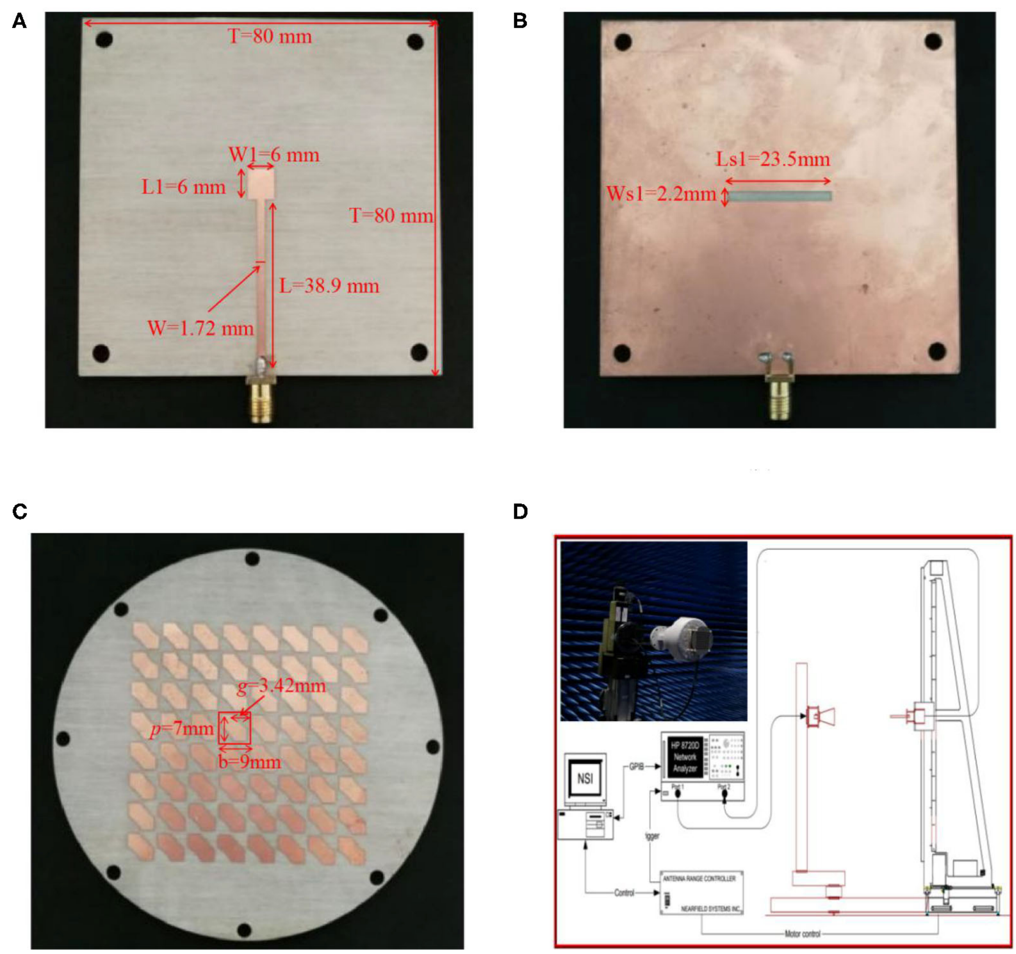

FIGURE 6 | Photograph of the designed antenna and Antenna test system. **(A)** feeder line of slot antenna. **(B)** surface of slot antenna. **(C)** surface of MS. **(D)** antenna measurement setup.

phase of the metasurface layer varies around $-\pi$, according to equation (5), the fabry-perot cavity has a minimum height h of $\sim\lambda/2$ when the fabry-perot resonator antenna operates at the first resonance ($n = 0$).

As we know, the Fabry-Perot cavity can improve the gain of antenna greatly. In this design, a slot patch antenna which is chosen has the potential of easy feed, stable transverse radiation and wide bandwidth. Complete schematic with the dimensions of feeder line of the source antenna is drawn in **Figure 2C**. The surface source antenna is drawn in **Figure 2D**.

To demonstrate the circular polarization (CP) characteristics of MS, the simulated current distribution on the MS antenna at different time points is shown in **Figure 3**. It is obvious that the electric field vector distribution varies and rotates with time. Numerical simulations have been performed by using the full wave electromagnetic simulator HFSS. **Figure 3A** shows the direction of rotation of the electric field vector of the metasurface's unit cell when $\theta = 0°$. According to the rotation direction of the electric field vector, the electric field is RHCP.

Figure 3B shows the direction of the electric field vector when $\theta = 45°$. According to the direction of the electric field vector, the electric field is LP at this time. The

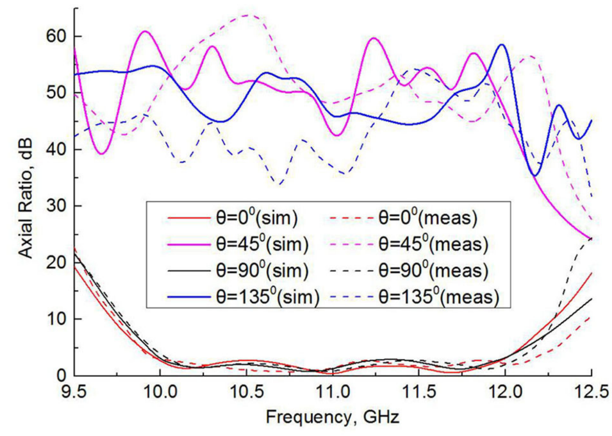

FIGURE 8 | Measured and simulated axial ratio with different rotation angle.

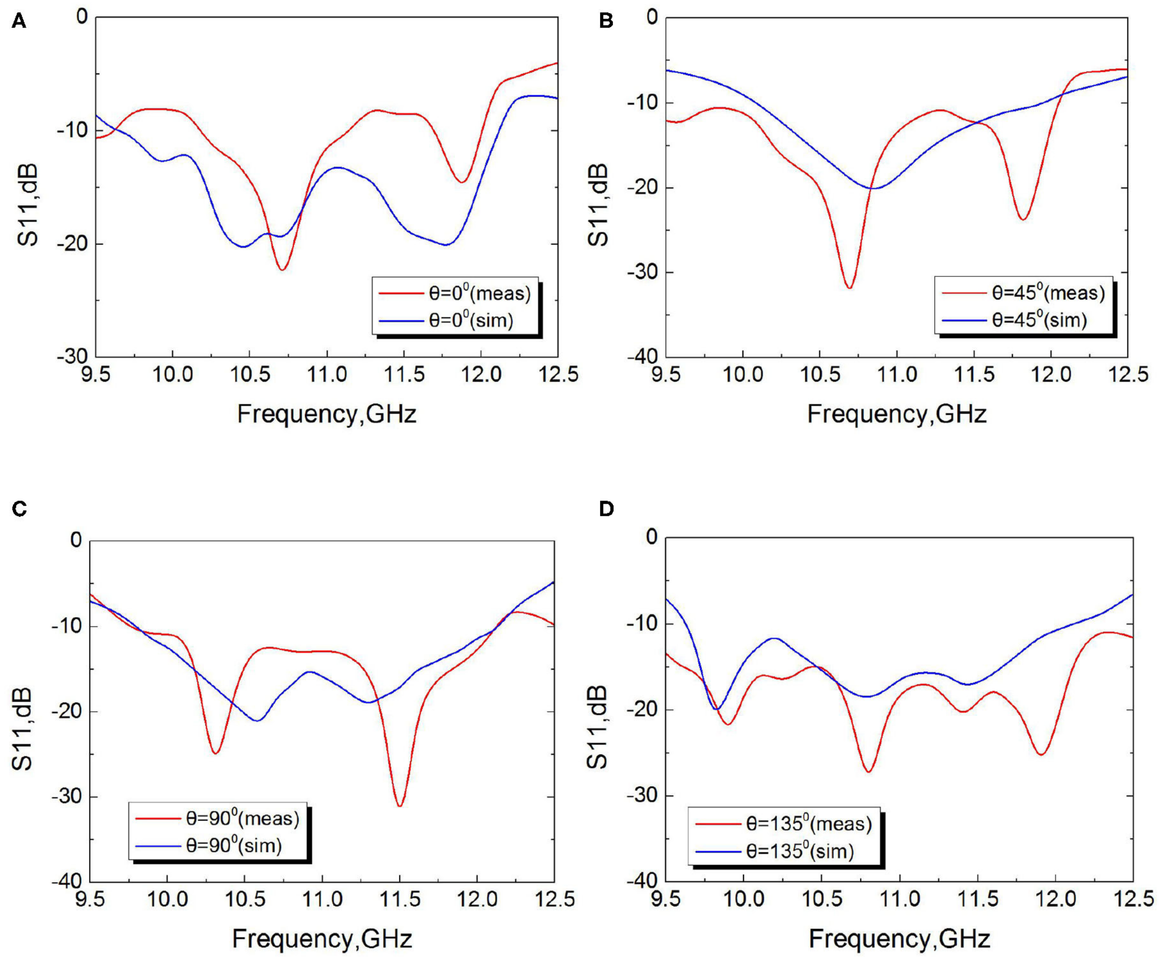

FIGURE 7 | Measured and simulated reflection coefficient S11 with different rotation angle. **(A)** $\theta = 0°$. **(B)** $\theta = 45°$. **(C)** $\theta = 90°$. **(D)** $\theta = 135°$.

simulated reflection and transmission coefficients of the metasurface's unit cell under normal incidence are plotted in **Figure 4**.

As described above, the size of the h_0 is affected by the reflection phase of the metasurface. However, the reflection phase of the metasurface also changes with frequency. The simulation results of reflection phase of the metasurface are shown in **Figure 5**. According to the size of h_o, the phase difference caused by the path difference can be calculated. **Figure 5** also shows the path difference φ_Δ, the reflection phase φ_m of the metasurface and the total phase difference Ψ at different frequencies. As shown in **Figure 5**, the total phase difference Ψ is close to 0 at 10.5 GHz when $\theta = 45°$, where the same phase superposition maximizes the gain of the antenna. When $\theta = 0°$, the total phase difference Ψ is close to 0 at 11 GHz. The maximum gain of antenna will appear at 11 GHz. The gain of the antenna will also change with the total phase difference Ψ.

POLARIZATION RECONFIGURABLE ANTENNA BASED ON METASURFACE

In order to verify the correctness of the antenna design method in the previous section, much research has been carried out and the experimental results show that when the cutting shape is fan-shaped, the bandwidth for circularly polarized has been greatly expanded. Photographs of antennas and test systems are shown in **Figure 6**.

The antenna is designed on RO4003C substrate with ε_r=3.55, 32 mil thickness. As shown in **Figure 5**, the optimized dimensions of the antenna are T = 80 mm, ho = 16.2 mm W1 = 6 mm, L1 = 6.7 mm, W = 1.72 mm, L = 38.9 mm, Ws1 = 2.2 mm, Ls1 = 23.5 mm, Ls = 41.1 mm, p = 7 mm, g = 3.42 mm, b = 9 mm. The simulated and measured S11 of the designed antenna with different rotation angles are shown in

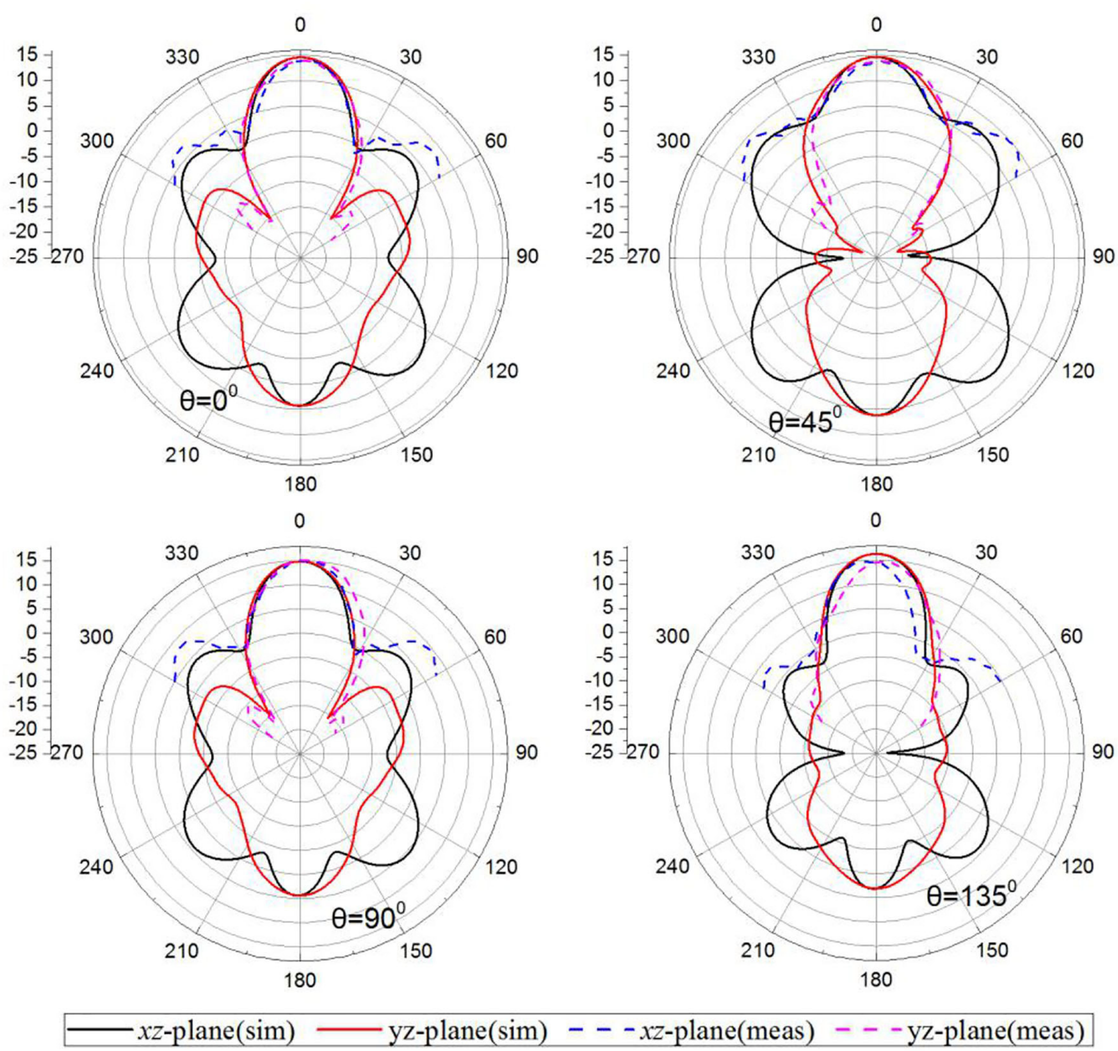

FIGURE 9 | Measured and simulated radiation patterns and gains with different rotation angle at 11 GHz.

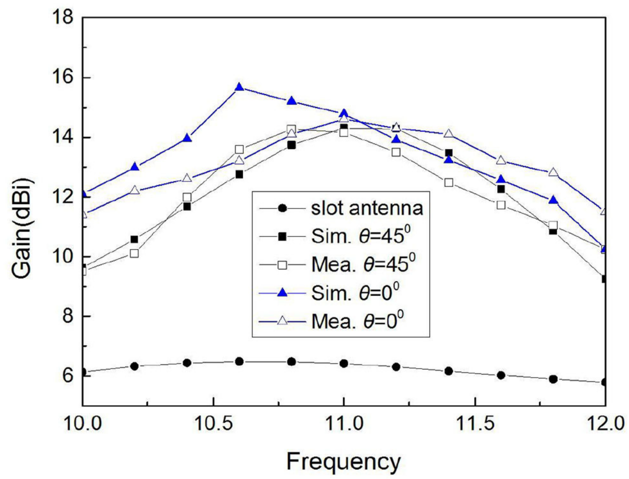

FIGURE 10 | Measured and simulated peak gains vs. frequency with different rotation angle.

TABLE 1 | Comparison of some published polarization reconfigurable antennas and our work.

	f_0 (GHz)	3 dB AR Bandwidth (%)	Peak gain (dBi)	Polarization
Kandasamy et al. [25]	4.35	2.7	6.5	LP/LHCP/RHCP
Liu et al. [26]	1.51	14.5	7	RHCP
Fan et al. [28]	10	16	17.9	LHCP
Li et al. [29]	8.9	13.8	11.2	LHCP
Hu et al. [30]	5.5	17.8	9.39	LP/LHCP/RHCP
Zhu et al. [31]	3.5	11.4	7.5	LP/LHCP/RHCP
This work	11	18.18	14.6	LP/LHCP/RHCP

Figure 7. The measured results are in good agreement with the simulated results.

The simulated and measured AR of the designed antenna with different rotation angle θ is shown in **Figure 8**. The measured 3 dB AR bandwidth is 10–12 GHz (relative bandwidth 18.18%) for the rotation angle $\theta = 0°$ and $\theta = 90°$. The simulated and measured radiation patterns and gains of the proposed antenna at 11 GHz are illustrated in **Figure 9**. The measurements of the antenna pattern are only performed around the main beam for achieving more accurate test results. The measured maximum gain of the designed antenna is more than 14 dBi, when $\theta = 0°$, $\theta = 45°$, $\theta = 90°$, and $\theta = 135°$. The maximum peak is 14.6 dBi at 11 GHz, when $\theta = 0°$. **Figure 10** shows the gain of the slot antenna and the gain of the reorganizable antenna. The gain of slot antenna is about 6–7 dBi. When the MS is placed atop the slot antenna, the gain of the antenna is obviously increased. The value of the gain increases by about 7 dBi on average.

The comparison between our work and some published polarization reconfigurable antennas is illustrated in **Table 1**. This work shows wider bandwidth and higher gain performance. The design method presented in this paper has proved that MS can be used to improve antenna performance more effectively.

CONCLUSIONS

A broadband high gain polarization reconfigurable antenna based on MS has been presented. The antenna is composed of a planar MS and a slot antenna. The proposed antenna can be reconfigured to LHCP, RHCP and LP by adjusting the relative position between the MS and the slot antenna. The antenna is studied and designed to operate at around 11 GHz. The S11, AR, radiation patterns and gain of the antenna are measured. The measured results show that the maximum gain of the proposed antenna is 14.6 dBi and that the 3 dB AR bandwidth is 10–12 GHz with state-of-the-art measured performance.

DATA AVAILABILITY STATEMENT

All datasets generated for this study are included in the article/supplementary material.

AUTHOR CONTRIBUTIONS

CN developed the concept and supervised the whole project. CL carried out the simulations and designed the structure and fabricated the sample. CN and CL analyzed the simulation data and contributed to writing and finalizing the paper. ZZ and LZ performed the experiments. MC contributed to paper revision and language editing. All authors contributed to the article and approved the submitted version.

FUNDING

This work was supported in part by Key Natural Science Projects in Education Commission of Anhui Province (grant KJ2020A0105), in part by the Project of Anhui Province Key Laboratory (grant 2019ZDSYSZY02), in part by the National Natural Science Foundation of China (grant 51477039), and in part by the Science and Technology Project of Anhui Province (1708085QF150).

REFERENCES

1. Huang Y, Yang L, Li J, Wang Y, Wen G. Polarization conversion of metasurface for the application of wide band low-profile circular polarization slot antenna. *Appl Phys Lett.* (2016) **109**:054101. doi: 10.1063/1.4960198
2. Peng L,Wen BJ, Li XF, Jiang X, Li SM. CPW fed UWB antenna by EBGs with wide rectangular notched-band. *IEEE Access.* (2017) **4**:9545–52. doi: 10.1109/ACCESS.2016.2646338
3. Jimenez-Guzman GA, Tirado-Mendez JA, Jardon-Aguilar H. Three-layered circular patch antennas array with UC-PBG for wider bandwidth and surface

wave propagation mode attenuation at X-band. *Microw Opt Technol Lett.* (2018) **60**:2676–83. doi: 10.1002/mop.31467
4. Liao WJ, Zhang WY, Hou YC, Chen ST, Kuo CY, Chou M. An FSS-integrated low-RCS radome design. *IEEE Antennas Wireless Propag Lett.* (2019) **18**:2076–80. doi: 10.1109/LAWP.2019.2937556
5. Li JF, Wu DL, Zhang G, Wu YJ, Mao CX. A left/right-handed dual circularly-polarized antenna with duplexing and filtering performance. *IEEE Access.* (2019) **7**:35431–7. doi: 10.1109/ACCESS.2019.2904189
6. Wan X, Zhang L, Jia SL, Yin JY, Cui TJ. Horn antenna with reconfigurable beam-refraction and polarization based on anisotropic huygens metasurface. *IEEE Trans Antennas Propag.* (2017) **65**:4427–34. doi: 10.1109/TAP.2017.2722829
7. Wu J, Zhang ZX, Ren XG, Huang ZX, Wu XL. A broadband electronically mode-reconfigurable orbital angular momentum metasurface antenna. *IEEE Antennas Wireless Propag Lett.* (2019) **18**:1482–86. doi: 10.1109/LAWP.2019.2920695
8. Yu J, Jiang W, Gong SX. Low-RCS beam-steering antenna based on reconfigurable phase gradient metasurface. *IEEE Antennas Wireless Propag Lett.* (2019) **18**:2016–20. doi: 10.1109/LAWP.2019.2936300
9. Tian JY, Li Q, Lu J, Qiu M. Reconfigurable all-dielectric antenna-based metasurface driven by multipolar resonances. *Opt Exp.* (2018) **26**:23918–25. doi: 10.1364/OE.26.023918
10. Chaimool S, Hongnara T, Rakluea C, Akkaraekthalin P, Zhao Y. Design of a PIN diode-based reconfigurable metasurface antenna for beam switching applications. *Int J Antennas Propag.* (2019) **2019**:7216324. doi: 10.1155/2019/7216324
11. Zhu HL, Liu XH, Cheung SW, Yuk TI. Frequency-reconfigurable antenna using metasurface. *IEEE Trans Antennas Propag.* (2014) **62**:80–5. doi: 10.1109/TAP.2013.2288112
12. Darvazehban A, Rezaeieh SA, Zamani A, Abbosh AM. Pattern reconfigurable metasurface antenna for electromagnetic torso imaging. *IEEE Trans Antennas Propag.* (2019) **67**:5453–62. doi: 10.1109/TAP.2019.2916576
13. Ni C, Chen MS, Zhang ZX, Wu XL. Design of frequency-and polarization-reconfigurable antenna based on the polarization conversion metasurface. *IEEE Antennas Wireless Propag Lett.* (2018) **17**:78–81. doi: 10.1109/LAWP.2017.2775444
14. Lian RN, Tang ZY, Yin YZ. Design of a broadband polarization-reconfigurable fabry-perot resonator antenna. *IEEE Antennas Wireless Propag Lett.* (2018) **17**:122–25. doi: 10.1109/LAWP.2017.2777502
15. Wang HF, Wang ZB, Cheng Y, Zhang YR. Dual-polarized lens antenna based on multimode metasurfaces. *Chinese Phys B.* (2018) **27**:118401. doi: 10.1088/1674-1056/27/11/118401
16. Chen SL, Karmokar DK, Qin PY, Ziolkowski RW, Guo YJ. Polarization-reconfigurable leaky-wave antenna with continuous beam scanning through broadside. *IEEE Trans Antennas Propag.* (2020) **68**:121–33. doi: 10.1109/TAP.2019.2935122
17. Wu HF, Wei YH, Chen TR, Row JS. Quad-polarization reconfigurable antenna with wideband operation. *Microw Opt Technol Lett.* (2019) **61**:2080–7. doi: 10.1002/mop.31865
18. Bronckers LA, Roc'h A, Smolders AB. A new design method for frequency-reconfigurable antennas using multiple tuning components. *IEEE Trans Antennas Propag.* (2019) **67**:7285–95. doi: 10.1109/TAP.2019.2930204
19. Asghari A, Azadi-Tinat N, Oraizi H, Ghalibafan J. Wideband frequency-reconfigurable antenna for airborne applications. *Wireless Pers Commun.* (2019) **109**:1529–40. doi: 10.1007/s11277-019-06625-2
20. Iqbal A, Smida A, Abdulrazak LF, Saraereh OA, Mallat NK, Elfergani I, et al. Low-profile frequency reconfigurable antenna for heterogeneous wireless systems. *Electron.* (2019) **8**:976. doi: 10.3390/electronics8090976
21. Liu F, Cheng X, Zhang F, Chen Y, Song HL, Huang YG, et al. Design and assembly of reconfigurable 3D radio-frequency antennas based on mechanically triggered switches. *Adv Electron Mater.* (2019) **5**:1900256. doi: 10.1002/aelm.201900256
22. Zhu HL, Cheung SW, Yuk TI. Mechanically pattern reconfigurable antenna using metasurface. *IET Microw Antennas Propag.* (2015) **9**:1331–6. doi: 10.1049/iet-map.2014.0676
23. Holloway CL, Kuester EF, Gordon JA, O'Hara J, Booth J, Smith DR. An overview of the theory and applications of metasurfaces: the two-dimensional equivalents of metamaterials. *IEEE Antennas Propag Mag.* (2012) **54**:10–35. doi: 10.1109/MAP.2012.6230714
24. Chen XF, Zhao YJ. Dual-band polarization and frequency reconfigurable antenna using double layer metasurface. *AEU Int J Electron C.* (2018) **95**:82–7. doi: 10.1016/j.aeue.2018.08.001
25. Kandasamy K, Majumder B, Mukherjee J, Ray KP. Low RCS and polarization reconfigurable antenna using cross-slot-based metasurface. *IEEE Antennas Wireless Propag Lett.* (2015) **14**:1638–41. doi: 10.1109/LAWP.2015.2415585
26. Liu SH, Yang DQ, Pan T. A low-profile circularly polarized metasurface antenna with wide axial-ratio beamwidth. *IEEE Antennas Wireless Propag Lett.* (2019) **18**:1438–42. doi: 10.1109/LAWP.2019.2938873
27. Marcuvitz N. *Waveguide Handbook*. Lexington, MA: Boston Technical (1964).
28. Fan Y, Wang JF, Li YF, Zhang JQ, Han YJ, Qu SB. Low-RCS and high-gain circularly polarized metasurface antenna. *IEEE Trans Antennas Propag.* (2019) **67**:7197–203. doi: 10.1109/TAP.2019.2920355
29. Li K, Liu Y, Jia YT, Guo YJ. A circularly polarized high-gain antenna with low RCS over a wideband using chessboard polarization conversion metasurfaces. *IEEE Trans Antennas Propag.* (2017) **67**:4288–92. doi: 10.1109/TAP.2017.2710231
30. Hu J, Luo GQ, Hao ZC. A wideband quad-polarization reconfigurable metasurface antenna. *IEEE Access.* (2018) **6**:6130–7. doi: 10.1109/ACCESS.2017.2766231
31. Zhu HL, Cheung SW, Yuk TI. Design of polarization reconfigurable antenna using metasurface. *IEEE Trans. Antennas Propag.* (2014) **62**:2891–98. doi: 10.1109/TAP.2014.2310209

Conflict of Interest: The authors declare that the research was conducted in the absence of any commercial or financial relationships that could be construed as a potential conflict of interest.

ORIGINAL RESEARCH
published: 26 August 2020
doi: 10.3389/fphy.2020.00334

Terahertz Nonreciprocal Isolator Based on Magneto-Plasmon and Destructive Interference at Room Temperature

Yunyun Ji[1,2], *Fei Fan*[1,2*], *Zhiyu Tan*[1,3] *and Shengjiang Chang*[1,3*]

[1] Institute of Modern Optics, Nankai University, Tianjin, China, [2] Tianjin Key Laboratory of Optoelectronic Sensor and Sensing Network Technology, Tianjin, China, [3] Tianjin Key Laboratory of Micro-Scale Optical Information Science and Technology, Tianjin, China

A terahertz isolator is demonstrated for the THz nonreciprocal reflections in the magneto-optical microstructure composed of InSb and metasurface with a dielectric interlayer. In the Voigt magnetic field configuration, the reflectance of the *p*-polarization waves obliquely impinging on the InSb wafer exhibits high nonreciprocity, while the reflectance of the *s*-polarized wave is reciprocal. Based on the unique magneto-plasmonic modes on the InSb surface, the nonreciprocal reflection in this device can be enhanced by using the destructive interference between the direct reflection and the multiple reflections in the resonance cavity between the InSb and metasurface. After the optimization, the isolation power of the device exceeds 55 dB with the insertion loss of only −3.92 dB under a very weak magnetic field of 0.2 T at room temperature. More importantly, the introduction of the metasurface can reduce the operating frequency of the isolator from 2.434 to 2.136 THz. This low-loss, weak magnetic field, room temperature operating, and high isolation THz isolator shows its broad potential in THz application systems.

Keywords: terahertz, isolators, magneto-optical device, metamaterials, surface plasmon

OPEN ACCESS

Edited by:
Lin Chen,
University of Shanghai for Science and Technology, China

Reviewed by:
Shen Xiaopeng,
China University of Mining and Technology, China
Jinhui Shi,
Harbin Engineering University, China

****Correspondence:***
Fei Fan
fanfei_gdz@126.com
Shengjiang Chang
sjchang@nankai.edu.cn

Specialty section:
This article was submitted to Optics and Photonics, a section of the journal Frontiers in Physics

Received: *13 February 2020*
Accepted: *20 July 2020*
Published: *26 August 2020*

Citation:
Ji Y, Fan F, Tan Z and Chang S (2020) Terahertz Nonreciprocal Isolator Based on Magneto-Plasmon and Destructive Interference at Room Temperature. Front. Phys. 8:334. doi: 10.3389/fphy.2020.00334

INTRODUCTION

The rapid development of terahertz (THz) science and technology has a high impact on fundamental science and practical applications, such as security, imaging, spectroscopy, and wireless communications, among others [1–4]. As the high-power THz sources and high-sensitive detectors develop rapidly, high-performance THz functional devices are also crucial to the further development of THz applications, such as modulator [5], filter [6], absorber [7], polarizer [8], and isolator [9], which can control and modulate THz waves in an efficient way. Among these devices, high-performance THz isolators are still in an urgent demand due to the lack of THz magneto-optic (MO) materials and the limitation of device fabrication. An isolator is a nonreciprocal device that allows light propagation in one direction and prevents the back-reflected light from passing in the opposite direction, which plays a crucial role in source protection, impedance matching, and noise-canceling [10, 11].

The ferrite isolators based on different nonreciprocal phenomena at the microwave regime, such as resonance absorption, Faraday rotation, and field displacement, have been implemented in many different media [12]. At visible and infrared wavelengths, the optical isolator typically relies on the Faraday effect and a pair of polarizers with relative 45° orientations to prevent the back-reflected beam from reaching the laser source [13]. However, both methods of using ferrite isolators at microwave frequencies and Faraday isolators at the infrared regime are inappropriate for THz frequencies, so the THz nonreciprocal transmission principles still need to be investigated more deeply. Recently, some materials have been explored as a suitable Faraday medium, such as high-mobility semiconductors [14, 15], graphene [16, 17], ferrofluids [18], and magnetic materials [10]. For example, Tamagnone et al. demonstrated a high-performance isolator based on graphene with the isolation of 18 dB and the insertion loss of 7.5 dB in an applied magnetic field of 7 T [17]. In 2017, Poumirol et al. observed the strong magneto-plasmonic resonances in continuous and patterned graphene at 250 K and 7 T, the magnetic circular dichroism and Faraday rotation can be modulated in intensity and tuned in frequency [19]. In 2018, Lin et al. reported a nonreciprocal THz reflective optical isolator of InSb with the Voigt MO configuration, and the isolation power of the device exceeds 35 dB with the insertion loss of only −6.2 dB [20]. Nevertheless, the present THz isolators are still limited to the large insertion loss, extremely high magnetic field, and low-temperature condition.

Recently, the introduction of MO materials into artificial microstructures provides a new strategy for the development of high-performance tunable THz MO devices. For example, Tan et al. developed a magnetically tunable gyrotropic P-B metasurface, which can obtain a broadband working frequency of 1.02–1.7 THz with the sweeping deflection angle from 36.6 to 83.5° and realize a nonreciprocal absorption with the isolation of 24 dB [21]. Li et al. investigated the THz faraday rotation of magneto-optical films enhanced by helical metasurface, the Faraday effect of the YIG metasurface is about three times that of the pure YIG film [22]. Moreover, the nonreciprocal dispersion of surface magneto-plasmons has been proposed for the one-way THz devices. Hu et al. proposed a one-way device based on nonreciprocal surface magneto plasmons, and the one-way-propagating frequency band can be broadly tuned by the external magnetic fields, which can be used to realize various high performance tunable plasmonic devices such as isolators, switches, and splitters [23]. Besides, some preliminary theoretical works for THz isolators have employed MO metasurfaces. Chen et al. have reported some THz nonreciprocal devices based on magneto microstructures composed of InSb to achieve high isolation ratio of over 40 dB [24]. Fan et al. proposed a THz nonreciprocal isolator based on a magneto-optical microstructure, where the nonreciprocal transmission of the InSb film is converted and enhanced by a pair of orthogonal artificial birefringence gratings, and the isolation reaches 24 dB with the insertion loss is <0.5 dB at room temperature and a low magnetic field [25]. But most of the reports show that the performance of MO isolators still needs to be improved in isolation, insertion loss, and operating frequency at room temperature.

In this paper, we introduce THz MO material into the artificial microstructure to form a resonance cavity between the InSb and metasurface, which realizes a THz reflective isolator in the Voigt MO configuration at room temperature. The unique nonreciprocal magneto-plasmonic properties of InSb/dielectric interface is demonstrated for the THz nonreciprocal reflections, and it can be enhanced by using the destructive interference between the direct reflection and the following multiple reflections in the resonance cavity between the InSb and metasurface. The results show that a high-performance THz optical isolator is achieved in the proposed MO microstructure at 2.136 THz, and the isolation power of the device exceeds 55 dB with the insertion loss of −3.92 dB under a weak magnetic field of 0.2 T at room temperature of 300 K.

RESULTS AND DISCUSSIONS

Magneto-Optical Property of InSb in the THz Regime

The MO material in this work is the InSb that possesses a temperature-tunable charge carrier density and high electron mobility [26]. When the biased magnetic field B is applied parallel to the InSb surface along the y direction, the dielectric function of InSb becomes a nonreciprocal tensor, which can be described by Han et al. [27], Fan et al. [9], and Chen et al. [24].

$$\begin{bmatrix} \varepsilon_{xx} & 0 & \varepsilon_{xz} \\ 0 & \varepsilon_{yy} & 0 \\ \varepsilon_{zx} & 0 & \varepsilon_{zz} \end{bmatrix} \tag{1}$$

where three different tensor components can be expressed as: [28, 29]

$$\begin{aligned} \varepsilon_{xx} = \varepsilon_{zz} &= \varepsilon_{\infty} - \frac{\omega_p^2\left(\omega^2 + i\gamma\omega\right)}{\left(\omega^2 + i\gamma\omega\right)^2 - \omega^2\omega_c^2} + \varepsilon_{ph}, \\ \varepsilon_{yy} &= \varepsilon_{\infty} - \frac{\omega_p^2}{\omega^2 + i\gamma\omega} + \varepsilon_{ph}, \\ \varepsilon_{zx} = -\varepsilon_{xz} &= \frac{i\omega_p^2\omega\omega_c}{\left(\omega^2 + i\gamma\omega\right)^2 - \omega^2\omega_c^2}, \\ \varepsilon_{ph} &= \varepsilon_{\infty}\left(\frac{\omega_t^2 - \omega_l^2}{\omega_t^2 - \omega^2 - i\gamma_{ph}\omega}\right) \end{aligned} \tag{2}$$

where $\varepsilon_{\infty} = 15.68$ is the high-frequency limit permittivity, and the cyclotron frequency ω_c is proportional to the magnetic field B by $\omega_c = eB/m^*$, where B is the magnetic flux density, e is the electron charge, m^* is the effective mass of the carrier, $m^* = 0.014\ m_e$, and m_e is the mass of electron. $\gamma = e/(\mu m^*)$ is the collision frequency of carriers, where μ is the carrier mobility, $\mu = 7.7 \times 10^4\ (T/300)^{-1.66}\ \mathrm{cm}^2 \cdot \mathrm{V}^{-1} \cdot \mathrm{s}^{-1}$ [30, 31]. ω_p is the plasma frequency, defined as $\omega_p = (Ne^2/\varepsilon_0 m^*)^{1/2}$, where ε_0 is the free-space permittivity; N is the carrier density, and the N strongly depends on the temperature T, which follows [32, 33]

$$\begin{aligned} N\left(cm^{-3}\right) &= 2.9\times10^{11}\,(2400-T)^{3/4}\left(1+2.7\times10^{-4}T\right)T^{3/2} \\ &\quad \times\exp\left[-\left(0.129 - 1.5\times10^{-4}T\right)/\left(k_bT\right)\right] \end{aligned} \tag{3}$$

where $k_b = 8.625 \times 10^{-5}$ eV/K is the Boltzmann constant. ε_{ph} is the phonon contribution to the dielectric function, where $\gamma_{\mathrm{ph}} = 3.77$ THz is the phonon damping rate, the transverse and longitudinal optical phonon frequencies are ω_t and ω_l, respectively, and $\omega_t/2\pi = 5.90$ THz, $\omega_l/2\pi = 5.54$ THz [15]. Therefore, the dielectric property of the InSb greatly depends on the magnetic field B and the temperature T. Under a weak magnetic field, the spin magnetic moment of free carrier in InSb will strongly couple with the external magnetic field, which forms the magnetized plasma with its cyclotron resonance frequency ω_c just falling in the THz band.

Nonreciprocal Reflectance of InSb Based on Magneto-Plasmonics

Firstly, we investigate the nonreciprocal of reflectance for the pure InSb at room temperature, and its schematic design is displayed in **Figure 1A**. THz waves are incident obliquely in the x–z plane on the devices with the linear p-polarization (i.e., THz electric field in the x–z plane), and an external magnetic field is applied in the Voigt geometry along the y axis. The Maxwell's equations and the continuity conditions for the fields $\overrightarrow{E}$ and $\overrightarrow{D}$ can be used to calculate the reflected THz amplitude at the air/InSb interface. The amplitude reflection coefficients r_p and r_s of the p- and s-polarized waves at the air/InSb interface can be expressed as follows [34], and the detailed derivation process can be found in **Supplementary Material**:

$$r_p = \frac{\kappa\varepsilon_{xx} + \varepsilon_{xz}\sin\alpha + \left(\varepsilon_{xx}^2 + \varepsilon_{xz}^2\right)\cos\alpha}{\kappa\varepsilon_{xx} + \varepsilon_{xz}\sin\alpha - \left(\varepsilon_{xx}^2 + \varepsilon_{xz}^2\right)\cos\alpha} \tag{4}$$

$$r_s = \frac{\cos\alpha - \sqrt{\varepsilon_{yy}}\cos\alpha_s{}'}{\cos\alpha + \sqrt{\varepsilon_{yy}}\cos\alpha_s{}'} \tag{5}$$

where α is the oblique incidence angle to the air/InSb interface (**Figure 1A**), α_s' is the refracted angle inside InSb given by Snell's law $\sin\alpha = \sqrt{\varepsilon_{yy}}\sin\alpha_s'$. The refracted angle α_p' in the p-polarization is different from α_s' and is given by the wave vector $k = (\omega/c)(\sin\alpha,\ 0,\ \kappa)$, where $\kappa = -\sqrt{\frac{(\varepsilon_{xx}^2+\varepsilon_{xz}^2)}{\varepsilon_{xx}} - \sin^2\alpha}$. Therefore, the magneto-optical property of the InSb wafer at room temperature depends not only on the external magnetic field but also strongly on the incident angle. According to Equations (2) and (4), the complex reflection coefficient r_p of the p-polarized wave are different for positive and negative angles α, resulting in a nonreciprocal reflection in the forward and backward directions, $r_p(+\alpha) \neq r_p(-\alpha)$, as shown in **Figure 1B**. Here, the difference between $r_p(+\alpha)$ and $r_p(-\alpha)$ is benefit from the difference is benefit from the nonreciprocity of the excited magneto-plasmonic mode, this nonreciprocity causes the coupling frequency of the forward and backward transmitted waves and the magneto-plasmonic to be different, one at high frequency and the other at low frequency, thus the coupling frequency splits. In fact, the degree of splitting is determined by the magnetic resonance frequency, which is proportional to the external magnetic field. Note that the reflectance of the s-polarized wave is reciprocal, according to Equation (5).

We theoretically calculated the forward reflectance $R(+\alpha) = -20 \times \log\left[r_p(+\alpha)\right]$ and the backward reflectance $R(-\alpha) = -20 \times \log\left[r_p(-\alpha)\right]$ with the external magnetic field increases from 0 to 0.4 T when the oblique incidence angle $\alpha = 60$, as shown in **Figures 2A,C** by using Equations (2–4). In the absence of an external magnetic field, $\varepsilon_{zx} = -\varepsilon_{xz} = 0$ and $\varepsilon_{xx} = \varepsilon_{yy}$, which leads to a reciprocal reflection $R(+\alpha) = R(-\alpha)$ on the air/InSb interface. When the external magnetic field is applied, the incident THz waves are strongly resonant with the magnetized plasma on the surface of InSb, forming the magneto-plasmonic mode. This surface mode is localized on the dielectric/InSb interface and the incident THz waves cannot be reflected, so some dark blue regions occur in **Figures 2A–D**, which just correspond to the very low reflection of the magneto-plasmonic mode. More importantly, as the external magnetic field increases, this mode splits: the resonance mode of forward

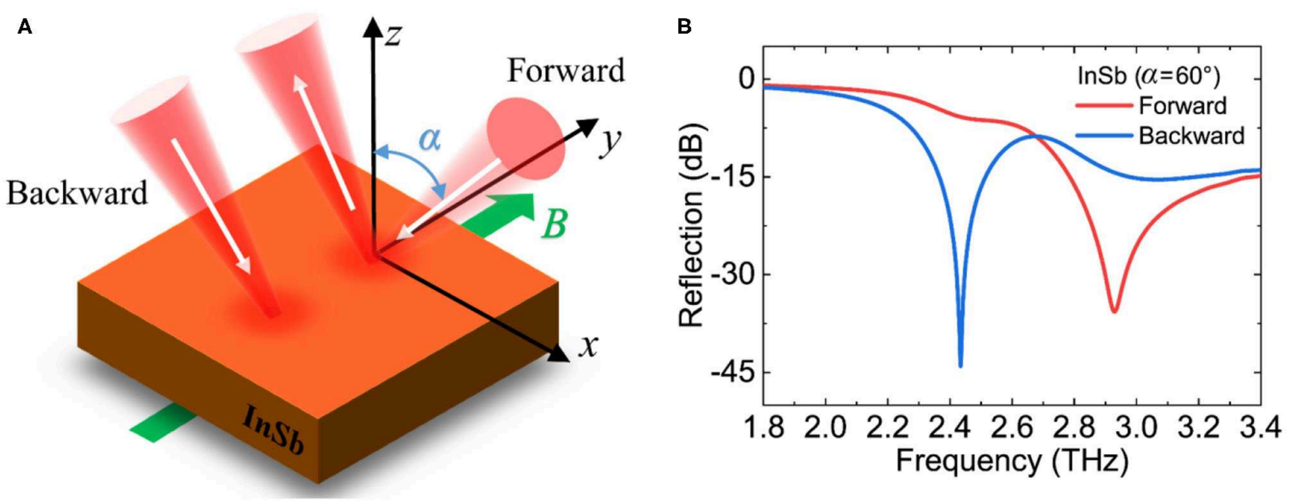

FIGURE 1 | (A) Schematic diagram of the THz optical isolator for the InSb wafer with magnetic field along the y axis. A THz beam is incident in the x–z plane with the incident angle of α and is p-polarized. **(B)** The reflection spectrum of the forward wave and backward wave when $\alpha = 60°$ and $B = 0.2$ T.

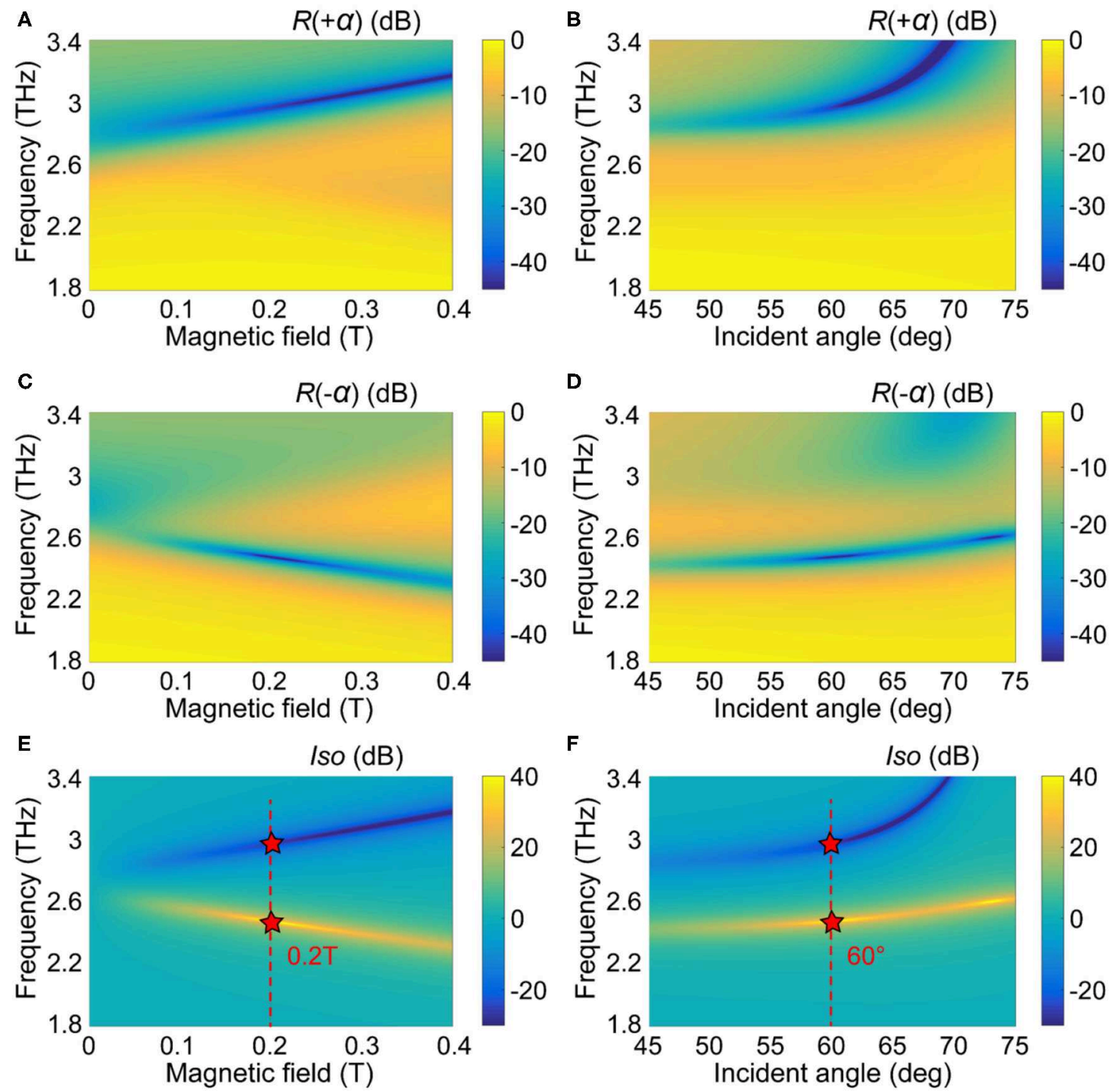

FIGURE 2 | The calculated reflections of the forward $R\,(+\alpha)$ **(A)** and backward wave $R\,(-\alpha)$ **(C)**, and the isolation *Iso* **(E)** for the InSb wafer with the different external magnetic fields at room temperature of 300 K when $\alpha = 60^\circ$. The calculated reflections of the forward $R\,(+\alpha)$ **(B)** and backward wave $R\,(-\alpha)$ **(D)**, and the calculated isolation *Iso* **(F)** for the InSb wafer with the different incident angles at room temperature when $B = 0.2\,\mathrm{T}$.

reflection gradually moves to the higher frequency, while the resonance mode of the backward reflection gradually moves to the lower frequency. A huge difference $R\,(+\alpha) \neq R\,(-\alpha)$ happens in the resonance frequency band at a certain magnetic field, which means a strong nonreciprocal reflection in the forward and backward directions defined as the isolation $Iso = R\,(+\alpha) - R\,(-\alpha)$. Two different isolation bands for forward (yellow region) and backward (dark blue region) reflections are shown in **Figure 2E**, and the maximum isolation can be obtained under an external magnetic field of 0.2 T. Moreover, the forward reflectance, the backward reflectance and the isolation with the increase of the incident angle from 45 to 75° are shown in **Figures 2B,D,F**, when the external magnetic field is fixed at 0.2 T. The resonance and isolation peaks of the forward and the backward reflections gradually move to the high frequency.

The two key performance parameters of the isolator need to be pointed out: one is the insertion loss, which depends on the reflectance of the forward or backward beam; the other is the isolation between the forward reflectance and backward reflectance. A relatively large isolation can be achieved in **Figure 2F** with the incident angle of around 60 or 73°. Here, we choose the optimized incident angle of 60° with the comprehensive consideration of the insertion loss and isolation. The simulation results from CST simulation shown in **Figure 1B** indicate that a nonreciprocal reflection can be obtained in the InSb with the optimized oblique incident angle of 60° under

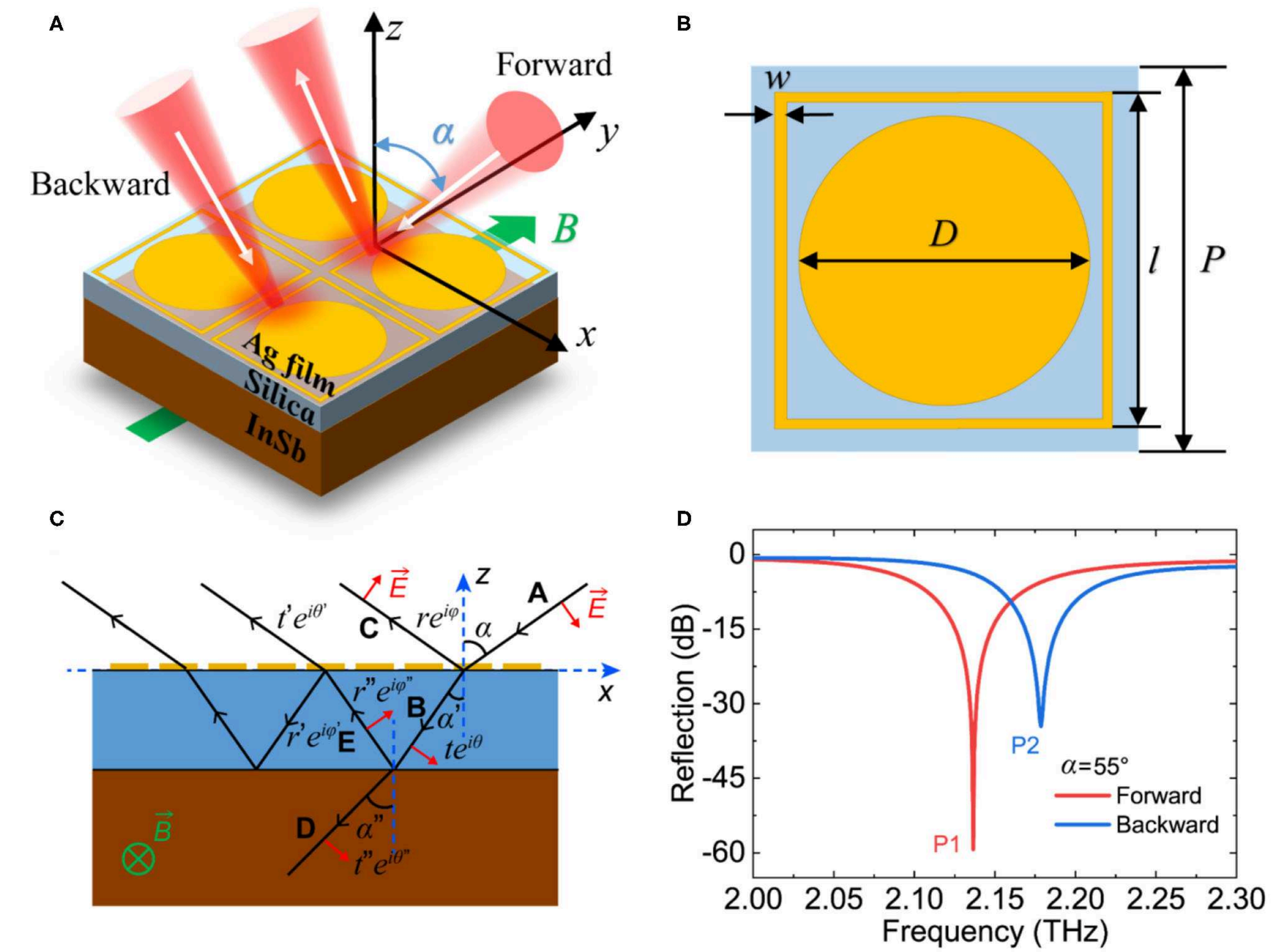

FIGURE 3 | **(A)** Schematic diagram of the proposed THz optical isolator for the InSb with metasurface. **(B)** The geometry of the unit cell metasurface, $P = 60\,\mu$m, $l = 57\,\mu$m, $w = 2\,\mu$m and $D = 49\,\mu$m. **(C)** Multiple reflections and interference model of the proposed THz optical isolator for the InSb with metasurface. **(D)** The reflection spectrum of the forward wave and backward wave when $\alpha = 55°$ and $B = 0.2$ T.

a weak magnetic field of 0.2 T: the reflectance in the forward direction is high, and the backward traveling beam is absorbed by InSb, so that the reflectance in the backward direction is almost zero. At 2.434 THz, the isolation is $Iso = R(+\alpha) - R(-\alpha) = 38.2$ dB and the insertion loss $R(+\alpha) = -5.8$ dB. Moreover, the isolation at 2.929 THz is $Iso = R(-\alpha) - R(+\alpha) = 21.4$ dB with the insertion loss $R(-\alpha) = -14.3$ dB.

Nonreciprocal Reflectance of MO Microstructure by Combining InSb With Metasurface

Furthermore, we designed a THz optical isolator by combining InSb with metasurface, the magnetic field is applied along the y axis in the Voigt geometry, and the linear p-polarized THz wave is incident on the MO microstructure at a certain oblique incident angle α to achieve a nonreciprocal reflection, as shown in **Figure 3A**. A periodically patterned metasurface with a thickness of 200 nm is coated on the silica spacer layer with a thickness of $d = 50\,\mu$m. The unit cell of the patterned metasurface is labeled in **Figure 3B**, and the unit cell period $P = 60\,\mu$m along the x and y axis. The outside length of the square ring is $l = 57\,\mu$m with the width is $w = 2\,\mu$m. The diameter of the inner ring is $D = 49\,\mu$m. The bottom layer is the InSb wafer substrate with a thickness of 500 μm.

As depicted in **Figure 3C**, the model contains two interfaces: the top air/metasurface interface and back dielectric/InSb interface. A plane wave incident upon the isolator at angle α. At the air/metasurface interface, the incident wave is divided into two parts, one of which is reflected into the air with a reflection coefficient $\tilde{r} = re^{i\phi}$, and the other transmits into the spacer with a transmission coefficient $\tilde{t} = te^{i\theta}$. The latter continues to propagate until it reaches the dielectric/InSb interface, with a complex propagation constant $\beta = -k_0\sqrt{\varepsilon_r}h/\cos\alpha'$, where k_0 is the wave vector in free space. Then the wave is transmitted to the dielectric/InSb interface at angle α', which partially reflects back to the dielectric with a reflection coefficient $\tilde{r}'' = r''e^{i\phi''}$ and

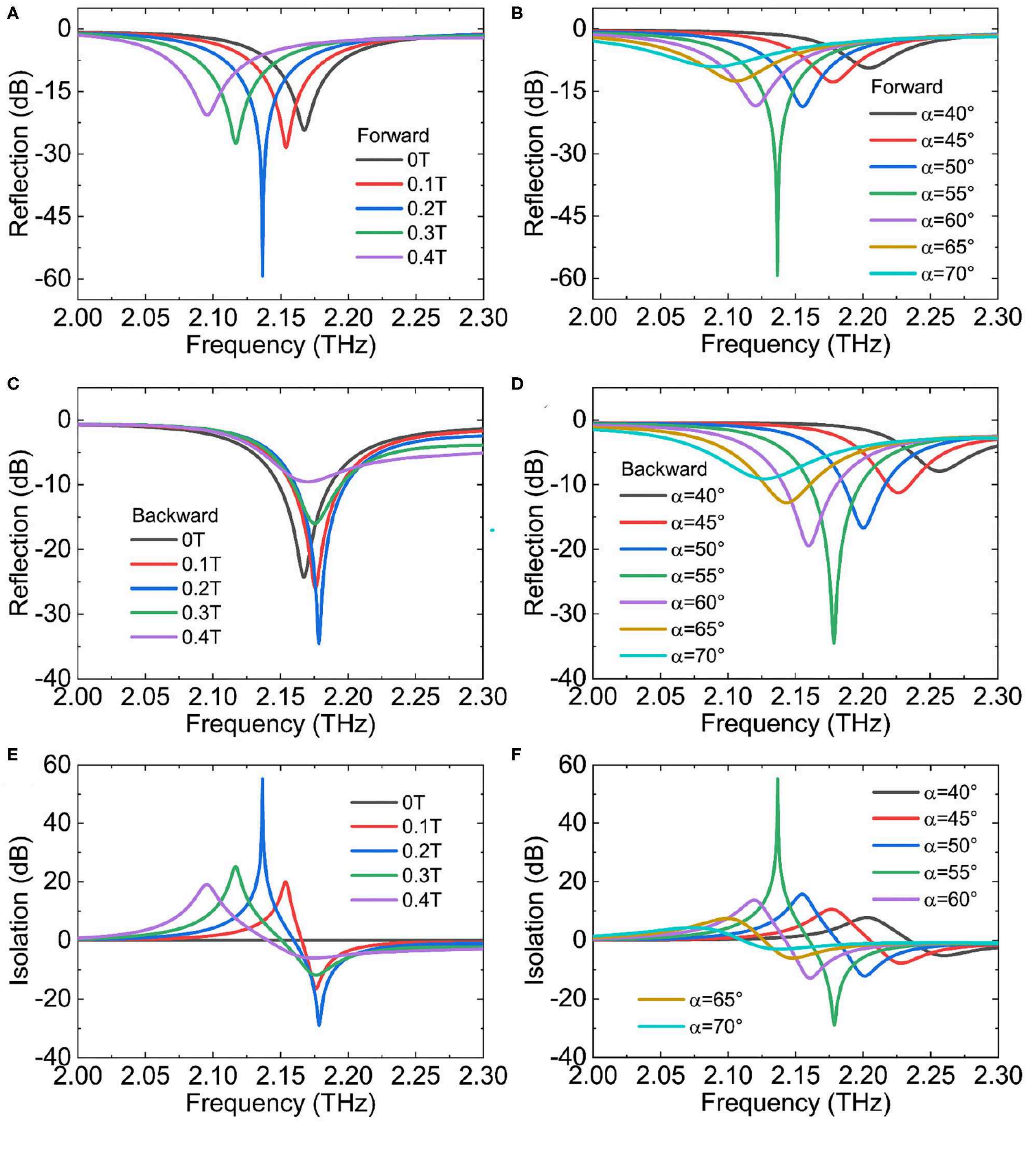

FIGURE 4 | (A) Reflection spectra of the forward waves, **(C)** reflection spectra of the backward waves and **(E)** isolation spectra under the different external magnetic fields when $\alpha = 55°$ at room temperature. **(B)** Reflection spectra of the forward waves, **(D)** reflection spectra of the backward waves and **(F)** isolation spectra under the different incident angles when $B = 0.2\,T$.

partially transmits into the InSb with a transmission coefficient $\tilde{t}'' = t''e^{i\theta''}$. After that, the reflected wave occurs again at the air/metasurface interface with coefficients $\tilde{r}' = r'e^{i\varphi'}$ and $\tilde{t}' = t'e^{i\theta'}$. The overall reflection is the superposition of the multiple reflections and transmissions at the two interfaces: [35]

$$\tilde{r} = \frac{re^{i\phi} - rr'r''e^{i(\varphi+\varphi'+\varphi''+2\beta)} + tt'r''e^{i\left(\theta+\theta'+\varphi''+2\beta\right)}}{1 - r'r''e^{i(\varphi'+\varphi''+2\beta)}} \tag{6}$$

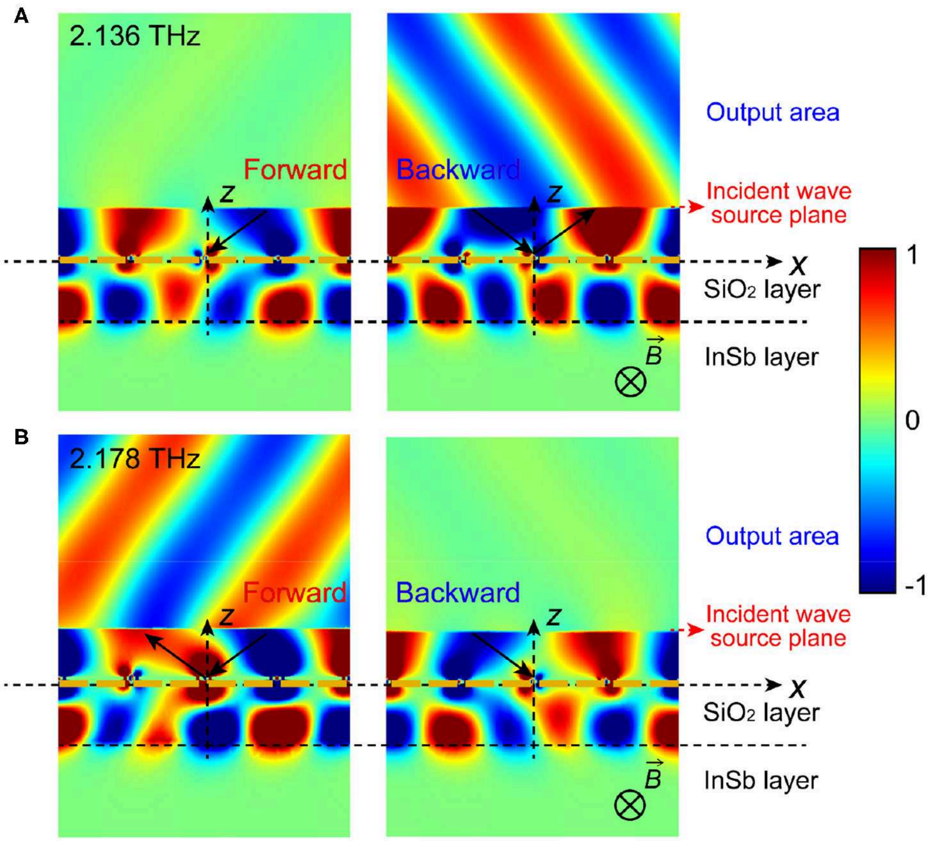

FIGURE 5 | The schematic diagrams of the proposed THz optical isolator when $\alpha = 55°$ and $B = 0.2$ T at room temperature and the near field distribution of the E_x component: the forward wave experiences negligible reflectance and the backward wave experiences high reflectance at 2.136 THz **(A)**; or the forward wave experiences high reflectance and the backward wave experiences negligible reflectance at 2.178 THz **(B)**.

where the reflection coefficient $\mathbf{r}''$ at the dielectric/InSb interface can also be derived by the Maxwell's equations and the continuity conditions for the fields $\vec{E}$ and $\vec{D}$ [34]. We then calculate the amplitude reflection coefficients r_p'' and r_s'' of the p- and s-polarized waves at the dielectric/InSb interface as follows, and the detailed derivation process can be found in Supplementary Material:

$$r_p'' = \frac{\sqrt{\varepsilon_r}\kappa\varepsilon_{xx} + \varepsilon_r\varepsilon_{xz}\sin\alpha' + \left(\varepsilon_{xx}^2 + \varepsilon_{xz}^2\right)\cos\alpha'}{\sqrt{\varepsilon_r}\kappa\varepsilon_{xx} + \varepsilon_r\varepsilon_{xz}\sin\alpha' - \left(\varepsilon_{xx}^2 + \varepsilon_{xz}^2\right)\cos\alpha'} \tag{7}$$

$$r_s'' = \frac{\sqrt{\varepsilon_r}\cos\alpha_s{}' - \sqrt{\varepsilon_{yy}}\cos\alpha_s{}''}{\sqrt{\varepsilon_r}\cos\alpha_s{}' + \sqrt{\varepsilon_{yy}}\cos\alpha_s{}''} \tag{8}$$

where α' is the incidence angle to the dielectric/InSb interface (**Figure 3C**), α_s'' is the refracted angle inside InSb given by Snell's law $\sqrt{\varepsilon_r}\sin\alpha_s' = \sqrt{\varepsilon_{yy}}\sin\alpha_s''$. The refracted angle α_p'' in the p-polarization is different from α_s'' and is given by the wave vector $k = (\omega/c)(\sin\alpha,\ 0,\ \kappa)$, where $\kappa = -\sqrt{\frac{(\varepsilon_{xx}^2+\varepsilon_{xz}^2)}{\varepsilon_{xx}} - \varepsilon_r\sin^2\alpha}$.

On account of the nonreciprocal dispersion of the magneto-plasmonic modes, the amplitude reflection coefficients $r_\mathbf{p}''$ for the p-polarized wave at the dielectric/InSb interface has the nonreciprocal effect (Equation 7), which further leads to an overall nonreciprocal reflection $\tilde{r}$ that superimposed of the multiple reflections and transmissions at the two interfaces (Equation 6). While the reflection coefficients r_s'' for the s-polarized wave at the dielectric/InSb interface is reciprocal (Equation 8), and the overall reflection $\tilde{r}$ is reciprocal accordingly. The metallic metasurface and the InSb substrate form a resonance cavity to generate the multiple reflections between the two interfaces, and a destructive interference occurs between the direct reflection and the following multiple reflections when the amplitude and phase meet the matching conditions, so that a sharper resonance peak can be achieved in the reflection spectrum. The localization effect between metasurface and InSb enhances the nonreciprocal magneto-plasmonic modes on the InSb surface. Compared to pure InSb, the performance of the MO microstructure is improved with a lower operating frequency, a greater isolation, and a lower insertion loss, as shown in **Figure 3D**.

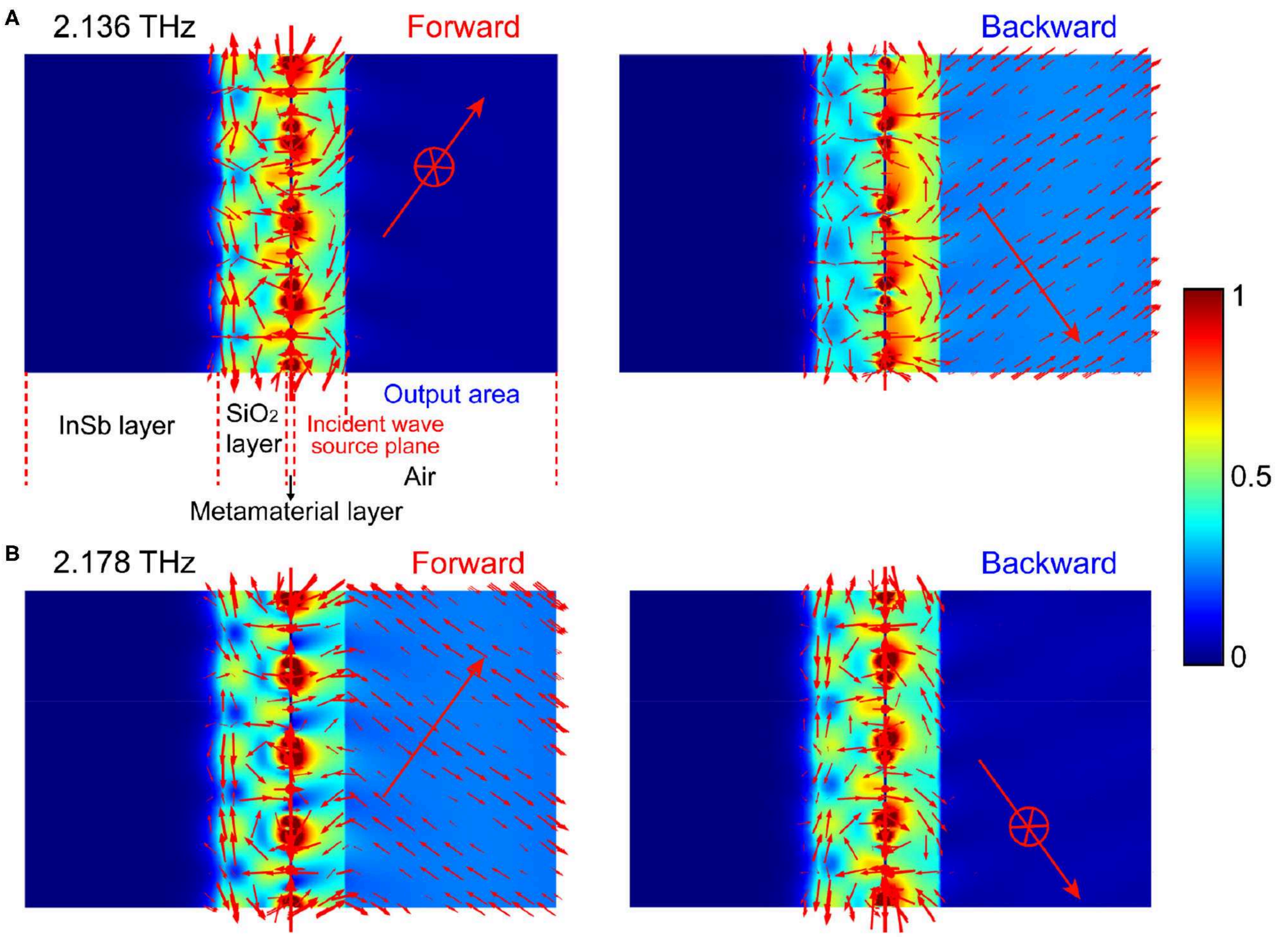

FIGURE 6 | The electric field (color) and the magnetic field (arrows) distributions of the proposed THz optical isolator when $\alpha = 55°$ and $B = 0.2\,\mathrm{T}$ at different frequencies: $f = 2.136$ THz **(A)** and $f = 2.178$ THz **(B)**. THz waves are incident from the source plane to the MO microstructure (i.e., to the left), and then reflected by the MO microstructure. The reflected wave finally enters the air on the right side. The left side of the source plane is the total field distribution, including the incident field and the reflected field. The right side of the source plane is the pure reflected field distribution.

Similarly, we discuss the influence of the external magnetic field and the incident angle. Firstly, the incident angle is fixed at $\alpha = 55°$, when the external magnetic field $B = 0\,\mathrm{T}$, the resonance peaks of the forward and the backward reflections are completely coincident, which means that the reflection exhibits reciprocal characteristics at this time. With the increase of the external magnetic field from 0 to 0.4 T, the resonance peak for the forward reflection gradually moves to the low frequency, as shown in **Figure 4A**. Meanwhile, the resonance peak for the backward reflection slightly moves to the high frequency, as shown in **Figure 4C**. Hence, the MO microstructure shows a nonreciprocal reflection, and the maximum isolation can be obtained under an external magnetic field of 0.2 T, as shown in **Figure 4E**. Then, we fixed the external magnetic field at 0.2 T, and the forward reflectance $R(+\alpha)$, the backward reflectance $R(-\alpha)$ and the isolation Iso as the incident angle increases from 40 to 70° are shown in **Figures 4B,D,F**. The results show that the resonance peaks for both the forward and the backward reflection gradually move to the low frequency, thus the isolation peaks gradually move to the low frequency. The maximum isolation can be achieved with an optimized incident angle of 55°. In this case, the isolation in 2.136 THz can be up to $Iso = R(+\alpha) - R(-\alpha) = 55.38$ dB with the insertion loss of $R(+\alpha) = -3.92$ dB. Besides, the isolation at 2.178 THz is $Iso = R(-\alpha) - R(+\alpha) = 28.94$ dB with the insertion loss of $R(-\alpha) = -5.58$ dB. It can be clearly seen that the MO microstructure based on InSb and metasurface has higher isolation and lower insertion loss than that of pure InSb, and its operating frequency to achieve nonreciprocal isolation is also reduced.

The near field distributions of forward and backward reflections are simulated to verify the nonreciprocal reflecting status of the MO microstructure by the FEM method from COMSOL. At 2.136 THz, the isolator only allows backward reflected light to pass through, and prohibits forward reflected light, as shown in **Figure 5A**. On the contrary, the isolator at 2.178 THz only allows forward reflected light to pass through, and prohibits backward reflected light, as shown in **Figure 5B**. The electric field distribution of the E_x component demonstrates the nonreciprocal reflection characteristics of the isolator, and the reflected angle is 55° in this case, as shown in **Figure 5**. It is worth mentioning here that the *p*-polarized reflected wave has not only the electric field of the E_x component but also the E_z component, and the electric field of the E_z component has similar distribution characteristics with the E_x component.

As previously mentioned, the occurrence of the resonance peak in the reflection spectrum is due to the destructive interference between the direct reflection and the following multiple reflections. Consequently, the resonance peak of the forward reflection is not at the same frequency as the backward reflection, thereby realizing a nonreciprocal isolation. This can be confirmed by the electric field patterns for the cutting plane and the spatial magnetic field distributions simulated in **Figure 6**. At 2.136 THz, for the forward wave, the electric field is mainly distributed at the interface of the metasurface and the dielectric layer between the metasurface and InSb, and the reflectance can be practically zero, indicating that the destructive interference occurs between the direct reflection at the metasurface/dielectric interface and the following multiple reflections. Hence, the wave can be effectively trapped in the cavity between the metasurface and InSb and the high absorption is achieved eventually. However, most of the waves are reflected at the metasurface/dielectric interface for the backward wave, whereas only a small part of the waves enters the dielectric layer, and the direct reflection and the following multiple reflections do not meet the conditions of destructive interference, consequently, the MO microstructure exhibits high reflectance, as shown in **Figure 6A**. On the contrary, at 2.178 THz, the destructive interference occurs in the backward wave, giving rise to a high absorption and a negligible reflectance, which is almost the same as the above case of the forward wave. Nevertheless, for the backward wave, although most of the waves enter the dielectric layer, the direct reflection and the following multiple reflections do not meet the conditions of destructive interference, which makes the MO microstructure exhibit high reflectance (**Figure 6B**).

Recently, some THz isolators about chiral metamaterials have been reported [36, 37], the high-performance asymmetric transmission has been theoretically and experimentally demonstrated in bilayer chiral metamaterial, and the anisotropy and chirality of the metamaterial give rise to cross-polarization conversion. Although the reciprocal transmission device can achieve an asymmetrical one-way transmission when the light of the same polarization state is incident on the device in forward and backward directions, it cannot be used as an isolator. In contrast, the device in our work relies on the nonreciprocal characteristic of MO materials, and the MO non-reciprocal device can realize the function of one-way isolation transmission.

CONCLUSIONS

In summary, we explored the nonreciprocal reflectance of MO microstructure in the applied magnetic field in the Voigt geometry. The InSb magnetized by an applied magnetic field in the Voigt geometry has unique nonreciprocal magneto-plasmonic modes in the THz regime. On this bases, we introduce a resonant cavity between the InSb and metasurface, which is used to cause destructive interference between the direct reflection and the following multiple reflections, and eventually causes the high absorption, thereby generating a nonreciprocal strong resonance peak in the reflection spectrum and thus achieving a high-performance THz isolator. At the optimal incidence angle (55°) and the weak applied magnetic field (0.2 T) at room temperature, the isolation exceeds 55 dB, and the insertion loss is only −3.92 dB at 2.136 THz, which is significantly improved compared to the pure InSb. This nonreciprocal reflection mechanism and device structures can promote the development of THz isolators toward working at room temperature and low magnetic field with lower insertion loss and higher isolation.

DATA AVAILABILITY STATEMENT

All datasets generated for this study are included in the article/supplementary material.

AUTHOR CONTRIBUTIONS

YJ and FF designed the proposed structure of the isolator, performed the simulations and theoretical calculations as well as the results analysis. YJ carried out the writing of the paper. FF and SC provided the guideline of the research and modified the language of the manuscript. ZT helped to finish the simulations. All authors read and approved the final manuscript.

FUNDING

This work was supported by National Key Research and Development Program of China (2017YFA0701000); National Natural Science Foundation of China (61831012 and 61971242); Natural Science Foundation of Tianjin City (19JCYBJC16600); Young Elite Scientists Sponsorship Program by Tianjin (TJSQNTJ-2017-12).

SUPPLEMENTARY MATERIAL

The Supplementary Material for this article can be found online at: https://www.frontiersin.org/articles/10.3389/fphy.2020.00334/full#supplementary-material

REFERENCES

1. Ho L, Pepper M, Taday P. Terahertz spectroscopy: signatures and fingerprints. *Nat Photonics.* (2008) **2**:541–3. doi: 10.1038/nphoton.2008.174

2. Cooper KB, Dengler RJ, Llombart N, Thomas B, Chattopadhyay G, Siegel PH. THz imaging radar for standoff personnel screening. *IEEE Trans Terah Sci Tech.* (2011) **1**:169–82. doi: 10.1109/TTHZ.2011.2159556

3. Kleine-Ostmann T, Nagatsuma T. A review on terahertz communications research. *J Infrared Millim Te.* (2011) **32**:143–71. doi: 10.1007/s10762-010-9758-1
4. Jin KH, Kim Y-G, Cho SH, Ye JC, Yee D-S. High-speed terahertz reflection three-dimensional imaging for nondestructive evaluation. *Opt Express.* (2012) **20**:25432–40. doi: 10.1364/OE.20.025432
5. Mittendorff M, Li S, Murphy TE. Graphene-based waveguide-integrated terahertz modulator. *ACS Photonics.* (2017) **4**:316–21. doi: 10.1021/acsphotonics.6b00751
6. Yang J, Gong C, Sun L, Chen P, Lin L, Liu W. Tunable reflecting terahertz filter based on chirped metamaterial structure. *Sci Rep.* (2016) **6**:38732. doi: 10.1038/srep38732
7. Tan W, Zhang C, Li C, Zhou X, Jia X, Feng Z, et al. Selective coherent perfect absorption of subradiant mode in ultrathin bi-layer metamaterials via antisymmetric excitation. *Appl Phys Lett.* (2017) **110**:181111. doi: 10.1063/1.4983087
8. Chang C-C, Zhao Z, Li D, Taylor AJ, Fan S, Chen H-T. Broadband linear-to-circular polarization conversion enabled by birefringent off-resonance reflective metasurfaces. *Phys Rev Lett.* (2019) **122**:237401. doi: 10.1103/PhysRevLett.123.237401
9. Fan F, Chang SJ, Gu WH, Wang XH, Chen AQ. Magnetically tunable terahertz isolator based on structured semiconductor magneto plasmonics. *IEEE Photonics Technol Lett.* (2012) **24**:2080–3. doi: 10.1109/LPT.2012.2219858
10. Shalaby M, Peccianti M, Ozturk Y, Morandotti R. A magnetic non-reciprocal isolator for broadband terahertz operation. *Nat Commun.* (2013) **4**:1558. doi: 10.1038/ncomms2572
11. Fan F, Chen S, Chang SJ. A review of magneto-optical microstructure devices at terahertz frequencies. *IEEE J Sel Top Quantum Electron.* (2017) **23**:8500111. doi: 10.1109/JSTQE.2016.2537259
12. Ghaffar FA, Bray JR, Vaseem M, Roy L, Shamim A. Theory and design of tunable full-mode and half-mode ferrite waveguide isolators. *IEEE Tran Magn.* (2019) **55**:4003408. doi: 10.1109/TMAG.2019.2910028
13. Hilico L, Douillet A, Karr JP, Tournié E. Note: a high transmission Faraday optical isolator in the 9.2 μm range. *Rev Sci Instrum.* (2011) **82**:096106. doi: 10.1063/1.3640004
14. Shuvaev AM, Astakhov GV, Pimenov A, Brune C, Buhmann H, Molenkamp LW. Giant magneto-optical faraday effect in HgTe thin films in the terahertz spectral range. *Phys Rev Lett.* (2011) **106**:107404. doi: 10.1103/PhysRevLett.106.107404
15. Arikawa T, Wang XF, Belyanin AA, Kono J. Giant tunable Faraday effect in a semiconductor magneto-plasma for broadband terahertz polarization optics. *Opt Express.* (2012) **20**:19484–92. doi: 10.1364/OE.20.019484
16. Shimano R, Yumoto G, Yoo JY, Matsunaga R, Tanabe S, Hibino H, et al. Quantum Faraday and Kerr rotations in graphene. *Nat Commun.* (2013) **4**:1841. doi: 10.1038/ncomms2866
17. Tamagnone M, Moldovan C, Poumirol J-M, Kuzmenko AB, Ionescu AM, Mosig JR, et al. Near optimal graphene terahertz non-reciprocal isolator. *Nat Commun.* (2016) **7**:11216. doi: 10.1038/ncomms11216
18. Shalaby M, Peccianti M, Ozturk Y, Clerici M, Al-Naib I, Razzari L, et al. Terahertz Faraday rotation in a magnetic liquid: high magneto-optical figure of merit and broadband operation in a ferrofluid. *Appl Phys Lett.* (2012) **100**:241107. doi: 10.1063/1.4729132
19. Poumirol JM, Liu PQ, Slipchenko TM, Nikitin AY, Martin-Moreno L, Faist J, et al. Electrically controlled terahertz magneto-optical phenomena in continuous and patterned graphene. *Nat Commun.* (2017) **8**:14626. doi: 10.1038/ncomms14626
20. Lin S, Silva S, Zhou JF, Talbayev D. A one-way mirror: high-performance terahertz optical isolator based on magnetoplasmonics. *Adv Opt Mater.* (2018) **6**:1800572. doi: 10.1002/adom.201800572
21. Tan Z, Fan F, Chang S. Active broadband manipulation of terahertz photonic spin based on gyrotropic pancharatnam-berry metasurface. *IEEE J Sel Top Quantum Electron.* (2020) **26**:1–8. doi: 10.1109/JSTQE.2020.2984560
22. Li T-F, Li Y-L, Zhang Z-Y, Yang Q-H, Fan F, Wen Q-Y, et al. Terahertz Faraday rotation of magneto-optical films enhanced by helical metasurface. *Appl Phys Lett.* (2020) **116**:251102. doi: 10.1063/5.0009704
23. Hu B, Wang QJ, Zhang Y. Broadly tunable one-way terahertz plasmonic waveguide based on nonreciprocal surface magneto plasmons. *Opt Lett.* (2012) **37**:1895–7. doi: 10.1364/OL.37.001895
24. Chen S, Fan F, Wang X, Wu P, Zhang H, Chang S. Terahertz isolator based on nonreciprocal magneto-metasurface. *Opt Express.* (2015) **23**:1015–24. doi: 10.1364/OE.23.001015
25. Fan F, Xiong CZ, Chen JR, Chang SJ. Terahertz nonreciprocal isolator based on a magneto-optical microstructure at room temperature. *Opt Lett.* (2018) **43**:687–90. doi: 10.1364/OL.43.000687
26. Yu SK, Heffernan KH, Talbayev D. Beyond the effective mass approximation: a predictive theory of the nonlinear optical response of conduction electrons. *Phys Rev B.* (2017) **95**:125201. doi: 10.1103/PhysRevB.95.125201
27. Han JG, Lakhtakia A, Qiu CW. Terahertz metamaterials with semiconductor split-ring resonators for magnetostatic tunability. *Opt Express.* (2008) **16**:14390–6. doi: 10.1364/OE.16.014390
28. Brion JJ, Wallis RF, Hartstein A, Burstein E. Theory of surface magnetoplasmons in semiconductors. *Phys Rev Lett.* (1972) **28**:1455–8. doi: 10.1103/PhysRevLett.28.1455
29. Hu B, Zhang Y, Wang QJ. Surface magneto plasmons and their applications in the infrared frequencies. *Nanophotonics.* (2015) **4**:383–96. doi: 10.1515/nanoph-2014-0026
30. Wang X, Belyanin AA, Crooker SA, Mittleman DM, Kono J. Interference-induced terahertz transparency in a semiconductor magneto-plasma. *Nature Phys.* (2010) **6**:126–30. doi: 10.1038/nphys1480
31. Mu QY, Fan F, Chen S, Xu ST, Xiong CZ, Zhang X, et al. Tunable magneto-optical polarization device for terahertz waves based on InSb and its plasmonic structure. *Photon Res.* (2019) **7**:325–31. doi: 10.1364/PRJ.7.000325
32. Oszwałldowski M, Zimpel M. Temperature dependence of intrinsic carrier concentration and density of states effective mass of heavy holes in InSb. *J Phys Chem Solids.* (1988) **49**:1179–85. doi: 10.1016/0022-3697(88)90173-4
33. Rivas JG, Janke C, Bolivar PH, Kurz H. Transmission of THz radiation through InSb gratings of subwavelength apertures. *Opt Express.* (2005) **13**:847–59. doi: 10.1364/OPEX.13.000847
34. Remer L, Mohler E, Grill W, Lüthi B. Nonreciprocity in the optical reflection of magnetoplasmas. *Phys Rev B.* (1984) **30**:3277–82. doi: 10.1103/PhysRevB.30.3277
35. Chen HT, Zhou JF, O'hara JF, Chen F, Azad AK, Taylor AJ. Antireflection coating using metamaterials and identification of its mechanism. *Phys Rev Lett.* (2010) **105**:073901–4. doi: 10.1103/PhysRevLett.105.073901
36. Shi J, Liu X, Yu S, Lv T, Zhu Z, Ma HF, et al. Dual-band asymmetric transmission of linear polarization in bilayered chiral metamaterial. *Appl Phys Lett.* (2013) **102**:191905. doi: 10.1063/1.4805075
37. Lv T, Chen X, Dong G, Liu M, Liu D, Ouyang C, et al. Dual-band dichroic asymmetric transmission of linearly polarized waves in terahertz chiral metamaterial. *Nanophotonics.* (2020). doi: 10.1515/nanoph-2019-0507. [Epub ahead of print].

Conflict of Interest: The authors declare that the research was conducted in the absence of any commercial or financial relationships that could be construed as a potential conflict of interest.

BRIEF RESEARCH REPORT
published: 04 September 2020
doi: 10.3389/fphy.2020.00349

Realization of Terahertz Wavefront Manipulation Using Transmission-Type Dielectric Metasurfaces

Jiaqi Li[1], Tingyin Ning[2], Min Zhang[1], Ireng Ling Li[1], Hong Su[1]* and Huawei Liang[1]*

[1] Shenzhen Key Laboratory of Laser Engineering, College of Physics and Optoelectronic Engineering, Shenzhen University, Shenzhen, China, [2] Shandong Provincial Engineering and Technical Center of Light Manipulations & Shandong Provincial Key Laboratory of Optics and Photonic Device, School of Physics and Electronics, Shandong Normal University, Jinan, China

Metasurfaces, composed of an array of subwavelength artificial structures, have attracted great interest, owing to their high ability in locally manipulating the wavefront of electromagnetic waves. Here, we propose a dielectric metasurface based on a fused silica resonator, consisting of a rectangular-shaped bar placed in the center of a cross net-shaped structure, to manipulate the wavefront of terahertz waves. As proof of concept, several transmission-type devices for spatial modulation are designed at the target frequency of 0.14 THz, including on-axis and off-axis focusing, generation of a non-diffracting Bessel beam, and multi-focus lens. The simulated efficiencies range from 45 to 62%. This novel approach for manipulating THz wavefronts can be also used for information storage and other phase-related techniques in the rapid development of THz applications.

Keywords: metasurface, THz wave, spatial modulation, Bessel beam, multi-focus lens

OPEN ACCESS

Edited by:
Fei Gao,
Zhejiang University, China

Reviewed by:
Weiren Zhu,
Shanghai Jiao Tong University, China
Zuojia Wang,
Shandong University, China

Correspondence:
Hong Su
hsu@szu.edu.cn
Huawei Liang
hwliang@szu.edu.cn

Specialty section:
This article was submitted to Optics and Photonics, a section of the journal Frontiers in Physics

Received: *16 March 2020*
Accepted: *23 July 2020*
Published: *04 September 2020*

Citation:
Li J, Ning T, Zhang M, Li IL, Su H and Liang H (2020) Realization of Terahertz Wavefront Manipulation Using Transmission-Type Dielectric Metasurfaces. Front. Phys. 8:349. doi: 10.3389/fphy.2020.00349

INTRODUCTION

The traditional electromagnetic (EM) devices are designed to realize the control functionalities by adjusting the physical geometrical shape and the component material [1]. Recently, metasurfaces, made of a large number of subwavelength structures, have performed very well to locally manipulate the wavefront of EM waves. Many EM controls have achieved by metasurfaces, including ultrathin planar lenses [2–4], multi-focal devices [5–9], vortex beam [10–12], and various holography [13, 14]. With the development of terahertz (THz) technology, highly efficient, compact functional devices are required, which can be provided by dielectric metasurfaces.

In this paper, we propose a transmission-type, fused silica metasurface to manipulate THz wavefront. Different from previous dielectric pillars on substrate [10, 11, 15] or cross shaped restorers [16–19], the metasurface unit cell consists of a cross net shaped structure with a rectangular pillar placed in the center. The weak coupling of each basic unit is formed by the high refractive index difference between the fused silica and the surrounding air, which concentrates the confined energy within the central structure. Compared with dielectric pillars, the proposed metasurface have more adjustable unit structural parameters. Moreover, the metasurface reduces the difficulty in fabricating because each of the basic unit is reciprocally freestanding by cross shaped restorers without substrates. Through this work, on-axis and off-axis focusing, generation of a non-diffracting Bessel beam, and multi-spot focusing are demonstrated. The total control efficiency could be as high as 62% in numerical simulation. These advantages of the proposed metasurface will enrich THz functional devices, and provide a novel way for the design of multifunctional miniaturized devices.

RESULTS AND DISCUSSION

Figure 1A schematically shows the metasurface structure and the inset shows the details of geometry basic unit cell. Both the width ***a*** and length ***b*** are in the range of 0.3–1.9 mm, respectively. The width of the cross net shaped structure ***w*** is set to 0.3 mm. The period ***T*** and thickness ***h*** are 2 mm and 3.6 mm, respectively. The amplitude transmission and corresponding phase delay for x-polarized incident waves are calculated using a commercially available software package COMSOL Multiphysics (**Figures 1B,C**). The phase shift can cover the range of 0–360°, which facilitates the wave control. Eight unit cells are selected as $(a, b) = (0.8, 1.6\,\text{mm})$, $(0.58, 1.5\,\text{mm})$, $(0.54, 1\,\text{mm})$, $(0.35, 0.35\,\text{mm})$, $(1.9, 1.86\,\text{mm})$, $(1.65, 1.75\,\text{mm})$, $(1.25, 1.7\,\text{mm})$, $(0.95, 1.65\,\text{mm})$ for fully covering the phase range with an interval of 45°, as shown in **Figure 1D**. The average amplitude transmittance of the unit cells is ∼93%. To demonstrate modulation ability of the proposed metasurface, several THz functional devices are designed based on the eight unit cells.

We first demonstrate on-axis and off-axis focusings achieved using the proposed metasurface. The phase distribution on the metasurface for realizing this focusing can be described as: $\varphi(x) = \frac{2\pi}{\lambda_0}\left(\sqrt{(x - x_0)^2 + L^2} - L\right)$, where λ_0 for free space, and x and x_0 are the position coordinates of basic units and the focal spot, respectively, and L is the focal length. The obtained phase profiles are quantized into eight values, ranging from 0 to 360°. The eight basic units are placed on the corresponding positions. When x-polarized THz waves are normally incident on the designed metasurface device, the metasurface modifies the wavefront. The transmitted waves are then focused into an on-axis spot with the propagation distance $L = 5$ cm, as shown in **Figure 2A**. The control efficiency is defined as the ratio of the power of E_x component on the focal plane to that of the incident wave. The on-axis focusing efficiency is 60%, which is much higher than the single-layer plasmonic metasurfaces [20].

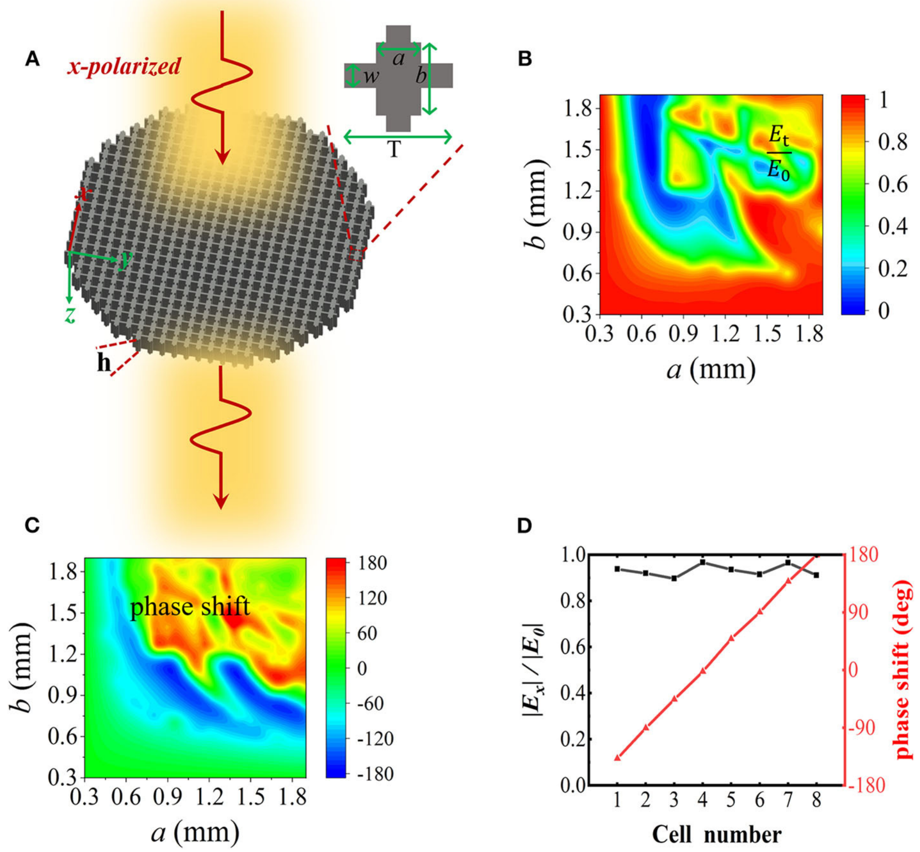

FIGURE 1 | Proposed dielectric metasurface and the control characteristics of metasurface unit cells. **(A)** Schematic of the proposed metasurface. The inset shows a basic unit cell of the metasurface. **(B,C)** Amplitude transmission and corresponding phase shift, respectively, of x-polarized wave with a frequency of 0.14 THz. **(D)** Phase shift and amplitude transmission for the selected eight unit cells.

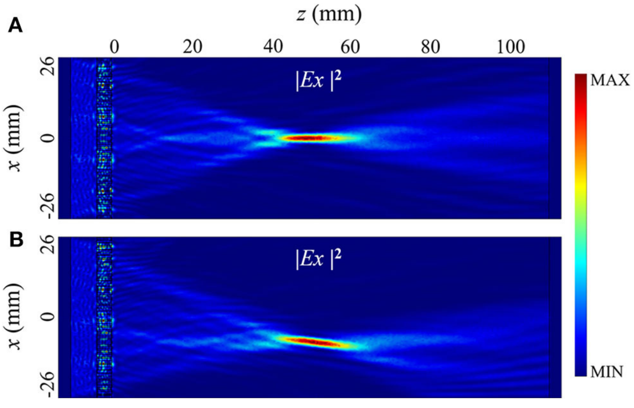

FIGURE 2 | Simulated intensity distributions of **(A)** on-axis and **(B)** off-axis focusings with a focal length $L = 5$ cm.

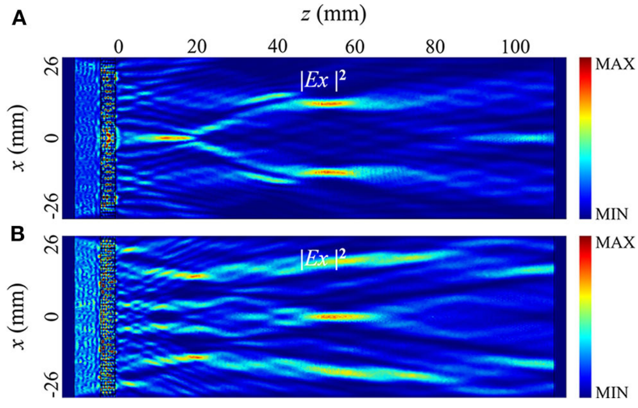

FIGURE 4 | Simulated intensity distributions of **(A,B)** double-spot and tri-spot focusing, respectively, with a focal length of 5 cm.

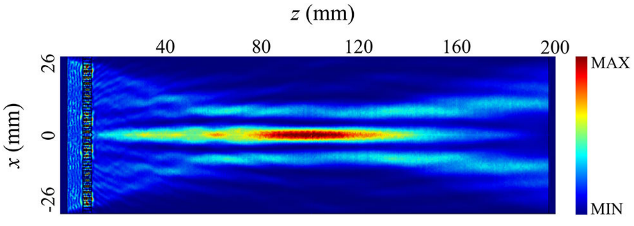

FIGURE 3 | Simulated intensity distribution of generation of a non-diffracting Bessel beam.

Furthermore, an off-axis focus lens with the same focal length ($L = 5$ cm) is designed. The off-axis distance is 8 mm, as shown by the simulated results in **Figure 2B**. The simulated control efficiency is 62%.

Furthermore, we demonstrate generation of a non-diffracting Bessel beam using the dielectric metasurface. The phase distribution on the metasurface for generating a Bessel beam can be described as: $\varphi(x) = C\frac{2\pi}{\lambda_0}|x|$, where C is a coefficient. When x-polarized waves are normally incident on the metasurface with a width of 52 mm, the arranged unit cells transform the wavefront into an axisymmetrical slope shape, so that a Bessel beam can be formed by the wave interference [21]. The simulated intensity distribution of a one-dimensional Bessel beam is shown in **Figure 3**. The control efficiency is 45%. Compared with the focusing in **Figure 2A**, the focal depth of the Bessel beam is much longer and the beam width changes much more slowly along the long propagation direction, which are consistent with the typical characteristics of the non-diffractive Bessel beam.

To demonstrate the versatile control of the proposed metasurface, a one-dimensional multi-spot focusing lens (MSFL) is designed. The phase distributions for obtaining one-dimensional double-spot and tri-spot focusing are calculated, respectively, using the Gerchberg-Saxton (GS) retrieval algorithm [22] on the basis of Fresnel diffraction. In the simulations using the COMSOL Multiphysics, the required phase distributions can be obtained by arranging the aforementioned unit cells in the one-dimensional metasurface with a width of 52 mm. Then the double-spot and tri-spot focusing are formed by the wave interference, respectively. The simulated intensity distribution of one-dimensional double-spot focusing is shown in **Figure 4A** (off-axis $\pm$ 11 mm). The control efficiencies for the two spots are 25 and 24% respectively. Thus, the total control efficiency is 49%. Tri-spot focusing with the same focal length is also demonstrated, as shown in **Figure 4B** (on-axis and off-axis $\pm$ 17 mm). The efficiency for each is 19, 18, and 18%, and thus the total control efficiency is 55%. The simulated field distributions on the focal plane are consistent with the predesigned results.

CONCLUSION

In summary, a dielectric metasurface based on a fused silica resonator, consisting of a cross net shaped structure with a rectangular pillar placed in the center, is proposed to manipulate THz waves. As a proof of concept, several transmission-type devices for THz spatial modulation are designed, including on-axis and off-axis focusing, generation of a non-diffracting Bessel beam, and multi-spot focusing. The simulated control efficiencies range from 45 to 62%. The versatile control with high efficiency makes the metasurface valuable for the practical applications in THz communications and imaging.

METHOD SECTION

All simulations were using a commercial finite element simulation software COMSOL multiphysics. The refractive index of fused silica at the target frequency of 0.14 THz is 1.95. The perfect matching layers (PML) with a thickness of 3 mm were used along z-direction. The periodic boundary conditions were used in both x- and y-directions to simulate the control characteristics of basic unit cells. In the simulations of functional devices, the scattering and periodic boundary conditions were used along the x- and y-directions, respectively.

DATA AVAILABILITY STATEMENT

The original contributions presented in the study are included in the article/supplementary materials, further inquiries can be directed to the corresponding author/s.

AUTHOR CONTRIBUTIONS

JL and HL proposed the idea and conceived and performed the simulations. TN designed the TMFL. MZ designed the Bessel beam. IL and HS guided the theoretical work. All authors analyzed and discussed the results.

FUNDING

This work was supported in part by the National Natural Science Foundation of China under Grant No. 11874270, the Fund Project for Shenzhen Fundamental Research Programme under Grant Nos. JCYJ20190808143409787 and JCYJ20180305125000525, and the China Scholarship Council under Grant No. 201908440615.

REFERENCES

1. Thompson KP, Rolland JP. Freeform optical surfaces: a revolution in imaging optical design. *Opt Photonics News*. (2012) **23**:30–5. doi: 10.1364/opn.23.6.000030
2. Gao S, Park CS, Lee SS, Choi DY. A highly efficient bifunctional dielectric metasurface enabling polarization-tuned focusing and deflection for visible light. *Adv Opt Mater*. (2019) **7**:1801337. doi: 10.1002/adom.201801337
3. Kamali SM, Arbabi E, Arbabi A, Horie Y, Faraon A. Highly tunable elastic dielectric metasurface lenses. *Laser Photonics Rev*. (2016) **10**:1002–8. doi: 10.1002/lpor.201600144
4. Lin D, Fan P, Hasman E, Brongersma ML. Dielectric gradient metasurface optical elements. *Science*. (2014) **345**:298–302. doi: 10.1126/science.1253213
5. Chen X, Zhang Y, Huang L, Zhang S. Ultrathin metasurface laser beam shaper. *Adv Opt Mater*. (2014) **2**:978–82. doi: 10.1002/adom.201400186
6. Ding X, Wang Z, Zhang K, Gu X, Wu Q, Fu J, editors. Multi-focus imaging utilizing huygens metasurface. In: *IEEE 2018 48th European Microwave Conference (EuMC)*. Madrid (2018). doi: 10.23919/eumc.2018.8541382
7. He J, Ye J, Wang X, Kan Q, Zhang Y. A broadband terahertz ultrathin multi-focus lens. *Sci Rep*. (2016) **6**:28800. doi: 10.1038/srep28800
8. Wang Y, Guan C, Ding X, Zhang K, Ratni B, Burokur SN, et al. Multi-focus hologram utilizing Pancharatnam–Berry phase elements based metamirror. *Opt Lett*. (2019) **44**:2189–92. doi: 10.1364/OL.44.002189
9. Zhu L, Xiong Z, Yu W, Tian X, Kong Y, Liu C, et al. Polarization-controlled tunable multi-focal plasmonic lens. *Plasmonics*. (2017) **12**:33–8. doi: 10.1007/s11468-016-0225-2
10. Yang Y, Wang W, Moitra P, Kravchenko II, Briggs DP, Valentine J. Dielectric meta-reflectarray for broadband linear polarization conversion and optical vortex generation. *Nano Lett*. (2014) **14**:1394–9. doi: 10.1021/nl4044482
11. Zhang H, Zhang X, Xu Q, Tian C, Wang Q, Xu Y, et al. High-efficiency dielectric metasurfaces for polarization-dependent terahertz wavefront manipulation. *Adv Opt Mater*. (2018) **6**:1700773. doi: 10.1002/adom.201700773
12. Ou K, Li G, Li T, Yang H, Yu F, Chen J, et al. High efficiency focusing vortex generation and detection with polarization-insensitive dielectric metasurfaces. *Nanoscale*. (2018) **10**:19154–61. doi: 10.1039/c8nr07480a
13. Dong F, Chu W. Multichannel-independent information encoding with optical metasurfaces. *Adv Mater*. (2019) **31**:1804921. doi: 10.1002/adma.201804921
14. Zang X, Dong F, Yue F, Zhang C, Xu L, Song Z, et al. Polarization encoded color image embedded in a dielectric metasurface. *Adv Mater*. (2018) **30**:1707499. doi: 10.1002/adma.201707499
15. Shao L, Zhu W, Leonov MY, Rukhlenko ID. Dielectric 2-bit coding metasurface for electromagnetic wave manipulation. *J Appl Phys*. (2019) **125**:203101. doi: 10.1063/1.5094561
16. Lin L, Goh XM, McGuinness LP, Roberts A. Plasmonic lenses formed by two-dimensional nanometric cross-shaped aperture arrays for Fresnel-region focusing. *Nano Lett*. (2010) **10**:1936–40. doi: 10.1021/nl1009712
17. Vashistha V, Vaidya G, Gruszecki P, Serebryannikov AE, Krawczyk M. Polarization tunable all-dielectric color filters based on cross-shaped Si nanoantennas. *Sci Rep*. (2017) **7**:1–8. doi: 10.1038/s41598-017-07986-z
18. Vashistha V, Vaidya G, Hegde RS, Serebryannikov AE, Bonod N, Krawczyk M. All-dielectric metasurfaces based on cross-shaped resonators for color pixels with extended gamut. *ACS Photonics*. (2017) **4**:1076–82. doi: 10.1021/acsphotonics.6b00853
19. Saifullah Y, Waqas AB, Yang G-M, Xu F. Multi-bit dielectric coding metasurface for EM wave manipulation and anomalous reflection. *Opt Express*. (2020) **28**:1139–49. doi: 10.1364/oe.383214
20. Zhang L, Zhang M, Liang H. Realization of full control of a terahertz wave using flexible metasurfaces. *Adv Opt Mater*. (2017) **5**:1700486. doi: 10.1002/adom.201700486
21. Akram MR, Mehmood MQ, Tauqeer T, Rana AS, Rukhlenko ID, Zhu W. Highly efficient generation of Bessel beams with polarization insensitive metasurfaces. *Opt Express*. (2019) **27**:9467–80. doi: 10.1364/oe.27.009467
22. Gerchberg RW. A practical algorithm for the determination of phase from image and diffraction plane pictures. *Optik*. (1972) **35**:237–46.

Conflict of Interest: The authors declare that the research was conducted in the absence of any commercial or financial relationships that could be construed as a potential conflict of interest.

ORIGINAL RESEARCH
published: 14 September 2020
doi: 10.3389/fphy.2020.00290

A Study of a Microstrip Patch Antenna With a Drilled Through-Holes Array Structure Based on the Line Source Analysis Method

Zhendong Ding, Dan Zhang and Chunyu Ma*

College of Information Science and Technology, Nanjing Forestry University, Nanjing, China

A novel periodic photonic crystal structure with through-holes drilled by a 4 × 7 array based on the line source analysis method was proposed in this paper to improve the gain and radiation of the microstrip antenna. The analysis results showed that, with the help of the line source analysis method, this through-hole structure could improve the gain and radiation of the antenna. The proposed through-hole structure was superior to other periodic structures. The sizes of the antenna and the patch used were 46.86 × 60.86 × 1.6 mm and 20.43 × 30.43 mm, respectively. Through-holes were made on three distinct layers: the patch, dielectric, and ground layers. The resulting operating frequency was 2.95 GHz, the bandwidth ranged from 84.7 MHz to 2.9085–2.9932 GHz, the return loss was 40.9455 dB, the voltage standing wave ratio (VSWR) was 1.011, and the maximum gain was 4.88 dBi. The return loss of the through-hole design was 69.1% higher than that of the structure without holes and 18.3% higher than that of the simulated structure. The gain increase of 58.4% was relatively non-porous. Good agreement between simulation and measurement could be observed, indicating that the proposed structure was effective. Its operating band can be used in radio navigation systems and positioning systems (2.9–3 GHz).

Keywords: line source, microstrip antenna, gain, return loss, through-hole

OPEN ACCESS

Edited by:
*Lin Chen,
University of Shanghai for Science and Technology, China*

Reviewed by:
*Yuan Yao,
Beijing University of Posts and Telecommunications (BUPT), China
Jiangtao Su,
Hangzhou Dianzi University, China
Bo Fang,
China Jiliang University, China*

****Correspondence:***
*Dan Zhang
zhangdan@njfu.edu.cn*

Specialty section:
This article was submitted to Optics and Photonics, a section of the journal Frontiers in Physics

Received: *18 January 2020*
Accepted: *26 June 2020*
Published: *14 September 2020*

Citation:
Ding Z, Zhang D and Ma C (2020) A Study of a Microstrip Patch Antenna With a Drilled Through-Holes Array Structure Based on the Line Source Analysis Method. Front. Phys. 8:290. doi: 10.3389/fphy.2020.00290

INTRODUCTION

Patch antennas are a type of the most commonly used printed antennas, and have been widely applied in many sectors due to their advantages of being light weight, small size, low profile, low cost, having good mechanical strength, a wide frequency band, high efficiency, high gain, high adaptability to surroundings, little radiation damage to the human body, and wide frequency coverage [1]. Characterized by their low quality, low cost, small size, and simple design, microstrip patch antennas are easy to manufacture, and are widely used in wireless communications, such as radar, satellite communication, mobile communication, and navigation systems [2]. Microstrip antennas are also very attractive in many transceiver system applications [3], but their use in most wideband wireless communication systems is restricted because, as resonating antennas, they have narrow bandwidths [4]. Therefore, the optimization of various independent antenna structures has become a hot topic in the microstrip antenna design field recently. Over the years, compact antennas, the radar cross section (RCS), and microstrip antennas have been extensively used in many modern communication systems [5–8]. Nowadays, science and technology, as well as economic progress, are greatly promoted by the 5G system, to which microstrip patch antennas are indispensable [9, 10]. Therefore, it is extremely important to develop a new antenna structure.

Microstrip antennas are known to have various feeding modes, such as microstrip wire, coaxial, coupled, and slot feeds. The wavelength of an electromagnetic wave is constant at a fixed frequency in free space. The radiation ability of an antenna is related to its size and shape. The lower the frequency, the longer the wavelength, and the larger the size of the antenna should be. For a typical rectangular patch antenna, the length L of the non-radiating side is usually $\lambda_0/3 < L < \lambda_0/2$ (λ_0 is the wavelength in the free space). In [11], two frequency bands (5.15–5.35 and 5.725–5.825 GHz) were generated via a coaxial feed by adjusting the position and size of the slots within an antenna with a fixed size of 12 × 8 mm. The antenna in [12] was a broadband antenna with an operating band of 2.67–13 GHz and a size of 60 × 60 × 0.8 mm. It is also possible for it to be larger in size. Article [13] reported a patch antenna with a size of 16.5 × 16.5 cm at 866.5 MHz, so it was not applicable to small-sized products. A ground plane integrated with a short-end coplanar waveguide (CPW) feed line was adopted in [14], but it achieved unsatisfactory results as its return loss was >20 dB (overall). The antenna in [15] was applied to the terahertz band, but it was only designed and simulated in the paper without the verification of test data. The study [16] used a metamaterial composed of a composite resonator cavity to design a 2.4 GHz frequency rectangular microstrip patch antenna, whose return loss reached 35 dB while VSWR was 2:1 at 20 MHz bandwidth. Even if the gain of the antenna was increased in [17], its return loss was only about 20 dB. The photonic crystal microstrip antenna designed by [18–20] showed an increased value of |S11|, but the photonic crystal structure was only assembled on the substrate of the microstrip antenna, not on the patch and the floor, making processing difficult. In order to solve the above problems, further studies on a variety of technologies are required.

As far as the author is aware, the application of the through-hole array to a microstrip antenna has not been achieved. In this paper, the analysis and calculation results suggested the photonic crystal band gap (PBG) could suppress the higher harmonics of the microstrip antenna and improve its gain and radiation. In the main mode excitation case, a coaxial feed technology in [21–25] was adopted and simulated via the corresponding electromagnetic simulation software. According to the theoretical analysis and structural comparison results, the antenna designed and optimized with a 4 × 7 through-hole array showed the best performance. The simulation results indicated that the measured return loss, VSWR, and the gain increased by 0.0269, 10.3944, and 1.87 dB, respectively, but the frequency and bandwidth remained almost unchanged. Theory and practice were also in good agreement.

ANTENNA ANALYSIS AND DESIGN

Antenna

A common microstrip antenna consists of a metal radiating plate connected to one side of a dielectric substrate, and it is much thinner than the working wavelength. A continuous metal layer is connected to the ground plane on the alternative side of the substrate. The metal radiation patches are made into different shapes according to different requirements. The structural representation of the proposed antenna is depicted in the common microstrip antenna, which is first printed onto an FR4 substrate with a relative dielectric constant of 4.4, a loss tangent 0.02, an area of L1 × W1, and a thickness of 1.6 mm. The 23.43 mm-long and 30.43-wide patch made of copper is then attached to the central position of the FR4 side of the substrate, while the other side of the substrate is the ground plane. In order to achieve 50 Ω of load welding, it should satisfy the condition of a >R1. In the proposed design, the larger the absolute value of the return loss, the better the antenna performance is likely to be.

The size of a common microstrip antenna patch is calculated as follows:

$$W_P = \frac{c}{2f}\left(\frac{\varepsilon+1}{2}\right)^{-\frac{1}{2}} \quad (1)$$

$$L_P = \frac{c}{2f}\left[\frac{\varepsilon+1}{2} + \frac{\varepsilon-1}{2}\left(1+12\frac{H}{W_P}\right)^{-\frac{1}{2}}\right]^{-\frac{1}{2}} - 2\Delta L \quad (2)$$

$$D_1 = \frac{L_P}{2}\left[1 - \left(\frac{\varepsilon+1}{2} + \frac{\varepsilon-1}{2}\left(1+12\frac{H}{L_P}\right)^{-\frac{1}{2}}\right)^{-\frac{1}{2}}\right] \quad (3)$$

where W_p is the patch width, L_p is the patch length, f is the central frequency, c is the speed of light (3 × 10^8m/s), ε is the relative dielectric constant of the substrate, H is the height of the substrate, and ΔL the equivalent radiation gap length.

The array through-hole structure is embedded in the common microstrip antenna with an improved structure, as shown in **Figure 1**.

Theoretical Method

The structure proposed in [26] was used as a reference in this paper, but unlike the omnidirectional calculation in [26], single direction analysis was adopted. **Figure 2** shows the geometry of photonic crystals and line sources. The impressed electric line source ($J_0(x,y)$) located at the origin O of the x-y coordinate system is sandwiched between two photonic crystals, with a separation distance of t_1. A common distance in the × direction is represented by h and the distance between cylinders is d1. The structure is arranged in a periodic array. The cylindrical elements on the same layer of the array should have the same material properties and dimensions, but those on difference layers do not necessarily have to be the same. a_1 is the radius of the cylinder and ε_{r1} is relative permittivity. The number of the photonic crystal layers above the X-axis is assumed to be N_1. The Y-axis is analyzed in this paper.

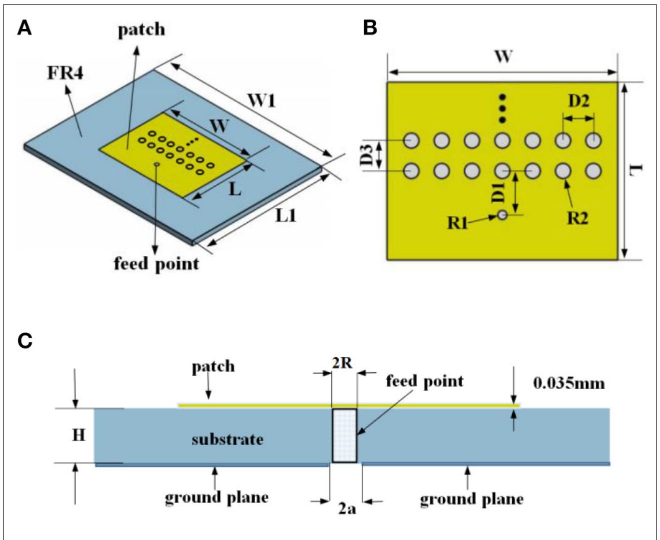

FIGURE 1 | The structural representation of the microstrip antenna. **(A)** The geometry of the proposed antenna, **(B)** The structure of the patch, **(C)** The cross-section view of the coaxial feed.

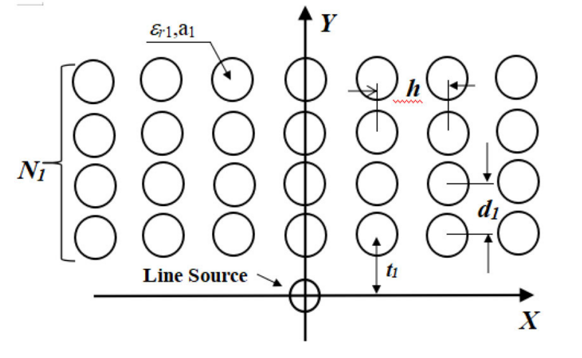

FIGURE 2 | Scheme of a localized Y line source embedded at the origin of the coordinate system of bounded two-dimensional photonic crystals.

The conventional Floquet mode expansion method cannot be directly used since the system concerned is not periodic. Therefore, the expression of the localized line source in terms of an infinite periodic array of linearly phased line sources in the spectral domain is considered using the identity [27]:

$$\delta\left(x\right) = \frac{1}{2\pi}\int_{-\infty}^{\infty} e^{i\xi x} d\xi = \frac{1}{2\pi}\sum_{\ell=-\infty}^{\infty} e^{i2\ell\pi x/h}\int_{-\pi/h}^{\pi/h} e^{i\xi x} d\xi \quad (4)$$

$$\delta\left(x\right) = \frac{h}{2\pi}\int_{-\pi/h}^{\pi/h}\left[\sum_{\ell=-\infty}^{\infty}\delta\left(x-\ell h\right)e^{i\ell h\xi}\right]d\xi \quad (5)$$

The electric field $E_{z,\mathrm{P}}(x,y,\xi)$ is radiated from a periodic array of line sources defined as:

$$J_P(x,y,\xi) = \sum_{\ell=-\infty}^{\infty}\delta(y)\delta(x-\ell h)e^{i\ell h\xi} \quad (6)$$

$$J_0(x,y) = \delta(x)\delta(y) \quad (7)$$

$$E_z(x,y) = \frac{h}{2\pi}\int_{-\pi/h}^{\pi/h} E_{z,P}(x,y,\xi)d\xi \quad (8)$$

Therefore, the problem can be simplified to the calculation of the electric field $E_{z,\mathrm{P}}(x,y,\xi)$ radiated from the infinite periodic array of linearly phased line sources $J_{\mathrm{P}}(x,y,\xi)$.

The primary field $E_z^i(x,y,\xi)$ radiated from the periodic line sources $J_{\mathrm{P}}(x,y,\xi)$ defined by Formula (13) is expressed using the Fourier integral representation of the Hankel function:

$$E_z^i(x,y,\xi) = \sum_{\ell=-\infty}^{\infty} e^{i\ell h\xi}H_0^{(1)}(k_0\rho\ell) \quad (9)$$

$$E_z^i(x,y,\xi) = \frac{2}{h}\sum_{\ell=-\infty}^{\infty}\frac{e^{i\left[\xi_\ell x+\kappa_\ell(\xi)y\right]}}{k_\ell(\xi)} \quad (10)$$

$$\xi_\ell = \xi + \frac{2\ell\pi}{h}, \kappa_\ell(\xi) = \sqrt{k_0^2 - k_\ell^2} \quad (11)$$

where $k_0 = 2\pi/\lambda_0$. The incidence of plane waves in the scattered fields can be calculated using the reflection and transmission matrices of layered periodic arrays in [28] since the primary field is expressed as a superposition of the Floquet mode. The space harmonics obtained by Formula (16) are described with the amplitude vector $\mathbf{s}(\xi)$ defined as:

$$\mathrm{s}(\xi) = \left[\frac{2}{h\kappa_\ell(\ell)}\right] \quad (12)$$

As shown in **Figure 3**, photonic crystal layers located above the line source may be substituted by the plane boundary at y=t_1. The said plane boundary is characterized by the generalized reflection and transmission matrices ($\overline{R}_{N_1}^{-}, \overline{F}_{N_1}^{+}$), whose derivation was described in [29].

Then, by ray tracing the orthogonal space harmonics, the following relations are obtained:

$$\mathrm{b}_{N_1}^{-}(\xi) = \overline{R}_{N_1}(\xi)\left[\mathrm{a}_{N_1}^{+}(\xi) + \Lambda_1(\xi)\cdot s(\xi)\right] \quad (13)$$

$$\mathrm{a}_{\mathrm{N}_1}^{+}(\xi) = \frac{\overline{M}(\xi)\cdot \mathrm{s}(\xi)}{D(\xi)} \quad (14)$$

$$\Lambda_1(\xi) = \left[e^{i\kappa_\ell(\xi)t_1}\delta_{\ell\ell}\right] \quad (15)$$

$$\mathrm{c}_{N_1}^{+}(\xi) = \overline{F}_{N_1}^{+}(\xi)\cdot\left[a_1^{+}(\xi) + \Lambda_1(\xi)\cdot s(\xi)\right] \quad (16)$$

$$\mathrm{c}_{N_1}^{+}(\xi) = \frac{\overline{N}^{+}(\xi)\cdot \mathrm{s}(\xi)}{D(\xi)} \quad (17)$$

$$E_{z,P}(x,y,\xi) = \frac{e^{+}(x,y,\xi)\cdot\overline{N}^{+}(\xi)\cdot s(\xi)}{D(\xi)} \quad (18)$$

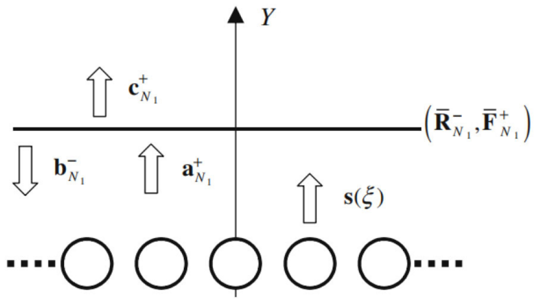

FIGURE 3 | Multiple scattering processes of space harmonics mainly radiated from the periodic array of line sources. The plane boundary characterized by the generalized reflection and transmission matrices $\overline{R}^-_{N_1}$, $\overline{F}^+_{N_1}$ takes the place of the photonic crystals.

The field $E_z(x,y)$ radiated from the localized line source (14) is obtained by plugging Formula (25) into Formula (15). A conventional numerical integration scheme is used to calculate the finite integral in Formula (15) with respect to the spectral parameter x. The singularities in the integrand are the poles that satisfy D(x) = 0, whose branch points meet $\kappa_\ell(\xi) = 0$. The poles correspond to the propagation constants of TE guided modes (usually limited within $y < t_1$). The far-zone fields are obtained from the spectral response for the propagating space harmonic components as follows:

$$E_z(\rho,\phi) = \frac{h}{\lambda_0}\sqrt{2\pi}\sin\phi\exp(-i\frac{\pi}{4})\frac{\exp(ik_0\rho)}{\sqrt{k_0\rho}} \times \sum_{\ell=-\infty}^{\infty}\sum_{m=-\infty}^{\infty}\left[\frac{\overline{N}_{\ell,m}(\xi)s_m(\xi)}{D(\xi)}\right]_{\xi=k_0\cos\phi} \tag{19}$$

where $\rho = \sqrt{x^2+y^2}$ and ϕ are the observation angles. The directive gain of the radiation $G(\phi)$ is given by:

$$G(\phi) = \frac{2\pi\left|\sum\limits_{\ell=-\infty}^{\infty}\sum\limits_{m=-\infty}^{\infty}\left[\frac{\overline{N}_{\ell,m}(\xi)s_m(\xi)}{D(\xi)}\right]_{\xi=k_0\cos\phi}\sin\phi\right|^2}{\int_0^{2\pi} d\phi\left|\sum\limits_{\ell=-\infty}^{\infty}\sum\limits_{m=-\infty}^{\infty}\left[\frac{\overline{N}_{\ell,m}(\xi)s_m(\xi)}{D(\xi)}\right]_{\xi=k_0\cos\phi}\sin\phi\right|^2} \tag{20}$$

The poles would degrade the radiation efficiency of the antenna and adjusting the lattice parameters of the photonic crystals could possibly eliminate the poles within the spectral range concerned. The pole removal can be easily achieved [28] by choosing the lattice parameters, enabling one of the eigenvalues η of the transfer matrix for space harmonics across the single layer of the array to satisfy |η|=1 in the far-zone radiation field. Without calculating the integration in Formula (15), the conventional asymptotic method [30] can be used to assess the contribution of the branch points. The photonic crystal array structure can significantly improve the radiation and gain of the antenna.

Technical Analysis

The through-hole structure is applied to the microstrip antenna in this paper. The equivalent circuit model of the structure with a single passing hole is shown in **Figure S1**, where the passing hole generates the parasitic capacitance of C and parasitic inductance of L.

$$C = 1.41\varepsilon_r H\frac{d1}{d2-d1} \tag{21}$$

$$L = 5.08H\left[\ln\left(\frac{4H}{d}\right)+1\right] \tag{22}$$

The outer diameter of the through-hole is $d1$, the diameter of the power separation zone is $d2$, the thickness of FR4 is H, ε_r is the relative dielectric constant of the substrate, and d is the inner diameter of the through-hole.

The resonance generated between capacitance and inductance of a single hole or the resonance produced between holes will greatly affect the performance of the excitation antenna.

The series resonance formula is

$$f_0 = \frac{1}{2\pi\sqrt{LC}} \tag{23}$$

$$Q = \frac{\omega_0 L}{R} = \frac{1}{\omega_0 CR} = \frac{1}{R}\sqrt{\frac{L}{C}} \tag{24}$$

The parallel resonance formula is

$$f_0 = \frac{1}{2\pi\sqrt{LC}} \tag{25}$$

$$Q = \omega_0 CR = \frac{R}{\omega_0 L} = R\sqrt{\frac{C}{L}} \tag{26}$$

where f_0 is resonance frequency, $\omega_\mathbf{0}$ is resonance angular frequency, Q is the quality factor, and R is the resistance value.

The through-hole on the antenna designed in this paper has the following characteristics:

The resonant effect between the capacitance and the inductance can improve the reflection in the antenna design. Holes also resonate with each other. The air hole in the proposed design results in the corresponding reduction of substrate material, increasing the gain of the substrate. The influence of the array hole on parameters needs parameter optimization.

The equivalent circuit model of an ordinary rectangular microstrip antenna is shown in **Figure S2A**, where Z_S is gap impedance and Z is impedance produced by the feeding point. The equivalent circuit of a microstrip antenna with drilling holes is shown in **Figure S2B**, where Z_k is the impedance of the hole. **Figure S2C** shows the resonance produced by C and L. f_0 and f_1 are not the same resonance frequency.

The resonance frequency is expressed as:

$$f_1 = \frac{1}{2\pi\sqrt{LC}} \tag{27}$$

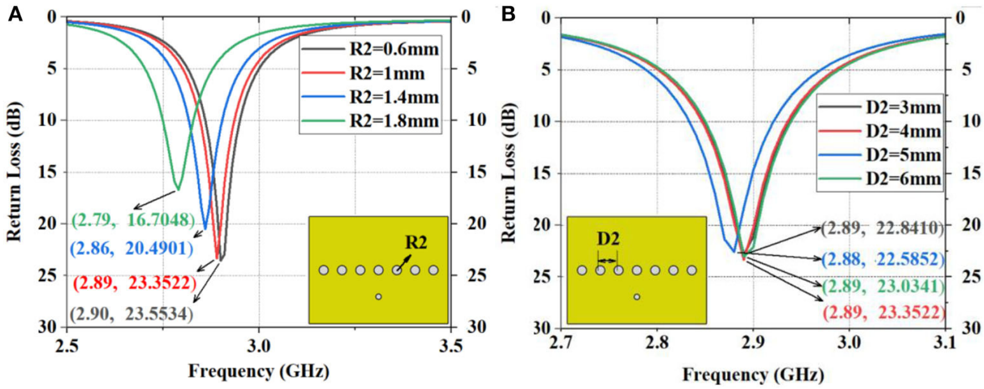

FIGURE 4 | The simulation of return loss of the antenna with one-line drilled holes on the patch center. **(A)** Different dimensions of R2, **(B)** Different dimensions of D2.

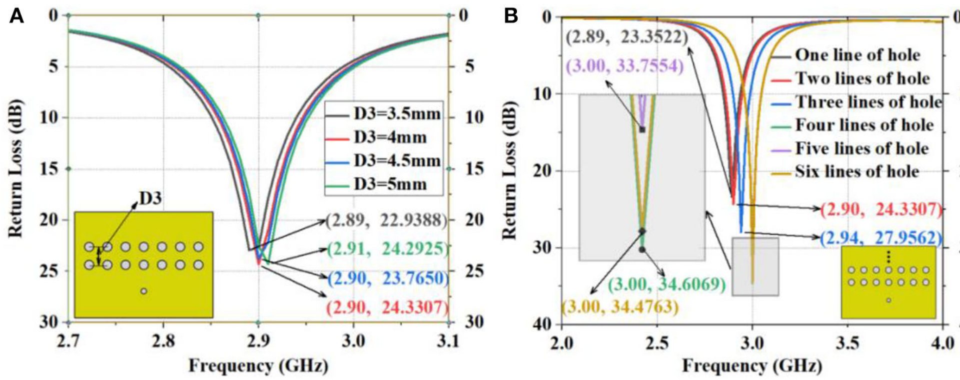

FIGURE 5 | The simulation of D3 and different lines of drilled holes. **(A)** Different dimensions of D3, **(B)** Return loss of antenna with 1, 2, 3, 4, 5, and 6 lines of holes.

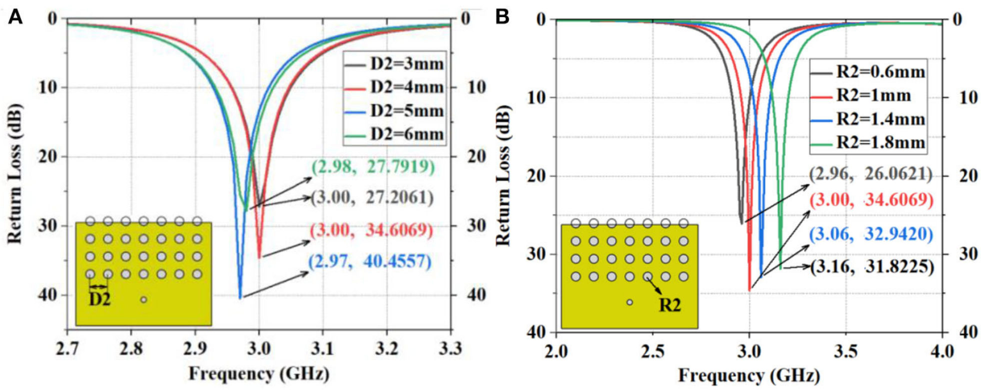

FIGURE 6 | The simulation of return loss of the antenna with four lines of drilled holes. **(A)** The different dimensions of R2, **(B)** The different dimensions of D2.

Antenna Design

The through-hole array made from an ordinary rectangular microstrip antenna is applied to the patch of the antenna proposed in this study. Three gigahertz is taken as the reference frequency of the antenna. The antenna elements are simulated via High Frequency Simulator Structure (HFSS.15), and the return loss value is simulated by adjusting the size, spacing distance, and number of drilled holes.

First, seven through-holes are embedded into the patch according to the patch width. Then, the radius of the through-holes and the distance between holes are simulated and analyzed, as shown in **Figures 4A,B**. According to **Figure 4A**, the return

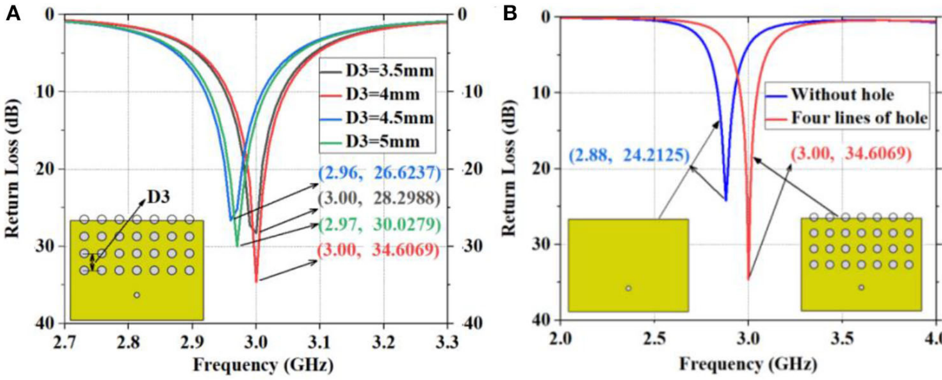

FIGURE 7 | The simulation of D3 as well as four-line and one-line holes. **(A)** The different dimensions of D3, **(B)** Comparison between the unperforated antenna and the antenna with four-row holes.

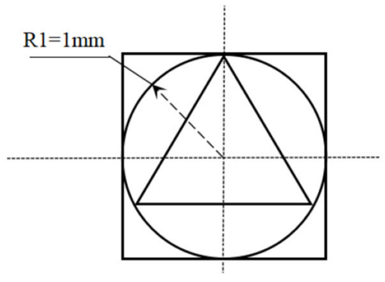

FIGURE 8 | The planar structure of the through hole, the square hole, and the triangular hole.

TABLE 1 | Comparison of perforated antennas with the unstructured antennas.

Name	Return loss (dB)	Difference value (dB)	Increased percentage (%)
Antenna (unstructured)	24.2125	/	/
Antenna 10	34.6069	10.3944	42.9
Antenna 11	32.2879	8.0754	33.3
Antenna 12	26.9484	2.7359	11.3
Antenna 13	26.9484	2.7359	11.3

TABLE 2 | Detailed parameters of the proposed antenna.

Parameter	Value (mm)	Parameter	Value (mm)
L1	46.86	R1	0.6
W1	60.86	R2	1
L	20.43	D1	5.8
W	30.43	D2	4
H	1.6	D3	4

loss shows little difference when R2 = 0.6 mm (23.5534 dB) and R2 = 1 mm (23.3522 dB). Thus, the radius of the holes on the designed antenna can take R2 = 1 mm. It can be seen from **Figure 4B** that the return loss effect is the best when D2 = 4 mm (23.3522 dB). When two rows of holes are drilled, the distance D3 should be adjusted and the value of D2 needs to be taken into account. The simulation results show that the return loss of the antenna is optimal at 2.9 GHz when D3 = 4, which is 24.3307 dB (**Figure 5A**).

Furthermore, 1, 2, 3, 4, 5, and 6 lines of holes are drilled on antennas with R2 = 1 mm, D2 = 4 mm, and D3 = 4 mm separately, and the resulting return loss of these six kinds of antennas are compared. As shown in **Figure 5B**, the return loss of antennas with one-line, two-line, three-line, four-line, five-line, and six-line holes is 23.3522 dB at 2.89 GHz, 24.3307 dB at 2.90 GHz, 27.9562 dB at 2.94 GHz, 34.6069 dB at 3.00 GHz, 33.7554 dB at 3.00 GHz, and 34.4763 dB at 3.00 GHz, respectively. The simulation results of the proposed antennas with multiple drilled holes are satisfying as the return loss reaches 34.6069 dB at 3 GHz (**Figure 5B**). D2, D3, and R2 of the four-line structure are optimized to eliminate uncertainties, as shown in **Figures 6A**, **7A**. The compassion between antennas with and without apertures reveals that the return loss of the designed antenna is 10.3944 dB higher than that of the antenna without apertures (**Figure 7B**).

Structural Comparison

After deciding to drill 4-line through-holes on the antenna structure, structures with square, triangular, and spherical holes are compared (**Figure 8**).

The comparison is made under unchanged D1, D2, and D3 in this paper, and only four rows are observed. In the one-line and two-line antennas (**Figure S3**), the triangle structure has better return loss. As for the three-line and four-line antennas (**Figure S4**), the through- hole structure has better return loss. This paper also compares the spherical holes with a radius of 0.8 mm (**Figure S5**). **Table 1** shows the comparison of return loss between perforated antennas and the unstructured antenna. From the above analysis, antenna 10 (the four-row through-hole structure) designed in this paper is the most ideal, which verifies the above design about through-hole structures.

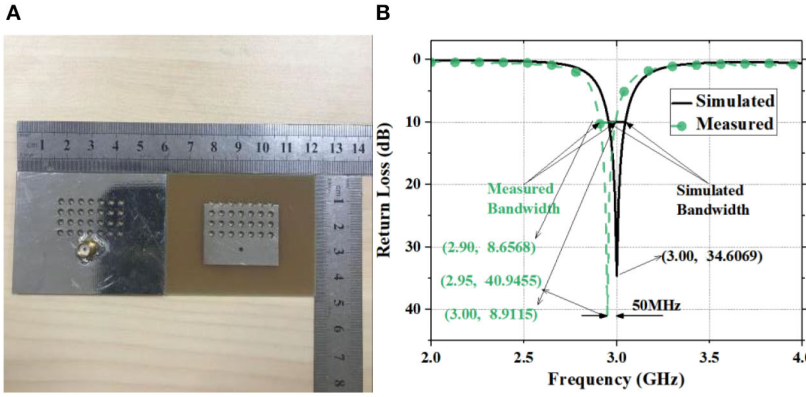

FIGURE 9 | (A) The photo of front and back of the designed antenna; **(B)** simulation and measurement data of the designed antenna.

TABLE 3 | Simulation and measurement results of the proposed antenna with four-line holes.

Name	Simulated	Measured
Frequency (GHz)	3	2.95
Return Loss (dB)	34.6069	40.9455
VSWR	1.0379	1.011
Bandwidth$\leq$-10 dB (MHz)	90.2	84.7
Gain (H-plane) (dB)	4.95	4.88
Gain (E-plane) (dB)	4.95	4.77
Gain (dBi)	4.95	4.88

Simulation Index

The above antennas with four-row holes are compared under different R2, D2, and D3 values. Some of the four-row drilled holes are on the patch and others are on the substrate. The best return loss effect is achieved at 3 GHz when R2 = 1 mm, D2 = 4 mm, and D3 = 4 mm, so the antenna with four-row holes meeting these parameters is designed. This antenna is then compared with the unperforated antenna. As shown in **Figure 7B**, the return loss of the designed antenna increases the output by 42.9%, when compared to the unperforated antenna, which has an overall return loss of 24.2125 dB.

The horizontal current on the surface of the patch at the TM mode with a coaxial feed coupling structure is distributed forward (please see **Figure S6**). The distribution of current is such that the reflection of electromagnetic waves is fine.

The return loss of the simulated antenna is 34.6069 dB and the corresponding VSWR is 1.0379. When the return loss is 10 dB, it has a 90.2 MHz bandwidth. The parameters of the proposed antenna are shown in **Table 2**.

As can be seen from the following figures, the simulation results of performance parameters of the designed antenna are satisfactory. Its gain is 4.9533 dBi at 3 GHz (**Figure S8B**), and its input impedance is about 50 Ω at 3 GHz (**Figure S9B**). For other simulation indicators, please see the figures in the **Supplementary Materials**.

MEASUREMENT

Precision machining and measurements of the four-row aperture structure designed in this paper were performed. The designed antenna was processed and tested using network analyzers (CETC41, AV3629A) in a 7 × 4 × 3 m rectangular microwave darkroom in the School of Electronic Engineering of Xidian University. Before the test, the most classic two-port system error calibrator, TOSM (through, open, short, match), also known as SOLT, was used for network analyzer calibration. Before the far-field test, the tester dealt with the test environment and equipment, including instrument calibration, cable loss zeroing, turntable debugging, etc. The 50 Ω SMA connector was used for back-feed at D1 from the center of the patch. To verify the results of the simulated design, a photo of the proposed antenna prototype was taken, and its return loss was simulated and measured (**Figure 9**). The patch is made from copper, and the antenna surface is coated with tin to prevent oxidation. **Table 3** shows the simulated and measured performance parameters of the proposed antenna with four-row holes. The measured 2-D radiation patterns (E-plane and H-plane) at 2.90, 2.95, and 3 GHz are shown in **Figure 10**. The simulated and measured peak gains are about 4.95 dB at 3 GHz and about 4.88 dB at 2.95 GHz, respectively. **Figure 11** shows the relationship between gain and frequency when both angles are zero. The simulation and measurement results of the antenna are basically identical. According to **Table 4**, the parameter improvement in this paper is effective.

As shown in **Figure 9B**, the difference between the measured and the simulated data is 50 MHz, which may be caused by a number of reasons. First, there are some errors between simulation and measurement. In general, the resonance frequency of the antenna after processing will be reduced, so it may lead to this situation. The HFSS software used for simulation in this study could be another reason. The method of selecting the feed and establishing the model by HFSS may be influencing factors. Third, the antenna processing accuracy, the feed welding during the test, the test cable loss in the antenna measurement, and the antenna test environment could also possibly result in the difference between the measured and the simulated data.

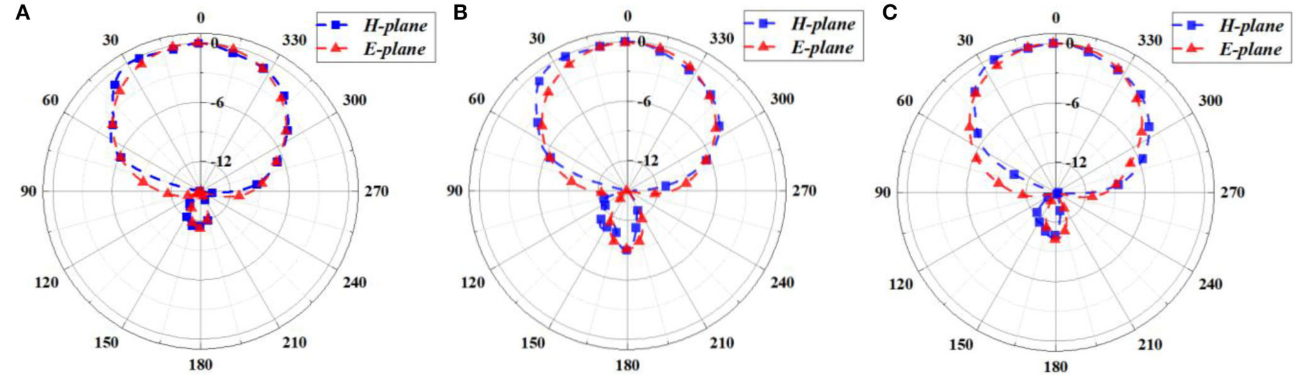

FIGURE 10 | Measured 2-D radiation patterns at **(A)** 2.90GHz, **(B)** 2.95GHz, and **(C)** 3GHz (E-plane and H-plane).

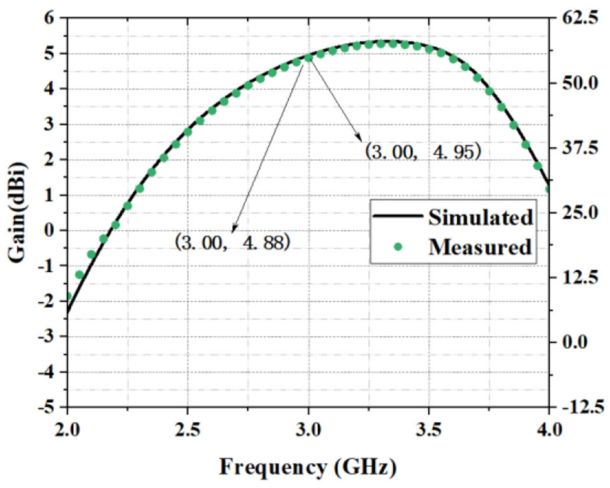

FIGURE 11 | Measured radiation gain of the proposed antenna.

TABLE 4 | The comparison of return loss and gain.

Number	Name	Return loss (dB)	Gain (dBi)
1	Antenna (no structure)	24.2125	3.08
2	Antenna10 (simulated)	34.6069	4.95
3	Antenna10 (measured)	40.9455	4.88
4	Compare (2 and 1)	42.3%	60.7%
5	Compare (3 and 1)	69.1%	58.4%

CONCLUSION

The process of antenna designing is subject to theoretical analysis, technical analysis, antenna design, antenna comparison, processing, and testing. This paper tries to achieve the design through theory discovery and software testing. The achieved return loss of the design is 69.1% higher than that of the antenna without holes and 18.3% higher than that of the simulated antenna. The gain increase of 58.4% is relatively non-porous. The results of this study suggest that a 4 × 7 array through-hole structure can improve the gain and radiation of microstrip antennas and can be realized based on the line source analysis and parameter optimization by using ANSYS HFSS. The simulation results are consistent with the experimental ones, even though there are some errors for the test frequency.

Innovations are made in the following four aspects: structure, theory, design optimization, and metrics improvement. First, in terms of structure, a 4 × 7 array through-hole structure is used to integrate the functions of photonic crystal and microstrip antennas. Second, theoretical analysis finds that the line source of the design structure, i.e., the 4 × 7 array hole, is different from the reference line source. The line source in a semicircle direction is also analyzed, with the corresponding formula deduced. The photonic crystal array structure can obviously improve the radiation and gain. Third, the structural design and optimization is investigated. The single-, double-, three-, four-, five-, and six-row holes are compared, and the hole spacing is explored. After design and optimization, the optimal scheme is finally determined for theoretical analysis and verification. Fourth, to improve the metrics, the 4 × 7 array structure is compared with a structure without holes. It is obvious that the return loss increases substantially. section Structural Comparison makes comparisons between several structures, which reveal that antenna 10, namely the 4 × 7 array structure, can deliver the best outcomes.

This paper promotes the research of photonic crystals and antennas and may offer help to researchers in the in-depth mining of the array hole structure in the future. This research also has some limitations. For instance, its bandwidth is not wide enough, but this issue will be improved in the future. The materials used to fabricate the prototype are low-cost, and the antenna is small in size, with easy heat dissipation and high mechanical strength. The simple structure can facilitate manufacturing and integration with other circuits. The wiring can also pass through the holes. The antenna designed in this paper can be used in the frequency band of radio navigation systems and positioning systems.

DATA AVAILABILITY STATEMENT

The raw data supporting the conclusions of this article will be made available by the authors, without undue reservation, to any qualified researcher.

AUTHOR CONTRIBUTIONS

All authors listed have made a substantial, direct and intellectual contribution to the work, and approved it for publication.

FUNDING

The authors would like to thank the National Natural Science Foundation of China and High-level talents program of Nanjing Forestry University for financially supporting this research under Contract Nos. 31170668 and 163070694.

SUPPLEMENTARY MATERIAL

The Supplementary Material for this article can be found online at: https://www.frontiersin.org/articles/10.3389/fphy.2020.00290/full#supplementary-material

REFERENCES

1. Shackelford A, Lee KF, Chatterjee D, Guo YX, Luk KM, Chair R. Small-size wide-bandwidth microstrip patch antennas. In: *IEEE Antennas and Propagation Society International Symposium.* USNC/URSI (2001). p. 86–9.
2. Balanis CA. *Antenna Theory-Analysis and Design*. Hoboken, NJ: John Wiley & Sons, Inc. (2005).
3. Pozar DM. Microstrip antennas and arrays on chiral substrates. *IEEE Trans Antennas Propagat.* (2001) **40**:86–9. doi: 10.1109/8.182462
4. Lee KF, Luk KM. *Microstrip Patch Antennas.* London: Imperial College Press (2011) doi: 10.1142/p669
5. Wang L, Tong J, Li, Y. River Chief System (RCS): an experiment on cross-sectoral coordination of watershed governance. *Front Environ Sci Eng.* (2019) **13**:1–3. doi: 10.1007/s11783-019-1157-9
6. Chen C, Guo Y, Wang, H. Wideband symmetrical cross-shaped probe dual-beam microstrip patch antenna. *IEEE Antennas Wirel Propag Lett.* (2015) **14**:622–5. doi: 10.1109/LAWP.2014.2375371
7. Liu S, Qi S, Wu W, Fang, D. Single-feed dual-band single/dual beam u-slot antenna for wireless communication application. *IEEE Trans Antennas Propagat.* (2015) **63**:3759–64. doi: 10.1109/TAP.2015.2438331
8. Carver K, Mink, J. Microstrip antenna technology. *IEEE Trans Antennas Propagat.* (1981) **29**:2–24. doi: 10.1109/TAP.1981.1142523
9. Lyu B, Yang Z, Gui, G. Non-orthogonal multiple access in wireless powered communication networks with SIC constraints. *IEICE Trans Commun.* (2017) **E101-B**:1094–101. doi: 10.1587/transcom.2017EBP3179
10. Wang L, Jiang F, Yuan Z, Yang J, Gui G, Sari H. Mode division multiple access: a new scheme based on orbital angular momentum in millimetre wave communications for fifth generation. *IET Commun.* (2018) **12**:1416–21. doi: 10.1049/iet-com.2017.1182
11. Chakraborty U, Kundu A, Chowdhury SK, Bhattacharjee AK. Compact dual-band microstrip antenna for IEEE 802.11a WLAN application. *IEEE Antennas Wirel Propag Lett.* (2014) **13**:407–10. doi: 10.1109/LAWP.2014.2307005
12. Pourahmadazar J, Ghobadi C, Nourinia J, Felegari N, Shirzad, H. Broadband CPW-Fed circularly polarized square slot antenna with Inverted-L strips for UWB applications. *IEEE Antennas Wirel Propagat Lett.* (2011) **10**:369–72. doi: 10.1109/LAWP.2011.2147271
13. Islam S, Latrach M. Design construction and testing of a compact size patch antenna for RFID applications. *Microwave Opti Technol Lett.* (2013) **55**:2920–5. doi: 10.1002/mop.27971
14. Wang W, Meng L, Ji R, Wang Z, Gao J, Liu Y, et al. A cpw-fed dual-beam shorted-patch antenna. *IEICE Electron Express.* (2018) **15**:1–6. doi: 10.1587/elex.15.20180100
15. Shimizu N, Nagatsuma, T. Photodiode-integrated microstrip antenna array for subterahertz radiation. *IEEE Photonics Technol Lett.* (2006) **18**:743–5. doi: 10.1109/LPT.2006.871131
16. Mahdia RAH, Taha SMR. Miniaturization of rectangular microstrip patch antenna using topology optimized metamaterial. *IEICE Electronic Express.* (2017) **14**:1–6. doi: 10.1587/elex.14.20170787
17. Boutayeb H, Denidni TA. Gain enhancement of a microstrip patch antenna using a cylindrical electromagnetic crystal substrate. *IEEE Trans Antennas Propagat.* (2007) **55**:3140–5. doi: 10.1109/TAP.2007.908818
18. Agi K, Mojahedi M, Minhas B, Schamiloglu E. The effects of an electromagnetic crystal substrate on a microstrip patch antenna. *IEEE Trans Antennas Propagat.* (2002) **50**:451–6. doi: 10.1109/TAP.2002.1003380
19. Lechen Y, Xiuli Z, Li H, Fu K, Zhang B. Ultra-wideband multi-frequency terahertz square microstrip patch antenna on hybrid photonic crystal substrate. *J Comput Theor Nanosci.* (2013) **10**:968–73. doi: 10.1166/jctn.2013.2794
20. Zhu XL, Liu B. Wang X. Design of compact mems antenna based on photonic crystal structure. *J Elect Eng Technol.* (2019) **14**:2085–90. doi: 10.1007/s42835-019-00233-7
21. Rodriguez-Berral R, Mesa F, Jackson DR. Excitation of an infinite microstrip line with a vertical coaxial feed. *IEEE Trans Microwave Theor Techniq.* (2008) **56**:1638–48. doi: 10.1109/TMTT.2008.925568
22. El-Raouf HEA, Prakash VVS, Yeo J, Mittra R. FDTD simulation of a microstrip phased array with a coaxial feed. *IEE Proc Microwaves Antennas Propagat.* (2004) **151**:193–8. doi: 10.1049/ip-map:20040269
23. Stutzke NA, Filipovic DS. Four-arm 2nd- mode slot spiral antenna with simple single-port feed. *IEEE Antennas Wirel Propag Lett.* (2005) **4**:213–6. doi: 10.1109/LAWP.2005.851006
24. Pregla, R. The analysis of general axially symmetric antennas with a coaxial feed line by the method of lines. *IEEE Trans Antennas Propagat.* (1998) **46**:1433–43. doi: 10.1109/8.725274
25. Lee CS, Nalbandian V. Planar circularly polarized microstrip antenna with a single feed. *IEEE Trans Antennas Propagat.* (1999) **47**:1005–7. doi: 10.1109/8.777124
26. Jandieri V, Yasumoto K, Toyama, H. Radiation from a line source placed in two-dimensional photonic crystals. *Int J Infrared Millimeter Waves.* (2007) **28**:1161–73. doi: 10.1007/s10762-007-9295-8
27. Lighthill MJ. *Introduction to Fourier Analysis and Generalized Functions*. Cambridge University Press. doi: 10.1017/CBO9781139171427
28. Yasumoto K, Toyama H, Kushta, T. Accurate analysis of two-dimensional electromagnetic scattering from multilayered periodic arrays of circular cylinders using lattice sums technique. *IEEE Trans Antennas Propag.* (2004) **52**:2603–11. doi: 10.1109/TAP.2004.834440
29. Yasumoto K, Jia, H. Modeling of pfshotonic crystals by layered periodic arrays of cylinders. *Electromag Theor Appl Photonic Cryst.* (2005) **3**:123–90. doi: 10.1201/9781315221106-3
30. Brekhovskikh LM. *Waves in Layered Media*. 2nd ed. Oxford: Academic Press (1980).

Conflict of Interest: The authors declare that the research was conducted in the absence of any commercial or financial relationships that could be construed as a potential conflict of interest.

ORIGINAL RESEARCH
published: 30 September 2020
doi: 10.3389/fphy.2020.582692

Broadband and High-Efficiency Excitation of Spoof Surface Plasmon Polaritons Through Rectangular Waveguide

Wenxuan Tang†, Jiangpeng Wang†, Xiaotian Yan, Junfeng Liu, Xinxin Gao, Lepeng Zhang and Tie Jun Cui**

State Key Laboratory of Millimeter Waves, School of Information Science and Engineering, Southeast University, Nanjing, China

Spoof surface plasmon polaritons (SPPs) are highly localized surface waves that can be supported on metal surfaces with subwavelength decorations. Mode matching and momentum matching have been investigated so as to efficiently excite the spoof SPPs through conventional planar waveguides (WGs) such as the microstrip (MS) line and the co-planar waveguide (CPW). In this work, a smooth and wideband bridge between the conventional rectangular waveguide and the plasmonic waveguide of spoof SPPs has been proposed and experimentally demonstrated. High efficiency is achieved in both simulation and experiment in a wide frequency range from 12 to 18 GHz. The high-efficiency and broadband excitation of spoof SPPs through rectangular waveguide has great potentials in microwave, millimeter-wave and terahertz circuits, and systems.

Keywords: spoof surface plasmon polaritons, microwave, rectangular waveguide, excitation, mode transition

OPEN ACCESS

Edited by:
Fei Gao,
Zhejiang University, China

Reviewed by:
Zhuo Li,
Nanjing University of Aeronautics and Astronautics, China
Kuang Zhang,
Harbin Institute of Technology, China

***Correspondence:**
Wenxuan Tang
wenxuant@seu.edu.cn
Tie Jun Cui
tjcui@seu.edu.cn

†These authors have contributed equally to this work

Specialty section:
This article was submitted to Optics and Photonics, a section of the journal Frontiers in Physics

Received: *13 July 2020*
Accepted: *21 August 2020*
Published: *30 September 2020*

Citation:
Tang W, Wang J, Yan X, Liu J, Gao X, Zhang L and Cui TJ (2020) Broadband and High-Efficiency Excitation of Spoof Surface Plasmon Polaritons Through Rectangular Waveguide. Front. Phys. 8:582692. doi: 10.3389/fphy.2020.582692

INTRODUCTION

Surface plasmon polaritons (SPPs) exist on the interface of two media (e.g., metal and the air) with opposite permittivities at optical frequencies [1]. When the electromagnetic (EM) field of incident waves interacts with the plasma of electrons near the surface of the metal, collective oscillations are excited, and propagate along the interface as a special type of surface wave. The SPPs possess some inherent characteristics such as strong confinement of EM field and sub-wavelength resolution, and hence have been developed in surface plasmon-based circuits for the purpose of biosensing, microscopy, extraordinary optical transmissions, near-field optics, etc. [2]. However, at lower frequencies such as terahertz and microwave, metals behave close to perfectly electric conductors (PECs) rather than plasmas. Due to this fact, "spoof" (or "designer") surface plasmon polaritons, which could be considered as one special type of metamaterials, have been created below the far-infrared frequency so as to obtain the SPP-like dispersion and propagation properties. The spoof SPPs are realized on metallic surfaces with sub-wavelength decorations [3], and have been experimentally demonstrated to inherit the features of natural SPPs in both the microwave and terahertz regimes [4–6].

Most recently, circuits composed of planar waveguides of spoof SPPs have been intensively investigated in microwave engineering for the development of compact circuits and advanced systems [7]. In particular, the spoof SPP transmission lines (TLs) are expected to offer new solutions for highly-integrated and reconfigurable circuits in view of their designable dispersion characteristics, extraordinary field confinement, sub-wavelength resolution, low cross-talks, and low interference with incident EM waves [8–10]. However, because of mode and momentum mismatch, the spoof SPP TL cannot be efficiently fed with monopoles in free space or coaxial cables or waveguides in which only guided-wave modes are supported. Instead, transitions from conventional TLs such as the coplanar waveguide (CPW), the microstrip (MS) line, and the substrate integrated waveguide (SIW) have been proposed so as to realize high-efficiency excitation of the spoof SPPs [11–13]. On the other hand, rectangular waveguides have been widely used in microwave because of their high power capacity and low insertion loss. Due to the increasing demands on high-speed communication in recent years, as well as the fast development of micro-machine, rectangular waveguides have been applied in millimeter wave and submillimeter wave systems as an effective transmission means. Therefore, high-efficiency transition between the rectangular waveguide and the spoof SPP TL is significant for plasmonic circuits in microwave, millimeter wave, and even Terahertz. Investigations have been carried out to excite spoof SPP waves in bulky microwave plasmonic waveguides through the rectangular waveguide and the coaxial one [14–16].

In this paper, we propose a broadband and high-efficiency conversion between the rectangular waveguide and the planar spoof SPP TL. Guided wave in the rectangular waveguide is firstly converted to quasi- transverse electromagnetic (TEM) wave on the microstrip line and then to the transverse-magnetic (TM) wave on the spoof SPP TL. Simulated and measured results have demonstrated that the spoof SPPs could be excited and propagate with high transmission and low reflection from 12 to 18 GHz. This kind of excitation could also be adopted in plasmonic circuits at millimeter wave and Terahertz.

DESIGNING METHOD

Conversion From Guided Wave to Spoof SPPs

Transmission lines composed of metallic grooves can support the propagation of spoof SPPs even if the thickness of metal is nearly infinite [7]. Since the spoof SPPs are collective charge oscillations propagating along the interface, they are essentially TM waves with the wave number being $>k_0$. However, in microwave engineering, TLs are usually fed with coaxial cables or waveguides in which only guided-wave modes are supported. Therefore, there exist problems of momentum and mode mismatch if the spoof SPP TLs are directly fed. To solve this problem, we propose a two-step transition to realize broadband and high-efficiency excitation of the spoof SPPs from rectangular waveguide.

The proposed transition between the rectangular waveguide and the spoof SPPs TL is shown in **Figure 1A** with five sections included. Section I is a standard rectangular waveguide which works in the dominant mode TE_{10}. In this work, the WR-62 waveguide is chosen for demonstration at Ku band. Section II is the stepped ridge which serves to efficiently convert the TE_{10} mode in the rectangular waveguide to the quasi-TEM mode in the microstrip line. The thickness, length and height of every ridge are described as jk, $L_i(i = 1, 2, 3, 4)$ and $d_i(i = 1, 2, 3, 4)$, respectively, as is shown in **Figure 1B**. Section III is the converting structure between the microstrip line and the spoof SPP TL with seven gradient grooves. **Figure 1C** gives the geometric description of the groove depth $h_i(i = 1, 2, \cdots, 7)$, thickness of metal $wh = 0.018$ mm and thickness of the substrate $jh = 0.406$ mm. In this section, the propagating mode is converted from quasi-TEM mode to TM mode. Section IV is the pure spoof SPP TL composed of uniform grooves. Two detailed units are illustrated in **Figure 1D**, with the groove

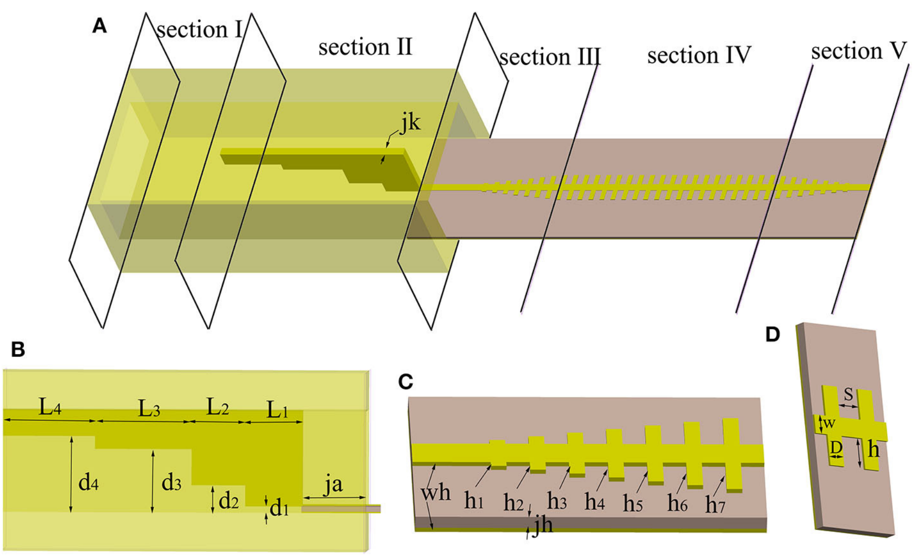

FIGURE 1 | (A) The proposed conversion between the rectangular waveguide and the spoof SPPs TL. **(B)** Section II, the detail and geometric parameters of the stepped ridge. **(C)** Section III, the detail and geometric parameters of the seven gradient grooves. **(D)** Two unit cells in section IV.

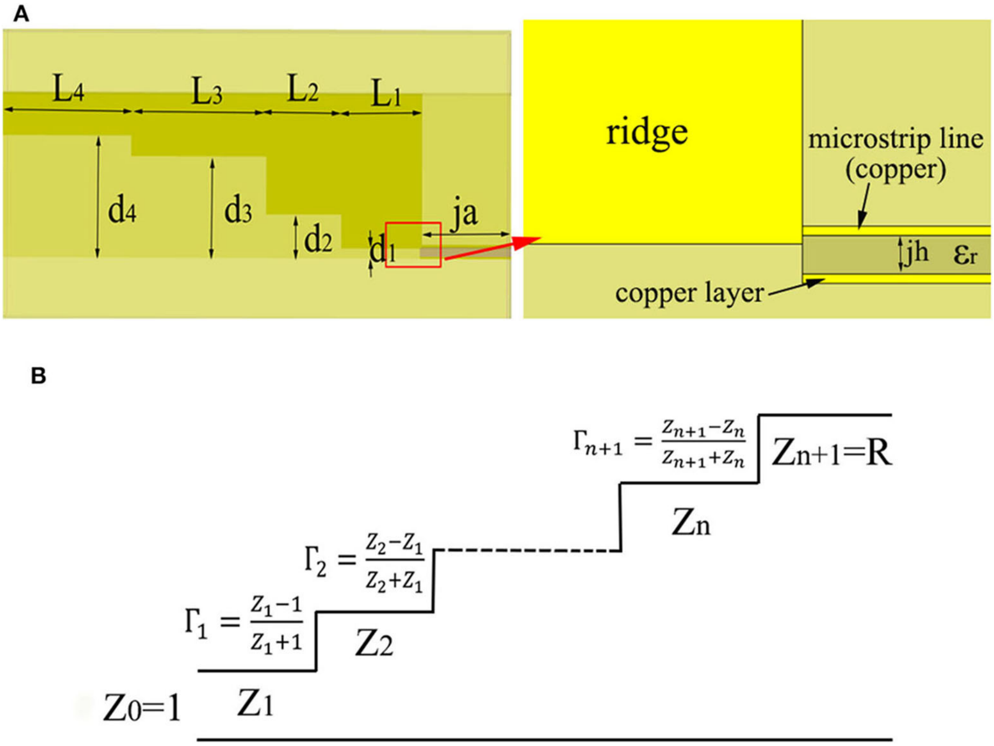

FIGURE 2 | (A) Side-view of the stepped ridge (left) and the details at the junction between the ridge and the microstrip line (right). **(B)** Schematic diagram of the quarter-wavelength multi-section impedance converter.

depth being h, the groove width S, the period $(S + D)$ and the width of strip w. Section V is the counterpart of section III, converting the spoof SPP TL to the microstrip line at the output so that the transmission performance can be easily tested.

Transition Between the Rectangular Waveguide and the Microstrip Line

Mode conversion and impedance matching between the rectangular waveguide and the microstrip line is achieved through stepped ridges, whose geometric features are depicted in **Figure 2A**. The principle of multi- quart-wavelength impedance transformation is applied, as sketched in **Figure 2B**. In this design, a four-step ladder ridge transition was adopted. By adjusting the length $L_i(i = 1, 2, 3, 4)$, height $d_i(i = 1, 2, 3, 4)$, and the ridge thickness jk, one is able to flexibly adjust the impedance of the stepped ridge and achieve impedance matching at multiple operating frequencies, that is, to achieve a smooth and efficient transition between the waveguide and the microstrip line, and to widen the operating frequency band for broadband application.

Parameter study was carried out in the commercial software of CST so as to optimize the transition between the rectangular waveguide and the microstrip line in the entire Ku band. It was found that the reflection, which is represented by S11, is mainly determined by d_1, L_1 and jk at the first ridge. **Figure 3A** indicates that in order to minimize the reflection in the entire working band, d_1 should be neither too large nor too small. In other words, the bottom of the first ridge should be slightly lower than the top of the strip of the microstrip line. It is also observed in **Figure 3B** that the length of the first step ridge L_1 has an optimal value around 4.6 mm. When L_1 varies from the optimal value, the reflection increased accordingly. **Figure 3C** shows that the reflection and bandwidth is also sensitive to the thickness of the ridge jk. Finally, we optimized these three parameters together to make sure that S_{11} is lower than −15 dB and S_{21} is higher than −0.5 dB from 12.77 to 17.46 GHz, as is plotted in **Figure 3D**. It is noted that as the impedance matching is designed at the center frequency, the reflection and insertion loss increase slightly at the upper and lower side-bands.

The above designed stepped ridge is demonstrated to effectively transfer the TE_{10} mode in the rectangular waveguide to the quasi-TEM mode in the microstrip line. **Figure 4** demonstrates the mode conversion visually. In the rectangular waveguide, electric and magnetic field distributions of TE_{10} mode are observed clearly. On the right side of the stepped ridge, there is only negligible longitudinal component of

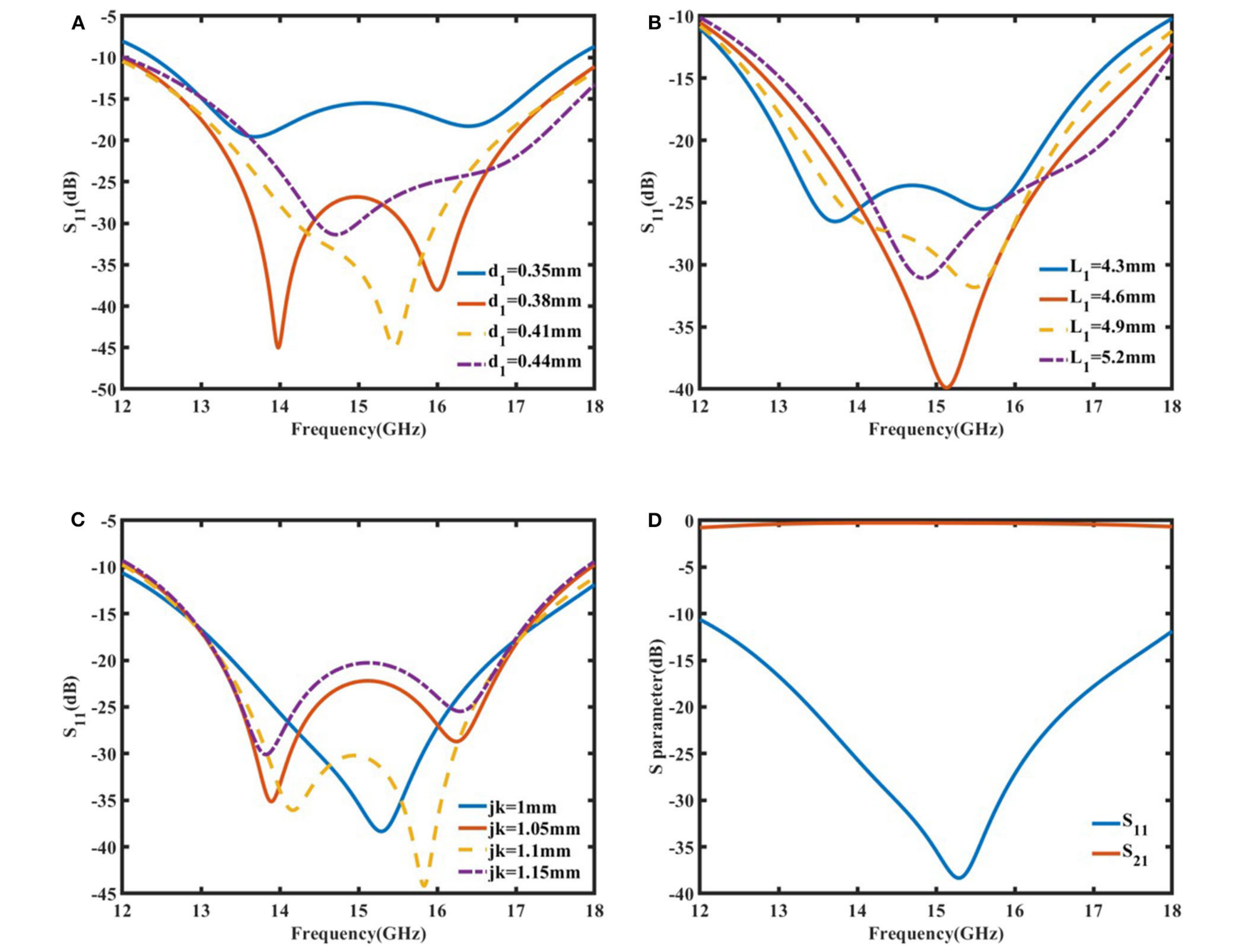

FIGURE 3 | The simulated reflection (S_{11}) when **(A)** the height d_1, **(B)** the length L_1, and **(C)** the thickness jk of the first ridge are changed. **(D)** The simulated reflection (S_{11}) and transmission (S_{21}) from the rectangular waveguide to the microstrip line when $d_1 = 0.42\ mm,\ L_1 = 4.8\ mm,\ jk = 1\ mm$.

electromagnetic field, indicating the quasi-TEM mode of the microstrip line.

Transition Between the Microstrip Line and the Spoof SPP TL

Grounded metallic grooves are designed to support the propagation of spoof SPPs. By modifying geometric parameters in the unit (e.g., S, D, h in **Figure 1D**), one is able to design the dispersion curve of spoof SPPs. It has been investigated that as the operating frequency approaches the cut-off frequency, the attenuation of the spoof SPP TL increases accordingly [17]. Therefore, the dispersion curve is investigated in Eigen-mode simulation and the cut-off frequency is set to about 25 GHz so that the designed spoof SPP TL presents high transmission from 12 to 18 GHz.

For the purpose of impedance and momentum matching, transition section is needed between the microstrip line and the spoof SPP TL. It is noticed that the groove depth h has significant impact on the dispersion curve, as is plotted in **Figure 5A**, that as h increases the dispersion curve deviates quickly from the light line. In view of this, seven gradient grooves have been designed in the transition section with the groove depth $h_i = ih/8\,(i = 1, 2, \cdots, 7)$ increasing evenly. The simulated S-parameters are shown in **Figure 5B**. In the entire Ku band, S_{11} is below -19 dB and S_{21} is above -1.2 dB. The insertion loss increases slightly as the frequency goes up toward the cut-off frequency, because the stronger field confinement results

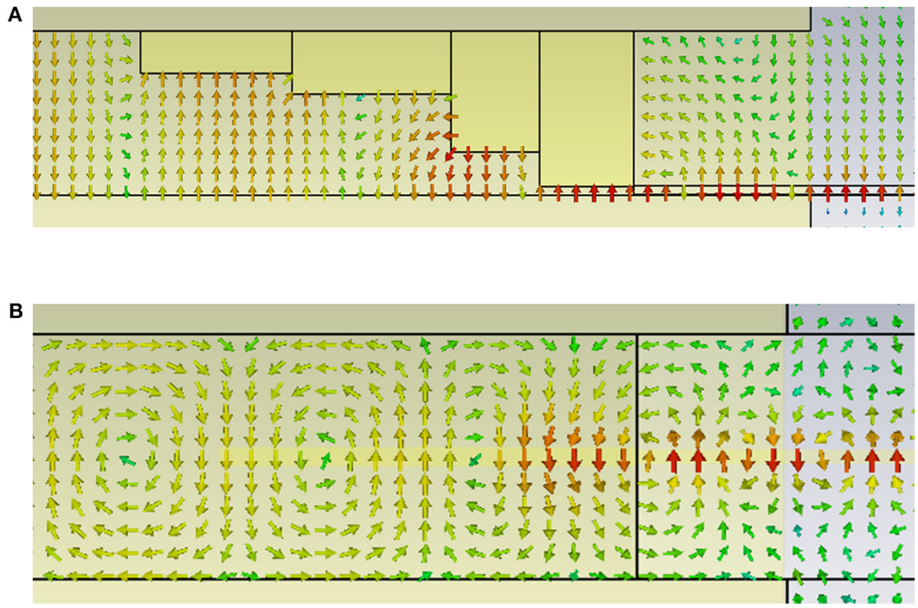

FIGURE 4 | Mode conversion from the rectangular waveguide to the microstrip line with stepped ridge. **(A)** (side view) Distribution of the electric field. **(B)** (top view) Distribution of the magnetic field.

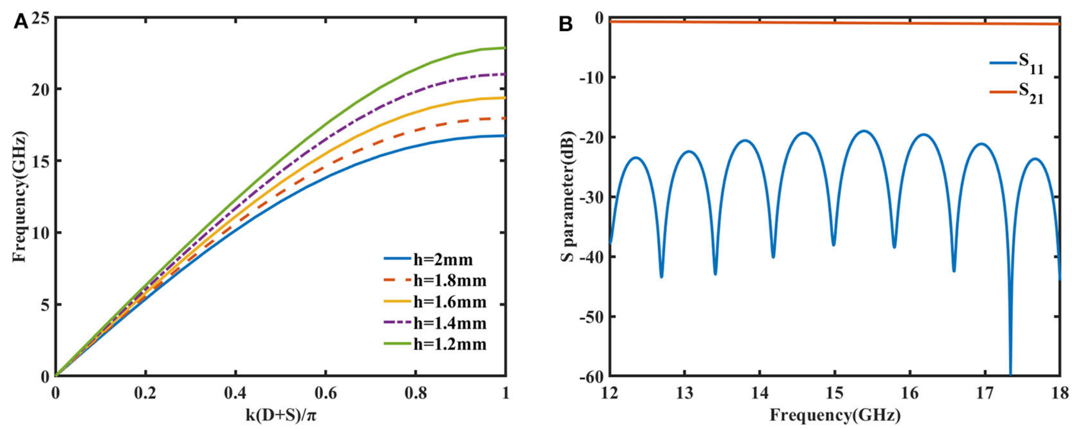

FIGURE 5 | (A) The dispersion curves of the spoof SPPs when the depth of groove *h* varies. **(B)** The simulated *S* parameters from the microstrip line to the spoof SPP TL when seven gradient grooves are adopted as the transition section.

in more loss in metal and dielectric substrate. Overall, the transition between the microstrip line and the spoof SPP TL is smooth with high transmission and low return loss.

The proposed gradient grooves gradually transform the quasi-TEM wave in microstrip line to the TM mode spoof SPPs. **Figure 6** gives the simulated electric and magnetic field distributions. Due to the existence of the grooves, the electric field gradually appears to have the longitudinal component, as is observed in **Figure 6A**. In contrast, the magnetic field in **Figure 6B** is always in the transverse plane, which guarantees the transverse magnetic mode of spoof SPPs.

FABRICATION AND EXPERIMENT

A prototype of the design is fabricated and measured for demonstration. A WR-62 standard rectangular waveguide with stepped ridges is manufactured using copper and assembled from three separately machined parts. The microstrip line and the spoof SPP TL are printed on the substrate of Rogers RO4003C with a thickness of 0.406 mm and the relative permittivity of 3.55. The ground of the TLs is seated on the bottom inner wall of the rectangular waveguide using two plastic screws, as is shown in **Figure 7**, so as to stably locate and assemble the TLs and the rectangular waveguide. Detailed parameters after optimization are listed in **Table 1** for the readers' information.

In measurement, the rectangular waveguide is connected to Port One of an Agilent Vector Network Analyzer (VNA) through a coaxial cable and a flange. At the output (on the right side in **Figure 7**), the microstrip line is connected to an SMA connector and then to Port Two of the VNA. The Scattering parameters are measured and plotted in **Figure 8**. It is observed that the measured reflection (S11) is always below −10 dB from 12 to 18 GHz, and below −15 dB from 12.3 to 17.75 GHz. The measured S11 curve is similar to the simulated one except for a slight shift to the higher frequency. Considering that the reflection is sensitive to some geometric parameters, e.g., d_1 and jk as shown in **Figure 3**, the slight difference between the simulated and measured results is mainly because of the inaccuracy during machining of the waveguide and assembling of the samples. On the other hand, the measured transmission coefficient (S21) is above −3.5 dB from 12 to 17.9 GHz, and above −3 dB from 12.3 to 17.2 GHz. It has been discussed above that in simulation the insertion loss comprises the losses in the two-step transition. In measurement, the S21 curve is as flat as the simulated one, although with a further reduction of about 1.5 dB. This further reduction may be due to the fabrication and assembling error of the prototype, or the loss of metal and substrate at Ku band. Nevertheless, the measured results have

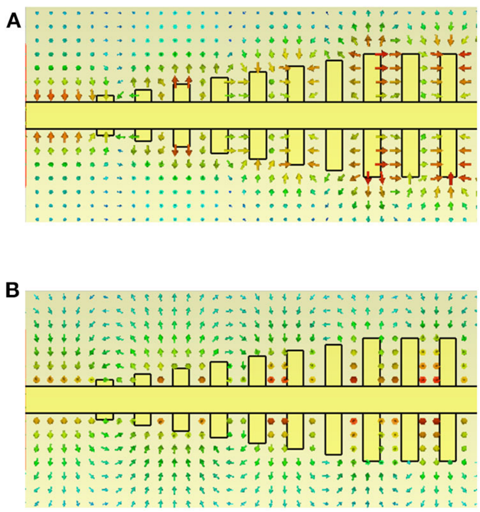

FIGURE 6 | Mode conversion from the microstrip line to the spoof SPP TL (top view). **(A)** Distribution of the electric field. **(B)** Distribution of the magnetic field.

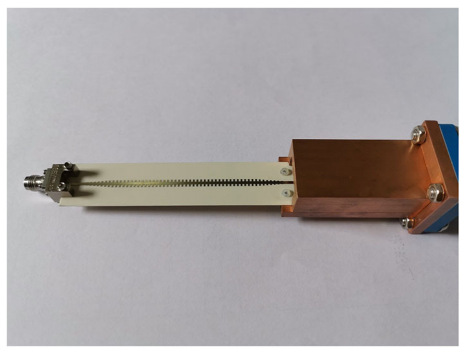

FIGURE 7 | Photo of the fabricated prototype.

TABLE 1 | Optimized parameters for the design.

Parameter	Value (mm)	Description	Parameter	Value (mm)	Description
a	15.8	Length of broad side of waveguide	b	7.9	Length of narrow side of waveguide
c	50	Length of waveguide	abh	3	Thickness of waveguide
L_1	4.8	Length of the 1st ridge	d_1	0.42	Height of the 1st ridge
L_2	4.5	Length of the 2nd ridge	d_2	2.05	Height of the 2nd ridge
L_3	8.1	Length of the 3rd ridge	d_3	4.85	Height of the 3rd ridge
L_4	7.7	Length of the 4th ridge	d_4	5.85	Height of the 4th ridge
jk	1	Thickness of ridge	w	0.92	Width of the microstrip
wh	0.018	Thickness of copper	jh	0.406	Thickness of substrate
ja	5.4	Length of MS inserted in WG	jb	15.8	Width of substrate
s1	3	Length of MS not inserted in WG	h	1	Depth of the groove
D	0.6	Width of the sawtooth	S	0.9	Width of the groove
m	7	Number of the gradient grooves	n	40	Number of spoof SPP units

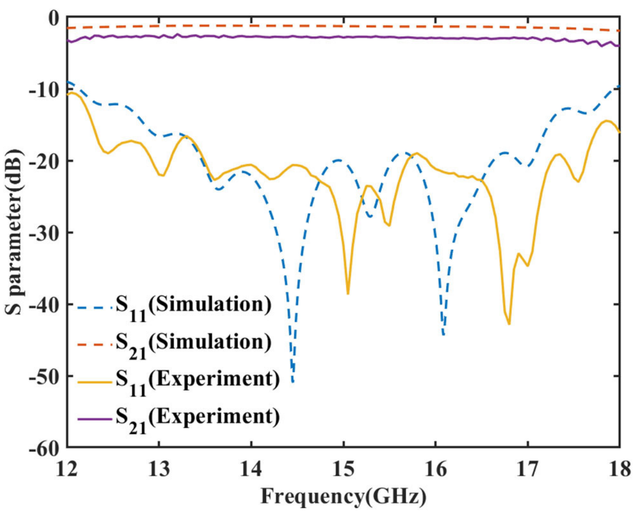

FIGURE 8 | Simulated and measured S parameters.

proved the broadband and high-efficiency excitation of spoof SPPs through the rectangular waveguide.

DISCUSSION AND CONCLUSION

In this work, we proposed a method to excite spoof SPPs through conventional rectangular waveguide with high efficiency and wideband performance. This is a two-step procedure with the first transition from the rectangular waveguide to the microstrip line and the second from the microstrip line to the spoof SPP TL. A prototype was designed, fabricated and measured from 12 to 18 GHz for demonstration. Good transmission and low reflection are observed in both simulation and measurement. The proposed scheme can be extended for non-grounded spoof SPP TLs with different transitions from the microstrip line [18]. This method may have great potentials to provide an easy and low-cost way to feed plasmonic circuits at microwave, millimeter wave and Terahertz.

DATA AVAILABILITY STATEMENT

All datasets presented in this study are included in the article/supplementary material.

AUTHOR CONTRIBUTIONS

WT and TC conceived the idea, suggested the designs, and supervised the work. WT and JW conducted the analytical modeling and wrote the manuscript. JW, XY, and JL conducted the numerical simulations and modifications. WT, XG, and LZ conducted sample assembly and measurements. All authors contributed to the article and approved the submitted version.

FUNDING

This work was supported in part from the National Science Foundation of China under Grant nos. 61631007 and 61971134, in part from the 111 Project under Grant no. 111-2-05, and in part from the Fundamental Research Funds for the Central Universities under Grant no. 2242020R40079.

REFERENCES

1. Raether H. *Surface Plasmons on Smooth and Rough Surfaces and on Gratings*. Berlin; Heidelberg: Springer (1988). doi: 10.1007/BFb0048317
2. Maier SA. *Plasmonics: Fundamentals and Applications*. New York, NY: Springer (2007). doi: 10.1007/0-387-37825-1
3. Pendry J, Martin-Moreno L, Garcia-Vidal F. Mimicking surface plasmons with structured surfaces. *Science.* (2004) **305**:847–8. doi: 10.1126/science.1098999
4. Hibbins AP, Evans BR, Sambles JR. Experimental verification of designer surface plasmons. *Science.* (2005) **308**:670–2. doi: 10.1126/science.1109043
5. Maier SA, Andrews SR, Martin-Moreno L, Garcia-Vidal FJ. Terahertz surface plasmon-polariton propagation and focusing on periodically corrugated metal wires. *Phys Rev Lett.* (2006) **97**:176805. doi: 10.1103/PhysRevLett.97.176805
6. Garcia-Vidal FJ, Martin-Moreno L, Pendry JB. Surfaces with holes in them: new plasmonic metamaterials. *J Opt A Pure Appl Opt.* (2005) **7**:S97–101. doi: 10.1088/1464-4258/7/2/013
7. Shen X, Cui TJ, Martin-Cano D, Garcia-Vidal FJ. Conformal surface plasmons propagating on ultrathin and flexible films. *Proc Nat Acad Sci USA.* (2013) **110**:40–5. doi: 10.1073/pnas.1210417110
8. Liu X, Feng Y, Zhu B, Zhao J, Jiang T. High-order modes of spoof surface plasmonic wave transmission on thin metal film structure. *Opt Express.* (2013) **21**:3155–65. doi: 10.1364/OE.21.031155
9. Wu JJ, Hou DJ, Liu K, Shen L, Tsai CA, Wu CJ, et al. Differential microstrip lines with reduced crosstalk and common mode effect based on spoof surface plasmon polaritons. *Opt Express.* (2014) **22**:26777–87. doi: 10.1364/OE.22.026777
10. Liang Y, Yu H, Zhang H,Chang Y, Cui TJ. On-chip sub-terahertz surface plasmon polariton transmission lines in CMOS. *Sci Rep.* (2015) **5**:14853. doi: 10.1038/srep14853
11. Ma HF, Shen X, Cheng Q, Jiang WX, Cui TJ. Broadband and high-efficiency conversion from guided waves to spoof surface plasmon polaritons. *Laser Photonics Rev.* (2014) 8:146–51. doi: 10.1002/lpor.201300118
12. Zhang WJ, Zhu GQ, Sun LG, Lin FJ. Trapping of surface plasmon wave through gradient corrugated strip with underlayer ground and manipulating its propagation. *Appl Phys Lett.* (2015) **106**:021104. doi: 10.1063/1.4905675
13. Zhang Q, Zhang HC, Wu H, Cui TJ. A hybrid circuit for spoof surface plasmons and spatial waveguide modes to reach controllable band-pass filters. *Sci Rep.* (2015) **5**:16531. doi: 10.1038/srep16531
14. Liu LL, Li Z, Xu BZ, Gu CQ, Chen C, Ning PP. High-efficiency transition between rectangular waveguide and domino plasmonic waveguide. *AIP Adv.* (2015) **5**:027105. doi: 10.1063/1.4907879
15. Liu LL, Li Z, Gu CQ, Chen C, Ning PP, Xu BZ, et al. Smooth bridge between guided waves and spoof surface plasmon polaritons. *Opt Lett.* (2015) **40**:1810–3. doi: 10.1364/OL.40.001810

16. Liu LL, Li Z, Xu BZ, Gu CQ, Xu J, Chen C, et al. Ultra low loss high-contrast gratings based spoof surface plasmonic waveguide. *IEEE Trans Microw Theory Tech*. (2017) **65**:2008–18. doi: 10.1109/TMTT.2017.2662235
17. Zhang HC, Zhang Q, Liu JF, Tang WX, Fan YF, Cui TJ. Smaller-loss planar SPP transmission line than conventional microstrip in microwave frequencies. *Sci Rep*. (2016) **6**:23396. doi: 10.1038/srep23396
18. Kianinejad A, Chen ZN, Qiu CW. Design and modeling of spoof surface plasmon modes-based microwave slow-wave transmission line. *IEEE Trans Microw Theory Tech*. (2017) **63**:1817–25. doi: 10.1109/TMTT.2015.2422694

Conflict of Interest: The authors declare that the research was conducted in the absence of any commercial or financial relationships that could be construed as a potential conflict of interest.

frontiers in Physics

ORIGINAL RESEARCH
published: 08 October 2020
doi: 10.3389/fphy.2020.546528

Influence of Atmospheric Turbulence Channel on a Super-Resolution Ghost Imaging Transmission System Based on Plasmonic Structure Illumination Microscopy

*Kaimin Wang[1], Zhaorui Wang[1], Chunyan Bai[1], Leihong Zhang[1], Bo Dai[1], Yuxing Zhang[1], Hualong Ye[1], Zhisheng Zhang[1], Xiaoxuan Han[1], Tong Xue[1], Meiyong Xu[2], Jiafeng Hu[3], Xiangjun Xin[2] and Dawei Zhang[1]**

[1] Ministry of Education and Shanghai Key Lab of Modern Optical System, Engineering Research Center of Optical Instrument and System, University of Shanghai for Science and Technology, Shanghai, China, [2] School of Electronic Engineering, Beijing University of Posts and Telecommunications, Beijing, China, [3] School of Physics and Electronics, East China Normal University, Shanghai, China

OPEN ACCESS

Edited by:
Wei E. I. Sha,
Zhejiang University, China

Reviewed by:
Jianming Wen,
Kennesaw State University,
United States
Nirmal Mazumder,
Manipal Academy of Higher
Education, India

***Correspondence:**
Dawei Zhang
dwzhang@usst.edu.cn

Specialty section:
This article was submitted to
Optics and Photonics,
a section of the journal
Frontiers in Physics

Received: 28 March 2020
Accepted: 25 August 2020
Published: 08 October 2020

Citation:
Wang K, Wang Z, Bai C, Zhang L, Dai B, Zhang Y, Ye H, Zhang Z, Han X, Xue T, Xu M, Hu J, Xin X and Zhang D (2020) Influence of Atmospheric Turbulence Channel on a Super-Resolution Ghost Imaging Transmission System Based on Plasmonic Structure Illumination Microscopy. Front. Phys. 8:546528. doi: 10.3389/fphy.2020.546528

Ghost imaging is a novel imaging technique that has various advantages over traditional imaging. However, most of the existing works on this technique do not achieve a better resolution than the diffraction limit. In this work, we presented a ghost imaging system with plasmonic structure illumination microscopy that achieved super-resolution imaging. The resolution reaches three to four times of the diffraction limit with surface plasmon polaritons and structure illumination microscopy theory. Since it can produce super-resolution images, this method has important implications in medical fields, such as in microimaging and endoscopy. We used the gamma–gamma intensity-fluctuation model to simulate the ghost imaging system in an atmospheric turbulence channel. By setting proper values of the transmission distance and refractive-index structure parameter, we obtain the peak signal-to-noise ratio (PSNR) performance and symbol-error rate (SER) performance. Finally, the PSNR and SER are used to evaluate the imaging quality, which provides a theoretical model to research the ghost-imaging algorithm further.

Keywords: surface plasmon polaritons, structure illumination microscopy, ghost imaging, super-resolution, atmospheric turbulence, gamma-gamma model

INTRODUCTION

Ghost imaging is a new quantum imaging technology that advances with the development of quantum technology. It utilizes the properties of quantum entanglement to achieve non-local image transmission [1]. Ghost imaging has various advantages over traditional optics due to the existence of correlation characteristics, such as anti-interference ability, weak optical imaging capability [2–4], and encryption capability. However, since ghost imaging is transmitted through the optical path, the resolution remains limited by optical diffraction conditions.

Ghost imaging has attracted significant attention in the field of image transmission [1–12]. It has been continuously developed in recent years, from entangled photon pair [1] to thermal sources [5], from traditional ghost imaging to computational ghost imaging (CGI) [6]. In addition, many improved methods have been proposed, such as compressed sensing [7] and differential correlation imaging [8]. With the improvement of image quality, super-resolution imaging has always been a focus of research. Ermeydan et al. proposed a millimeter-wave-based compression-sensing super-resolution algorithm [9]. A new compressive imaging approach using a strategy called cake cutting, which optimally reorders the deterministic Hadamard basis, is also reported [10]. Deep learning with computational correlation imaging was combined to achieve super-resolution [11]. These ghost imaging super-resolution methods perform super-resolution imaging at the software level, such as encoding and restoration algorithms; however, they have not been improved from the hardware level. Recently, two colors of light were used for imaging to achieve super-resolution, which refers to two-photon microscope imaging [12].

Plasmonic structure illumination microscopy (PSIM) is a super-resolution imaging technology with great research value. As a combination of structure illumination microscopy (SIM) technology and dynamically controllable surface plasmon polaritons (SPPs) field, it can improve the resolution significantly. It has the advantages of super-resolution, wide field, and fast imaging [13, 14], which has been used in the super-resolution enhancement of Raman spectral signals [15]. Combining the above two technologies, one can design a method for detecting or imaging objects in the micro- or nanoscale.

In this study, we applied PSIM to ghost imaging to achieve super-resolution imaging. The ghost imaging is based on the surface-to-point single image transmission of the CGI. After the process of encoding, transmittance, reception, and reconstruction, the final resolution can reach three to four times of the diffraction limit. This work has great implications in biomedical fields such as microscopic imaging and endoscopy.

The rest of this paper is organized into three sections: The theories of ghost imaging, PSIM, and atmospheric turbulence channel are presented in *Theory of Computational Ghost Imaging*, *Theory of Plasmonic Structure Illumination Microscopy*, and *Theory of Atmospheric Turbulence Channel Model*, respectively. *Theory of Ghost Imaging Based on Plasmonic Structure Illumination Microscopy* contains the scheme for the ghost imaging system under the gamma–gamma atmospheric turbulence channel. The results of the peak signal-to-noise ratio (PSNR) and symbol-error rate (SER) simulations and the measurement of the performance of proposed scheme are presented in *Simulation and Results*. The PSNR and SER performance are determined by the refractive-index structure parameter C_n^2 and the transmission distance d, as further discussed in *Analysis of the Influence under Different Conditions of Transmission Distance* and *Analysis of the Influence under Different Conditions of Refractive-Index Structure Parameter*. The conclusion of this research is presented in *Conclusion*.

THEORY

Theory of Computational Ghost Imaging

Ghost imaging is a new type of imaging technique; it can acquire the target image information non-locally by calculating the intensity correlation function between the reference light and the detection light. It is also known as correlated imaging or two-photon imaging. Unlike classical optical imaging, ghost imaging can be independent of the light speed. This is an important feature of ghost imaging, which distinguishes quantum optics from classical theory.

Traditional ghost imaging requires two optical paths. The requirement will cause some operational problems, such as experimental difficulties and large space occupation. To solve these problems, Shapiro proposed CGI [16], which was further improved by Bromberg et al. [17]. Instead of rotating the ground glass, they applied a spatial light modulator to simplify the two light paths into one. Then, Duarte successfully realized CGI with the digital micromirror device (DMD) [18]. The schematic of CGI is shown in **Figure 1**.

The two most important devices in CGI are the digital micromirror device (DMD) and the bucket detector [19]. The device modulates the light from the laser by loading a series of random modulation matrices $\varphi_i(x, y)$ onto the DMD. Then, the light is transmitted through the object $T(x, y)$ and detected by the bucket detector (only the total light intensity of the transmitted object is detected, without any resolution). The total intensity R_i, where i refers to the sample number, is calculated as

$$R_i = \int dxdy\varphi_i(x, y) \times T(x, y) \tag{1}$$

After sampling N times, the modulation matrix and the value from the bucket detector are correlated. Finally, the image of the object is reconstructed. The correlation function $C_{CGI}(x, y)$ is expressed as [20]:

$$C_{CGI} = \frac{1}{N}\sum_{i=1}^{N}(R_i - \langle R\rangle)\varphi_i(x, y) = \langle R\phi(x, y)\rangle - \langle R\rangle\langle\varphi(x, y)\rangle \tag{2}$$

Here, $\langle R\rangle$ is the average value of light intensity.

Theory of Plasmonic Structure Illumination Microscopy

The plasmonic structure illumination microscopy technology is a proposed far-field super-resolution microimaging technology that has been gaining attention in recent years. It has the characteristics of wide field, super-resolution, and fast imaging; therefore, it is of great research value with excessive application prospects. The development of PSIM was inspired by two technologies, namely, surface plasmon polaritons and structure light imaging. Both can improve the imaging resolution; however, the principle of improving the resolution is different. For instance, to improve the resolution, the former breaks through

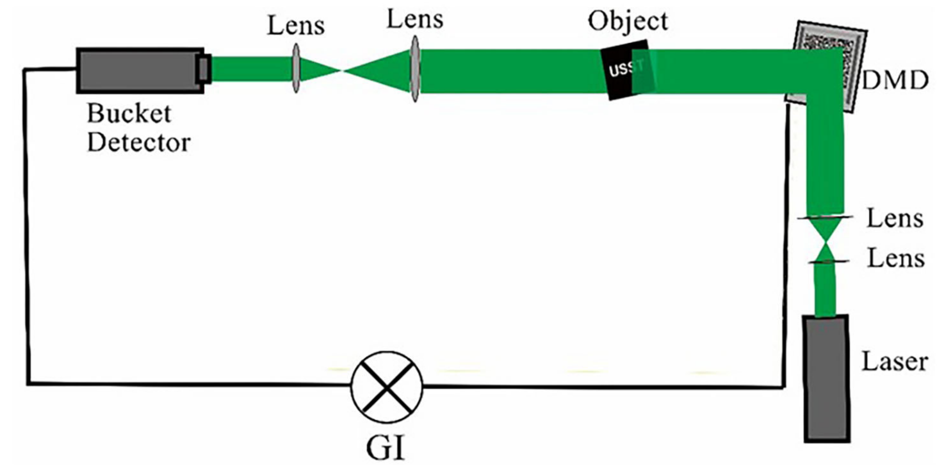

FIGURE 1 | Schematic of computational ghost imaging system, which consists of laser digital micromirror device (DMD) and bucket detector.

the diffraction limit by the wavelength of SPPs, while the latter uses the high-frequency information through the structure algorithm. Therefore, combining the two techniques can further improve the resolution of the imaging.

Theory and Excite Method of Surface Plasmon Polaritons

SPPs are a type of collective oscillation electromagnetic mode formed by the resonance of photons and free electrons in a metal surface—that is, it is a mixed excited state formed by the coupling of electrons and photons [21]. SPPs are a surface wave propagating along the metal surface, and its field strength decays exponentially in the direction perpendicular to the surface. Due to the characteristics of breaking the diffraction limit, near-field enhancement, and surface localization, SPPs has a wide application prospect in optical imaging, super-resolution nano-lithography, micro–nanophotonics, information processing, biomedical, and other fields [22]. As a result, it has attracted much attention in the past decade.

SPPs are the electromagnetic field generated by the resonance coupling: when light waves are incident on the interface between metal and other media, the oscillation frequency of the electrons is consistent with the frequency of the incident light waves; then, resonance occurs and forms a special surface electromagnetic mode that strengthens the incident field by several orders of magnitude. SPPs is a mixed mode of surface electromagnetic waves and free-electron oscillations generated by the interaction between light and metal on the metal surface, as shown in **Figure 2**. The wavelength of the light passing through the SPPs is smaller than that of the incident light.

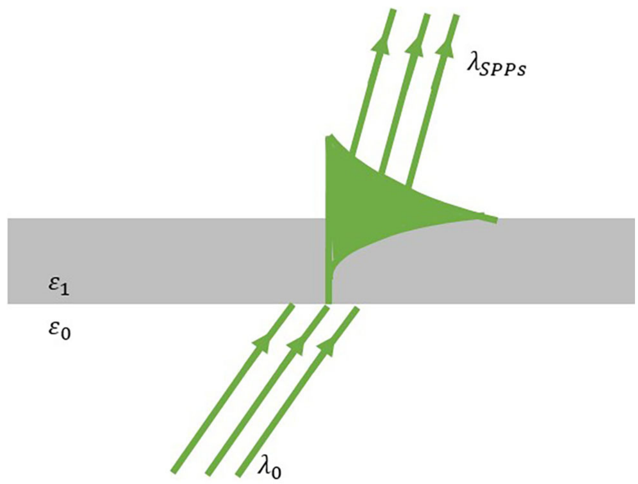

FIGURE 2 | Schematic for surface plasmon polaritons (SPPs) at the metal–dielectric interface.

However, the incident beams cannot be directly coupled to form the SPPs on the metal surface. According to the dispersion equation of the SPPs on the semi-infinite metal–dielectric interface [23], in the range of visible and near-infrared wavelengths, the wave vector of the SPPs is larger than that of the light in free space. Therefore, to excite SPPs effectively, the wave vector of the excitation beam must be compensated to match the wave vector of the SPP. The wave vector matching is the key condition for SPPs excitation. Commonly used excitation methods for SPPs are the prism coupling method, near field scattering excitation method, tight focus excitation method, and grating excitation method, which are shown in **Figure 3**.

Prism coupling method [24] is a simple and effective method with the advantages of low loss and high coupling accuracy. It is widely used in the field of biophotonics sensing. However, the size of the system is too large to be applied to optical integrated devices. The method of near-field scattering excitation [25] can realize the excitation of SPPs without being restricted by the wave vector matching conditions. The principle of the tight focus coupling is that a high numerical aperture microscope objective is utilized to increase the incident angle of the excitation beam.

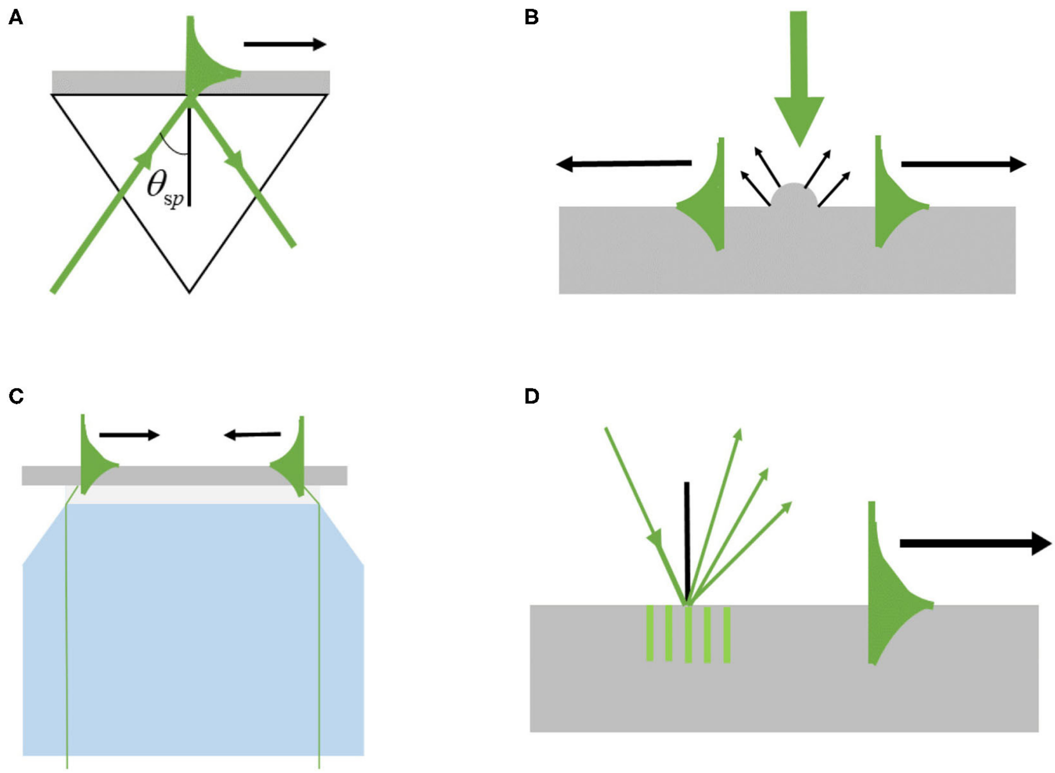

FIGURE 3 | Common excitation methods for surface plasmon polaritons (SPPs). **(A)** Prism-coupled excitation; **(B)** Near-field scattering excitation; **(C)** Tight focus excitation; **(D)** Grating excitation.

If the maximum incident angle is greater than the total reflection angle, SPPs can be excited on the metal surface by part of the light field satisfying the excitation condition [26]. Because it can be integrated with traditional microscopy systems and the metal film can be replaced at any time, it is widely used in imaging. The method of grating coupling excitation adds an additional grating vector to the wave vector in free space. This method excites SPPs with high efficiency, and the compact structure allows the grating to be applied to photoelectric surface plasma devices [27]. In this study, the grating excitation method with a slit array is used to excite SPPs.

The SPPs waves propagating along the interface between metal and air can be generated by exciting the grating. When the z-direction is defined to be perpendicular to the air–metal interface, the z-component of the SPPs wave at distance r along the x–y plane can be expressed as [28–30]

$$E_z(r,t) = E_{SPP}\exp\left[i\left(k_{SPP}r - \omega t\right) + i\phi_{SPP}\right]\exp\left(-\frac{r}{2L_{SPP}}\right) \tag{3}$$

where ω is the angular frequency of the incident beam, ϕ_{SPP} is the phase of the SPPs wave, and k_{SPP} is the SPPs wave vector.

According to Equation (3), two counter-propagating SPP waves are generated through exciting two independent parallel gratings and interfere with each other in the middle area to form an SPPs standing wave. When the distance between the two gratings is $2r$, the expression of SPPs standing wave is [31]

$$E_z^{1,2}(r,t) = 2E_0\cos\left(\frac{\phi_{SPP1} - \phi_{SPP2}}{2}\right)\exp\left(i\frac{\phi_{SPP1} + \phi_{SPP2}}{2}\right) \tag{4}$$

where $E_0 = E_{SPP}\exp\left(-r/2L_{SPP}\right)\exp\left[i\left(k_{SPP}r - \omega t\right)\right]$, and ϕ_{SPP1} and ϕ_{SPP2} are the phases of the two SPPs waves, respectively. From Equation (4), the electric field intensity of the SPPs standing wave at the center of the structure depends on the phase difference of the two SPPs waves. However, the phase difference of the SPPs wave is related to the phase difference of the incident beam. When two gratings are illuminated by two beams with the same polarization directions, respectively, the phase difference between two SPPs waves can be expressed as

$$\phi_{SPP1} - \phi_{SPP2} = (\phi_1 - \phi_2) + \pi \tag{5}$$

where ϕ_1 and ϕ_2 are the phases of the two excitating beams, respectively. It can be seen from Equation (5) that the SPPs standing wave can be dynamically moved by adjusting the phase of the incident beams. In addition, because two SPPs wave propagate in the opposite directions and with the same field strength, the transverse electric field components from two SPPs waves will counteract. The light intensity of the standing wave can be expressed as

$$I_0 = \left[E_z^{1,2}(r,t)\right]^2 \tag{6}$$

Therefore, based on the characteristics of the breaks, diffraction limit, field enhancement, and flexible movement, the SPPs standing wave can be combined with SIM technology to improve the resolution of imaging further.

Principles of Structure Illumination Microscopy

SIM is a far-field super-resolution optical imaging technology. By employing specific structured light as the illuminating light, it can obtain high-frequency information and break the diffraction limit. Structure illumination imaging technology was first realized by adding a sinusoidal grating in the illumination light path [32], and the piezoelectric ceramic controller was used to move the grating to achieve the phase shift of the structured light; however, this mechanical moving device reduced the stability of the system. In the later stage, the spatial light modulator [33–35] and digital micromirror device [36], which can be controlled dynamically, are used instead of the grating to realize structured light illumination. Structured light illumination has the ability of tomographic imaging; it uses the moire fringes formed by the frequency components of structured light and sample to improve the resolution. By irradiating the object with the structure light modulated by space, encoding the high-frequency information of the object field space, and extracting the high-frequency information by calculation, the resolution can be increased to twice the diffraction limit frequency. Note that the imaging resolution value and the structure light wave vector are positively correlated; therefore, increasing the structure light wave vector improves the system's ability to receive high-frequency information, which also improves the spatial resolution of the imaging.

Because the structured light illumination frequency and source image frequency are both limited by the system's diffraction limit frequency, the output of the system is expressed as [37]:

$$\begin{aligned} D(k) &= I_0\left\{\frac{1}{2}e^{i\varphi}T(k-k_0)+T(k)+\frac{1}{2}e^{-i\varphi}T(k+k_0)\right\}\cdot F_{OT} \\ &= \frac{1}{2}I_0e^{i\varphi}D_{N-}(k-k_0)+I_0D_N(k)+\frac{1}{2}I_0e^{-i\varphi}D_{N+}(k+k_0) \end{aligned} \tag{7}$$

where I_0 is the average intensity, φ is the initial phase, and k_0 is the fringe spatial frequency (reciprocal of the fringe period). $D(k)$ represents the information recorded by the CCD, where D_N is the low-frequency information, which reflects the outline of the object; D_{N-} and D_{N+} are high-frequency information, which reflect the details of the object.

The SIM system obtains the mixed information of low- and high-frequency information beyond the diffraction limit. To recover the image, the low-frequency and two high-frequency information should be separated first, and then, the high-frequency information should be moved back to the corresponding position and fused with the low-frequency information. Finally, the super-resolution image can be recovered using a deconvolution operation [38]. Due to the need for separating the spectrum components, the phase is evidently the most appropriate modulation parameter. The reconstruction of SIM with three different initial phases are expressed as [39]:

$$\begin{bmatrix} T(k) \\ T(k+k_0) \\ T(k-k_0) \end{bmatrix} = \begin{bmatrix} I_0 & \frac{I_0}{2} & \frac{I_0}{2} \\ I_0 & \frac{I_0}{2}e^{i\varphi_1} & \frac{I_0}{2}e^{-i\varphi_1} \\ I_0 & \frac{I_0}{2}e^{i\varphi_2} & \frac{I_0}{2}e^{-i\varphi_2} \end{bmatrix}^{-1} \begin{bmatrix} D(k) \\ D(k+k_0) \\ D(k-k_0) \end{bmatrix} \tag{8}$$

After the reconstruction of the SIM algorithm, the maximum spatial frequency of the system can reach twice the diffraction limit. However, it is only scanning in a single direction that may lead to information leakage. Generally, SIM reconstruction will be carried out again in the intersection direction to realize the information reconstruction of the whole plane. Finally, the resolution will be doubled.

Basic Principles of Plasmonic Structure Illumination Microscopy

PSIM, combining SIM technology with SPPs, can resolve the resolution of traditional SIM without the help of non-linear effects. The resolution is increased from two times the traditional diffraction limit frequency to three to four times. The SPPs interference fringes are stable standing wave field generated by the interference of two SPPs waves propagating in opposite directions. The fringe period depends on the SPPs wavelength. Because the SPPs wavelength can be much smaller than the wavelength of free space light, the period of the SPPs interference fringes is much smaller than the diffraction limit. Therefore, it can be used as a structured light field that breaks through the diffraction limit and applied to the SIM imaging system. Consequently, as a new type of super-resolution wide-field microscopic imaging technology, PSIM combining the advantages of SIM and SPPs can further improve the imaging resolution [33–35, 40–43]. The design of horizontal and vertical excitation modes on the excitation medium can meet the imaging requirements of SIM in the plane space so that SPPs and SIM can be combined to achieve better super-resolution imaging effects.

The wavelength of the SPPs can be calculated as [31]:

$$\lambda_{spps} = \lambda_0\sqrt{\frac{\varepsilon_1^{'}+\varepsilon_0}{\varepsilon_1^{'}\times\varepsilon_0}} \tag{9}$$

where λ_0 is the wavelength of the excitation source, ε_0 is the dielectric constants of the air, and $\varepsilon_1^{'}$ is the real part of the dielectric constants of metal.

According to Equation (9), we can calculate the wavelengths of the SPPs. The SPPs are obtained by utilizing various metals and material. Then, by the SIM system, we can finally improve the resolution, as well as obtain the enhancement on spatial resolution. The results of enhancement in different materials and light source wavelengths are given in **Table 1**; Ag and Al_2O_3 are used in this work. The enhancement on spatial resolution is 3.86 times.

TABLE 1 | Multiple of plasmonic structure illumination microscopy (PSIM) and diffraction limit of silver in different materials and wavelengths.

Material	λ_0	ε_1'	ε_0	$a = \frac{(\varepsilon_1'+\varepsilon_0)}{(\varepsilon_1'\times\varepsilon_0)}$	$\sqrt{a}$	λ_{Spp}	Enhancement
Air	633	−18.2950	1.3400	0.6916	0.8316	526.4220	2.404914854
Water	633	−18.2950	1.5200	0.6032	0.7767	491.6397	2.57505632
Al_2O_3	633	−18.3450	3.0976	0.2683	0.5180	327.8914	3.861033988
Air	1030	−53.9790	1.3400	0.7277	0.8531	878.6709	2.344450119
Water	1030	−53.9790	1.5200	0.6394	0.7996	823.5937	2.501233307
Al_2O_3	1030	−53.9790	3.0976	0.3043	0.5516	568.1875	3.625563822

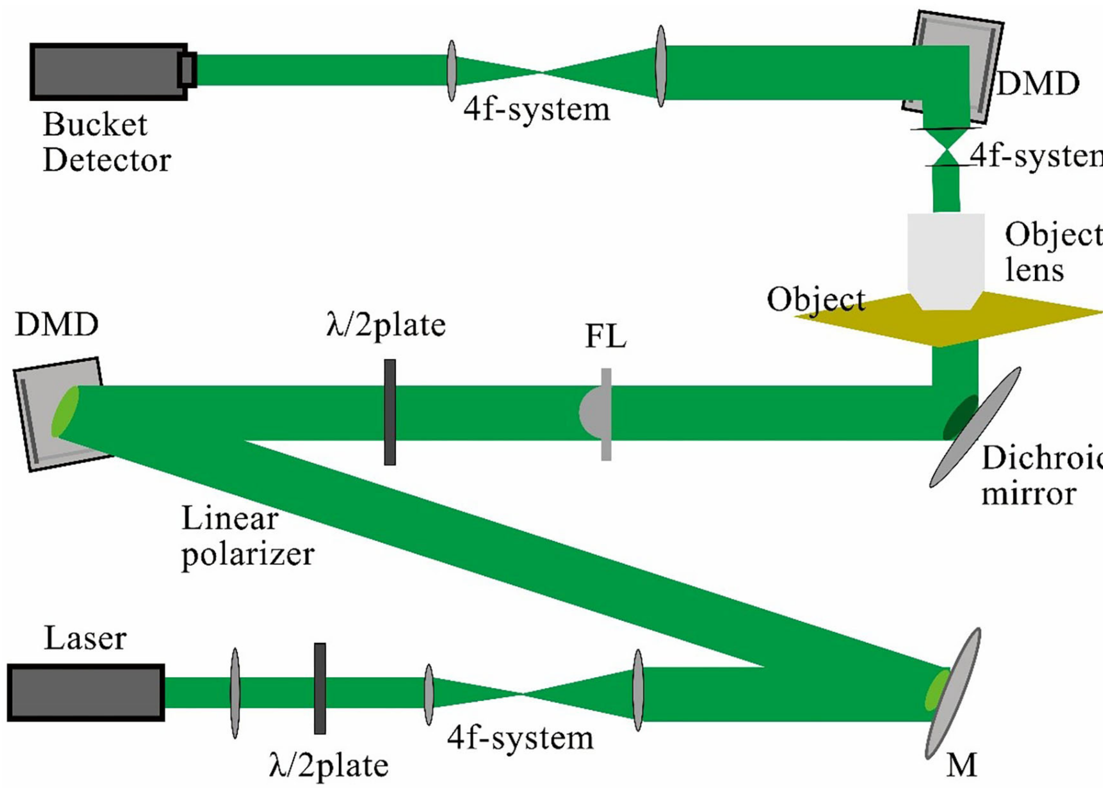

FIGURE 4 | Schematic of ghost imaging based on plasmonic structure illumination microscopy (PSIM-GI) system.

Theory of Ghost Imaging Based on Plasmonic Structure Illumination Microscopy

The super-resolution ghost imaging based on plasmonic structure illumination microscopy is abbreviated as PSIM-GI. The system schematic is shown in **Figure 4**. The light from the light source is radiated to the DMD through the lens, filter, and 4f system. After being modulated by the structured light algorithm, it is radiated to the object platform composed of the metal film, which excites SPPs and irradiates to the detection object. After passing through the object, the light is converged by the objective lens, irradiated to the DMD for correlation modulation and emission. Finally, the light is received by the bucket detector. After demodulating and reconstructing the information received by the bucket detector, the super-resolution object image is finally obtained.

The correlation function of PSIM-GI can be written as:

$$\{R_i\} = \int \{\varphi_i\} \times \{T\} \tag{10}$$

$$\begin{aligned} C_{CGI} &= \frac{1}{N}\sum_{i=1}^{N}\left(R_i - \langle\{R_i\}\rangle\right)\varphi_i\left(x,y\right) \\ &= \left\langle\{R_i\}\,\varphi\left(x,y\right)\right\rangle - \langle\{R_i\}\rangle\left\langle\varphi\left(x,y\right)\right\rangle \end{aligned} \tag{11}$$

where $\{T\}$ is the fusion of high- and low-frequency information in the image by the SIM algorithm.

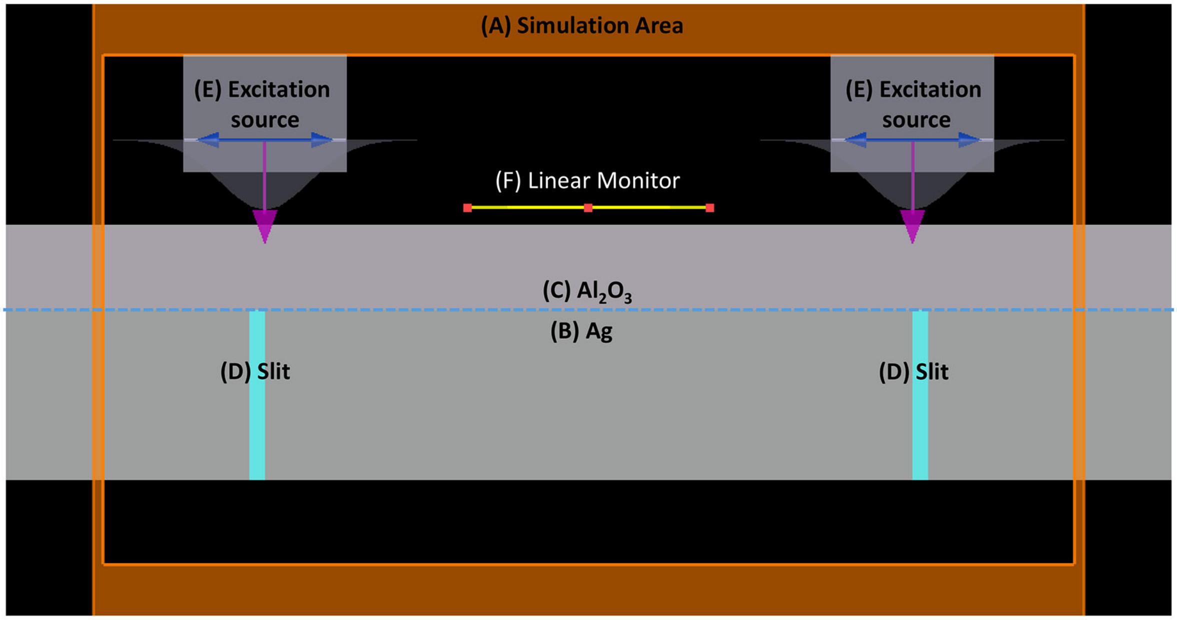

FIGURE 5 | The diagram of surface plasmon polaritons (SPPs) excitation by two slits structure: **(A)** simulation area, **(B)** Ag film, **(C)** layer of Al_2O_3, **(D)** slits, **(E)** excitation sources, and **(F)** linear monitor.

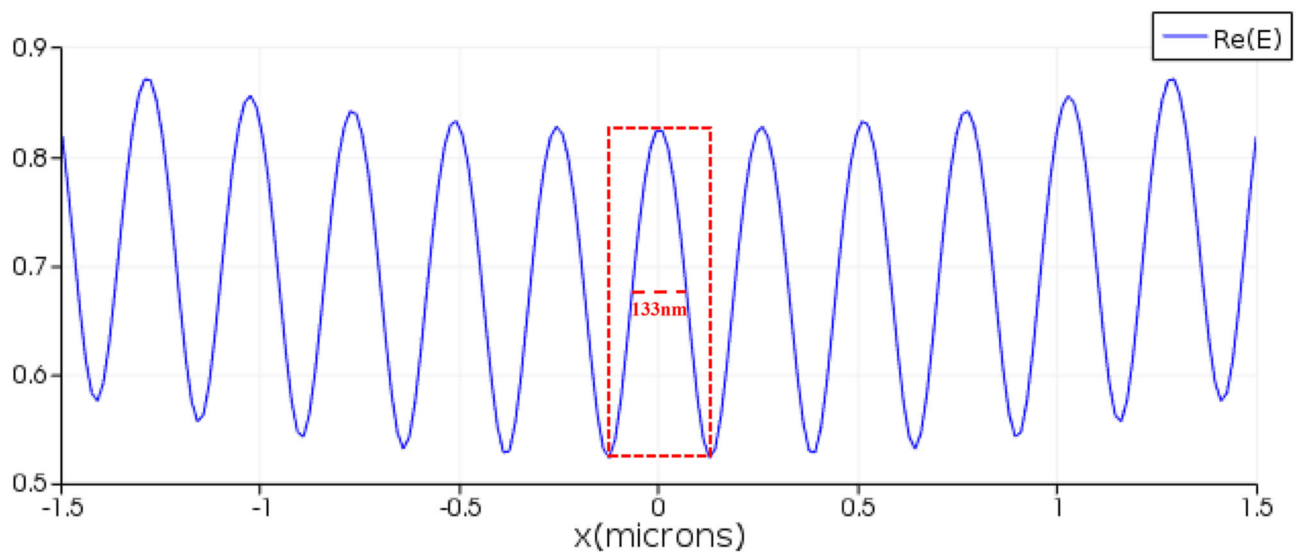

FIGURE 6 | The electromagnetic field distribution of the surface plasmon polariton (SPP) standing wave.

Theory of Atmospheric Turbulence Channel Model

The ghost imaging system propagates by light and is inevitably affected by atmospheric turbulence when it is transmitted in the atmosphere. It is of great practical significance to study the influence of atmospheric turbulence on the error performance of the ghost imaging system. The atmospheric turbulence occurs because of the changes in the upper atmosphere's pressure and temperature, which are influenced by wind and other factors, which causes the intensity fluctuations of the received signal. In a ghost imaging system, the total intensity of the transmission image is received by the bucket detector, so the phase of each pixel in the image is not a concern. Therefore, we apply the intensity distribution model to simulate turbulence. The gamma–gamma model is a classical model to describe light-intensity distribution. It is suitable for a broad range of turbulences (from weak to strong). In addition, both large- and small-scale intensity fluctuations can be described by a gamma–gamma distribution. The gamma–gamma distribution is given as [44].

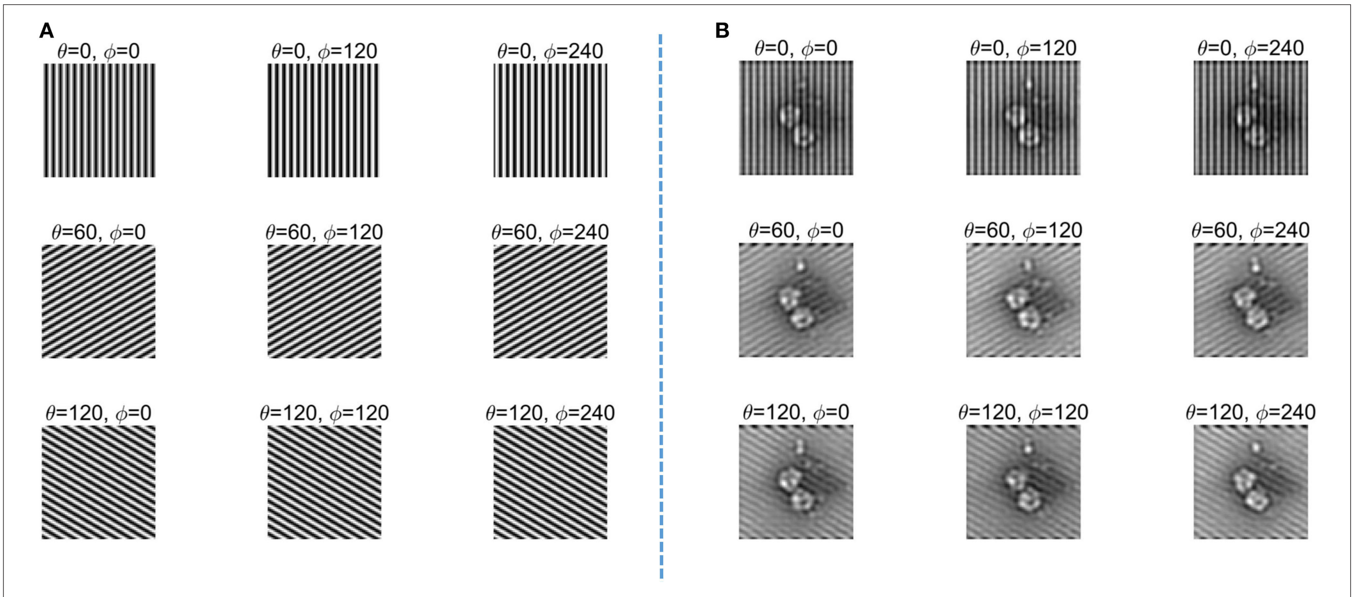

FIGURE 7 | (A) Structure illumination microscopy (SIM) modulation fringes. **(B)** Modulated object image.

$$p(I) = \frac{2(\alpha\beta)^{\frac{(\alpha+\beta)}{2}}}{\Gamma(\alpha)\,\Gamma(\beta)} I^{\frac{(\alpha+\beta)}{2}-1} K_{\alpha-\beta}\left[2(\alpha\beta I)^{\frac{1}{2}}\right], I > 0 \quad (12)$$

where I refers to the intensity of the channel output, under the intensity of the channel output value being 1.

$$\alpha = \frac{1}{\sigma_x^2} \cong \left\{ exp\left[\frac{0.49\sigma_1^2}{\left(1+1.11\sigma_1^{\frac{12}{5}}\right)^{\frac{7}{6}}}\right] - 1 \right\}^{-1}, \text{and}$$

$$\beta = \frac{1}{\sigma_y^2} \cong \left\{ exp\left[\frac{0.51\sigma_1^2}{\left(1+0.69\sigma_1^{\frac{12}{5}}\right)^{\frac{7}{6}}}\right] - 1 \right\}^{-1} \quad (13)$$

$$\sigma_1^2 = 1.23 C_n^2 k^{\frac{7}{6}} d^{\frac{11}{6}} \quad (14)$$

In Equation (14), $k = 2\pi/\lambda$ is the optical wave number, λ is the wavelength, d is the transmission distance, and C_n^2 is the refractive-index structure parameter that describes the degree of atmospheric refractive-index fluctuation.

According to the H–V model of International Telecommunication Union (ITU)-R, the relationship between $C_n^2(h)$ and altitude h can be expressed in Equation (15) [45, 46].

$$C_n^2(h) = 8.148 \times 10^{-56} v_{RMS}^2 h^{10} e^{-h/1,000} + 2.7 \times 10^{-16} e^{-h/1,500} + C_{n0}^2 e^{-h/100} \quad (15)$$

In Equation (15), the conditions are set as follows: the root mean square on the vertical path $v_{RMS} = \{11, 21, 31\}$ and the refractive-index structure parameter near the ground plane $C_{n0}^2 = \{10^{-13}, 10^{-15}, 10^{-17}\}$. When h is lower than 4,000 m, we find that C_n^2 is approximately invariant with v_{RMS}; in this case, C_n^2 is considered constant. The values of C_n^2 under different degrees of the turbulence are as follows:

$C_n^2 = 10^{-17}\ m^{\frac{-2}{3}}$ for weak turbulence
$= 10^{-15}\ m^{\frac{-2}{3}}$ for moderate turbulence
$= 10^{-13}\ m^{\frac{-2}{3}}$ for strong turbulence

When gamma–gamma turbulence is added, the received light intensity formula, in Equation (1), of ghost imaging becomes:

$$R_i = \int dxdy\varphi_i(x,y) \times \vartheta_i(x,y) \times T(x,y) \quad (16)$$

where $\vartheta_i(x,y)$ is multiplicative noise with a gamma–gamma distribution.

SIMULATION AND RESULTS

We simulated the PSIM-GI system according to the above principles. We used PSNR and symbol-error rate (SER) to measure the quality of the reconstructed image and the error performance of the system.

PSNR is the most common objective evaluation index that is an objective evaluation indicator for image quality. PSNR is typically used for comparison of the maximum of the signal to the background noise. The larger the PSNR value, the less the distortion, and the better the quality of the image. PSNR can be calculated using the following equations

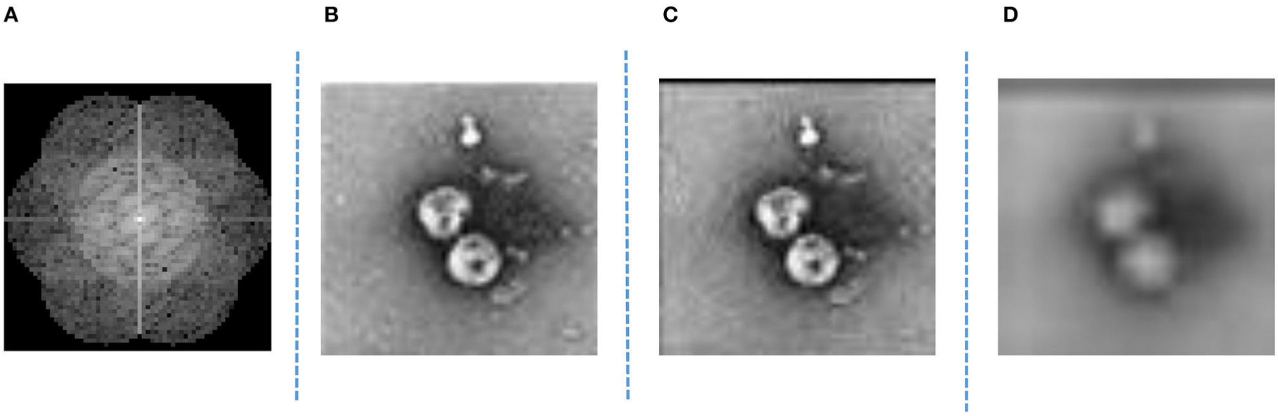

FIGURE 8 | (A) Schematic of imaged wave vector space. **(B)** Object. **(C)** Ghost imaging (GI) with plasmonic structure illumination microscopy (PSIM). **(D)** GI without PSIM.

TABLE 2 | Imaging effects for different transmission distances (in meters).

Distance d	**150**	**120**	**100**	**70**	**30**	**10**	
$C_n^2 = 10^{-14}$			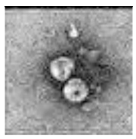	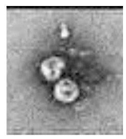	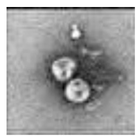	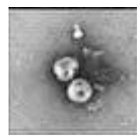	GI with PSIM
	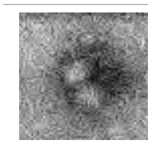	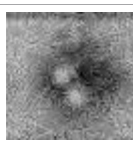	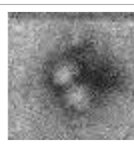	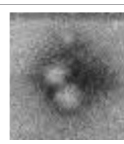	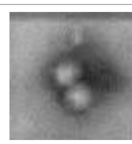	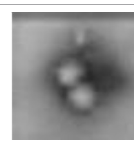	GI without PSIM
Distance d	**500**	**300**	**150**	**100**	**50**	**30**	
$C_n^2 = 10^{-15}$		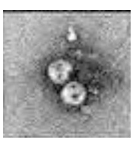	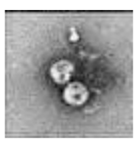	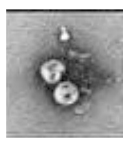	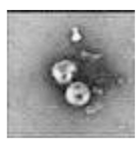	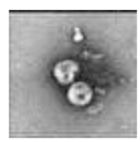	GI with PSIM
	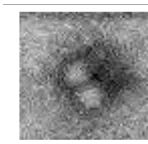		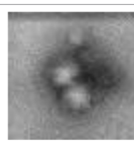	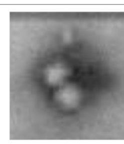	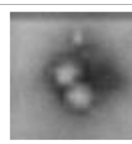	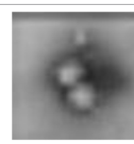	GI without PSIM
Distance d	**500**	**450**	**400**	**300**	**150**	**100**	
$C_n^2 = 10^{-16}$	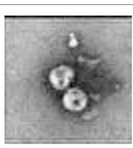	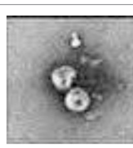	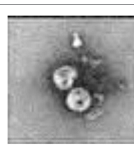		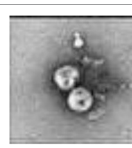		GI with PSIM
	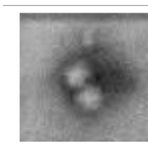			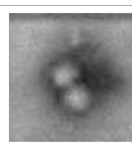	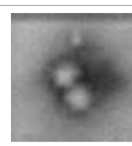	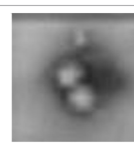	GI without PSIM

TABLE 3 | Imaging effects for different values of the refractive-index structure parameter C_n^2.

C_n^2	9×10^{-13}	5×10^{-13}	1×10^{-13}	9×10^{-14}	5×10^{-14}	1×10^{-14}	
d = 10	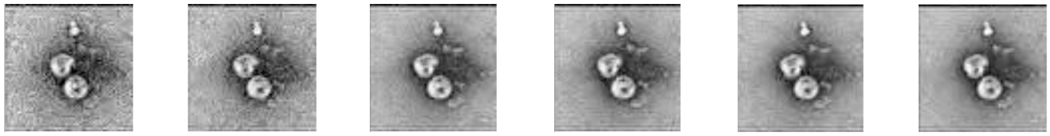						GI with PSIM
	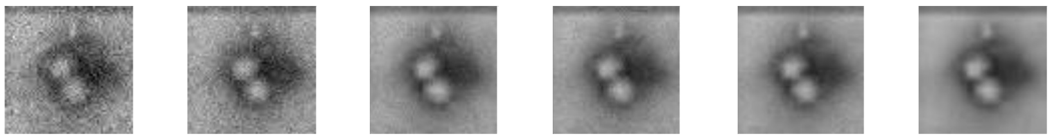						GI without PSIM
C_n^2	9×10^{-15}	5×10^{-15}	1×10^{-15}	9×10^{-16}	5×10^{-16}	1×10^{-16}	
d = 100	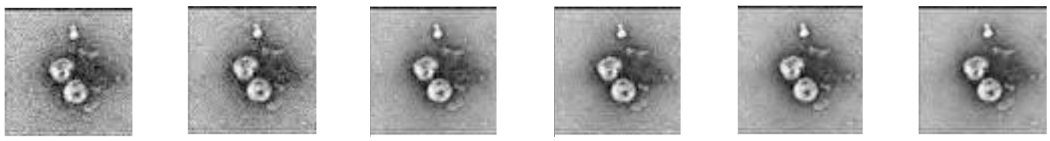						GI with PSIM
	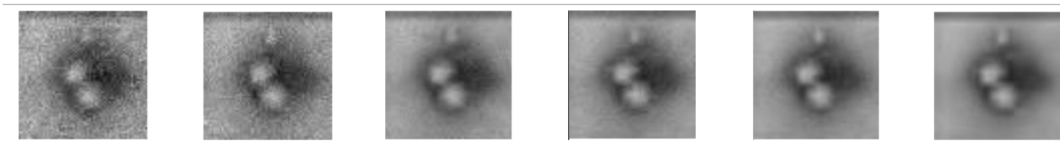						GI without PSIM
C_n^2	9×10^{-16}	5×10^{-16}	1×10^{-16}	9×10^{-17}	5×10^{-17}	1×10^{-17}	
d = 500	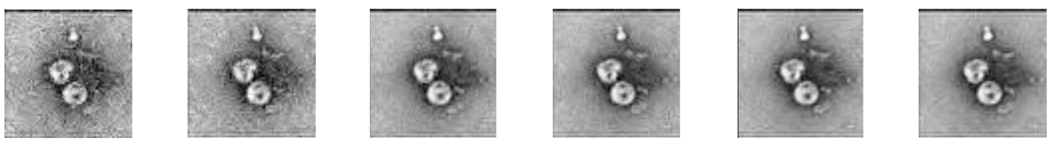						GI with PSIM
	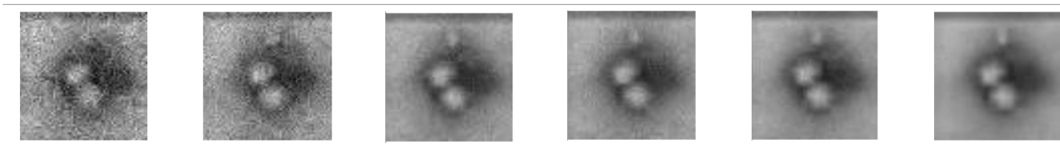						GI without PSIM

$$MSE = \frac{1}{mn}\sum_{i=1}^{m}\sum_{j=1}^{n}\left\| C_{CGI}\left(i,j\right) - T\left(i,j\right)\right\|^2 \quad (17)$$

$$PSNR = 20 \cdot log_{10}\left(\frac{C_{max}}{\sqrt{MSE}}\right) \quad (18)$$

Here, MSE is the mean square error between the compared image and the original image, and $C_{\max} = 2^k - 1$, indicating the maximum value of the image's color; for grayscale images, k is 8 bits.

SER is also an indicator of the accuracy and reliability of a transmission system. It is defined by the percentage of misclassified symbols [47] expressed as

$$P_e = \frac{number\ of\ error\ symbols}{number\ of\ all\ symbols} * 100\% \quad (19)$$

In this article, Equation (19) is specified as

$$P_e = \frac{N_{OUT_{xy}-IN_{xy}<n}}{c*r} * 100\% \quad (20)$$

$N_{OUT_{xy}-IN_{xy}}$ is the number of input and output pixels with a nonzero difference; n is the difference between pixels. When the difference between output and input is less than n, we define output to be equal to the input. $c*r$ is the total number of pixels.

Simulation and Results of PSIM-GI

The finite difference time domain (FDTD) method is utilized to simulate the excitation of the SPPs. The diagram of the SPP excitation is shown in **Figure 5**: the simulation area is indicated by (A); the silver film with the thickness of 120 nm is indicated by (B); two slits etched on the silver film are indicated by (D); and the layer of Al_2O_3 with thickness of 50 nm is indicated by (C). Two excitation sources with horizontally polarization directions

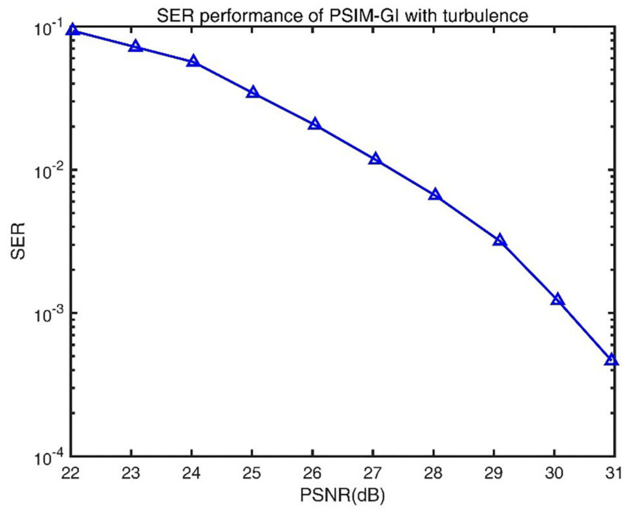

FIGURE 9 | Symbol-error rate (SER) performance of ghost imaging based on plasmonic structure illumination microscopy (PSIM-GI) with turbulence.

and wavelength of 633 nm are indicated by (E). The excitation sources are used to illuminate two slits normally from the front side, respectively. An SPP standing wave is generated by the interference of two counter-propagating SPPs at the center of the structure. A linear monitor at 20 nm above the silver surface with length of 3 μm is used to obtain the electromagnetic field distribution of the SPP standing wave. The intensity distribution of the SPP standing wave from −1.5 to 1.5 μm is shown in **Figure 6**. It can be calculated that the full width at half maximum (FWHM) of the standing wave is 133 nm, which demonstrated that the wavelength of the SPPs is shorter than the excitation sources. The SIM uses a dynamically controllable DMD instead of the grating to generate horizontal and vertical modulation fringes, as shown in **Figure 7A**. The modulated structured light irradiates and modulates the object, encodes the high-frequency information of the object in the spatial domain, and uses the moire fringes formed by the structured light frequency and object frequency components to improve the resolution and achieve structure illumination microscopy imaging. The light passing through the object after modulation is shown in **Figure 7B**. The schematic diagram of the wave vector space of imaging is shown in **Figure 8A**. The object that we used in this study is a grayscale image of negative-stained 2019-nCoV particles [48], as shown in **Figure 8B**. Then, high-frequency information is calculated and extracted to achieve super-resolution imaging. Finally, super-resolution imaging is achieved. The resolution is increased to three to four times of the diffraction limit frequency.

As shown in **Figure 4**, the light after passing through the PSIM system enters the GI system, that is, the light is modulated on the DMD, and the emitted light is finally received by the bucket detector. The image is restored after demodulation and reconstruction, as shown in **Figure 8C**. For comparison, we present the results without PSIM (reference system), as shown in **Figure 8D**; more results after ghost imaging system without PSIM are shown in **Tables 2**, **3**. Then, the reconstructed image is analyzed, and PSNR and SER indexes are calculated to measure the reconstructed image. The PSNR is 30.09. When n is 17–23, SER is 10^{-3}; when n is 24–26, SER is 10^{-4}; when n is >27, SER is almost 0.

The relationship between the PSNR and the SER of a PSIM-GI system with turbulence is shown in **Figure 9**. N of the system is set to full pixel numbers of the image to eliminate the inherent error of the ghost imaging. Changing the refractive-index structure parameter C_n^2 and transmission distance d, the value of PSNR and SER under different situations are recorded. We selected the value of PSNR closest to the integer and calculated the corresponding SER to obtain the graph of PSNR and SER. **Figure 9** shows that SER decreases with increasing PSNR. For PSNR values between 22 and 27 dB, the SER remains high ($> 10^{-2}$). When the PSNR is >27 dB, the SER decreases sharply. The SER decreases by one order of magnitude, while the PSNR only increases by 3 dB, and it has dropped below 10^{-3} when the PSNR is over 30 dB.

Analysis of the Influence Under Different Conditions of Transmission Distance

When analyzing the influence of transmission distances, the refractive-index structure parameter C_n^2 is taken as 10^{-14}, 10^{-15}, and 10^{-16}; the distance between the transmitter and the receiver d is set to a series of values according to the different values of C_n^2; N is set to the full pixel numbers of the image. The results of ghost imaging at different d are presented in **Table 2**.

When $C_n^2 = 10^{-14}$, the imaging performance significantly changes from fine to coarse, while the value of d changes from 10 to 150 m. Similar trends in imaging performance are observed for $C_n^2 = 10^{-15}$ with d ranging from 30 to 500 m and for $C_n^2 = 10^{-16}$ with d ranging from 100 to 500 m. PSNR and SER performance with d are shown in **Figure 10**.

Notably, PSNR declines and SER increases with increasing d. Both tend to stabilize when d increases to a specific value, which varies with C_n^2.

Analysis of the Influence Under Different Conditions of Refractive-Index Structure Parameter

Similarly, when analyzing the influence of C_n^2, the transmission distance d is set to 10, 100, and 500 m, respectively; C_n^2 is set to a series of values according to the different values of d; N is also set to 100%. Imaging effects for different d are presented in **Table 3**.

When $d = 10$ m, the imaging performance significantly changes from fine to coarse while the range of C_n^2 changes from 1×10^{-14} to 9×10^{-13}. Similar trends in imaging performance are observed for $d = 100$ m with C_n^2 ranging from 1×10^{-16} to 9×10^{-15} and for $d = 500$ m with C_n^2 ranging from 1×10^{-17} to 9×10^{-16}. PSNR and SER performance with varying C_n^2 are shown in **Figure 11**.

The trend in **Figure 11** is the same as **Figure 10**: PSNR declines and SER increases with increasing C_n^2. Both tend to stabilize when C_n^2 increases to a specific value that varies with d.

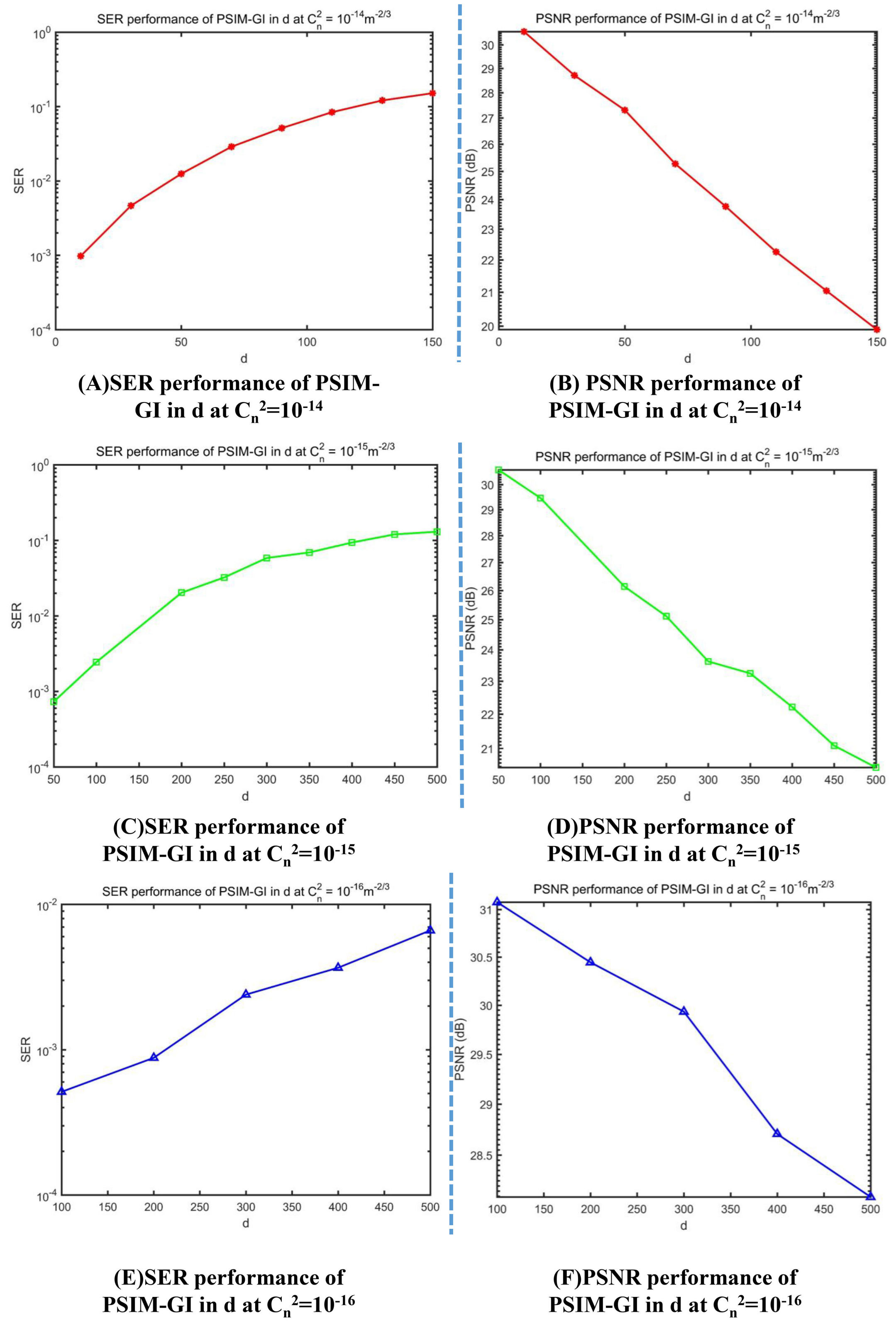

FIGURE 10 | Symbol-error rate (SER) and peak signal-to-noise ratio (PSNR) curves for various transmission distances. **(A)** SER performance of PSIM-GI in *d* at $C_n^2 = 10^{-14}$. **(B)** PSNR performance of PSIM-GI in *d* at $C_n^2 = 10^{-14}$ **(C)** SER performance of PSIM-GI in *d* at $C_n^2 = 10^{-15}$. **(D)** SER performance of PSIM-GI in *d* at $C_n^2 = 10^{-15}$. **(E)** SER performance of PSIM-GI in *d* at $C_n^2 = 10^{-16}$. **(F)** SER performance of PSIM-GI in *d* at $C_n^2 = 10^{-16}$.

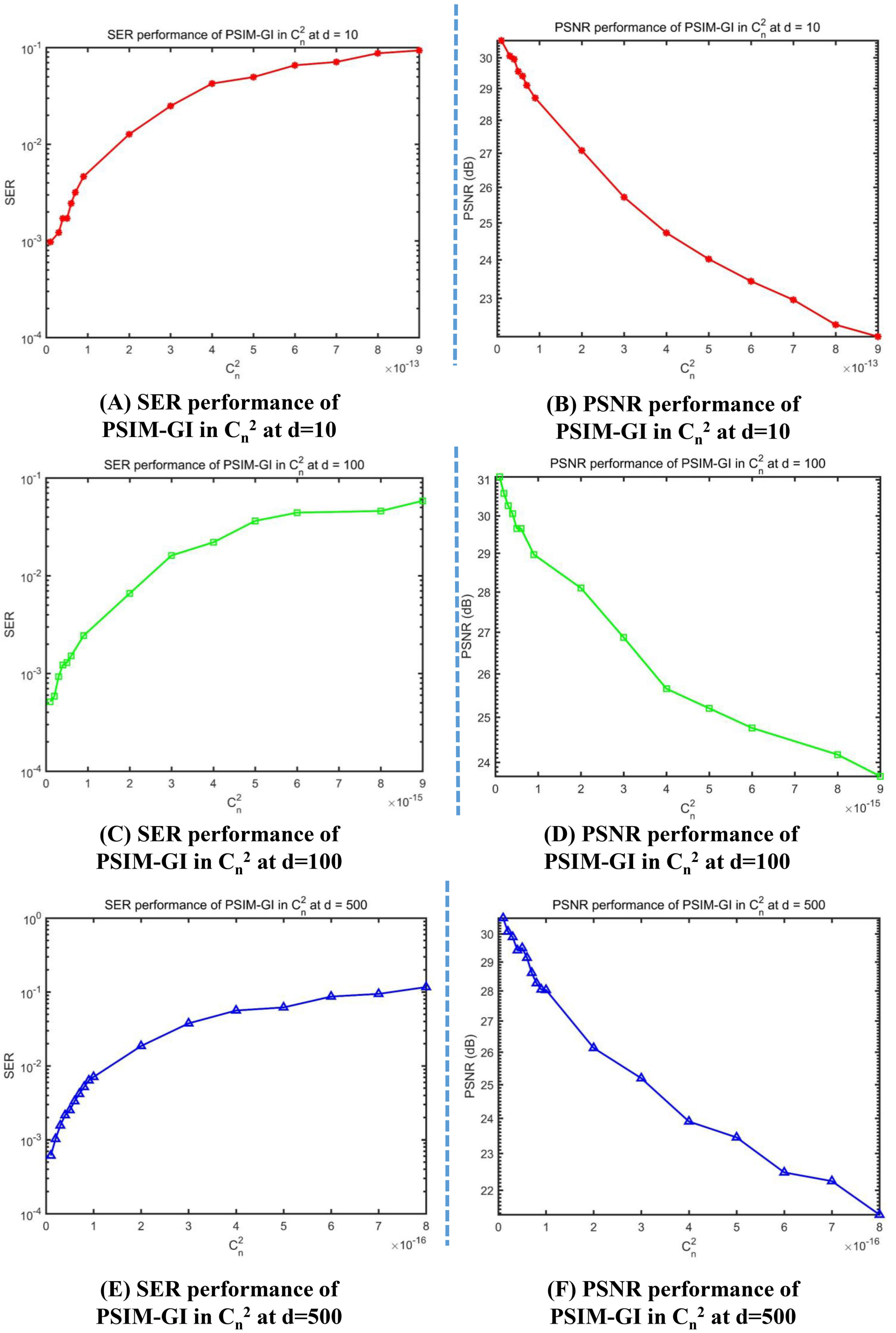

FIGURE 11 | Symbol-error rate (SER) and peak signal-to-noise ratio (PSNR) curves for different values of the refractive-index structure parameter. **(A)** SER performance of PSIM-GI in C_n^2 at $d = 10$. **(B)** PSNR performance of PSIM-GI in C_n^2 at $d = 10$. **(C)** SER performance of PSIM-GI in C_n^2 at $d = 100$. **(D)** PSNR performance of PSIM-GI in C_n^2 at $d = 100$. **(E)** SER performance of PSIM-GI in C_n^2 at $d = 500$. **(F)** PSNR performance of PSIM-GI in C_n^2 at $d = 500$.

CONCLUSION

In this study, plasmonic structure illumination microscopy is applied io ghost imaging, and a PIM-GI imaging method is proposed. Using SPPs and SIM to enhance the resolution, super-resolution imaging is achieved. Using the FDTD software, two pairs of orthogonal slits are designed on the surface of the silver film to realize the excitation of SPPs. The SIM and GI algorithms are used to encode, transmit, receive, reconstruct, and finally obtain a clear image. The final resolution can reach three to four times the diffraction limit. The PSNR and SER of the PSIM-GI system are also calculated to measure the quality of the reconstructed image and simultaneously meet the sharpness of actual needs. The method proposed in this study has great research and application value in biomedical fields such as microimaging and endoscopy.

Furthermore, the influence of gamma–gamma turbulence to ghost imaging has also been simulated and analyzed. The intensity influence is mediated by two key parameters; they are refractive-index structure parameter C_n^2 and transmission distance d. According to results and analyses, both these parameters are negatively correlated with PSNR and positively correlated with SER. When C_n^2 or d increases sufficiently, the PSNR and SER nearly become constants and remain stable. This work provides a basis for a theoretical model and reference for a practical ghost-imaging system transmitting through an atmospheric turbulence channel.

DATA AVAILABILITY STATEMENT

All datasets presented in this study are included in the article/supplementary material.

AUTHOR CONTRIBUTIONS

KW contributed to the present and design the system. ZW, CB, HY, YZ, and ZZ contributed to simulation. XH and TX contributed to drawing. LZ, BD, MX, JH, XX, and DZ contributed to modification and suggestion in this paper. All authors contributed to the article and approved the submitted version.

FUNDING

This work was supported by the National Natural Science Foundation of China (Grant Nos. 61805144, 61875125, 61405115, and 61775140), the Shanghai Rising-Star Program (Grant No. 20QA1407000), Natural Science Foundation of Shanghai (Grant Nos. 18ZR1425800 and 14ZR1428400), and Shanghai Sailing Program (Grant No. 17YF1429400).

ACKNOWLEDGMENTS

We would like to thank Editage (www.editage.com) for English language editing.

REFERENCES

1. Pittman TB, Shih YH, Strekalov DV, Sergienko AV. Optical imaging by means of two-photon quantum entanglement. *Phys Rev A.* (1995) **52**:R3429–32. doi: 10.1103/PhysRevA.52.R3429
2. Lei Z, Wang C, Zhang D, Wang L, Gong W. Second-order intensity-correlated imaging through the scattering medium. *IEEE Photonics J.* (2017) **9**:7500207. doi: 10.1109/JPHOT.2017.2772265
3. Li Z, Zhao Q, Gong W. Experimental investigation of ghost imaging in background light environments. *J Opt.* (2020) **22**:025201. doi: 10.1088/2040-8986/ab613e
4. Leihong Z, Zhisheng Z, Yi K. Research on double-layers optical information encryption based on ghost imaging. *Opt Commun.* (2019) **455**:124585. doi: 10.1016/j.optcom.2019.124585
5. Meyers RE, Deacon KS. Quantum ghost imaging experiments at ARL. *Proc SPIE.* (2010) **815**:78150I. doi: 10.1117/12.864270
6. Shapiro JH. Computational ghost imaging. *Phys Rev A.* (2008) **78**:061802. doi: 10.1103/PhysRevA.78.061802
7. Bai X, Li YQ, Zhao SM. Differential compressive correlated imaging. *Acta Phys Sin.* (2013) 62:44209. doi: 10.7498/aps.62.044209
8. Ferri F, Magatti D, Lugiato LA, Gatti A. Differential ghost imaging. *Phys Rev Lett.* (2010) **104**:253603. doi: 10.1103/PhysRevLett.104.253603
9. Ermeydan ES, Çankaya I, Sahin AB. Super-resolution algorithm applied to images acquired at millimeter wave frequency in single pixel and computational ghost imaging configurations. *J Electromag Waves Appl.* (2019) **33**:2328–40. doi: 10.1080/09205071.2019.1678525
10. Yu WK. Super sub-nyquist single-pixel imaging by means of cake-cutting hadamard basis sort. *Sensors.* (2019) **19**:4122. doi: 10.3390/s19194122
11. Barbastathis G, Ozcan A, Situ G. On the use of deep learning for computational imaging. *Optica.* (2019) **6**:000921. doi: 10.1364/OPTICA.6.000921
12. Karmakar S. Super-resolution noninvasive confocal quantum microscope. *Optik.* (2019) **198**:163209. doi: 10.1016/j.ijleo.2019.163209
13. Wang Q, Bu J, Tan PS, Yuan GH, Teng JH, Wang H, et al. Subwavelength-sized plasmonic structures for wide-field optical microscopic imaging with super-resolution. *Plasmonics.* (2012) **7**:427–33. doi: 10.1007/s11468-011-9324-2
14. Cao S, Wang T, Yang J, Hu B, Levy U, Yu W. Numerical analysis of wide-field optical imaging with a sub-20 nm resolution based on a meta-sandwich structure. *Sci Rep.* (2017) **7**:1328. doi: 10.1038/s41598-017-01521-w
15. Ertsgaard CT, Mckoskey RM, Rich IS, Lindquist NC. Dynamic placement of plasmonic hotspots for super-resolution surface-enhanced raman scattering. *ACS Nano.* (2014) **8**:10941–6. doi: 10.1021/nn504776b
16. Erkmen BI, Shapiro JH. Unified theory of ghost imaging with gaussian-state light. *Phys Rev A.* (2008) **77**:043809. doi: 10.1103/PhysRevA.77.043809
17. Bromberg Y, Katz O, Silberberg Y. Ghost imaging with a single detector. *Phys Rev A.* (2009) **79**:053840. doi: 10.1103/PhysRevA.79.053840
18. Duarte MF, Davenport MA, Takhar D, Laska JN, Sun T, Kelly KF, et al. Single-pixel imaging via compressive sampling. *IEEE Signal Process Mag.* (2008) **25**:83–91. doi: 10.1109/MSP.2007.914730
19. Tian-Yi M, Qian C, Wei-Ji H, Jia-Yan Z, Yun-Hao Z, Dong-Hui D, et al. Optical communication in turbid and turbulent atmosphere. *Acta Phys Sin.* (2016) **65**:084207. doi: 10.7498/aps.65.084207
20. Leihong Z, Ye H, Dawei Z. Study on the key technology of image transmission mechanism based on channel coding ghost imaging. *IEEE Photonics J.* (2018) **10**:1–13. doi: 10.1109/JPHOT.2018.2858823
21. Salomon L, Bassou G, Aourag H, Dufour JP, de Fornel F, Carcenac F, et al. Local excitation of surface plasmon polaritons at discontinuities of a metal film: theoretical analysis and optical near-field measurements. *Phys Rev B.* (2002) **65**:125409. doi: 10.1103/PhysRevB.65.125409
22. Chen L, Liao DG, Guo XG, Zhao JY, Zhu YM, Zhuang SL. Terahertz time-domain spectroscopy and micro-cavity components for probing samples: a review. *Front Inform Technol Electron Eng.* (2019) **20**:591–607. doi: 10.1631/FITEE.1800633

23. Raether H. *Surface Plasmons on Smooth and Rough Surfaces and on Gratings*. Berlin: Springer-Verlag Press (1986).
24. Kretschmann E, Raether H. Notizen: radiative decay of non radiative surface plasmons excited by light. *Zeitschrift für Naturforschung A*. (1968) **23**:2135–6. doi: 10.1515/zna-1968-1247
25. Hecht B, Bielefeldt H, Novotny L, Inouye Y, Pohl DW. Local excitation, scattering, and interference of surface plasmons. *Phys Rev Lett*. (1996) **77**:1889–92. doi: 10.1103/PhysRevLett.77.1889
26. Kano H, Mizuguchi S, Kawata S. Excitation of surface-plasmon polaritons by a focused laser beam. *J Opt Soc Am B*. (1998) **15**:1381–6. doi: 10.1364/JOSAB.15.001381
27. Nash DJ, Cotter NPK, Wood EL, Bradberry GW, Sambles JR. Examination of the +1, −1 surface plasmon mini-gap on a gold grating. *Opt Acta Int J Opt*. (1995) **42**:243–8. doi: 10.1080/09500349514550191
28. Chang SH, Gray S, Schatz G. Surface plasmon generation and light transmission by isolated nanoholes and arrays of nanoholes in thin metal films. *Opt Express*. (2005) **13**:3150–65. doi: 10.1364/OPEX.13.003150
29. Yang J, Xiao X, Hu C, Zhang WW, Zhou SX, Zhang JS. Broadband surface plasmon polariton directional coupling. *Nano Lett*. (2014) **14**:704–9. doi: 10.1021/nl403954h
30. Kuo CF, Chu SC. Dynamic control of the interference pattern of surface plasmon polaritons and its application to particle manipulation. *Opt Express*. (2018) **26**:19123–36. doi: 10.1364/OE.26.019123
31. Bai CY, Chen J, Zhang YX, Zhang DW, Zhan QW. Dynamic tailoring of an optical skyrmion lattice in surface plasmon polaritons. *Opt Express*. (2020) **28**:10320–8. doi: 10.1364/OE.384718
32. Betzig E, Patterson GH, Sougrat R, Lindwasser OW, Olenych S, Bonifacino JS, et al. Imaging intracellular fluorescent proteins at nanometer resolution. *Science*. (2006) **313**:1642–5. doi: 10.1126/science.1127344
33. Tan PS, Yuan XC, Yuan GH, Wang Q. High-resolution wide-field standing-wave surface plasmon resonance fluorescence microscopy with optical vortices. *Appl Phys Lett*. (2010) **97**:241109. doi: 10.1063/1.3525173
34. Wei S, Lei T, Du L, Zhang C, Chen H, Yang Y, et al. Sub-100nm resolution PSIM by utilizing modified optical vortices with fractional topological charges for precise phase shifting. *Opt Express*. (2015) **23**:30143–8. doi: 10.1364/OE.23.030143
35. Zhang, C, Min C, Du L, Yuan XC. Perfect optical vortex enhanced surface plasmon excitation for plasmonic structured illumination microscopy imaging. *Appl Phys Lett*. (2016) **108**:201601. doi: 10.1063/1.4948249
36. Dan D, Lei M, Yao B, Wang W, Winterhalder M, Zumbusch A, et al. DMD-based LED-illumination Super-resolution and optical sectioning microscopy. *Sci Rep*. (2013) **3**:1116. doi: 10.1038/srep01116
37. Rego EH, Shao L, Macklin JJ, Winoto L, Johansson GA, Kamps-Hughes N, et al. Nonlinear structured-illumination microscopy with a photoswitchable protein reveals cellular structures at 50-nm resolution. *Proc Nat Acad Sci USA*. (2012) **109**:E135–43. doi: 10.1073/pnas.1107547108
38. Chakrova N, Rieger B, Stallinga S. Deconvolution methods for structured illumination microscopy. *J Opt Soc Am A*. (2016) **33**:B12–20. doi: 10.1364/JOSAA.33.000B12
39. Lal A, Shan C, Xi P. Structured illumination microscopy image reconstruction algorithm. *IEEE J Select Top Quantum Electron*. (2016) **22**:50–63. doi: 10.1109/JSTQE.2016.2521542
40. Wei F, Liu Z. Plasmonic structured illumination microscopy. *Nano Lett*. (2010) **10**:2531–6. doi: 10.1021/nl1011068
41. Wei F, Lu D, Shen H, Wan W, Ponsetto JL, Huang E, et al. Wide field super-resolution surface imaging through plasmonic structured illumination microscopy. *Nano Lett*. (2014) **14**:4634–9. doi: 10.1021/nl501695c
42. Fernández-Domínguez AI, Liu Z, Pendry JB. Coherent four-fold super-resolution imaging with composite photonic–plasmonic structured illumination. *ACS Photonics*. (2015) **2**:341–8. doi: 10.1021/ph500342g
43. Ponsetto JL, Wei F, Liu Z. Localized plasmon assisted structured illumination microscopy for wide-field high-speed dispersion-independent super resolution imaging. *Nanoscale*. (2014) **6**:5807–12. doi: 10.1039/C4NR00443D
44. Al-Habash A, Andrews LC, Phillips RL. Mathematical model for the irradiance probability density function of a laser beam propagating through turbulent media. *Opt Eng*. (2001) **40**:1554–63. doi: 10.1117/1.1386641
45. Ghassemlooy Z, Popoola W, Rajbhandari S. *Optical Wireless Communications System and Channel Modelling with MATLAB*. New York, NY: CRC Press (2012).
46. ITU-R. *P.618: Propagation Data and Prediction Methods Required for the Design of Earth-space Telecommunication Systems (Internationnal Telecommunication Union, 2017)*. (2017). Available online at: https://www.itu.int/rec/R-REC-P.618-13-201712-I/en (accessed February 16, 2020).
47. Hou YS, Xia GQ, Jayaprasath E, Yue DZ, Wu ZM. Parallel information processing using a reservoir computing system based on mutually coupled semiconductor lasers. *Phys Rev B*. (2020) **126**:40. doi: 10.1007/s00340-019-7351-4
48. Zhu N, Zhang D, Wang W, Li X, Yang B, Song J, et al. A novel coronavirus from patients with pneumonia in China, 2019. *N Engl J Med*. (2020) **382**:727–33. doi: 10.1056/NEJMoa2001017

Conflict of Interest: The authors declare that the research was conducted in the absence of any commercial or financial relationships that could be construed as a potential conflict of interest.

frontiers in Physics

ORIGINAL RESEARCH
published: 22 October 2020
doi: 10.3389/fphy.2020.576419

Check for updates

Two-Way Fano Resonance Switch in Plasmonic Metamaterials

Yong Jin Zhou[1,2]*, *Li Hui Dai*[1], *Qiao Yu Li*[1] *and Zhong Yin Xiao*[1]

[1] *Key Laboratory of Specialty Fiber Optics and Optical Access Networks, Shanghai University, Shanghai, China,* [2] *State Key Laboratory of Millimeter Waves, Southeast University, Nanjing, China*

A two-way Fano resonance switch in the plasmonic metamaterials has been proposed and experimentally demonstrated. The electrical Fano switch is composed of two concentric spoof localized surface plasmon (LSP) resonators. By adjusting the slit in the inner spoof LSP resonator, two different Fano resonance modes could be supported. By loading a Schottky barrier diode (SBD)across the slit in the inner LSP resonator, both Fano resonance modes can be simultaneously switched when the SBD is forward biased or reverse biased, and their switch status is opposite. Both simulated and measured results agree well at microwave frequencies and verify the two-way Fano resonance switch. The devices could be applied in many applications such as plasmonic circuits, multiway sensing or switching, and so on.

Keywords: Fano resonance, localized surface plasmons (LSPs), plasmonic, metamaterials (MMs), switchable

OPEN ACCESS

Edited by:
Lin Chen,
University of Shanghai for Science and Technology, China

Reviewed by:
Dejun Liu,
Shanghai Normal University, China
Bai Cao Pan,
Hangzhou Dianzi University, China

****Correspondence:***
Yong Jin Zhou
yjzhou@shu.edu.cn

Specialty section:
This article was submitted to Optics and Photonics, a section of the journal Frontiers in Physics

Received: *26 June 2020*
Accepted: *22 September 2020*
Published: *22 October 2020*

Citation:
Zhou YJ, Dai LH, Li QY and Xiao ZY (2020) Two-Way Fano Resonance Switch in Plasmonic Metamaterials. Front. Phys. 8:576419. doi: 10.3389/fphy.2020.576419

INTRODUCTION

In 1961, Ugo Fano discovered a new type of resonance in the study of the autoionizing states of atoms [1]. Unlike the symmetric lineshape of the Lorentzian resonance, the Fano resonance exhibits a distinctly asymmetric lineshape, which results from the destructive interference of a narrow discrete resonance with a broad continuum of states. The Fano interference is a universal phenomenon because the manifestation of configuration interference does not depend on the matter [2], which has been realized in many systems, such as photonic crystals [3], plasmonic nanostructures [4–9], metamaterials [10–13], plasmonic metamaterials [14–16], etc. Fano resonance may be used for the design of spin filters [17], switches [18], chemical or biological sensors [19–26], etc.

Active metamaterials are promising for the multifunctional systems with tunable, switchable, and non-linear functionalities [27]. For example, to conquer the bottleneck of Fano resonance sensing that the high Q factor Fano resonance is accompanied with an extremely small resonance intensity [28, 29], gain-assisted active spoof plasmonic Fano resonance is proposed to enhance both the Q factor and resonance intensity simultaneously [30]. Active Fano resonance switches were also demonstrated. The on–off switching of the Fano resonance of a plasmonic cluster by its incorporation into a polarization rotating liquid crystal device was demonstrated in a voltage-dependent manner [31]. Electrically controlled damping of Fano resonance in a graphene-nanoantenna hybrid device was observed [32]. Active photoswitching of sharp Fano resonances in silicon-implanted terahertz asymmetric metallic split-ring resonator structure was demonstrated, where the strength of the Fano resonance is modulated by changing the optical pump powers [33]. By changing the pH value of the solution environment, the active plasmonic Fano resonance switching is enabled by varying the refractive index of a layer of polyaniline between the Au nanosphere and the Au nanoplate [34]. The Fano resonance generated in Si nanosphere dimers on a VO_2 layer can be actively tuned by utilizing the phase transition of VO_2 with temperature

[35]. However, there are still great challenges that are difficult to overcome, such as slow switching speed, high operation voltage, low contrast of modulation, etc. Furthermore, it is impossible to achieve two-way or multiway Fano switches based on the discussed mechanisms.

Here, we investigated an electrically two-way Fano resonance switch in the plasmonic metamaterials, which is composed of two concentric spoof localized surface plasmon (LSP) resonators. It has been demonstrated that there would be two different Fano resonance modes when adjusting the slit in the inner spoof LSP resonator. By loading a Schottky barrier diode (SBD) across the slit in the inner LSP resonator, both Fano resonance modes can be simultaneously controlled (OFF/ON) when the SBD diode is forward biased or reverse biased. Hence, a two-way Fano resonance switch can be realized. Both simulated and measured results agree well at microwave frequencies.

PASSIVE SPOOF PLASMONIC FANO RESONANCE

To understand the physical mechanism of the two-way Fano resonance switch, we first investigate the Fano resonances of two spoof plasmonic Fano resonance Structures A and B. The three-dimensional (3D) schematic of Structure A is illustrated in **Figure 1A**, which contains two vertically stacked layers. The top layer is the spoof plasmonic Fano resonator, and the bottom layer is a microstrip feeding line. The top view and side view of Structure A are shown in **Figure 1B**, where the length l of the spoof plasmonic Fano resonator is 52 mm. The width w of the microstrip line is 1.3 mm, and the thickness h of the substrate and the thickness t_m of the copper are 0.5 and 0.018 mm, respectively. As demonstrated in **Figure 1C**, the spoof plasmonic Fano resonator is composed of two concentric spoof LSP resonators. The outer and inner corrugated metallic rings are printed on the dielectric substrate (F4B), whose relative dielectric permittivity is 2.65, and loss tangent is 0.002. The radiuses r_1 and r_2 of the inner and outer corrugated rings are 1.5 and 10.5 mm, respectively. Both the lengths l_1 and l_2 are 2.5 mm, and the groove depths l_3 and l_4 are 5 and 7.5 mm, respectively.

The transmission coefficients (S_{21}) are plotted in **Figure 2a**, which are obtained by using the commercial software HFSS. The driven modal solver is used. The wave port and the radiation boundary condition are adopted. The minimum mesh size is 0.06 mm. The spoof LSP modes with Lorentzian lineshapes of outer and inner corrugated rings are marked as O_1, O_2, O_3, and I_1 modes. The corresponding resonant frequencies are 1.0, 2.02, 2.78, and 2.52 GHz, respectively. **Figure 2b** illustrates the 2D E_z-field distributions on the *xoy* plane 2 mm above the spoof LSP resonators, where it can be seen that the spoof LSP modes O_1-O_3 are dipolar mode ($n = 1$), quadrupolar mode ($n = 2$), and hexapolar mode ($n = 3$) for the outer corrugate ring. The spoof LSP mode I_1 is the dipolar mode ($n = 1$). For structure A, the resonant peaks are denoted by A_1, A_2, A_3, and A_4. The corresponding resonant frequencies are 1.03, 1.98, 2.44, and 2.65 GHz, respectively. It can be seen that there exists an asymmetric Fano lineshape between A_2 and A_4, which stems from the destructive interference of the narrow discrete spoof LSP mode I_1 with the broad continuum state between modes O_2 and O_3 of the outer corrugated ring. **Figure 2c** illustrates the 2D E_z-field distributions on the *xoy* plane 2 mm above Structure A. It can be clearly observed that the modes A_1, A_2, and A_4 are corresponding to the spoof LSPs modes O_1, O_2, and O_3, respectively, while the resonant peak A_3 corresponds to the spoof LSPs mode I_1.

Next is structure B, whose 3D schematic is illustrated in **Figure 3A**. The top view of Structure B is shown in **Figure 3B**. From **Figure 3C**, it can be seen that Structure B is also composed of two concentric LSP resonators. The difference with Structure A is that there is a slit in the inner corrugated ring, where the slit is cut at the position of $\theta = 90°$.

The simulation transmission coefficients S_{21} of Structure B, outer corrugated ring, and inner corrugated ring with a slit are given in **Figure 4a**. The LSP modes are different for the inner corrugated ring and the corrugated ring with a slit. Here, the spoof LSP modes of outer and inner corrugated rings are also marked as O_1, O_2, O_3, and I_1 modes. **Figure 4b** illustrates the corresponding 2D E_z-field distributions on the *xoy* plane 2 mm above the spoof LSP resonators. The resonant frequencies of the outer corrugated ring are the same, and the spoof LSP modes E_z-field distributions are also unchanged, as shown in **Figure 4b**. It can be seen that the resonant frequency of the inner ring with a slit has changed from 2.52 to 1.76 GHz, as the mode I_1 of the inner ring with a slit is the half-integer LSP mode ($n = 0.5$). For structure B, the resonant peaks are marked as B_1, B_2, B_3, and B_4. The corresponding resonant frequencies are 1.12, 1.53, 2.22, and 3.05 GHz, respectively. We can see that there appears an asymmetric Fano lineshape between B_1 and B_3, which results from the destructive interference of the narrow discrete mode I_1 with the broad continuum state between modes O_1 and O_2 of the outer corrugated ring, and there is no resonance mode between modes O_2 and O_3 of the outer corrugated ring. **Figure 4c** illustrates the 2D E_z-field distributions on the *xoy* plane 2 mm above Structure B. It can be clearly observed that the modes B_1, B_3, and B_4 are corresponding to the spoof LSPs modes O_1, O_2, and O_3, respectively, whereas the resonant peak B_2 corresponds to the mode I_1.

ACTIVE TWO-WAY FANO RESONANCE SWITCH

Considering the responses of passive Structure A and Structure B, it can be concluded that when there exists a slit in the inner corrugated ring, the Fano resonance appears between the O_1 and O_2 modes, and when there is no slit in the inner corrugated ring, the Fano resonance appears between the O_2 and O_3 modes. Hence, if a switch diode is loaded across the slit, the two Fano resonance modes could be switched. As there is no charge carrier depletion region at the junction, the SBD diode has a shorter recovery time than the PIN diode. For a small signal, the switching time of the SBD diode is only 100 ps. Here, an SBD diode (MACOM MA4E 1317) is used to switch the Fano resonance mode, whose operating bias voltage is 0.6–0.8 V. The optimum bias voltage is 0.75 V. The DC voltage source

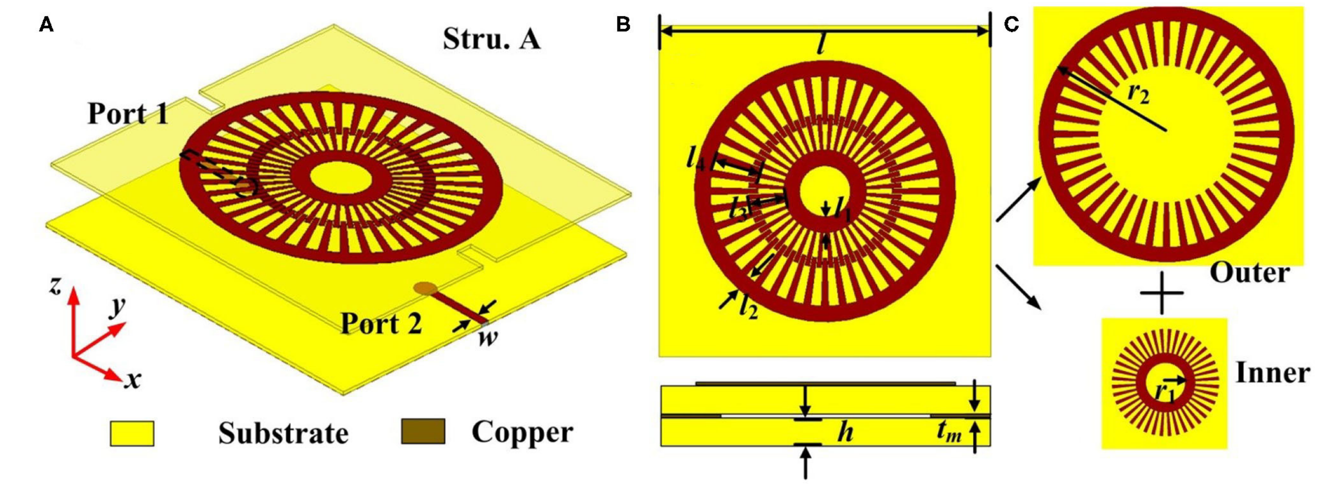

FIGURE 1 | Spoof plasmonic Fano resonance Structure A. **(A)** Three-dimensional schematic of Structure A, **(B)** top view and side view of Structure A, and **(C)** outer and inner corrugated rings.

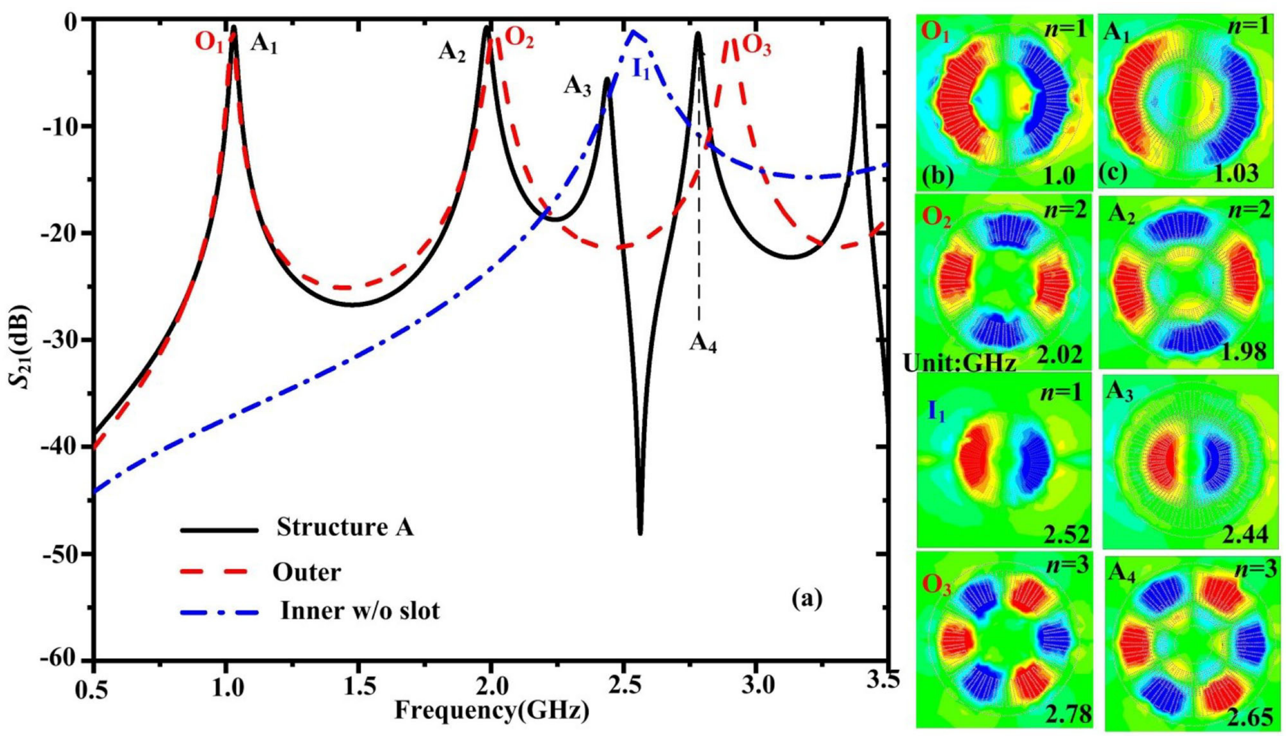

FIGURE 2 | (a) Simulation transmission coefficients S_{21} of Structure A, outer corrugated ring, and inner corrugated ring. Two-dimensional E_z-field distributions on the *xoy* plane 2 mm above **(b)** the spoof localized surface plasmon (LSP) resonators and **(c)** Structure A.

is GW Instek linear DC power supplies GPS-1850D. **Figure 5a** illustrates the schematic of the active two-way Fano resonance switch, where an SBD diode is mounted across the slit in the inner corrugated ring. The capacitance is used to isolate the DC signal, whereas the inductance is used to isolate the AC signal. The fabricated sample is shown in **Figure 5b**. In the simulation, the SBD is equivalent to an *RLC* series circuit, where R_s is the series resistance, L_s is the inductance arising from the metallic contacting strap, and C_j is the diode junction capacitance, and the values are 4 Ω, 0.45 nH, and 0.02 pF, respectively. The simulated transmission coefficients S_{21} are plotted in **Figure 5c**. It can be seen that when the SBD diode is forward biased (ON), there is no

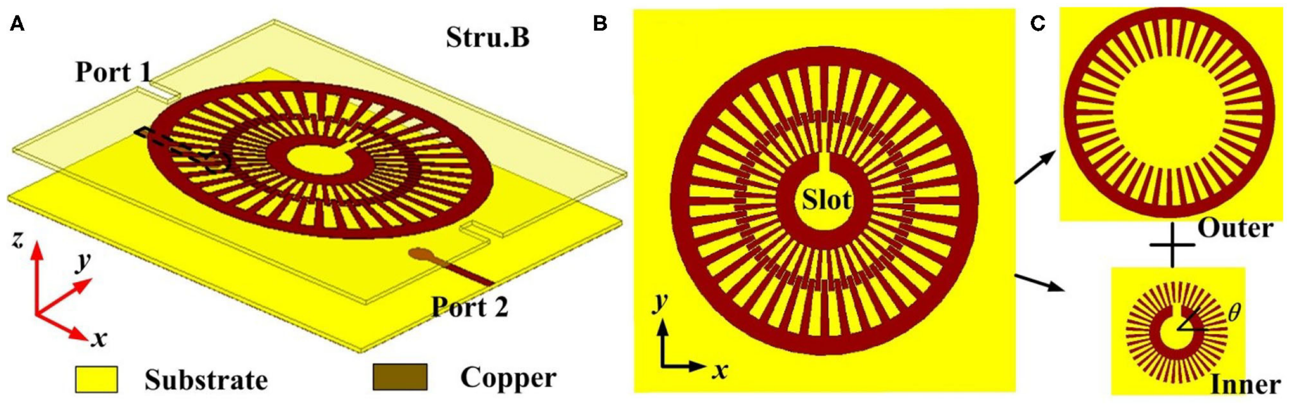

FIGURE 3 | Spoof plasmonic Fano resonance Structure B. **(A)** Three-dimensional schematic of Structure B, **(B)** top view of Structure B, and **(C)** outer corrugated ring and the inner corrugated ring with a slit.

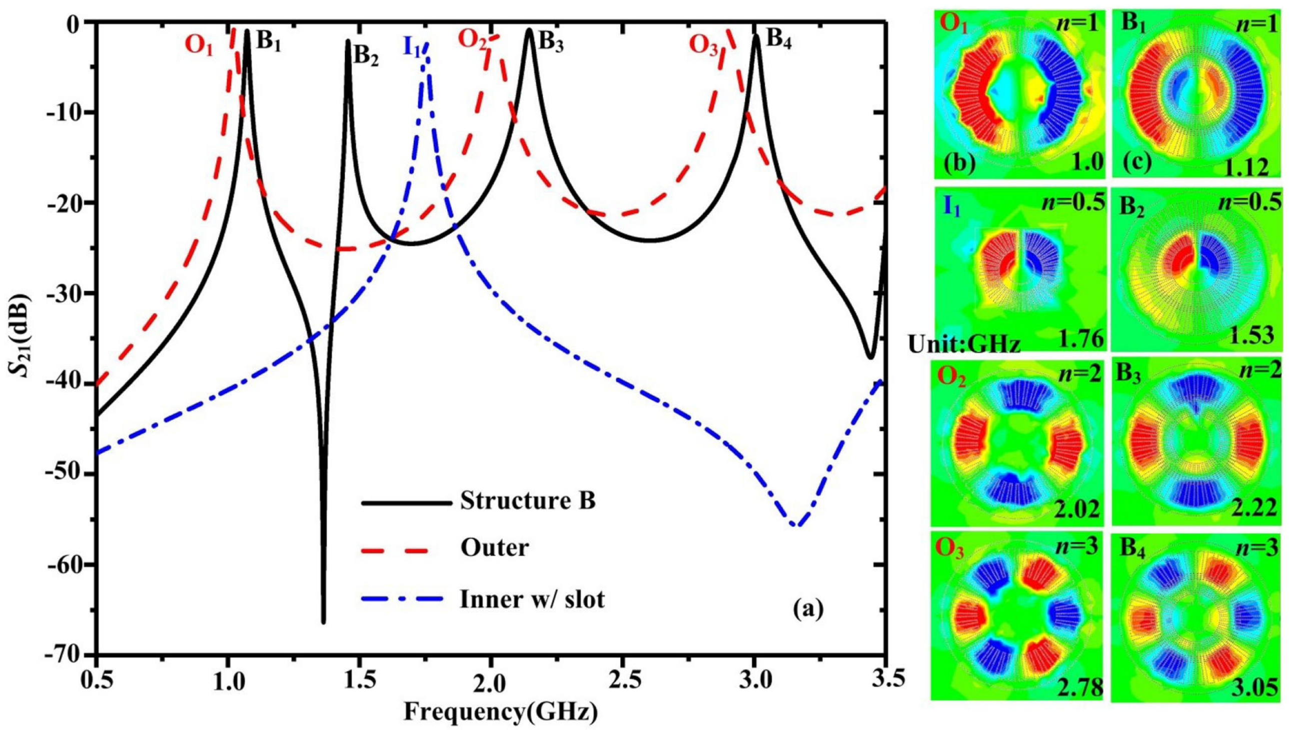

FIGURE 4 | (a) Simulation transmission coefficients S_{21} of Structure B, outer corrugated ring, and inner corrugated ring with a slit. Two-dimensional E_z-field distributions on the *xoy* plane 2 mm above **(b)** the spoof LSPs resonators and **(c)** Structure B.

slit in the corrugated ring. The structure is equivalent to Structure A, where the second Fano resonance appears. When the SBD diode is reverse biased (OFF), there is a slit in the corrugated ring. The structure is equivalent to Structure B, where the first Fano resonance appears. Hence, a two-way Fano resonance switch could be realized. The sample is measured by using a vector network analyzer (Agilent N5227A). The experimental results shown in **Figure 5d** agree well with the simulation results. When the diode is ON, the Fano resonance appears between the quadrupolar mode and hexapolar mode. When the diode is OFF, the Fano resonance appears between the dipolar mode and the quadrupolar mode. The measured transmission coefficients are almost 10 dB lower than the simulation results, which may be caused by the higher series resistance R_s and the welding quality in the measurements.

CONCLUSION

In summary, we have proposed and experimentally demonstrated an active two-way Fano resonance switch in the microwave

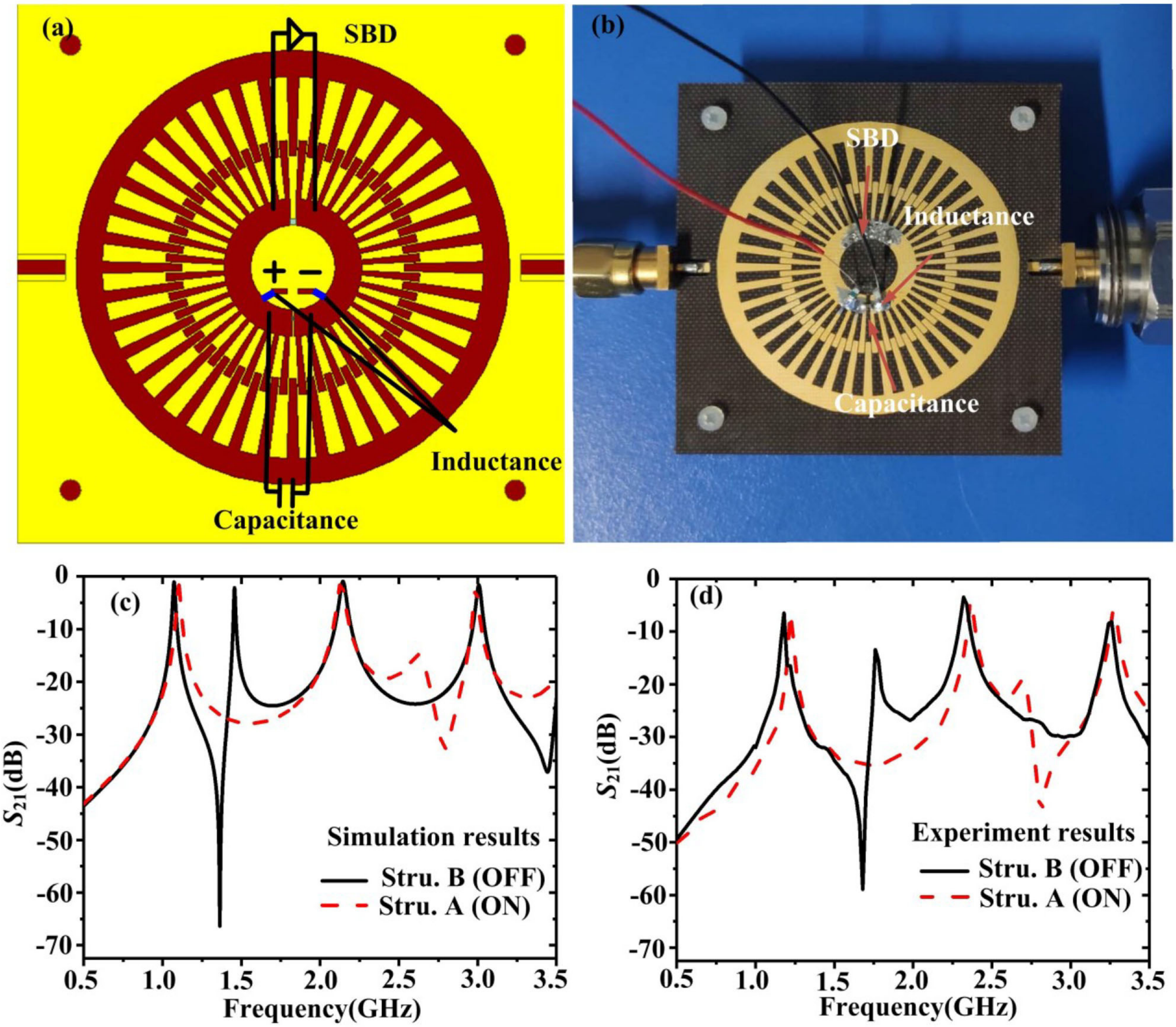

FIGURE 5 | **(a)** Schematic of the active two-way Fano resonance switch. **(b)** Fabricated sample. **(c)** Simulated and **(d)** measured transmission coefficients S_{21} of the active two-way Fano resonance switch.

frequency. When the SBD diode is forward biased, the second Fano resonance appears between the quadrupole mode and hexapole mode. When the SBD diode is reverse biased, the first Fano resonance appears between the dipolar mode and the quadrupole mode. The experimental results agree well with the simulated results. The Fano resonance switch has advantages such as two-way switches, fast switching speed, and low operation voltage, which could find applications in plasmonic circuits, sensors, devices, etc.

DATA AVAILABILITY STATEMENT

All datasets presented in this study are included in the article/supplementary material.

AUTHOR CONTRIBUTIONS

All authors listed have made a substantial, direct and intellectual contribution to the work, and approved it for publication.

FUNDING

This work was supported in part by the National Natural Science Foundation of China under grant no. 61971469, in part by the Science and Technology Commission of Shanghai Municipality (STCSM) under grant no. 18ZR1413500, and in part by the Open Project Program of the State Key Laboratory of Millimeter Waves under grant no. K202109.

REFERENCES

1. Fano U. Effects of Configuration Interaction on Intensities and Phase Shifts. *Phys Rev*. (1961) **124**:1866–78. doi: 10.1103/PhysRev.124.1866
2. Yong S.J, Arkady MS and Chang SK. Classical analogy of Fano resonances. *Phys Scr*. (2006) **74**:259–66. doi: 10.1088/0031-8949/74/2/020
3. Rybin MV, Khanikaev AB, Inoue M, Samusev KB, Steel MJ, Yushin G, et al. Fano resonance between Mie and Bragg scattering in photonic crystals. *Phys Rev Lett*. (2009) **103**:023901. doi: 10.1103/PhysRevLett.103.023901
4. Bachelier G, Russier AI, Benichou E. Fano profiles induced by near-field coupling in heterogeneous dimers of gold and silver nanoparticles. *Phys Rev Lett*. (2008) **101**:197401. doi: 10.1103/PhysRevLett.101.197401
5. Liu N, Langguth L, Weiss T. Plasmonic analogue of electromagnetically induced transparency at the Drude damping limit. *Nat Mater*. (2009) **8**:758–762. doi: 10.1038/nmat2495
6. Verellen N, Sonnefraud Y, Sobhani H. Fano resonances in individual coherent plasmonic nanocavities. *Nano Lett*. (2009) **9**:1663–7. doi: 10.1021/nl9001876
7. Sonnefraud Y, Verellen V, Sobhani H, Guy AE, Victor VM. Experimental realization of subradiant, superradiant, and Fano resonances in ring/disk plasmonic nanocavities. *ACS Nano*. (2010) **4**:1664–70. doi: 10.1021/nn901580r
8. Miroshnichenko AE, Flach S, Kivshar YS. Fano resonances in nanoscale structures. *Rev Mod Phys*. (2010) **82**: 2258–90. doi: 10.1103/RevModPhys.82.2257
9. Fu YH, Zhang JB, Yu YF. Generating and manipulating higher order fano resonances in dual-disk ring plasmonic nanostructures. *ACS Nano*. (2012) **6**:5130–7. doi: 10.1021/nn3007898
10. Fedotov VA, Rose M, Prosvirnin SL, Papasimakis N, Zheludev NI. Sharp trapped-mode resonances in planar metamaterials with a broken structural symmetry. *Phys Rev Lett*. (2007) **99**:147401. doi: 10.1103/PhysRevLett.99.147401
11. Zhang S, Genov DA, Wang Y, Liu M, Zhang X. Plasmon-induced transparency in metamaterials. *Phys Rev Lett*. (2008) **101**:047401. doi: 10.1103/PhysRevLett.101.047401
12. Boris L, Nikolay IZ, Stefan AM, Naomi JH, Peter N, Harald G, et al. The fano resonance in plasmonic nanostructures and metamaterials. *Nat Mater*. (2010) **9**:707–15. doi: 10.1038/nmat2810
13. Singh R, Al-Naib IAI, Koch M, Zhang W. Sharp fano resonances in THz metamaterials. *Opt Express*. (2011) **19**:6312–9. doi: 10.1364/OE.19.006312
14. Liao Z, Pan BC, Shen XP, Cui TJ. Multiple fano resonances in spoof localized surface plasmons. *Opt Express*. (2014) **22**:15710. doi: 10.1364/OE.22.015710
15. Xiao QX, Yang BJ, Zhou YJ. Spoof localized surface plasmons and Fano resonances excited by flared slot line. *J Appl Phys*. (2015) **118**:233112. doi: 10.1063/1.4938153
16. Chen L, Xu NN, Singh L, Cui TJ, Singh R, Zhu YM, et al. Defect-induced fano resonances in corrugated plasmonic metamaterials. *Adv Opt Mat*. (2017) **5**:1–7. doi: 10.1002/adom.201600960
17. Song JF, Ochiai Y, Bird JP. Fano resonances in open quantum dots and their application as spin filters *Appl Phys Lett*. (2003) **82**:4561. doi: 10.1063/1.1586788
18. Sámson ZL, MacDonald KF, De Angeils F. Metamaterial electro-optic switch of nanoscale thickness. *Appl Phys Lett*. (2010) **96**:143105. doi: 10.1063/1.3355544
19. Chung YC, Jay Guo L. Biochemical sensors based on polymer microrings with sharp asymmetrical resonance. *Appl Phys Lett*. (2003) **83**:1–4. doi: 10.1063/1.1605261
20. Lahiri B, Khokhar AZ, De La Rue RM, McMeekin SG, Johnson NP. Asymmetric split ring resonators for optical sensing of organic materials. *Opt Express*. (2009) **17**:1107–15. doi: 10.1364/OE.17.001107
21. Liu N, Weiss T, Mesch M. Planar metamaterial analogue of electromagnetically induced transparency for plasmonic sensing. *Nano Lett*. (2010) **10**:1103–7. doi: 10.1021/nl902621d
22. Hua L, Xueming L, Dong M, Guoxi W. Plasmonic nanosensor based on fano resonance in waveguide-coupled resonators. *Opt Lett*. (2012) **37**:3780. doi: 10.1364/OL.37.003780
23. Ranjan S, Wei C, Ibraheem A, Longqing C, Withawat W, Weili Z. Ultrasensitive terahertz sensing with high-Q fano resonances in metasurfaces. *Appl Phys Lett*. (2014) **105**:1–6. doi: 10.1063/1.4895595
24. Elena S, Ran D, George S, Ravindra P. Sensing based on fano-type resonance response of all-dielectric metamaterials. *Sensors*. (2015) **15**:9344–59. doi: 10.3390/s150409344
25. Kuang LL, Hsuan YH, Meng LY, Chia CC, Ming YP, Xu S, et al. Highly sensitive aluminum based biosensors using tailorable fano resonances in capped nanostructures. *Sci Rep*. (2017) **7**:44104. doi: 10.1038/srep44104
26. Chen J, Gan F, Wang Y. Plasmonic sensing and modulation based on fano resonances. *Adv Opt Mater*. (2018) **6**:1701152. doi: 10.1002/adom.201701152
27. Zheludev NI, Kivshar YS. From metamaterials to metadevices. *Nat Mater*. (2012) **11**:917–24. doi: 10.1038/nmat3431
28. Cong LQ, Manjappa M, Xu NN, Al NI, Zhang WL, Singh R. Fano resonances in terahertz metasurfaces: a figure of merit optimization. *Adv Opt Mater*. (2015) **3**:1537. doi: 10.1002/adom.201500207
29. Bochkova E, Han S, Lustrac A, Singh R, Burokur SN, Lupu A. High-Q fano resonances via direct excitation of an antisymmetric dark mode. *Opt Lett*. (2018) **43**:3818. doi: 10.1364/OL.43.003818
30. Zhou YJ, Li QY, Zhao HZ, Cui TJ. Gain-assisted active spoof plasmonic fano resonance for high-resolution sensing of glucose aqueous solutions. *Adv Mater Technol*. (2019) **5**:1900767. doi: 10.1002/admt.201900767
31. Chang WS, Lassiter JB, Swanglap P, Sobhani H, Khatua S, Nordlander P, et al. A plasmonic fano switch. *Nano Lett*. (2012) **12**:4977–82. doi: 10.1021/nl302610v
32. Emani NK, Chung TF, Kildishev AV, Shalaev VM, Chen YP, Boltasseva A. Electrical modulation of fano resonance in plasmonic nanostructures using graphene. *Nano Lett*. (2014) **14**:78–82. doi: 10.1021/nl403253c
33. Manukumara M, Yogesh KS, Longqing C, Ibraheem AN, Ranjan S. Active photo switching of sharp fano resonances in THz metadevices. *Adv Mater*. (2017) **29**:1603355. doi: 10.1002/adma.201603355
34. Lu W, Cui X, Chow TH, Shao L, Wang H, Chen H, et al. Switching plasmonic fano resonance in gold nanosphere-nanoplate heterodimers. *Nanoscale*. (2019) **11**:9641–53. doi: 10.1039/C9NR01653H
35. Huang Y, Yan J, Ma C, Yang G. Active tuning of the fano resonance from a Si nanosphere dimer by the substrate effect. *Nanoscale Horiz*. (2019) **4**:148–57. doi: 10.1039/C8NH00198G

Conflict of Interest: The authors declare that the research was conducted in the absence of any commercial or financial relationships that could be construed as a potential conflict of interest.

frontiers in Physics

ORIGINAL RESEARCH
published: 29 October 2020
doi: 10.3389/fphy.2020.527394

Wide-Angle Circular Polarization Converter Based on a Metasurface of Z-Shaped Unit Cells

Mingjun Wang[1,2,3]* *and Zhizhu Zhai*[1]*

[1] *School of Automation and Information Engineering, Xi'an University of Technology, Xi'an, China,* [2] *School of Physics and Telecommunications Engineering, Shaanxi University of Technology, Hanzhong, China,* [3] *Shaanxi Civil-Military Integration Key Laboratory of Intelligence Collaborative Networks, Xi'an, China*

Since it is designable, metasurface was widely used in various fields, especially the design of polarization converters. However, most of the polarization converters currently designed can only work under normal incidence or small angle incidence, which hugely limits the application of the device. In this paper, a chiral metasurface based on the z-shaped unit cell, which can manipulate circular polarization wave, is proposed. The simulation result shows that this converter can maintain the polarization state of circular polarization after reflection from 8.18 to 13.988 GHz with a polarization conversion ratio of more than 90%. Moreover, the structure is insensitive to the incidence angle, which can keep a stable performance both for left-handed circularly polarized wave and right-handed circularly polarized waves as the incident angle increase to 75°. The proposed metasurface with simple structure and angular stability can be used in communication and polarization manipulating devices.

Keywords: circular polarization converter, metasurface, wide-angle, high-efficiency, microwave band

OPEN ACCESS

Edited by:
Lin Chen,
University of Shanghai for Science and Technology, China

Reviewed by:
Weiren Zhu,
Shanghai Jiao Tong University, China
Hui Feng Ma,
Southeast University, China
Xiaofei Zang,
University of Shanghai for Science and Technology, China

****Correspondence:***
Mingjun Wang
wangmingjun@xaut.edu.cn
Zhizhu Zhai
2223574498zzz@gmail.com

Specialty section:
This article was submitted to Optics and Photonics, a section of the journal Frontiers in Physics

Received: *16 January 2020*
Accepted: *26 August 2020*
Published: *29 October 2020*

Citation:
Wang M and Zhai Z (2020) Wide-Angle Circular Polarization Converter Based on a Metasurface of Z-Shaped Unit Cells. Front. Phys. 8:527394. doi: 10.3389/fphy.2020.527394

INTRODUCTION

Polarization, as one of the basic characteristics of electromagnetic (EM) waves, can be divided into three types: linear polarization, circular polarization, and elliptical polarization. Due to the features of circular polarization [1], circularly polarized (CP) antennas play an important role in communication systems such as satellites and rockets. With the diversification of application scenarios, it is necessary to manipulate the polarization state flexibly. Traditional polarization regulators are implemented using birefringent crystals, but such devices usually have a large volume, which greatly limits their application range. Therefore, people have always been working to find polarization converters with better performance and more relaxed application conditions.

Metasurfaces, artificially constructed two-dimensional materials, are periodically arranged by micro-units, showing unique EM properties that have not been found in nature [2]. Different unit structures, materials, and arrangements can achieve different functions, so metasurfaces have strong designability and functional customization. This new material that can design EM properties provides new ideas for the design of polarization regulators.

In recent years, various types of polarization converters based on metasurfaces have been successively proposed, including linear polarization (LP) to LP (that is 90° polarization rotator) [3–6], LP to circular polarization (CP) [7–9], CP to CP (that is circular polarization rotation direction regulator) [10], and multiple conversion modes [11, 12]. Great progress has been made in frequency band [13–15], bandwidth [16–18], volume [2], robustness [19, 20], etc. However, most of the attention was focused on the LP converter, and the research on CP regulators is relatively few. Recently, Akram et al. [18] proposed an ultra-wideband metasurface working at both transmission and reflection modes; however, they do not pay attention to oblique incidence. Huang [10] proposed one in 2017, which has a simple structure and can regulate the rotation direction of circularly polarized waves in the range of 8.16–15.32 GHz. However, the polarization converter is extremely sensitive to the angle. When the incident angle is $>30°$, the working bandwidth becomes obviously narrow and the polarization conversion ratio decreases rapidly. The existing polarization converters currently all have such a common defect that they can only work under small-angle incidence, which puts restrictions on the application of the device.

In this paper, we carried out works to overcome the shortcomings of the strong angle sensitivity of existing polarization converters and proposed a reflective CP regulator using a chiral metasurface based on the unit cell having a z-shaped structure. The polarization converter can maintain the polarization state of circular polarization after reflection from 8.18 to 13.988 GHz, basically covering the X-band that is 8–12 GHz. Compared with published designs, the proposed CP regulator has a simple geometry but a superior angular tolerance and hence can be used in many applications.

MODEL AND DESIGN

Our designed metasurface is composed of 20 × 20 unit cells as shown in **Figure 1A**. Every unit cell has three layers: the metal ground, the middle dielectric substrate, and the surface metal figure. The copper ground can prevent the transmission of the EM, reducing energy loss. The metal pattern on the surface is a copper material with a conductivity of $5.8 \times 10^7 S/$, and the intermediate dielectric layer is an FR-4 material with $\varepsilon_r = 4.4$, $\mu_r = 1$, and $\tan\delta = 0.025$, which is rotated 45° with respect to the Y-axis. The thickness of the underlying layer is 0.3 mm, and the surface Z-shaped pattern with the thickness of 0.035 mm is placed along the diagonal position of the substrate material. **Figure 1B** shows the specific parameters of the structure, where $p = 10.5$mm, $l = 6$mm, $w = 1.6$mm.

The numerical simulation is carried out via the CST software, which utilizes a finite integration method and the Floquet mode to analyze the frequency response of the periodical structure. We set the unit cell conditions in the x and y directions, and the open and add space conditions in the z-direction. Incident left-handed circularly polarized (LCP) wave and right-handed circularly polarized (RCP) waves propagate along the opposite of the z-direction.

SIMULATION AND PERFORMANCE ANALYSIS

When the circular waves were normally incident on the metasurface, the reflection wave can be expressed as [10]

$$\begin{pmatrix} \mathbf{E}_+^r \\ \mathbf{E}_-^r \end{pmatrix} = \begin{pmatrix} \mathbf{r}_{++} & \mathbf{r}_{+-} \\ \mathbf{r}_{-+} & \mathbf{r}_{--} \end{pmatrix} \begin{pmatrix} \mathbf{E}_+^i \\ \mathbf{E}_-^r \end{pmatrix}$$

where the superscripts i and r represent the incident and reflected waves, respectively, and the subscripts + and − denote the RCP and LCP, respectively. The first subscript indicates the polarization of the reflected wave, and the second subscript indicates the polarization of the incident wave. Thus, $\mathbf{E}_+^i$,$\mathbf{E}_-^i$ represent the electric fields of incident RCP and LCP, respectively. Similarly, $\mathbf{E}_+^r$ and $\mathbf{E}_-^r$ represent the reflected ones. Elements in the matrix are all reflection coefficients; identical subscripts indicate co-polarized reflection coefficients, while different subscripts indicate cross-polarized reflected coefficients. The above reflection coefficients $r_{mn}\left(m, \mathrm{n} = +, -\text{ and } m \neq \mathrm{n}\right)$ are the complex reflection coefficients, containing both amplitude $r_{mn} = |r_{mn}|$ and phase information. We know that when EM waves are normally incident on the metasurface, the handedness of the reflected CP wave will be changed. We regulate the rotation direction of the reflected wave, that is, to maintain the handedness of the circularly polarized wave. Therefore, it is

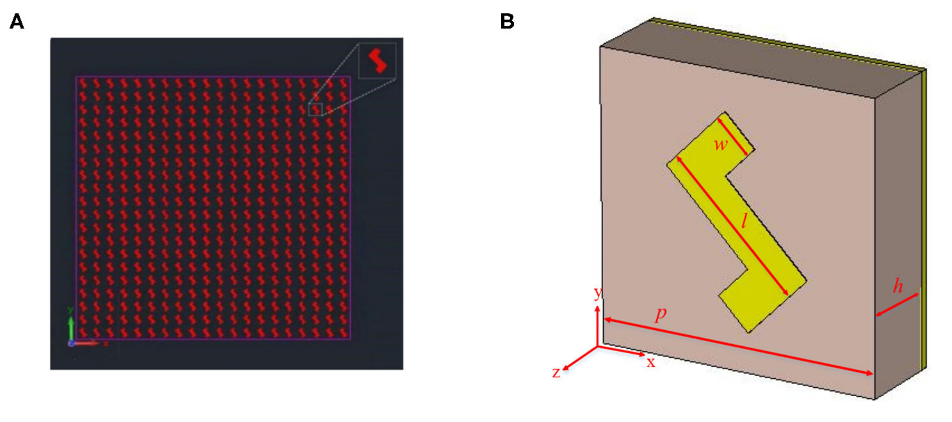

FIGURE 1 | (A) Perspective view of designed metasurface. **(B)** Schematic picture of the unit cell structure.

possible to define the polarization conversion rate (PCR) of two different modes of circularly polarized waves.

$$PCR_m = |r_{mm}|^2 / \left(|r_{mm}|^2 + |r_{nm}|^2\right)$$

To show the performance of this device, we simulated the reflection coefficient and PCR of LCP and RCP at normal incidence, as shown in **Figure 2**. The results show that the reflection coefficients curves of the two cases almost wholly coincide; the PCR also satisfies this rule. For the reflection coefficient, the co-polarized reflection coefficient is > 0.9 in the range of 8.432–13.036 GHz, and the cross-polarized reflection coefficient is <0.2 in the range of 8.672–13.508 GHz, which indicates that the reflected CP does achieve a polarization regulation in this band. For the polarization conversion ratio, PCR is > 0.9 in the range of 8.18–13.988 GHz, covering all the X-band, which proves the high efficiency of the regulator. Besides, we can observe that there are three resonant frequencies (at 9.22, 10.17, and 13.12 GHz) in this range.

In practical applications, we need to consider the situation of oblique incidence. So we calculate the bandwidth to discuss the oblique incidence performance. The schematic diagram of the incident angle is shown in **Figure 3B**. **Figure 3A** shows the relation between the bandwidth when the PCR is higher than 0.9 (the bandwidth in the paper all refers to the continuous bandwidth with a PCR > 0.9) and the incident angle. Obviously, for the two incident modes of LCP and RCP, the angle has different effects on the performance of the polarization converter, and the influence of the angle on the bandwidth is not monotonous. For the RCP waves, when the angle of incidence is $<75°$, the bandwidth decreases monotonically with an increasing angle, reaching a minimum value of 3.756 GHz at 75°. When the incident angle continually increases, the bandwidth expands rapidly. For the LCP waves, the bandwidth reaches a maximum of 5.988 GHz when the angle of incidence is around 30°; when

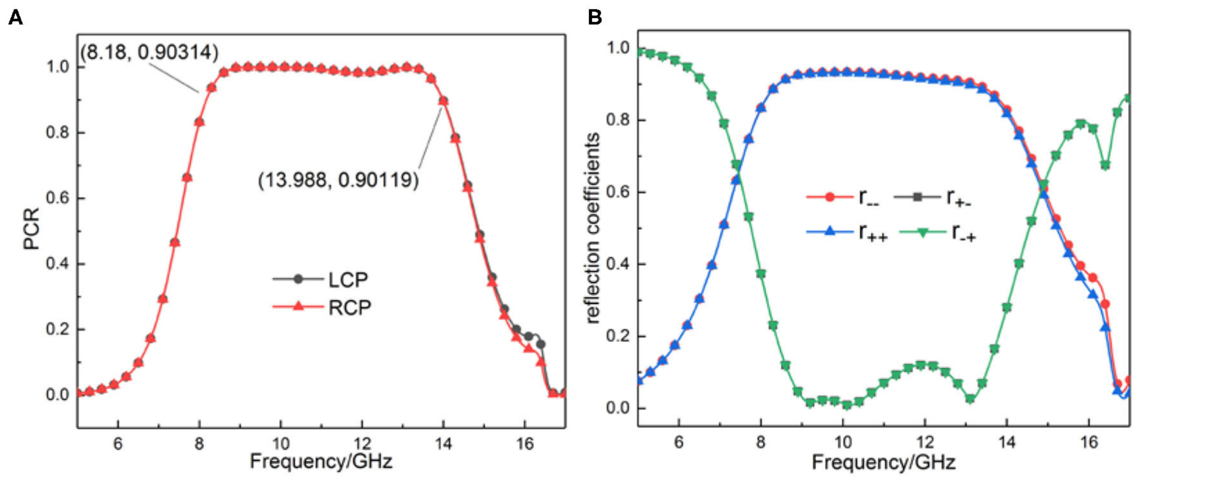

FIGURE 2 | (A) PCR and **(B)** reflection coefficient under the normal incident CP waves.

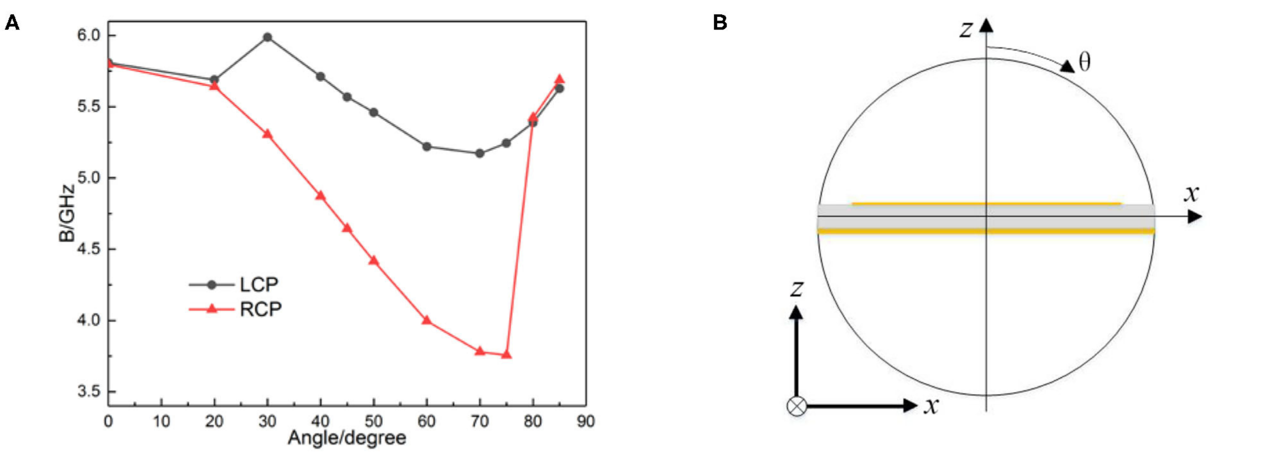

FIGURE 3 | (A) Relation between the bandwidth and the angle. **(B)** Schematic diagram of the incident angle.

the angle enlarges again, the bandwidth shows a downward trend, but the decline rate is slower, reaching a minimum value of 5.172 GHz when the incident angle reaches 70°. The bandwidth also increases when the incident angle increases again.

To show the influence of the angle on the performance of the converter in more detail, we simulated the PCR of the two types of CP waves at different incident angles, respectively. For LCP waves, the incidence angles are 0°, 30°, 45°, and 70°, respectively, as shown in **Figure 4A**. For RCP waves, the incidence angles are 0°, 30°, 45°, and 75°, respectively, as shown in **Figure 4B**. The result shows that the device still works well for both LCP and RCP in the X-band, though under a super large incident angle. For LCP waves, the incidence angle has little effect on the PCR and the bandwidth. According to **Figure 3**, under the LCP incoming wave, the bandwidth reaches the minimum when the incident angle is equal to 70°. In combination with **Figure 4A**, in the same angle, the PCR is > 0.9 in the range from 8.108 to 13.28 GHz, covering the 97.3% X-band. At other angles, the bandwidth coverage is broader, and the performance is better. For RCP waves, although the continuous bandwidth is narrow, the PCR is kept high, and the performance in the X-band is still great. With the analysis of **Figure 3**, the bandwidth reaches a minimum when the angle of incidence is 75°. According to **Figure 4B**, when the angle of incidence is 75°, the frequency band with a PCR > 0.9 is 8.144–11.792 GHz, which can still regulate the handedness of the CP waves in the X-band 91.2% frequency band. Besides, due to the drooping frequency point in the high-frequency band, the continuous bandwidth becomes smaller, and the working field changes from a single wideband to a dual band; in other words, the regulation performance outside the X-band is also excellent.

To show the advantages of the device more clearly, we provide a parameter comparison with a previous circular polarization regulator as shown in **Table 1**. It shows that our design has the advantages of simple structure, small loss, and strong angular tolerance.

MECHANISM DISCUSSION

In the following, we explain the mechanism of the excellent performance of the device through formula derivation and simulation results. When the incident CP wave is decomposed into LP waves $\mathbf{E}_x^i$ and $\mathbf{E}_y^i$, the reflected wave can also be expressed as and $\mathbf{E}_x^r$, and $\mathbf{E}_y^r$ the relationship between the incident field and the reflected field can be expressed as [10]

$$\begin{pmatrix}\mathbf{E}_x^r\\ \mathbf{E}_y^r\end{pmatrix} = \begin{pmatrix}\mathbf{r}_{xx} & \mathbf{r}_{xy}\\ \mathbf{r}_{yx} & \mathbf{r}_{yy}\end{pmatrix}\begin{pmatrix}\mathbf{E}_x^i\\ \mathbf{E}_y^i\end{pmatrix} = R\begin{pmatrix}\mathbf{E}_x^i\\ \mathbf{E}_y^i\end{pmatrix}$$

that is, $\mathbf{E}_x^r = \mathbf{r}_{xx}\mathbf{E}_x^i + \mathbf{r}_{yx}\mathbf{E}_y^i$, $\mathbf{E}_y^r = \mathbf{r}_{yy}\mathbf{E}_y^i + r_{xy}\mathbf{E}_x^i$, where $\mathbf{r}_{xx}$ and $\mathbf{r}_{yx}$ represent the co-polarized and cross-polarized reflection coefficients under the x-polarized wave incidence; others are similar. Then, the reflected wave can be described as

$$\mathbf{E}^r = (\mathbf{r}_{xx}\mathbf{E}_x^i + \mathbf{r}_{xy}\mathbf{E}_y^i)\hat{x} + (\mathbf{r}_{yy}\mathbf{E}_y^i + \mathbf{r}_{yx}\mathbf{E}_x^i)\hat{y}$$

There are four cases in this expression: $\mathbf{r}_{xx}\mathbf{E}_x^i\hat{x} + \mathbf{r}_{yy}\mathbf{E}_y^i\hat{y}$, $\mathbf{r}_{xy}\mathbf{E}_y^i\hat{x} + \mathbf{r}_{yx}\mathbf{E}_x^i\hat{y}$, $\mathbf{r}_{xx}\mathbf{E}_x^i\hat{x} + \mathbf{r}_{xy}\mathbf{E}_y^i\hat{x}$, $\mathbf{r}_{yy}\mathbf{E}_y^i\hat{y} + \mathbf{r}_{yx}\mathbf{E}_x^i\hat{y}$. For convenience, they are expressed as $f_{xx} + f_{yy}$, $f_{xy} + f_{yx}$, $f_{xx} + f_{xy}$, and $f_{yy} + f_{yx}$, where $f_{xx} + f_{yy}$ and $f_{xy} + f_{yx}$ express the reflected co-polarization terms under the CP incoming wave; the other two items express the reflected LP wave under the same incident situation. Based on

TABLE 1 | Comparison with other published circular polarization regulator.

Works	Bandwidth/GHz	Structure	Angle/degree	Loss
Our work	8.18–13.988	Simple	75	<0.2
Huang et al. [10]	8.16–15.32	Simple	30	<0.2
Yang et al. [11]	5.5–8.94 and 13.1–15.5	Simple	No calculation	>0.2
Tang-Jing et al. [21]	12–15.5	Complex	No calculation	<0.1

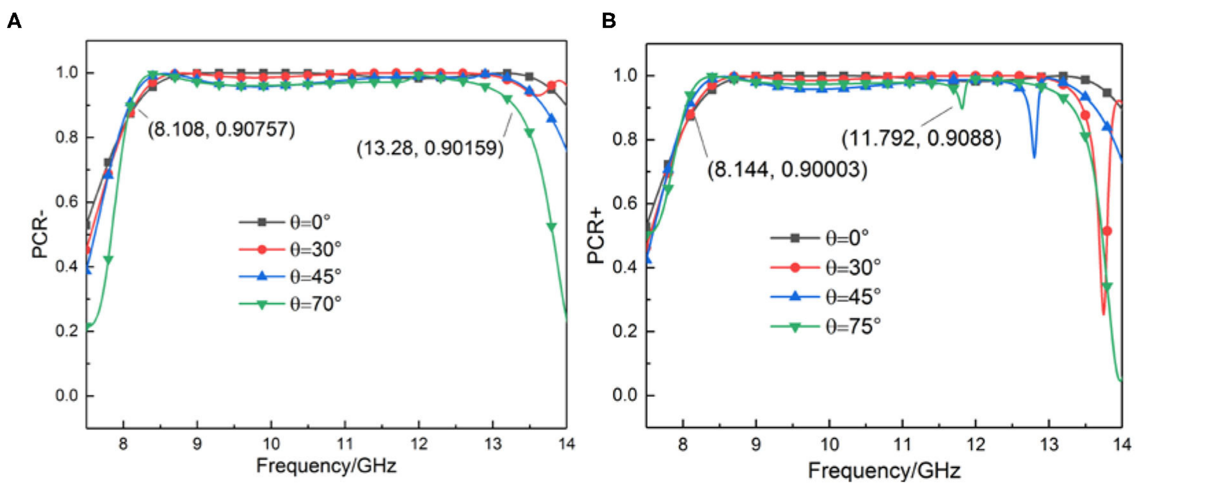

FIGURE 4 | Simulation result of PCR under a different angle for **(A)** LCP and **(B)** RCP incident waves.

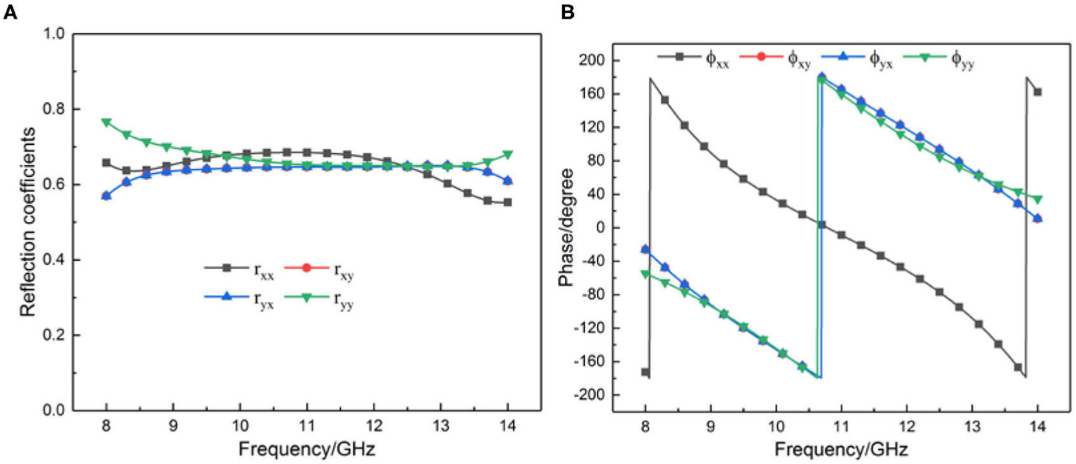

FIGURE 5 | Simulation result of linearly polarized incoming wave under normal incidence. **(A)** Reflection coefficient. **(B)** Phase.

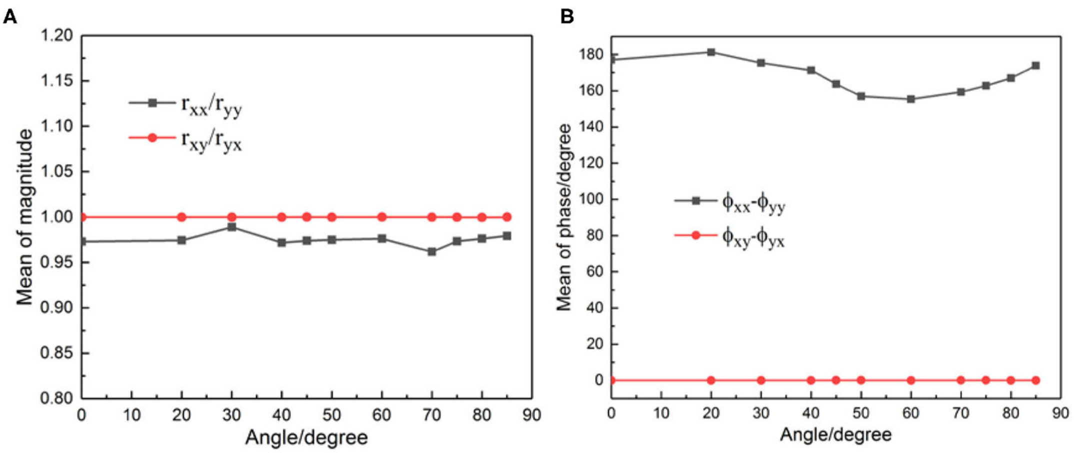

FIGURE 6 | Simulation result of linearly polarized incoming wave under oblique incidence. **(A)** Mean of amplitude ratio. **(B)** Mean of phase difference.

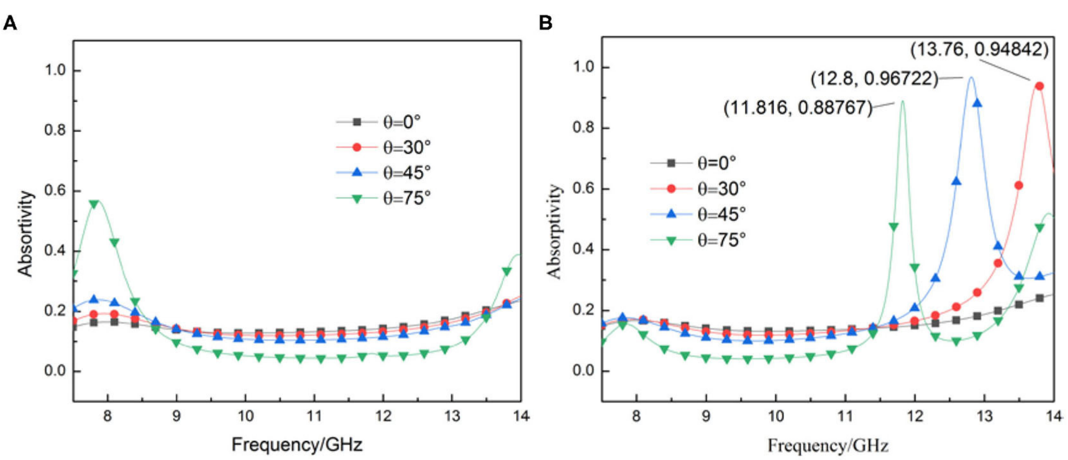

FIGURE 7 | Absorption spectra for different incoming wave. **(A)** LCP incoming waves. **(B)** RCP incoming waves.

the above definition, to maintain the handedness of reflected waves, the structure must meet the conditions that $r_{yx} = r_{xy}$, $\phi_{yx} = \phi_{xy}$, $r_{xx} = r_{yy}$, $\left|\phi_{yy} - \phi_{xx}\right| = \pi$. **Figure 5** shows the reflection coefficient and phase under the LP incoming wave. We can see that ϕ_{xy} and ϕ_{yx} are entirely coincident; the difference of ϕ_{yy} and ϕ_{xx} is close to 180°; r_{yx} and r_{xy} are completely coincident; the difference of r_{xx} and r_{yy} is > 0.13. In addition, at the three resonant frequencies ($f = 9.22$, 10.17, 13.12 GHz), $\left|\phi_{yy} - \phi_{xx}\right| = \pi$. We can see that the results satisfied all the amplitude and phase conditions mentioned above. Therefore, we confirmed that the circular polarization-keeping reflection is realized.

For the case of oblique incidence, we calculated the mean values of $\mathrm{r}_{xx}/\mathrm{r}_{yy}$, $\mathrm{r}_{xy}/\mathrm{r}_{yx}$, $\left|\phi_{xx} - \phi_{yy}\right|$, and $\left|\phi_{xy} - \phi_{yx}\right|$ within the bandwidth with different incident angles, as shown in **Figure 6**. The result indicates that $\frac{\mathrm{r}_{xy}}{\mathrm{r}_{yx}} = 1$ and the values of $\mathrm{r}_{xx}/\mathrm{r}_{yy}$ are all larger than 0.96, which are close to 1, at any angle of incidence. In **Figure 6B**, ϕ_{xy} and ϕ_{yx} are wholly coincident, and the difference of ϕ_{yy} and ϕ_{xx} is close to 180°, meeting the regulation conditions. Therefore, the device has a robust angular-tolerance performance.

Circular dichroism also can be used to explain the physical mechanism of the device. Our design is a reflective chiral device with circular dichroism, that is, it has different absorptivity for LCP waves and RCP waves. The selective absorption of waves by the device will reduce the component of co-polarized reflected waves, resulting in a drop in the PCR. The absorption spectra of different incident waves are shown in **Figure 7**.

Comparing **Figure 7A** with **Figure 7B**, it can be found that the absorption rate of the LCP incident wave is kept at a low level in the working frequency band, basically below 0.2, with the increase in the incident angle. When the incident angle reaches 75°, absorption peaks appear at low frequency and high frequency, which leads to a slight narrowing of the bandwidth of the polarization converter, which is consistent with the results in **Figure 4A**. For the case of the RCP incident wave, with the increase in the incident angle, the absorption peak of the device for the RCP wave gradually shifts to the left, corresponding to the tips of the polarization conversion rate in **Figure 4B**.

CONCLUSION

We proposed a reflective circular polarization handedness regulator based on metasurface, which contains 20 × 20 resonant units. The structure is simple and easy to fabricate. Simulations and mechanisms have proven that our devices exhibit excellent performance in the X-band. Compared with previous papers, our design not only can achieve high-efficiency broadband polarization conversion performance under the normal incidence but also has robust angular tolerance. At large incident angles, they can also effectively keep circular polarization handedness. Indeed, the device also has disadvantages. Our work still does not address the problem of different responses to RCP and LCP waves, which should be considered in the application. Anyway, this metasurface has great significance for the application due to the good regulation function and robust angular tolerance.

DATA AVAILABILITY STATEMENT

All datasets generated for this study are included in the article/supplementary material.

AUTHOR CONTRIBUTIONS

MW tutored and revised the paper. ZZ conducts deductive calculations, plots, and thesis writing. All authors contributed to the article and approved the submitted version.

FUNDING

This work was supported by the National Natural Science Foundation of China (Grants No. 61771385), Science and Technology on Solid-State Laser Laboratory (Grants No. 6142404180301), and Science and Technology research plan of Xi'an city (Grant No. GXYD14.26).

REFERENCES

1. Luo Q, Zhu F, Gao S. *Circularly Polarized Antennas.* West Sussex: John Wiley & Sons, Ltd (2013).
2. Gao X, Han X, Cao WP, Li HO, Ma HF, Cui TJ. Ultrawideband and high-efficiency linear polarization converter based on double V-shaped metasurface. *IEEE T Antenn Propag.* (2015) **63**:3522–30. doi: 10.1109/TAP.2015.2434392
3. Xu Y, Shi Q, Zhu Z, Shi J. Mutual conversion and asymmetric transmission of linearly polarized light in bilayered chiral metamaterial. *Opt Express.* (2014) **22**:411–4. doi: 10.1364/OE.22.025679
4. Huang X, Yang D, Yang H. Multiple-band reflective polarization converter using U-shaped metamaterial. *J Appl Phys.* (2014) **115**:13–9. doi: 10.1063/1.4868076
5. Huang X, Xiao B, Yang D, Yang H. Ultra-broadband 90° polarization rotator based on bi-anisotropic metamaterial. *Opt Commun.* (2015) **338**:416–21. doi: 10.1016/j.optcom.2014.11.010
6. Zhang L, Zhou P, Lu H, Zhang L, Xie J, Deng L. Realization of broadband reflective polarization converter using asymmetric cross-shaped resonator. *Opt Mater Express.* (2016) **6**:1393–404. doi: 10.1364/OME.6.001393
7. Li Y, Zhang J, Qu S, Wang J, Zheng L, Pang Y et al. Achieving wide-band linear-to-circular polarization conversion using ultra-thin bi-layered metasurfaces. *J Appl Phys.* (2015) **117**:7. doi: 10.1063/1.4906220
8. Zhuang YQ, Wang GM, Zhang XK, Zhang CX, Cai T, Li HP. Design of reflective linear-circular polarization converter based on phase gradient metasurface. *Acta Phys Sin-Ch Ed.* (2016) **65**:154102. doi: 10.7498/aps.65.154102
9. Jia Y, Liu Y, Zhang W, Wang J, Wang Y, Gong S et al. Ultra-wideband metasurface with linear-to-circular polarization conversion of an electromagnetic wave. *Opt Mater Express.* (2018) **8**:597. doi: 10.1364/OME.8.000597
10. Huang X, Chen J, Yang H. High-efficiency wideband reflection polarization conversion metasurface for circularly polarized waves. *J Appl Phys.* (2017) **122**:43102. doi: 10.1063/1.4996643

11. Yang D, Lin H, Huang X. Dual broadband metamaterial polarization converter in microwave regime. Progress in electromagnetics research. *Letters.* (2016) **61**:71–6. doi: 10.2528/PIERL16033004
12. Lin B, Guo J, Chu P, Huo W, Xing Z, Huang B et al. Multiple-band linear-polarization conversion and circular polarization in reflection mode using a symmetric anisotropic metasurface. *Phys Rev Appl.* (2018) **9**:024038. doi: 10.1103/PhysRevApplied.9.024038
13. Fu YN, Zhang XQ, Zhao GZ, Li YH, Yu JY. A broadband polarization converter based on resonant ring in terahertz region. *Acta Phys Sin-Ch Ed.* (2017) **66**:180701. doi: 10.7498/aps.66.180701
14. Grady NK, Heyes JE, Chowdhury DR, Zeng Y, Reiten MT, Azad AK et al. Terahertz metamaterials for linear polarization conversion and anomalous refraction. *Science.* (2013) **340**:1304–7. doi: 10.1126/science.1235399
15. Mun SE, Kim SJ, Hong J, Lee B. Polarization conversion in toroidal metamaterial in optical spectral range. In: *2018 Conference on Lasers and Electro-Optics Pacific Rim, CLEO-PR.* Hong Kong (2018). doi: 10.1364/CLEOPR.2018.W3A.146
16. Yu JB, Ma H, Wang JF, Feng MD, Li YF, Qu SB. High-efficiency ultra-wideband polarization conversion metasurfaces based on split elliptical ring resonators. *Acta Phys Sin-Ch Ed.* (2015) **64**:178101. doi: 10.7498/aps.64.178101
17. Khan MI, Fraz Q, Tahir FA. Ultra-wideband cross polarization conversion metasurface insensitive to incidence angle. *J Appl Phys.* (2017) **121**:45103. doi: 10.1063/1.4974849
18. Akram MR, Ding G, Chen K, Feng Y, Zhu W. Ultrathin single layer metasurfaces with ultra-wideband operation for both transmission and reflection. *Adv Mater.* (2020) **32**:1907308. doi: 10.1002/adma.2019 07308
19. Xie Y, Yang C, Wang Y, Shen Y, Deng X, Zhou B et al. Anomalous refraction and reflection characteristics of bend V-shaped antenna metasurfaces. *Sci Rep.* (2019) **9:**6700. doi: 10.1038/s41598-019-43138-1
20. Huan X, Yang H, Yu S, Hui W. Dual-functional metamaterial for reflection and transmission polarization conversion. Singapore: IEEE. (2017) 1–2. doi: 10.1109/CLEOPR.2017.8118652
21. Tang-Jing L, Jian-Gang L, Hai-Peng L. Broadband circularly polarized high-gain antenna design based on single-layer reflecting metasurface. *Acta Phys Sin-Ch Ed.* (2016) **66**:064102. doi: 10.7498/aps.65.104101

Conflict of Interest: The authors declare that the research was conducted in the absence of any commercial or financial relationships that could be construed as a potential conflict of interest.

frontiers in Physics

ORIGINAL RESEARCH
published: 27 January 2021
doi: 10.3389/fphy.2020.595732

Realization of Accurate Load Impedance Characterization for On-Wafer TRM Calibration

Jiangtao Su, Jianhua Wang, Fei Wang and Lingling Sun*

Key Laboratory of RF Circuits and Systems, Ministry of Education, HangZhou, China

In this paper, the uncertainty and the impact of imperfect load calibration standard for on-wafer Through-Reflect-Match calibration method are analyzed with the help of 3D electromagnetic simulations. Based on the finding that load impedance can lead to significant errors in calibration, an automatic algorithm to determine the complex impedance of the load standard is proposed. This method evaluates the resistance as well as the parasitic inductance introduced by the misalignment of the probe tip to the substrate pad at mm-wave frequencies or the non-precize load standard. The proposed algorithm was verified by practical measurement, and the results show that by incorporating actual load impedance into the calibration algorithm, the deviations of RF measurement results are greatly suppressed.

Keywords: calibration, on-wafer, vector network measurement, through-reflect-match, load impedance

Edited by:
Lin Chen,
University of Shanghai for Science and Technology, China

Reviewed by:
Jianming Wen,
Kennesaw State University, United States
Bin Chen,
Hefei University of Technology, China

****Correspondence:***
Jiangtao Su
jtsu@hdu.edu.cn

Specialty section:
This article was submitted to Optics and Photonics, a section of the journal Frontiers in Physics

Received: *17 August 2020*
Accepted: *16 November 2020*
Published: *27 January 2021*

Citation:
Su J, Wang J, Wang F and Sun L (2021) Realization of Accurate Load Impedance Characterization for On-Wafer TRM Calibration. Front. Phys. 8:595732. doi: 10.3389/fphy.2020.595732

1 INTRODUCTION

In order to research and develop the application of millimeter wave devices in the commercial world, accurate on-wafer measurement is a key requirement since it eliminates the additional errors and uncertainties introduced by the device package [1–3]. For this purpose, careful on-wafer calibrations must be employed to eliminate the systematic errors typically caused by system directivity, loss/delay of measurement paths, or the mismatch of measurement ports. The calibration process of determining error coefficients involves the measurement of a set of pre-defined calibration standards, and various calibration algorithms have been developed and named according to the types of calibration standards being used [4]. Those standards are assumed to have either known or partially known "ideal" characteristics. However, at higher frequencies, due to the difficulty in manufacturing precise calibration standards, it is widely accepted that TRL calibration, which consists of measuring Through, Reflect, and Transmission Line standards, is the most accurate method since it has the least requirement for precise calibration standards and lumped models [5].

However, the TRL technique sets the reference impedance after the calibration by the characteristic impedance of the through/lines used. The accurate determination of the frequency-dependent calibration lines' characteristic impedance thus becomes a key requirement to allow for the correct S-parameter measurement. At lower frequencies, when radiation losses and surface waves can be neglected, the line's characteristic impedance can be calculated using quasi-static approaches like con-formal mapping [6–8]. But with the frequency increasing and the substrate becoming complex, these become less accurate. Many techniques have since been proposed to solve this issue, such as extracting from S-parameter measurements [9], estimating from capacitance per unit length [10], using 3D EM simulation to estimate transmission line impedance [11], or relating the characteristic impedance of the line to an ideal pure-real load [12, 13].

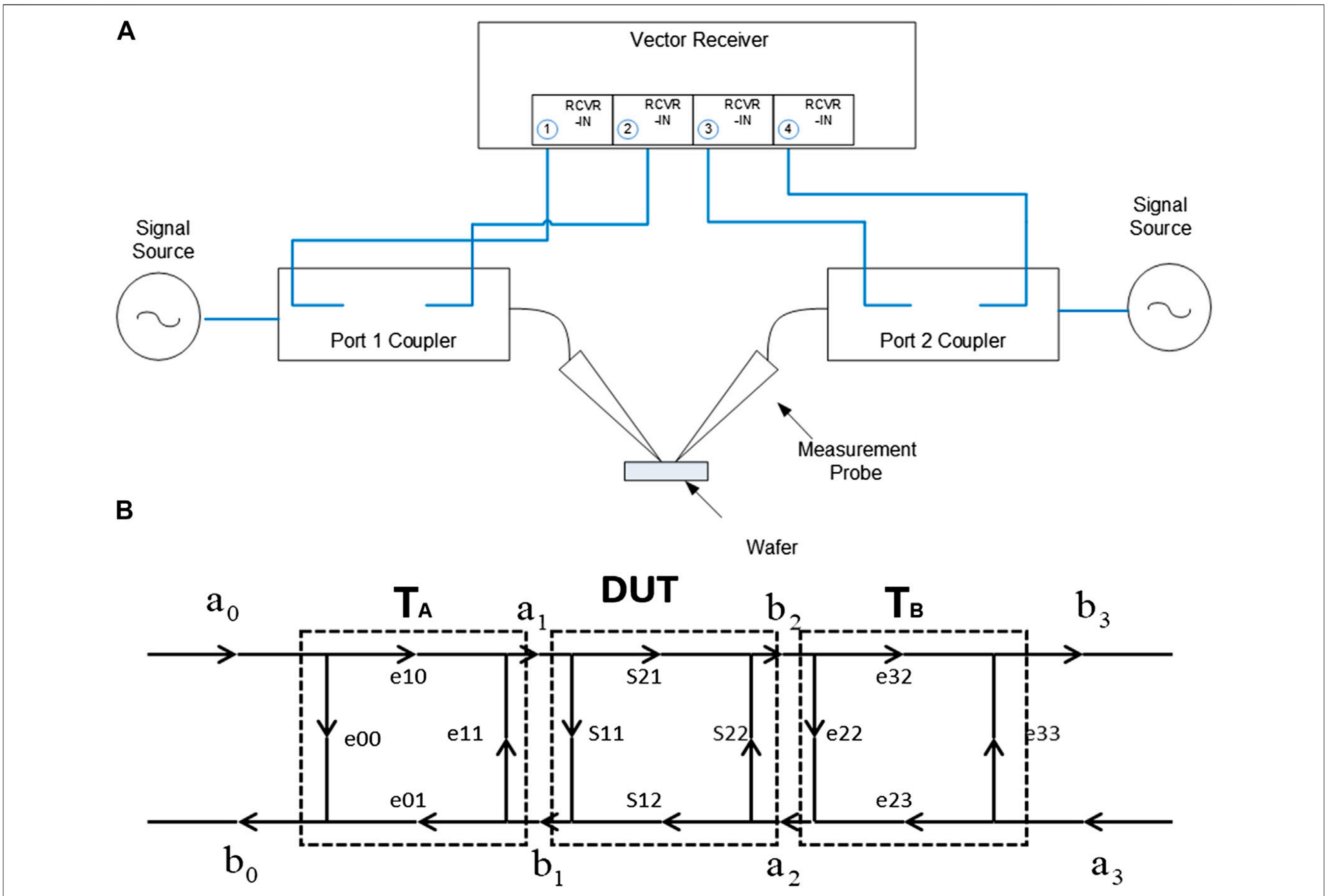

FIGURE 1 | Typical on-wafer measurement system structure: **(A)** Topology diagram and **(B)** Simplified error network diagram.

The issue of accurate characteristic impedance of lines, along with other shortcomings of TRL calibration, such as how multiple lines are required to cover greater than an 8:1 frequency band and the impractically long length of lines at lower frequencies, calls for an alternative calibration approach to TRL calibration [14, 15]. Recently, the Through-Reflect-Match (TRM) method has shown the potential to be widely used in on-wafer measurement [16, 17]. TRM is very similar to TRL calibration in that it does not require accurate specification of the reflect standard coefficient. However, unlike TRL calibration, the through standards must be a non-zero length through (line). Additionally, the perfect match standard is substituted for the line standard in the TRL method, which in practical terms can be conceived as an infinitely long line. In TRM calibration, the match standard is the only impedance that needs to be defined. Moreover, the reflect needs only to be identical for each port so that a fixed-size well-behaved coplanar resistor is enough for broadband and accurate on-wafer measurement systems [18, 19].

However, the biggest problem with TRM calibration is its reliance on a precise and predictable load standard. When the assumption of a non-reflecting match standard is not fulfilled, calibration introduces extra residual errors, which degrades the measurement accuracy. However, the ideal load standard to provide a perfect match can never be realized in practice [20] Moreover, due to the overlap between the probe tip and the calibration pad, parasitic load inductance also rises. The accurate determination of the load impedance thus becomes a key requirement of TRM calibrations, and the actual value of the match standard must be incorporated into the calculation of the error coefficients. Many researchers have noticed this issue, and several complex algorithms to estimate and to correct the effect of the load reactance have been proposed [21–23]. These methods still have the assumption that the resistance of the load is frequency independent and has the same impedance with the thru lines. Other reported techniques include using precisely known frequency-dependent load [17, 24] or using LRRM methods [25] and TMRR [26] to overcome the inaccuracy of the match standard.

In this paper, we propose an improved method to characterize the imperfect match standard for precise on-wafer TRM calibration. Firstly, an uncertainty analysis of TRM calibration using imperfect calibration standards is carried out. Next, a model of the load standard is established using 3D EM simulation. A smart automatic load impedance determination algorithm is thus elucidated. Finally, in **section 4**, the proposed method is verified on a real on-wafer measurement bench, showing the effectiveness of this method.

2 UNCERTAINTY ANALYSIS OF TRM CALIBRATION

A simplified block diagram of an on-wafer measurement system is shown in **Figure 1A**, where the main instruments used are a probe station and a Vector Network Analyser (VNA) and its simplified error network can be expressed as in **Figure 1B**. If the isolation and non-symmetry between the non-measurement ports can be dismissed, the standard 16-term error model can be simplified to a standard eight-term error model, where e_{00},e_{11},e_{01}, and e_{10} are the error terms of block A, and e_{22},e_{23},e_{23}, and e_{32} are error terms of bock B. The calibration process can thus be inferred to determine the eight error terms from a set of uncorrected S-parameters measured on a set of calibration standards. For a two-port network, the S-parameter S_{ij} of calibration items are therefore linearly related to the raw S-parameter measurement data by error terms e_{00} e_{32}. For TRM calibration, the raw S-parameter measurement data measured by the Vector Network Analyzer can be expressed as

$$S_{raw11} = \frac{(e_{00} - S_{11}U)(1 - S_{22}e_{22}) - S_{21}S_{12}e_{22}U}{N} \tag{1}$$

$$S_{raw22} = \frac{(e_{33} - S_{22}V)(1 - S_{11}e_{11}) - S_{21}S_{12}e_{11}V}{N} \tag{2}$$

$$S_{raw12} = \frac{(S_{12}(e_{00}e_{11} - U))}{KN} \tag{3}$$

$$S_{raw12} = \frac{(S_{21}K(e_{22}e_{33} - V))}{N}, \tag{4}$$

where

$$U = e_{00}e_{11} - e_{01}e_{10} \tag{5}$$

$$U = e_{22}e_{33} - e_{23}e_{32} \tag{6}$$

$$K = \frac{e_{01}}{e_{23}} \tag{7}$$

In order to evaluate the measurement deviations ∂S_{ij}, it is necessary to find the deviations of error terms $\partial e_{00}, \partial e_{11}, \partial e_{22}, \partial e_{33}, \partial U, \partial V, \partial K$. Assume that the deviation of the original measured value of the S-parameter is 0, calculate the differentials the **Eqs 1–4**, and we have

$$\partial S_{raw_{ij}} = \frac{\partial S_{raw_{ij}}}{\partial S_{11}}\partial S_{11} + \frac{\partial S_{raw_{ij}}}{\partial S_{12}}\partial S_{12} + \frac{\partial S_{raw_{ij}}}{\partial S_{22}}\partial S_{22} + \frac{\partial S_{raw_{ij}}}{\partial e_{00}}\partial e_{00} + \ldots$$
$$+ \frac{\partial S_{raw_{ij}}}{\partial U}\partial U + \frac{\partial S_{raw_{ij}}}{\partial V}\partial V + \frac{\partial S_{raw_{ij}}}{\partial K}\partial K = 0\,(i = 1, 2; j = 1, 2) \tag{8}$$

By **Eq. 8**, the deviations of measurement S parameters, ∂S_{ij}, can be represented by the deviations of error terms from the calibration. Typically for on-wafer measurement system $|K| = 1, |U| \approx -1$, $|V| \approx -1$, and $|e_{00}|, |e_{11}|, |e_{22}|, and |e_{33}| \leqslant 0.1$. Based on the TRM calibration algorithm, for a two-port network, its reflection coefficient S_{11} and S_{22} are mainly influenced by the deviations $S\partial e_{00}$ and ∂e_{33}, respectively. The transmission coefficient S_{12} and S_{21} are mainly influenced by the deviations $S\partial e_{01}$, ∂e_{23}, and $S\partial e_{32}$, ∂e_{10}, respectively. The deviations from the ideal S-parameters associated with Through, Match, and Reflect standard measurement can therefore be described by the deviations scattering matrices as

$$R_m = \begin{bmatrix} \Gamma_{actual} + \delta S_{11} & 0 \\ 0 & \Gamma_{actual} + \delta S_{22} \end{bmatrix} \tag{9}$$

$$T_m = \begin{bmatrix} \delta T_{11} & 1 + \delta T_{12} \\ 1 + \delta T_{21} & \delta T_{22} \end{bmatrix} \tag{10}$$

$$M_m = \begin{bmatrix} \delta M_{11} & 0 \\ 0 & \delta M_{22} \end{bmatrix} \tag{11}$$

In the above equations, the R_m, T_m, and M_m correspond to the measured S parameters of the Reflect, Thru, and Match standards, respectively. In the scenario that the calibration standards are not ideal, the deviations of the S parameters are calculated as

$$R_m = \begin{bmatrix} \Gamma_{actual} + \partial S_{11} & 0 \\ 0 & \Gamma_{actual} + \partial S_{22} \end{bmatrix} \tag{12}$$

$$T_m = \begin{bmatrix} \partial T_{11} & 1 + \partial T_{12} \\ 1 + \partial T_{21} & \partial T_{22} \end{bmatrix} \tag{13}$$

$$M_m = \begin{bmatrix} \partial M_{11} & 0 \\ 0 & \partial M_{22} \end{bmatrix} \tag{14}$$

In the above equations, the R_m, T_m, and M_m correspond to the measured S parameters of the Reflect, Thru, and Match standards respectively. In the scenario that the calibration standards are not ideal, the deviations of the S parameters are calculated as follows.

For non-ideal Reflection standard:

$$\partial S_{ii} = -\frac{S_{ii}}{2 \cdot \Gamma}\partial \Gamma \tag{15}$$

For non-ideal Thru standard:

$$\partial S_{12} = -(S_{12} \cdot \partial T_{11} - \partial T_{12} - S_{11}\partial T_{22})S_{12} \tag{16}$$

For non-ideal Match standard:

$$\begin{aligned} \partial S_{12} &= S_{12}S_{22}\partial M_{11} + S_{11}S_{12}\partial M_{22} \\ \partial S_{11} &= -(1 + S_{12}S_{21}\partial M_{11} + S_{11}S_{11}\partial M_{22}) \end{aligned} \tag{17}$$

The above analysis suggests that the non-ideal reflect standard does not affect the measured reflection coefficient, whilst the deviation of the through and match standards would cause degradation of the measured impedance and insertion loss. In other words, the errors in the TRM calibration mainly come from the asymmetry of a through/line standard and the deviation of the load standard from 50 Ω.

The error comes from the first source and can be minimized by introducing an additional reverse injected active VNA measurement as proposed in Ref. 18, but the latter has to rely on perfect fabrication of load standard or accurate characterizing the load impedance. However, the impedance of most on-wafer loads is non-ideal; it is not only limited by the fabrication process but could also contribute to the variation in environment temperature. This would lead to significant error

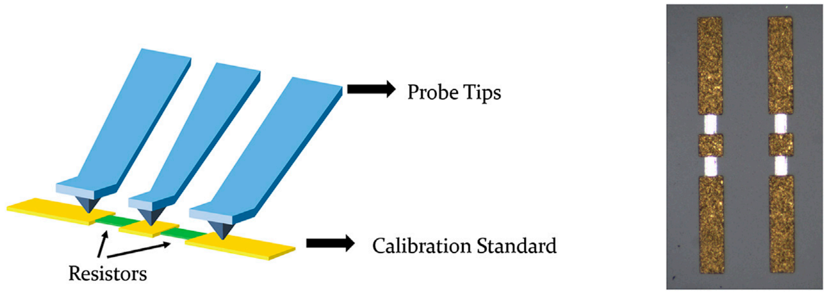

FIGURE 2 | The full structure including probes, pad and calibration standard **(left)**, and the microscope view of a real load standard **(right)**.

in the subsequent measurement, especially in mm-wave and further high-frequency bands. It is therefore necessary to characterize the actual load impedance and incorporate them to TRM calibration.

3 DETERMINE THE ON-WATER LOAD IMPEDANCE

3.1 Model of the Match Standard

For on-wafer measurement, the calibration standard is typically fabricated in the form of coplanar waveguide (CPW) geometry. As shown in **Figure 2**, the load consists of two 100 Ω resistors in between the Ground-Signal-Ground (GSG) pads, which are typically made of thin film gold to connect with the probe tips. **Figure 2** also shows the real image of a typical microscope view of the load standard under the probe station. Because the probe tip is fragile, the connection between the probe tip and the calibration standards may vary during different measurements. Moreover, since the probe position to the pad relies wholly on the operators' manipulation under microscopic observation, the contact point between the probe tips and the pads may differ from one measurement to another. Usually for high-frequency measurement, the complete calibration measurement must be iterated several times before acceptable measurement results are obtained.

To better understand the influence of the probe-pad alignment on the load impedance, EM simulation using HFSS software was carried out. In the simulation, the meshed ground planes were simplified considering a continuous metal connection, both vertically and horizontally. This simplification provides a good approximation of the electrical response of the structure, the openings in the metal mesh being much smaller than the wavelength. The signal pad is modeled as a 50*50*3.4 um metal with conductivity of 4.9E7 S/m, and the distance from the signal pad to ground is 100 um. The load consists of two identical zero-thickness rectangular sheets in contact with the signal pad and the ground with a boundary condition of 100 lumped resistance. The CPW line is excited by a wave-guide port considering parasitic effects.

Figure 3 provides the electric field distribution at the wave feeding port, indicating a gentle discontinuity when load resistance is present. This mainly comes from the simulation

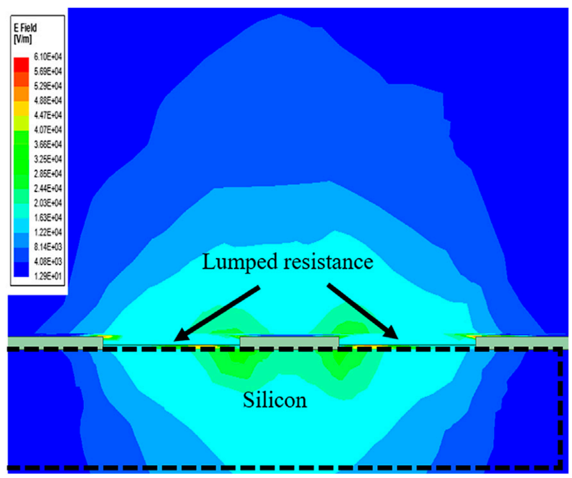

FIGURE 3 | Field distribution of match standard at 100 GHz simulated by Ansoft HFSS Software.

process where resistance presents a large topological discontinuity, and the boundary conditions therefore lead to the numerical solution deviations in the finite-element numerical simulation process. **Figure 4** shows that by putting the probe tip at three different positions 40 um apart, a non-negligible deviation in the impedance emerges, which indicates a possible source of calibration error.

A lumped elements model, as shown in **Figure 5**, was constructed to further analyse the impedance of the match standard, which takes account of the distributed nature of the load, as well as the coupling between the probe and the calibration standard. During the measurement, the capacitance across the resistor stayed nearly constant, but the inductance changed significantly due to the change of probe tip contact position. Since the capacitance was very small and can be regarded as negative inductance, a simplified first order inductance in series with the resistor, also as shown in **Figure 5**, can be used to simplify the analysis. It is also worth noting that the value of this inductance now includes different probe contacts between different measurements.

As can be seen in **Figure 6**, the simplified model accounts for the DC resistance of the load and the series inductance fits well

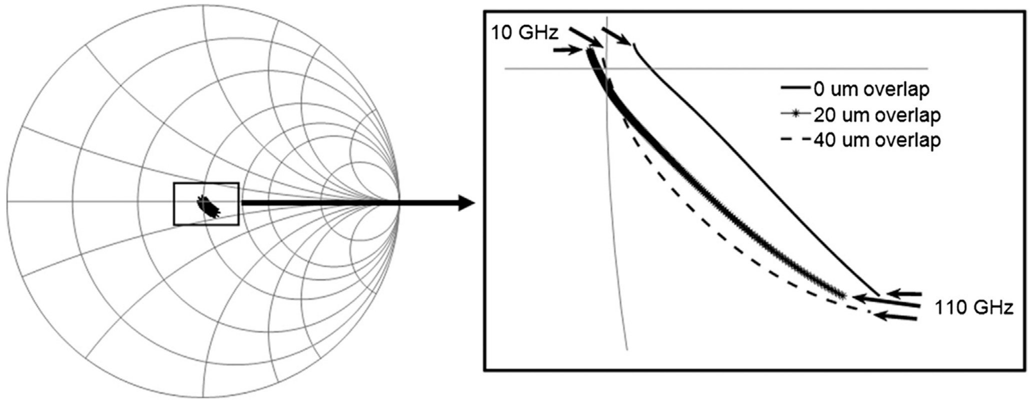

FIGURE 4 | The variation of match standard impedance with different probe tip position on pads.

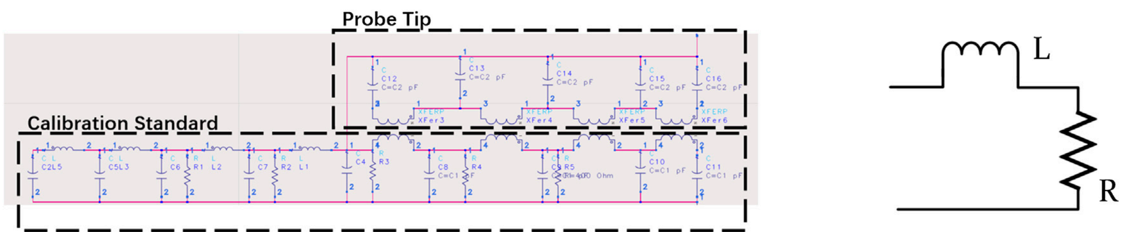

FIGURE 5 | The lumped circuit model for probe contacting with the calibration standard in ADS simulation software **(left)** and simplified equivalent circuit model **(right)**.

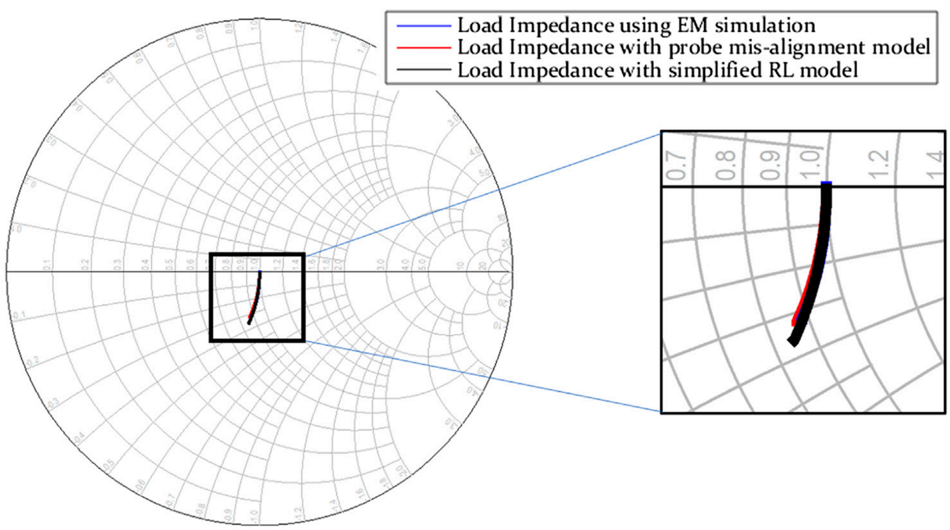

FIGURE 6 | The load impedance using EM simulation, probe misalignment model and simplified model.

with the complicated mis-alignment model and the EM simulation. It is therefore possible to use the simplified model alone to determine the resistance and inductance of the load.

3.2 Evaluation of Actual Match Impedance

From the analysis in **section 2**, if the TRM calibration is performed with the assumption that the match is ideal, while in reality it is not, an offset will be introduced into the measured

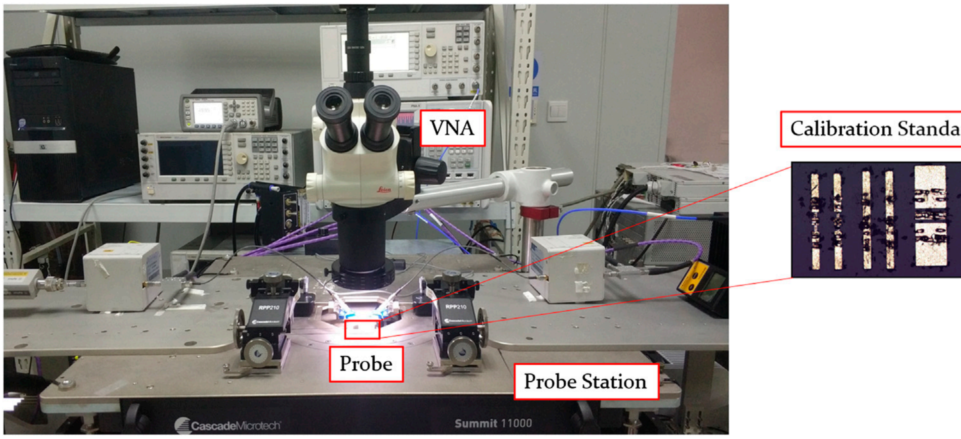

FIGURE 7 | The measurement bench and the imperfect calibration standard used in the experiment.

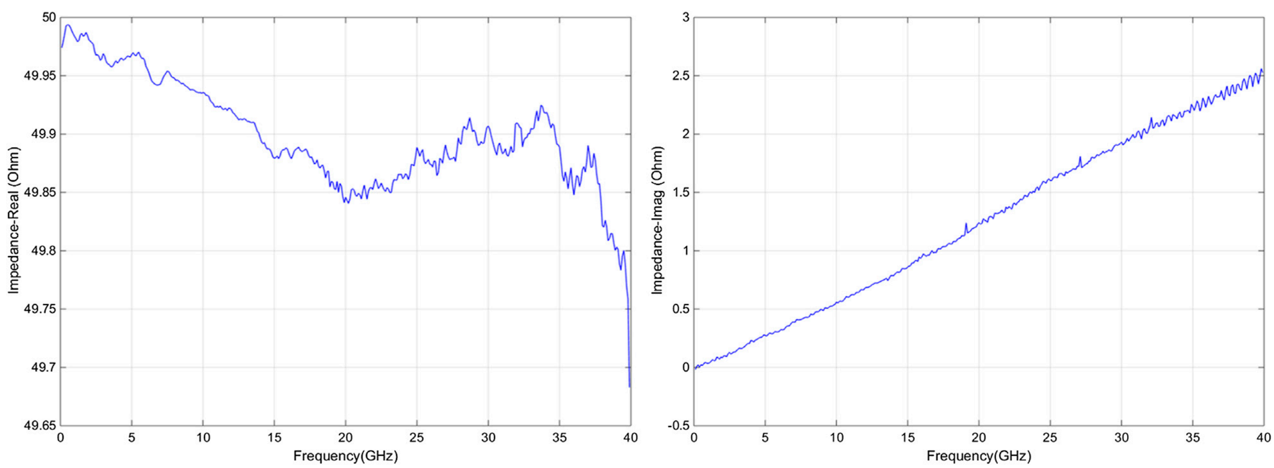

FIGURE 8 | The real part of load impedance **(left)** and the imaginary part of the load impedance **(right)** calculated load measured.

DUT impedance. Supposing the load has an actual impedance of $Z_L = R + jX$, then a one-port DUT with actual impedance Z_{act} will have the measured impedance equals to $Z_{meas} = Z_{act}Z_0/Z_L$, where $Z_0 = 50\ \Omega$.

The TRM calibration method, by definition, always solves the error terms with the reference plane at the center of the Through standard. The probes-in-air open therefore actually corresponds to a negative-length open stub with a length one-half that of the Through standard and with the reflection coefficient magnitude of unity. If the match standard used in the calibration is offset, it would appear to have a magnitude different from one; additionally, as the on-wafer ISS short standard typically has the same length as the Through line, the short standard will have the reflection coefficient magnitude of unity but in the admittance chart. The open and short calibration standard thus provides a convenient means of determining how far the match standard is offset from the standard 50 Ω.

Returning to the calibration models described in **Figure 1**, supposing the same match standard is used in both port 1 and port 2 measurement, the complete measurement matrix of T_A can be represented as

$$T_A = \begin{bmatrix} A_A & B_A \\ C_A & D_A \end{bmatrix} \tag{18}$$

Z_M represents the impedance of the loads used as the match standard at measurement port. The terms A_A, B_A, C_A, and K_A are determined by the raw calibration measurement of Reflect and Through measurement. In the case of measuring match standard, the Y parameter, or the admittance of the match standard, can be expressed as

$$Y_{load} = \frac{D_A}{B_A} = K_A \tag{19}$$

As the K_A is solely decided by the match standard, for one port, DUT is measured at port 1, **Eq. 16** is still valid, and the measured Y parameter of the DUT can be expressed as

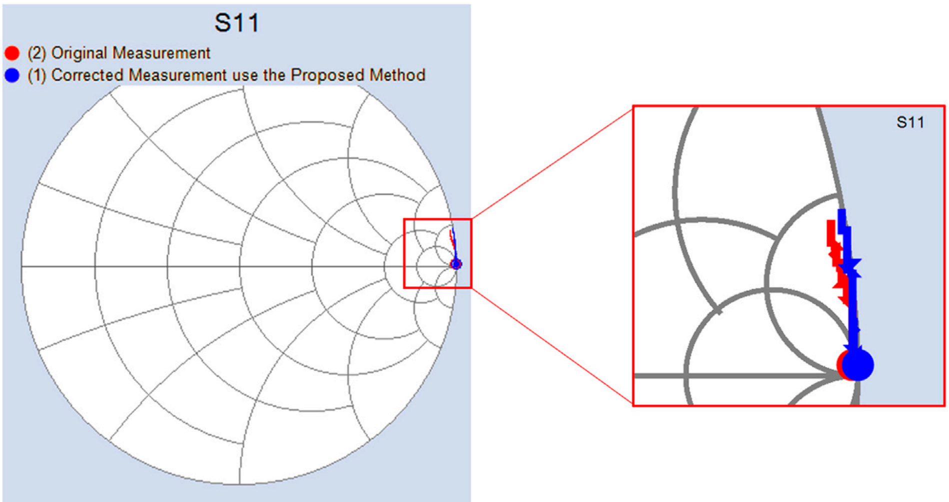

FIGURE 9 | The re-measured open standard with conventional TRL calibration method (red) and the correction method proposed in this work (blue).

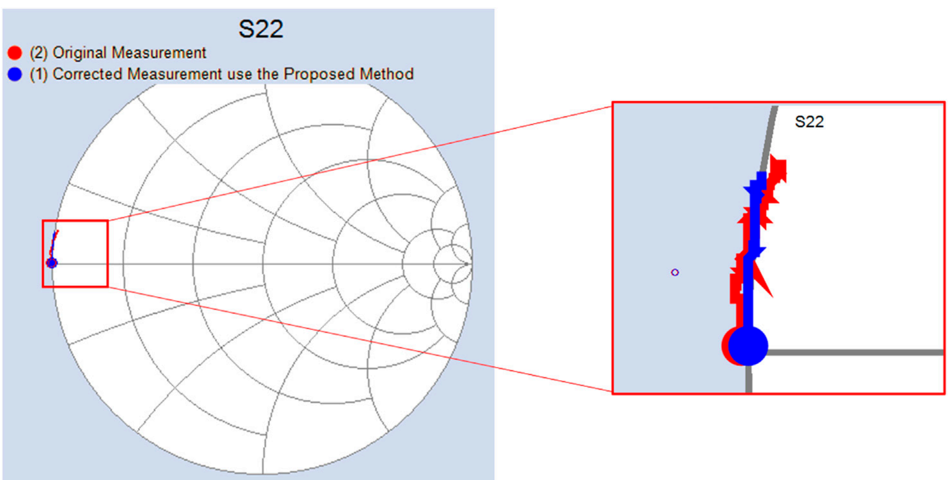

FIGURE 10 | The re-measured short standard with conventional TRL calibration method (red) and the correction method proposed in this work (blue).

$$Y_{dut-measure} = T_A \cdot T_{dut} = K_A \cdot Y_{dut-real} \tag{20}$$

If the match standard is improperly defined, the above function will behave as

$$Y_{dut-measure} = \frac{Y_{load-ideal}}{Y_{load-real}} \cdot Y_{dut-real} \tag{21}$$

Obviously, the Y parameter of the ideal load and actual load can be separately defined as

$$Y_{load-ideal} = \frac{1}{50} Y_{load-actual} = \frac{1}{R + jwL} \tag{22}$$

Considering the scenario that the DUT is a pure reflection such as an open standard, and combining **Eqs 12** and **13**, we have

$$Y_{open-measure} = G + jB = \frac{R + jwL}{50} Y_{open-real} \tag{23}$$

Similarly, considering the DUT is a pure reflection as short standard, we have

$$Z_{short-measure} = R + jX = \frac{50}{(R + jwL)} Z_{short-real} \tag{24}$$

According to **Eqs 20** and **21**, therefore, after TRM calibration, if we have the ideal open and short calibration standard, the correct impedance and inductance of the load can be calculated. However, this algorithm so far still has the assumption that the loss from the probe tip to the center-of-through is 0. Since the length of the Through standard typically is very short, the loss usually is so small that it can be considered negligible. For example, the FormFactor 101-190 ISS calibration standard has a loss of 0.04 dB at 40 GHz. However, at higher frequencies on the mm-Wave band, the Through loss becomes an issue which would make the reflection coefficient of the open/short standard not equal, nor equal to unity, thus rendering the extracted load impedance no longer accurate.

To correct the limitations of the proposed algorithm, an iteration process is thus being introduced, which will take account of the length of the Through and the Short standard. The full calibration steps can thus be summarized as follows:

1. Make a TRM calibration with the assumption that the load standard is ideal 50 Ω impedance.
2. Use the calculated error coefficients to measure the S-parameters of the open and short standard.
3. Calculate the actual impedance of the load standard as the guess value.
4. Recalculate the error terms from the calculated actual load impedance.
5. Re-measure the S parameters of the open, short, and through standard with the corrected error terms.
6. Calculate a difference between the expected reflect coefficient of open, short, and thru standard.
7. Repeat step 3 to step 6 to minimizes the errors and obtain the desired load impedance.

4 MEASUREMENT RESULTS OF THIS CALIBRATION METHOD

In order to validate the method proposed, we built a measurement bench composed of a manual probe station, Cascade Summit 11,000, and a Keysight PNA-X Vector Network Analyser. A detailed photo of the measurement bench is shown in **Figure 7**. A used FormFactor 101-190 ISS substrate, which was clearly worn and by no means in its best condition, was selected to verify if the proposed method could correct the calibration error from the imperfect calibration standard. The measurement frequency was from 0.1 to 40 GHz. The calibration algorithm was implemented using Python as was the instrument control method.

Figure 8 shows the real and imaginary parts of the calculated load impedance extracted using the proposed method. The impedance of the load standard, though perhaps very precise when it was fabricated, is away from 50 and disperses with frequency. This was very probably caused by the worn surface, which can be clearly seen via the microscope, as shown in **Figure 7**. The dispersion with the frequency also suggests that the parasitic inductance of the load standard changes with the frequency.

Next, we drew the S-parameter measurements of the open and short standard, by both the classical TRM calibration method and the impedance correction method proposed in this work. As can be seen in **Figure 9** and **Figure 10**, the ideal probe-on-air open standard has negative inductance, and the short standard is also inductive with the magnitude of unity. Due to the imperfection of the load standard, both the open and short standard are offset from the unity circle using the classical TRM calibration method, which was effectively corrected with the calculated load impedance to recalculate the error coefficients.

5 CONCLUSION

In this paper, a comprehensive analysis of the error source of TRM calibration is presented, leading to the conclusion that load impedance is the most important determinant of on-wafer calibration quality. Based on full wave 3D EM simulations, it is shown that the imperfect load impedance was not only caused by the non-precize DC resistance of the load but also by the overlap between the probe tips and the pads on the substrate.

An improved load impedance estimation algorithm has therefore been presented, which automatically calculates the load's complex impedance in the calibration process. Actual measurements on worn calibration standards up to 40 GHz show that the RF performance due to the variations of imperfect load standard can be corrected by accommodating the calculated load impedance into the TRM calibration method. The novelty of the estimation method lies in is its immune to pad-to-tip discontinuities since it calculates the actual impedance at the time of calibration. Moreover, the dependence on a fully automated probe station or an operator experienced in on-wafer measurement is eliminated with the proposed smart impedance calculation method. The proposed algorithm would find immediate application in the on-wafer characterization of mm-wave or higher frequencies device.

DATA AVAILABILITY STATEMENT

The raw data supporting the conclusions of this article will be made available by the authors, without undue reservation.

AUTHOR CONTRIBUTIONS

First Author conceived of the presented idea, JS and JW developed the algorithm and performed the computations. JS and FW. verified the analytical methods with experiment. LS encouraged authors to investigate this calibration issue and supervised the findings of this work. All authors discussed the results and contributed to the final manuscript.

FUNDING

This work is funded by the National Natural Science Foundation of China (No.61827806, No.61871161) and the Key Lab Research Foundation of Science and Technology on Electronic Test & Measurement Laboratory (6142001190103).

REFERENCES

1. Deng M, Quémerais T, Bouvot S, Gloria D, Chevalier P, Lépilliet S, et al. Small-signal characterization and modelling of 55 nm sige bicmos hbt up to 325 ghz. *Solid State Electron* (2017) 129:150–6. doi:10.1016/j.sse.2016.11.012
2. Seelmann-Eggebert M, Ohlrogge M, Weber R, Peschel D, Maßler H, Riessle M, et al. On the accurate measurement and calibration of s-parameters for millimeter wavelengths and beyond. *IEEE Trans Microw Theor Tech* (2015) 63:2335–42. doi:10.1109/tmtt.2015.2436919
3. Yau K, Dacquay E, Sarkas I, Voinigescu SP. Device and ic characterization above 100 ghz. *IEEE Microw Mag* (2012) 13:30–54. doi:10.1109/mmm.2011.2173869
4. Williams DF, Young AC, Urteaga M. A prescription for sub-millimeter-wave transistor characterization. *IEEE Trans Terahertz Sci Technol* (2013) 3:433–9. doi:10.1109/tthz.2013.2255332
5. Williams DF, Marks RB, Davidson A. Comparison of on-wafer calibrations. *38th ARFTG Conf Dig (IEEE)* (1991) 20:68–81. doi:10.1109/arftg.1991.324040
6. Veyres C, Fouad Hanna V. Extension of the application of conformal mapping techniques to coplanar lines with finite dimensions. *Int J Electron* (1980) 48: 47–56. doi:10.1080/00207218008901066
7. Carlsson E, Gevorgian S. Conformal mapping of the field and charge distributions in multilayered substrate cpws. *IEEE Trans Microw Theor Tech* (1999) 47:1544–52. doi:10.1109/22.780407
8. Wen CP. Coplanar waveguide: a surface strip transmission line suitable for nonreciprocal gyromagnetic device applications. *IEEE Trans Microw Theor Tech* (1969) 17:1087–90. doi:10.1109/tmtt.1969.1127105
9. Eo Y, Eisenstadt W. High-speed vlsi interconnect modeling based on s-parameter measurements. *IEEE Trans Compon Hybrids Manuf Technol* (1993) 16:555–62. doi:10.1109/33.239889
10. Williams DF, Marks RB. Transmission line capacitance measurement. *IEEE Microw Guid Wave Lett* (1991) 1:243–5. doi:10.1109/75.84601
11. Galatro L, Spirito M. Millimeter-wave on-wafer trl calibration employing 3-d em simulation-based characteristic impedance extraction. *IEEE Trans Microw Theor Tech* (2017) 65:1315–23. doi:10.1109/tmtt.2016.2609413
12. Marks RB, Williams DF. Interconnection Transmission Line Parameter Characterization. 40th ARFTG Conference Digest, Orlando, FL, USA, 1992. pp. 88–95. doi:10.1109/ARFTG.1992.327004
13. Williams DF, Arz U, Grabinski H. Characteristic-impedance measurement error on lossy substrates. *IEEE Micro Wireless Compon Lett* (2001) 11:299–301. doi:10.1109/7260.933777
14. Rumiantsev A, Sweeney SL, Corson P.L. Comparison of on-wafer multiline TRL and LRM+ calibrations for RF CMOS applications. 2008 72nd ARFTG Microwave Measurement Symposium, Portland, OR, USA, 2008, pp. 132–136. doi:10.1109/ARFTG.2008.4804291
15. Chen L, Zhang C, Reck TJ, Arsenovic A, Bauwens M, Groppi C, et al. Terahertz micromachined on-wafer probes: repeatability and reliability. *IEEE Trans Microw Theory Tech* (2012) 60:2894–902. doi:10.1109/TMTT.2012.2205016
16. Eul HJ, Schiek B. Thru-Match-Reflect: One Result of a Rigorous Theory for De-Embedding and Network Analyzer Calibration. 1988 18th European Microwave Conference, Stockholm, Sweden, 1988, pp. 909–914. doi:10.1109/EUMA.1988.333924
17. Doerner R, Rumiantsev A. Verification of the wafer-level LRM+ calibration technique for GaAs applications up to 110 GHz. 65th ARFTG Conference Digest, 2005. Spring 2005, Long Beach, CA, USA, 2005, doi:10.1109/ARFTGS.2005.1500562
18. Su J, Yang B, Gao H, Huang X, Cai J, Wang X, et al. A Novel TRM Calibration Method for Improvement of Modelling Accuracy at mm-wave Frequency. 2018 IEEE/MTT-S International Microwave Symposium - IMS, Philadelphia, PA, 2018, pp. 1300–1303. doi:10.1109/MWSYM.2018.8439263
19. Pulido-Gaytán MA, Reynoso-Hernández JA, Loo-Yau JR, Zarate-de Landa A, del Carmen Maya-Sanchez M. Generalized theory of the thru-reflect-match calibration technique. *IEEE Trans Microw Theor Tech* (2015) 63:1693–9. doi:10.1109/TMTT.2015.2417860
20. Kirby P, Dunleavy L, Weller T. The effect of load variations on on-wafer lumped element based calibrations. 54th ARFTG Conference Digest, Atlanta, GA, USA, 2000, pp. 1–10. doi:10.1109/ARFTG.1999.327368
21. Davidson A, Jones K, Strid E. Lrm and lrrm calibrations with automatic determination of load inductance. *36th ARFTG Conf Dig (IEEE)* (1990) 18: 57–63. doi:10.1109/ARFTG.1990.323996
22. Williams DF, Marks RB. Lrm probe-tip calibrations using nonideal standards. *IEEE Trans Microw Theory Tech* (1995) 43:466–9. doi:10.1109/22.348112
23. Hayden L. An enhanced Line-Reflect-Reflect-Match calibration. 2006 67th ARFTG Conference, San Francisco, CA, USA, 2006, pp. 143–149. doi:10.1109/ARFTG.2006.4734364
24. Scholz RF, Korndorfer F, Senapati B, Rumiantsev A. Advanced technique for broad band on-wafer rf device characterization. In IEEE Arftg 63rd conference. Fort Worth, TX: Spring 2004 (2004). 83–90.
25. Purroy F, Pradell L. New theoretical analysis of the lrrm calibration technique for vector network analyzers. *IEEE Trans Instrument Meas* (2001) 50, 1307–1314. doi:10.1109/19.963202
26. Rumiantsev A, Fu T, Doerner R. Improving wafer-level calibration consistency with tmrr calibration method. In 91st ARFTG conference digest. ; Philadelphia, PA IEEE (2018). p. 1–4.

Conflict of Interest: The authors declare that the research was conducted in the absence of any commercial or financial relationships that could be construed as a potential conflict of interest.

Advantages of publishing in Frontiers

OPEN ACCESS
Articles are free to read for greatest visibility and readership

FAST PUBLICATION
Around 90 days from submission to decision

HIGH QUALITY PEER-REVIEW
Rigorous, collaborative, and constructive peer-review

TRANSPARENT PEER-REVIEW
Editors and reviewers acknowledged by name on published articles

Frontiers
Avenue du Tribunal-Fédéral 34
1005 Lausanne | Switzerland

Visit us: www.frontiersin.org
Contact us: frontiersin.org/about/contact

REPRODUCIBILITY OF RESEARCH
Support open data and methods to enhance research reproducibility

DIGITAL PUBLISHING
Articles designed for optimal readership across devices

FOLLOW US
@frontiersin

IMPACT METRICS
Advanced article metrics track visibility across digital media

EXTENSIVE PROMOTION
Marketing and promotion of impactful research

LOOP RESEARCH NETWORK
Our network increases your article's readership